Four-wave mixing in rubidium vapour with structured light and an external cavity

Rachel Frances Offer

Experimental Quantum Optics and Photonics Group
Department of Physics and SUPA

University of Strathclyde

A thesis presented in the fulfilment of the requirements for the degree of

Doctor of Philosophy

2018

This thesis is the result of the author's original research. It has been composed by the author and has not been previously submitted for examination which has led to the award of a degree.

Signed:

Date:

Abstract

Thermal atomic vapours are an experimentally simple and efficient system in which to study wave mixing processes. We investigate a resonantly enhanced four-wave mixing (FWM) process in rubidium vapour, which coherently converts 780 nm and 776 nm light to 5.2 µm and 420 nm.

Firstly, we use this system to explore the coherent frequency conversion of structured light, in particular Laguerre-Gauss (LG) beams. These modes, and more generally the orbital angular momentum (OAM) that they carry, are important research tools for optical manipulation, imaging and communication. Previous qualitative studies have demonstrated OAM transfer from the near-infrared pump beams to the generated 420 nm light. We investigate this further by making the first quantitative measurements of the 420 nm transverse mode for a range of values of pump OAM. Our results indicate that the FWM process is likely to be an efficient source of OAM-entangled 5.2 µm and 420 nm light, with a spiral bandwidth that increases with increasing pump OAM.

Using independently shaped pump beams, we also study FWM for more general pump modes, including beams carrying opposite handedness of OAM, coherent superpositions of LG modes, and for the first time in this system, radial LG modes. This work shows the importance of OAM conservation and Gouy phase matching in the FWM process, and is relevant for similar schemes involving the inscription and storage of transverse modes in atomic vapours.

Finally, we report the first use of a ring cavity to both increase the output power and narrow the linewidth of the generated 420 nm light. For Gaussian pump beams, the low-finesse cavity, which is singly resonant with the 420 nm light, increases the maximum 420 nm output power from 340 µW (single pass) to 940 µW (cavity-enhanced), and narrows the linewidth from 33 MHz (single pass) to < 1 MHz (cavity-enhanced), resulting in a narrow linewidth, tunable light source suitable for near resonant rubidium studies.

Acknowledgements

When I started my PhD I honestly could not imagine getting to a point, some time in the future, when I would hand in a thesis. I have many people to thank for helping me get here.

Firstly, Aidan, thank you for giving me the opportunity to work on this project, and for all of your help throughout. Your support has ensured my enthusiasm for physics has been maintained, even when the going was tough. Thank you for putting up with me for (nearly..) four years. Secondly, Sonja, thank you for providing an invaluable second opinion when two lasers and a vapour cell proved to be more complicated than first thought. I would also like to thank Erling for bringing together an inspiring group of people to work with and for providing support as my second supervisor.

Thank you to everyone who has been a part of the EQOP group during my time here. For the help tracking down various bits of lab equipment, for the ice cream and for the occasionally questionable lunch time chat. Special thanks must go to Griff and Jon, for always making time whenever I had a question, and also for providing helpful comments and feedback on this thesis. Also, thank you to Vicki for providing moral support. Johnny, thank you for your company in the lab, and when you moved next door, for continuing to put up with my many questions. To anyone else within the wider physics department who has lent a hand - thank you.

Those in the Optics group at Glasgow; thank you for always making feel welcome whenever I came across. In particular, to Tom, Neal and Adam. I very much enjoyed working together on the SLM project.

To Mum and Dad, thank you for encouraging my interest in science, and for your ongoing support.

And finally, thank you to Ben for keeping me sane, and to Julia for taking the week-day shifts. I could not have done it without either of you.

Contents

List of Figures

List of Tables

Chapter 1

Introduction

When light is incident on an atom, the oscillating electric field induces an oscillating atomic polarisation [1]. The relationship between the atomic polarisation and the incident field, which is characterised by the susceptibility, determines the optical properties of the atom. If the susceptibility is linear, the atom absorbs or changes the phase of the light. Often, the susceptibility can be highly nonlinear [2]. In this case, the polarisation induced by one optical field can cause the coherent generation of a new optical field at a different frequency - a process described as wave mixing [3].

In this thesis, we study an efficient wave mixing process that can be carried out in a rubidium vapour [4]. We use this process to coherently frequency convert structured light, which has transverse variations in intensity and phase. If the light is shaped so that it has helical phase fronts, the beam carries an associated orbital angular momentum (OAM) [5], and we observe the transfer of this momentum in our wave mixing process. Structured light, and OAM in particular, have potential applications in increasing the bandwidth of both classical [6] and quantum communication [7].

We also investigate the effect of feedback, in the form of an external cavity, on the wave mixing process. A low-finesse ring cavity is constructed, singly resonant with one of the generated fields. We consider the effect of the cavity on the linewidth, output power and transverse mode of the generated light.

This research lies at the intersection of nonlinear optics, structured light and atomic physics. The remainder of the introduction will provide a brief overview of the relevant aspects of these topics, before providing more detail on the work presented here.

1.1 Nonlinear Optics

The optical response of a medium is nonlinear only for sufficiently intense fields, concentrated enough in frequency space. Following the development of the laser in 1960 [8], these conditions became more easily achievable and many demonstrations of nonlinear phenomena quickly followed [9].

Wave mixing was among the first to be demonstrated. In 1961, Franken *et al.* [10] passed light from one of the early ruby lasers through a quartz crystal and observed second harmonic generation - some of the light was converted to double the input frequency, converting two pump photons for each doubled photon. Later experiments showed that if two pump lasers are used then light at linear combinations of the input frequencies can be generated [11, 12], known as sum and difference frequency generation.

The immediate application of wave mixing is to generate wavelengths that are otherwise difficult to generate directly. In processes where the conversion efficiency is small, the frequency converted power can be enhanced by adding feedback to the system. Optical parametric oscillators work in much the same way as lasers, but the gain is provided by a wave mixing process, rather than stimulated emission [13, 14].

For symmetry reasons, the simplest wave mixing process that can occur in an atomic vapour is four-wave mixing (FWM) - energy transfer between four optical fields [15, 16]. The FWM process investigated in this thesis is illustrated in Fig. 1.1. Two pump fields, at 780 nm and 776 nm generate two new optical fields at 5.2 µm and 420 nm.

Wave mixing processes are parametric; the initial and final quantum state of

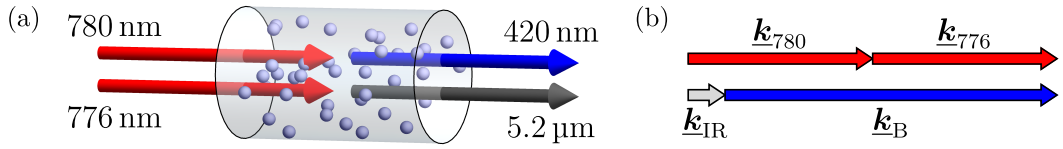

Figure 1.1: (a) Input beams at 780 nm and 776 nm generate 5.2 µm and 420 nm light via FWM in a rubidium vapour. (b) Schematic of the phase matching condition in Eq. 1.1.2

the medium are the same. In order to conserve energy the angular frequency of the fields in our FWM process must satisfy

$$\omega_{780} + \omega_{776} = \omega_{\mathrm{B}} + \omega_{\mathrm{IR}}. \tag{1.1.1}$$

Furthermore, for the wave mixing process to be efficient, the generated light must remain in phase with the pump light as the fields propagate through the medium. This condition is known as phase matching [17], and requires that the wave vectors of the light satisfy

$$\underline{\boldsymbol{k}}_{780} + \underline{\boldsymbol{k}}_{776} = \underline{\boldsymbol{k}}_{\mathrm{B}} + \underline{\boldsymbol{k}}_{\mathrm{IR}}, \tag{1.1.2}$$

which is equivalent to momentum conservation. In this thesis we investigate the wider consequences of this *phase coherence* in the case of FWM with structured light.

Whenever a wave mixing process generates two new photons, the photon pair is described by a highly correlated two-photon state [18]. For spontaneous paramteric down conversion [19–21], where a single pump photon is converted to two lower energy photons, this state can be entangled in a variety of degrees of freedom, including transverse position [22] and polarisation [23, 24]. Entangled photon pairs are an important tool and are key to processes such as quantum teleportation [25], entanglement swapping [26, 27] and quantum key distribution [28–30].

1.2 Structured Light

Light interacts very little with the environment, and possesses many degrees of freedom that can be used to encode information, for example intensity, frequency, phase or polarisation. As a result, classical states of light, transmitted via optical fibres, are used to transfer vast amounts of information across the world every second, whilst quantum communication relies on quantum states of light to carry information with minimal decoherence [31].

With all communication systems, the achievable bandwidth is a critical parameter. One method of increasing the bandwidth of optical communication is to use structured light [6,32,33], where the intensity and phase of the light varies transversely across the beam. Examples of structured light include the Hermite-Gauss and Laguerre-Gauss modes [34], more complex transverse patterns, and even more general vector vortex beams [35], where the polarisation also varies transversely. Aside from communication, structured light has many applications, including optical tweezers [36], super resolution imaging [37] and complex trapping potentials for cold atoms [38–40].

In this thesis we study the coherent frequency conversion of Laguerre-Gauss modes, as illustrated in Fig. 1.2. These modes modes have an $e^{i\ell\theta}$ transverse phase dependence (where θ is the azimuthal coordinate in the plane perpendicular to the direction of propagation), resulting in helical phase fronts and an associated orbital angular momentum (OAM) of $\ell\hbar$ [5, 41–43]. Unlike the spin angular momentum related to the polarisation of the field, OAM can take on a theoretically infinifte number of quantised values. When these modes are used in wave mixing,

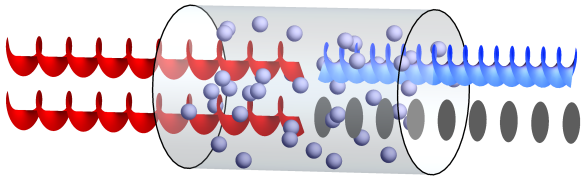

Figure 1.2: Helical phase fronts of Laguerre Gauss beams in FWM.

conservation of transverse phase requires that the generated light must also have helical phase fronts; the OAM carried by the pump beam is transferred to the generated fields [44–46].

If a wave mixing process generates pairs of photons, then the OAM carried by each is not necessarily well-defined and can take any number of values so long as the total OAM is conserved. In this case the photon pairs are generated in an OAM-entangled state [47, 48], with the number of entangled modes determined by the correlated width of the OAM probability distribution of the individual photons - the spiral bandwidth [49]. These higher dimensional entangled states, as well as single photon OAM states, have the potential to increase both the bandwidth and security of quantum communication [50].

1.3 Atomic Vapours

The study of atomic vapours, whether thermal or laser-cooled [51], underpins a huge body of research. Experiments range from fundamental studies of Bose-Einstein condensates [52] and atom interferometry [53], to developing ultra-sensitive and precise magnetometers [54] and atomic clocks [55]. Still further experiments are developing components necessary for future quantum networks [30, 56], including photon pair sources [57, 58] and quantum memories [59, 60].

Understanding, or making use of, the nonlinear interaction between light and atoms is a central theme to many of the above research areas. When optical fields are tuned close to atomic transitions the resonant atomic response leads to a large nonlinear susceptibility. This allows wave mixing processes to be carried out with significantly enhanced efficiency compared to similar processes in bulk materials [61–63].

Resonantly enhanced four-wave mixing (FWM), which is the subject of this thesis, has been carried out in both thermal [64–74] and cold [75–83] atomic vapours. Like SPDC, these FWM processes have been shown to produce highly correlated photon pairs [81–83], as well as polarisation [80] and OAM [66] entan-

gled photons and entangled images [67]. In other experiments, FWM has been used to generate heralded single photons [70, 71, 84], and to frequency convert quantum states [79]. Atomic vapours also present a clean system in which to study the frequency conversion of structured light, and the transfer of OAM [46, 85–88] and transverse images [89] between different frequencies has been demonstrated.

1.4 Thesis summary

The FWM process investigated in this thesis was first studied by Zibrov *et al.* in 2002 [4], and has since been carried out by many other groups [90–95]. We use a thermal rubidium vapour to efficiently convert 780 nm and 776 nm pump beams to 420 nm and 5.2 µm light. The four fields are quasi-resonant with a closed loop of atomic transitions within ^{85}Rb, resulting in a large resonant enhancement of the wave mixing process. In an optimised experiment previously carried out at Strathclyde, 1 mW of 420 nm emission was generated for a total pump power of around 40 mW [92] . Although only the 420 nm light was measured in this experiment, both the 420 nm and 5.2 µm light are generated as coherent, directional beams [4, 96]. Further work at Strathclyde [46], and elsewhere [87, 88], has demonstrated that OAM carried by the pump beams is transferred to the generated 420 nm field, thus confirming that this efficient frequency conversion process is indeed phase coherent.

In this thesis we quantitatively explore the transfer of OAM in the "blue light" FWM system. We examine, both theoretically and experimentally, the phase matching conditions that determine the OAM carried by each generated field. We find that this wave mixing process may be an efficient source of OAM-entangled pairs, with a spiral bandwidth which increases with increasing pump OAM. The frequency conversion of more general structured light is also studied, including pump modes carrying opposite handedness of OAM, radial Laguerre-Gauss modes and modal superpositions.

The results presented in this thesis demonstrate a means of frequency convert-

ing and generating a range of OAM states. Although we work only with classical light, our results will inform future experiments at the single photon level, and are therefore of importance for the development of higher-dimensional quantum communication. Understanding the coherent interaction between structured light and atomic vapours is also relevant for transverse mode quantum memories [97–100], where transverse states of light are mapped onto a collective excitation of an atomic cloud, and then read out some time later. Our results are directly applicable to other FWM schemes which allow frequency conversion to wavelengths within the telecomunications band [79, 96, 101]. Frequency conversion of transverse modes to these wavelengths would allow atomic systems to interface with fibre-based communication systems [32, 102].

We also study the effect of adding an external cavity to the FWM system. With Gaussian pump beams, we find that even a low-finesse cavity ($F = 3.5$), singly-resonant with the 420 nm light, nearly triples the generated 420 nm power and narrows the linewidth to < 1 MHz. As a final experiment, we investigate cavity-enhanced FWM with Laguerre-Gauss pump beams. This allows the possibility of controlling the cavity output mode through the phase coherence of the FWM process. We find that the cavity output mode is determined by a combination of the FWM process and the feedback provided by the cavity.

1.4.1 Chapter descriptions

Chapter 2: A brief overview of the theory describing FWM and the resonant interaction between light and atoms is given.

Chapter 3: The particular FWM system under consideration is introduced in more detail. The basic experimental setup required to carry out FWM is then described, including the laser frequency stabilisation techniques used and the heated rubidium cell.

Chapter 4: The digital holography techniques used to shape the near-infrared pump beams will be detailed, including an experimental comparison of different

hologram generation methods. The main conclusions from an additional numerical comparison are also included. Finally, the mode decomposition method used to analyse the transverse mode of the generated 420 nm light is described. This chapter will cover the relevant material from publications [P1] and [P2].

Chapter 5: The transfer of OAM in the FWM process is studied. A theoretical model is developed to describe the two-photon transverse state in which the 420 nm and 5.2 µm light is generated. The results are compared to experimental measurements of the mode decomposition of the 420 nm light. This chapter is based on publication [P3], which is currently under consideration.

Chapter 6: Four-wave mixing with more general transverse modes is investigated, including OAM modes of opposite handedness, radial Laguerre-Gauss modes and superpositions. The material in this chapter is currently being prepared for publication [P4].

Chapter 7: A low-finesse ring cavity is added to the setup, and the effect on the FWM conversion efficiency and 420 nm linewidth is investigated. This study was carried out initially for Guassian pump beams, but some qualitative results for shaped pump beams are also included. The Gaussian pump beam results in this chapter are published in Ref. [P5].

Chapter 8: The main results and open questions from this work are summarised.

1.4.2 Publications

The work presented in this thesis has contributed to three publications:

[P5] R. F. Offer, J. W. C. Conway, E. Riis, S. Franke-Arnold, and A. S. Arnold, "Cavity-enhanced frequency up-conversion in rubidium vapour," Opt. Lett. **41**, 2177 (2016).

[P1] T. W. Clark, R. F. Offer, S. Franke-Arnold, A. S. Arnold, and N. Radwell, "Comparison of beam generation techniques using a phase only spatial light modulator," Opt. Express **24**, 6249 (2016).

[P2] N. Radwell, R. F. Offer, A. Selyem, and S. Franke-Arnold, "Optimisation of arbitrary light beam generation with spatial light modulators," J. Opt. **19**, 095605 (2017).

A further two publications are currently in preparation:

[P3] R. F. Offer, D. Stulga, E. Riis, S. Franke-Arnold, and A. S. Arnold, "Spiral bandwidth of four-wave mixing in rubidium vapour." arXiv[physics.atom-ph]1805.08190.

[P4] R. F. Offer, E. Riis, S. Franke-Arnold, and A. S. Arnold, "Coherent beam shaping via four-wave mixing in rubidium vapour."

1.4.3 Author contributions

The experimental work for publication [P5] was undertaken by Offer and Conway, with the analysis of the results performed by Offer. All authors contributed to the writing of the paper. The experimental work for publication [P1] was carried out by Clark and Offer. Clark and Radwell carried out the majority of the analysis of the results and the theoretical simulations, with all authors contributing to the writing of the paper. The simulations for publication [P2] were carried out by Radwell. All authors contributed to the interpretation of the results and the writing of the paper. The experiment for publications [P3] and [P4] was built by Offer, who also took the experimental data and analysed the results. Offer and Stulga carried out the theoretical analysis, and all authors contributed to writing the paper and interpreting the results.

Chapter 2

Four-wave mixing and atom-light interactions

The aim of this chapter is to briefly outline the theory behind wave mixing, and to justify the resonant enhancement of these processes that can be achieved in atomic vapours. We start by considering the nonlinear effects which occur in a medium with a third-order nonlinearity, and then use the semi-classical model of a two-level atom to illustrate the resonant light-atom interaction. The content of this chapter is standard textbook material and is drawn from Refs. [1, 2, 18].

2.1 Electric susceptibility

When an oscillating electric field, $\underline{\boldsymbol{E}}$, is incident on a medium, it induces an oscillating polarisation per unit volume, $\underline{\boldsymbol{P}}$, given by [2, 18]

$$\underline{\boldsymbol{P}} = \varepsilon_0 \chi \underline{\boldsymbol{E}}, \tag{2.1.1}$$

where χ is the electric susceptibility of the medium. The induced polarisation, which is equivalent to a moving charge, in turn generates light which interferes with the incident field. The effect this has on the propagation of $\underline{\boldsymbol{E}}$ is described by

$$\nabla^2 \underline{\boldsymbol{E}} - \frac{1}{c^2}\frac{\partial^2 \underline{\boldsymbol{E}}}{\partial t^2} = \frac{1}{\varepsilon_0 c^2}\frac{\partial^2 \underline{\boldsymbol{P}}}{\partial t^2}, \tag{2.1.2}$$

which can be derived from Maxwell's equations in the case of no free charges.

To highlight the importance of the susceptibility in describing this light-matter interaction, we insert Eq. 2.1.1 into Eq. 2.1.2 to give

$$\nabla^2 \underline{\boldsymbol{E}} - \frac{1+\chi}{c^2}\frac{\partial^2 \underline{\boldsymbol{E}}}{\partial t^2} = 0, \tag{2.1.3}$$

which for a scalar field propagating in one dimension has the solution

$$E(z,t) = E_0 e^{i(nkz-\omega t)}, \quad n = \sqrt{1+\chi}, \tag{2.1.4}$$

with wave vector, k, angular frequency, ω, and refractive index, n. In general the susceptibility is small and complex, so the refractive index can be rewritten in terms of its real and imaginary parts as

$$n = \sqrt{1+\chi} \simeq 1 + 1/2\chi = 1 + \chi'/2 + i\chi''/2, \quad \chi = \chi' + i\chi''. \tag{2.1.5}$$

By substituting this back into the electric field we arrive at an important result

$$E(z,t) = E_0 e^{-\chi'' kz/2} e^{i(1+\chi')kz/2} e^{-i\omega t}. \tag{2.1.6}$$

The real part of the susceptibility (in phase with the incident field) changes the phase velocity of the field, whilst the imaginary part (out of phase with the incident field) corresponds to absorption. There is also another possibility; if $\chi'' < 0$ then the incident field experiences gain.

Far from resonance, in an isotropic medium, and for weak fields the susceptibility is a simple constant of proportionality; the polarisation of the medium responds linearly to the field. However, as the incident intensity increases, the response of the medium can become *nonlinear*. This effect is usually treated via a Taylor expansion of the susceptibility [2, 18]:

$$\underline{\boldsymbol{P}} = \varepsilon_0 \left[\chi^{(1)} + \chi^{(2)}\underline{\boldsymbol{E}} + \chi^{(3)}\underline{\boldsymbol{E}}^2 + ...\right]\underline{\boldsymbol{E}}, \tag{2.1.7a}$$

$$= \varepsilon_0 \chi^{(1)}\underline{\boldsymbol{E}} + \left[\varepsilon_0 \chi^{(2)}\underline{\boldsymbol{E}}^2 + \varepsilon_0 \chi^{(3)}\underline{\boldsymbol{E}}^3 + ...\right], \tag{2.1.7b}$$

$$= \underline{\boldsymbol{P}}^{(1)} + \underline{\boldsymbol{P}}^{(NL)}, \tag{2.1.7c}$$

with the medium's response to each order of the electric field described by each $\chi^{(i)}$.

2.1.1 Third-order nonlinearity

In centrosymetric materials, such as an atomic vapour, the even $\chi^{(i)}$ vanish and $\chi^{(3)}$ is the leading order nonlinearity. In this subsection we discuss some of the effects that can occur in such a medium [15], where the nonlinear polarisation is given by

$$P^{(NL)} = \varepsilon_0 \chi^{(3)} E^3. \tag{2.1.8}$$

Both P and E are in general vectors (or tensors), but for clarity in this section the underline notation will be dropped.

Four-wave mixing

Most importantly for this thesis, the third-order nonlinearity can lead to Four-wave mixing (FWM). To illustrate this, consider the effect of three incident fields of different angular frequency, such that

$$E(z,t) = E_1 e^{i(k_1 z - \omega_1 t)} + E_2 e^{i(k_2 z - \omega_2 t)} + E_3 e^{i(k_3 z - \omega_3 t)} + c.c., \tag{2.1.9}$$

with $k_i = n_i \omega_i / c$. Calculating $P^{(NL)}$ for this incident field generates many terms oscillating at different linear combinations of the input frequencies. One of these terms is [2]

$$P^{(FWM)} = 6\varepsilon_0 \chi^{(3)} E_1 E_2 E_3^* e^{i[(k_1+k_2-k_3)z-(\omega_1+\omega_2-\omega_3)t]}, \tag{2.1.10}$$

which oscillates at a new angular frequency, ω_4, such that

$$\omega_1 + \omega_2 = \omega_3 + \omega_4. \tag{2.1.11}$$

The wave equation (Eq. 2.1.2) can be rewritten using Eq. 2.1.7c as

$$\nabla^2 E_i - \frac{n^2}{c^2}\frac{\partial^2 E_i}{\partial t^2} = \frac{1}{\varepsilon_0 c^2}\frac{\partial^2 P_i^{(NL)}}{\partial t^2}, \tag{2.1.12}$$

where the i subscripts indicate that the equation holds at each angular frequency, ω_i, at which E and P oscillate, and $n = \sqrt{1+\chi^{(1)}}$ is the linear refractive index. The nonlinear polarisation in Eq. 2.1.10 therefore acts as a driving term, generating a new frequency component of the electric field with angular frequency ω_4.

To conserve energy, the field with frequency ω_3 must also be amplified. In fact it is not necessary to drive the FWM process with three fields, both E_3 and E_4 can be generated spontaneously from the vacuum [103].

The transfer of energy between the four optical fields can be described mathematically by inserting $P^{(FWM)}$ into Eq. 2.1.12. Working in one dimension, and under the assumption that the amplitudes E_i only vary slowly in z, we find that

$$\begin{aligned} \frac{dE_1}{dz} &= i\kappa_1 E_2^* E_3 E_4 e^{-i\Delta kz}, \quad \frac{dE_2}{dz} = i\kappa_2 E_1^* E_3 E_4 e^{-i\Delta kz}, \\ \frac{dE_3}{dz} &= i\kappa_4 E_1 E_2 E_4^* e^{i\Delta kz}, \quad \frac{dE_4}{dz} = i\kappa_4 E_1 E_2 E_3^* e^{i\Delta kz}, \\ \kappa_i &= \frac{3\chi^{(3)}\omega_i}{n_i c}, \quad \Delta k = k_1 + k_2 - k_3 - k_4. \end{aligned} \tag{2.1.13}$$

The third order nonlinearity, contained in the coupling coefficients, κ_i, parametrically couples the amplitude of the four optical fields, allowing energy to transfer between them.

These equations highlight some important features of FWM. Firstly, to have maximal energy transfer, the process must be phase matched, i.e. $\Delta k = 0$. For perfect phase matching, the generated fields maintain a fixed phase relationship with the polarisation created by the pump fields, allowing maximum energy to be extracted from the pump light. Furthermore, integration of the equation for E_4 over z, shows that in the limit of no depletion of the pump fields, the intensity of the generated light scales with the product of the intensity of the other fields, and will grow quadratically with propagation distance.

Although we deal only with classical fields in this thesis, wave mixing processes, and the light generated by them, are fundamentally quantum mechanical. For a complete theoretical treatment a quantised description of the optical fields is required, as presented in Ref. [18]. In this picture the FWM process described above corresponds to the simultaneous annihilation of two pump photons, with angular frequency ω_1 and ω_2, and creation of two new photons with angular frequency ω_3 and ω_4 [2, 103]. For energy to be conserved the two new photons must be generated at exactly the same time, creating pairs of photons described by a two-photon state. At the single photon level, the phase matching condition is

equivalent to conservation of photon momentum.

Kerr lensing

Another important third-order nonlinear effect is the *optical Kerr effect* [2]. If a single optical field, $E(t) = E_1 \cos(\omega t)$, propagates through a $\chi^{(3)}$ medium then the nonlinear polarisation is given by

$$\begin{aligned} P^{(NL)} &= \varepsilon_0 \chi^{(3)} E_1^3 \cos^3(\omega t) \\ &= \frac{1}{4}\varepsilon_0 \chi^{(3)} E_1^3 \cos(3\omega t) + \frac{3}{4}\varepsilon_0 \chi^{(3)} E_1^3 \cos(\omega t). \end{aligned} \tag{2.1.14}$$

The first term generates an optical field with frequency 3ω - the third harmonic of the input field. The second term generates a field at the same frequency as the input field. This field interferes with the incident field leading to an intensity dependent refractive index, given by

$$n = n_0 + n_2 I, \quad n_2 = \frac{3}{2n_0^2 \varepsilon_0 c}\chi^{(3)}. \tag{2.1.15}$$

This has significant consequences for the propagation of the beam. For a Gaussian beam, with peak intensity in the centre and decreasing intensity in the wings, different parts of the beam experience a different refractive index. This can lead to Kerr lensing, where, depending on the sign of n_2, the beam focuses or defocuses as it propagates [104, 105].

2.2 The two-level atom

The previous section described two nonlinear effects which can occur when a medium has a third-order nonlinear response to an incident field: FWM and Kerr lensing. We now consider the *resonant* interaction between light and atoms. This is a very different regime to the off resonant interaction described in the previous section. The strong response of the atom leads to a large, strongly frequency-dependent nonlinearity, but also absorption of the fields. To illustrate this we consider the susceptibility an atomic vapour made up of a two-level atoms.

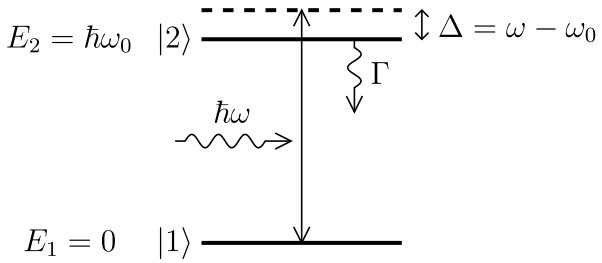

Figure 2.1: The two-level atom with ground state $|1\rangle$ ($E_1 = 0$), excited state $|2\rangle$ ($E_2 = \hbar\omega_0$), spontaneous decay rate Γ, and an incident field with angular frequency ω.

A semi-classical approach is used, treating the light as a classical field but the atom as a quantum mechanical object, as is described in Refs. [1, 2, 18].

Each two-level atom has a ground state $|1\rangle$, whose energy is set as the zero energy, and an excited state $|2\rangle$ at an energy of $\hbar\omega_0$, as shown in Fig. 2.1. The incident light, $\underline{\boldsymbol{E}}(t) = \underline{\boldsymbol{\epsilon}} E_0 \cos(\omega t)$, is a monochromatic field, linearly polarised along $\underline{\boldsymbol{\epsilon}}$, and is detuned from the atomic transition by $\Delta = \omega - \omega_0$. The polarisation of each atom due to this incident electric field is described by the dipole moment $\underline{\boldsymbol{d}} = e\,\underline{\boldsymbol{r}}$, where e is the electronic charge and $\underline{\mathbf{r}}$ is the position vector of the displaced electron with respect to the atom's centre of mass. The polarisation per unit volume of the vapour is given by $\underline{\boldsymbol{P}} = N \langle \underline{\boldsymbol{d}} \rangle$, where N is the atomic number density. We include one incoherent process in the model: the atom can decay from the excited state $|2\rangle$ with a decay rate Γ.

2.2.1 The density matrix

The atomic state of each atom, including its response to the incident field, is described by the density matrix, ρ, which for a two-level atom is given by

$$\rho = \begin{pmatrix} \rho_{11} & \rho_{12} \\ \rho_{21} & \rho_{22} \end{pmatrix}. \tag{2.2.16}$$

The diagonal terms ρ_{11} and ρ_{22} are the *populations* - the probability of finding the atom in $|1\rangle$ or $|2\rangle$. The off diagonal terms ρ_{12} and ρ_{21} are the *coherences* - a

measure of how well the phases of $|1\rangle$ and $|2\rangle$ are defined. These terms describe the response of the atom at the driving frequency, and are directly related to the susceptibility of the vapour by [2],

$$\chi = \frac{2Nd_{12}}{\varepsilon_0 E_0}\tilde{\rho}_{12}, \quad d_{12} = -e\left\langle 1\right|\underline{\hat{\mathbf{r}}}.\underline{\boldsymbol{\epsilon}}\left|2\right\rangle, \tag{2.2.17}$$

where d_{12} is the dipole matrix element.

The evolution of the density matrix elements, in the presence of the incident electric field, is described by the optical Bloch equations [1, 2, 18]

$$\dot{\tilde{\rho}}_{11} = -i\frac{\Omega}{2}\left(\tilde{\rho}_{21} - \tilde{\rho}_{12}\right) + \Gamma\tilde{\rho}_{22}, \tag{2.2.18a}$$

$$\dot{\tilde{\rho}}_{12} = -i\frac{\Omega}{2}\left(\tilde{\rho}_{22} - \tilde{\rho}_{11}\right) - i\Delta\tilde{\rho}_{12} - \frac{\Gamma}{2}\tilde{\rho}_{12}, \tag{2.2.18b}$$

$$\dot{\tilde{\rho}}_{21} = -i\frac{\Omega}{2}\left(\tilde{\rho}_{11} - \tilde{\rho}_{22}\right) + i\Delta\tilde{\rho}_{21} - \frac{\Gamma}{2}\tilde{\rho}_{21}, \tag{2.2.18c}$$

$$\dot{\tilde{\rho}}_{22} = -i\frac{\Omega}{2}\left(\tilde{\rho}_{12} - \tilde{\rho}_{21}\right) - \Gamma\tilde{\rho}_{22}, \quad \Omega = \frac{d_{12}E_0}{\hbar}, \tag{2.2.18d}$$

where Ω is the Rabi frequency, which characterises the strength of the coupling between the two atomic states. These equations can be solved, with the additional constraints that $\rho_{11} + \rho_{22} = 1$ and $\rho_{21} = \rho_{12}^*$, to find the steady state response of the atoms. In the limit $\dot{\rho} \to 0$ the coherence ρ_{12} is given by

$$\rho_{12} = i\frac{\Omega}{2}\frac{i\Delta + \Gamma/2}{\Delta^2 + \Gamma^2/4 + \Omega^2/2}. \tag{2.2.19}$$

2.2.2 Frequency dependent, nonlinear susceptibility

Substituting Eq. 2.2.19 into Eq. 2.2.17 gives the susceptibility of the two-level atom

$$\chi = -\frac{Nd_{12}^2}{\hbar\varepsilon_0}\frac{\Delta - i\Gamma/2}{\Delta^2 + \Gamma^2/4 + \Omega^2/2}. \tag{2.2.20}$$

This susceptibility contains both linear and nonlinear contributions, and is strongly dependent in the frequency of the driving field. To highlight the intensity dependence, Eq. 2.2.20 can be rewritten in terms of the saturation intensity, I_{sat}, as

$$\chi = -\frac{Nd_{12}^2}{\hbar\varepsilon_0}\frac{\Delta - i\Gamma/2}{\Delta^2 + \Gamma^2/4\left(1 + I/I_{\text{sat}}\right)}, \quad \frac{I}{I_{\text{sat}}} = \frac{2\Omega^2}{\Gamma^2}. \tag{2.2.21}$$

The real and imaginary parts of Eq. 2.2.21 are plotted in Fig. 2.2, showing the absorption and refractive index of the vapour for a range of incident intensities. The atom absorbs light over a Lorentzian lineshape centered on zero detuning, with the peak absorption on resonance given by [1]

$$\alpha = \frac{3N\lambda^2}{2\pi}\frac{1}{1+I/I_{\text{sat}}}, \quad I = I_0 e^{-\alpha z}. \tag{2.2.22}$$

As the incident intensity increases the absorption *saturates*, and the peak absorption decreases. The decrease in absorption is accompanied by a broadening of the absorption feature - known as power broadening. The full width half maximum of the Lorentzian lineshape is given by [1]

$$\Delta\omega_{\text{FWHM}} = \Gamma\sqrt{1+I/I_{\text{sat}}}. \tag{2.2.23}$$

The physical origin of this nonlinear response is the increasing population of the excited state $|2\rangle$, which leads to a reduction in the net absorption with increasing incident intensity. When the population of the ground and excited states are equal an incoming photon is equally likely to cause stimulated emission as it is to be absorbed and the absorption tends to zero.

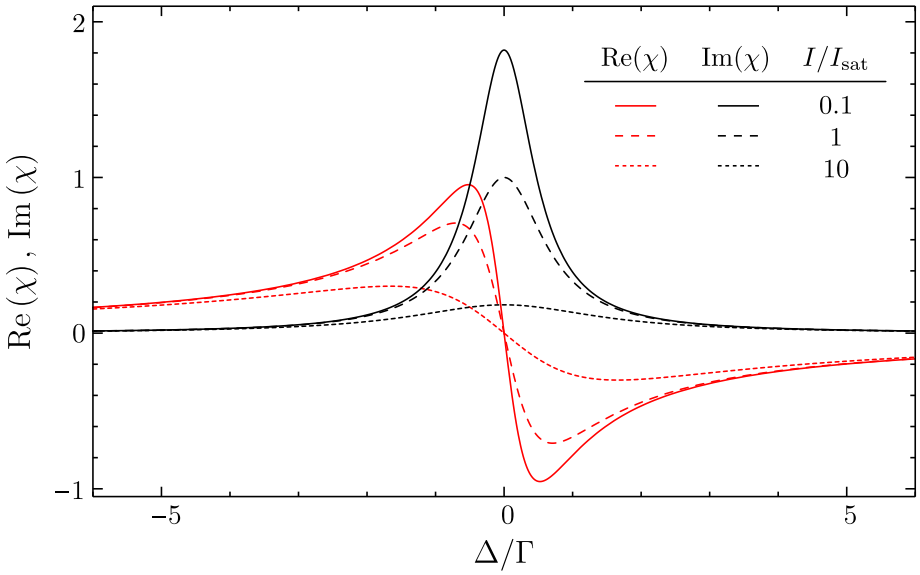

Figure 2.2: Real and imaginary parts of the two-level atom susceptibility as a function of detuning and for different values of I/I_{sat}.

Third order nonlinearity

Equation 2.2.20 can be separated into its linear and nonlinear parts by carrying out a power series expansion in Ω^2. Keeping only the first two terms, the susceptibility becomes

$$\chi = -\frac{Nd_{12}^2\left(\Delta - i\Gamma/2\right)}{\hbar\varepsilon_0\left(\Delta^2 + \Gamma^2/4\right)}\left(1 - \frac{\Omega^2}{2\left(\Delta^2 + \Gamma^2/4\right)}\right). \tag{2.2.24}$$

Equating this with $\chi = \chi^{(1)} + \chi^{(3)}E_0^2$, shows that the effective linear and third order susceptibilities are given by

$$\chi^{(1)} = -\frac{Nd_{12}^2\left(\Delta - i\Gamma/2\right)}{\hbar\varepsilon_0\left(\Delta^2 + \Gamma^2/4\right)}, \tag{2.2.25a}$$

$$\chi^{(3)} = \frac{Nd_{12}^4\left(\Delta - i\Gamma/2\right)}{2\hbar^3\varepsilon_0\left(\Delta^2 + \Gamma^2/4\right)^2}. \tag{2.2.25b}$$

Fig. 2.3 shows plots of these results. The third order susceptibility is the opposite sign to the linear susceptibility, which stems from its origin in the saturation of the optical response, and shows a strong resonant enhancement for zero detuning.

The resonant enhancement of $\chi^{(3)}$ is key for the work in this thesis. It allows wave mixing to be carried out with far greater efficiency than in bulk materials. The best demonstration of this is to note that before the use of atomic vapours,

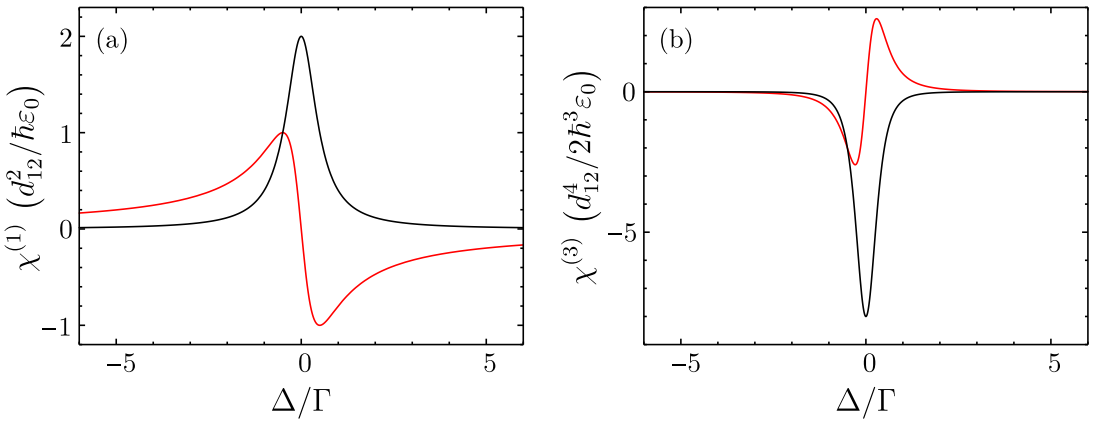

Figure 2.3: Real (red) and imaginary (black) parts of the (a) linear, $\chi^{(1)}$, and (b) third-order, $\chi^{(3)}$, contributions to the two-level atom susceptibility.

FWM was always carried out with high power, pulsed lasers. In resonantly enhanced systems, wave mixing can be carried out efficiently with tens of mW of continuous wave light [61, 62].

An estimate of the third-order susceptibility of an atomic vapour can be found by calculating $\chi^{(3)}$ for typical values of the relevant parameters. As an example, the required parameters for the $5S_{1/2}$ $F = 3 \rightarrow 5P_{3/2}$ $F' = 4$ transition in ^{85}Rb are shown in table 2.1, along with the calculated value for $\chi^{(3)}$. For comparison a typical value of $\chi^{(3)}$ for a nonlinear crystal, CaF, is also included [2].

Dipole matrix element*, d_{12}	1.659×10^{-29}	C m
Spontaneous decay rate*, Γ	$2\pi \times 6.066$	MHz
Effective atom number†, n	2×10^{13}	
Detuning†, Δ	$2\pi \times 1.6$	GHz
Third order susceptibility ^{85}Rb, $\chi^{(3)}$	7×10^{-14}	m^2V^{-2}
Third order susceptibility CaF, $\chi^{(3)}$	7×10^{-22}	m^2V^{-2}

Table 2.1: Values used to calculate $\chi^{(3)}$ for the $5S_{1/2}$ $F = 3 \rightarrow 5P_{3/2}$ $F' = 4$ transition in ^{85}Rb. *From [106], †typical experimental values used later in this thesis. n is calculated assuming $n = NV$, where N is the atomic density and V is the interaction region.

2.2.3 Doppler broadening

In the previous calculation of $\chi^{(3)}$ there was an implicit assumption that each atom interacts identically with the incident field. In the case of a thermal vapour this is not the case due to the range of atomic velocities in the vapour, which leads to an effect known as Doppler broadening.

When a moving atom interacts with an incident optical field, the frequency of the light in the rest frame of the atom is Doppler shifted. This Doppler shift is given by $\delta = -kv_z$ (or in vector form $\underline{\boldsymbol{k}}.\underline{\boldsymbol{v}}$), where k is the wavevector of the light

and v_z is the component of the atoms velocity in the direction of propagation. As a result the atom will absorb light that is detuned from resonance by $-\delta$ in the lab frame.

In the vapour, the atoms move at speeds described by a Maxwell-Boltzmann distribution. For an individual atom, the probability that v_z lies in the range v_z to $v_z + dv_z$ is given by [1]

$$f(v) = \frac{1}{\bar{v}_z\sqrt{\pi}} \exp\left(-\frac{v_z^2}{\bar{v}_z^2}\right), \quad \bar{v}_z = \sqrt{\frac{2k_BT}{M}}, \tag{2.2.26}$$

where M is the atomic mass. This leads to a Gaussian distribution of Doppler shifts with a FWHM, Γ_D, given by

$$\Gamma_D = \frac{2\sqrt{\ln 2}\,\bar{v}_z}{\lambda}. \tag{2.2.27}$$

To find the susceptibility of the vapour one must average over this distribution. At room temperature, the resulting absorption profile is the convolution of the Gaussian distribution of Doppler shifts ($\Gamma_D \sim 500\,\mathrm{MHz}$) with the Lorentzian absorption lineshape of each atom ($\Gamma = 6\,\mathrm{MHz}$): a Voigt profile [107]. The example widths provided are for the $5S_{1/2}$ $F = 3 \rightarrow 5P_{3/2}$ $F' = 4$ transition in ^{85}Rb.

This also means that for any particular detuning, the light interacts with only a small fraction of the atoms - those in the velocity class whose Doppler shift is less than the natural linewidth of the transition. This fraction is given by

$$\frac{\Gamma}{\Gamma_D} \propto \frac{\Gamma}{\sqrt{T}/\lambda}, \tag{2.2.28}$$

and therefore both the absorption and third-order nonlinearity is reduced by a factor of $\sim 1/100$.

2.3 Summary

This chapter has introduced a basic description of FWM and atom-light interactions. In the first section we showed that a third-order nonlinearity allows energy

to be transferred between four optical fields, and can also cause Kerr lensing. We then considered the resonant interaction between light and atoms. Using the two-level atom as an illustration, important features of the light atom-interaction were highlighted, including saturated absorption, power broadening, Doppler broadening, and, most importantly, the resonantly enhanced nonlinearity.

Chapter 3

Resonantly enhanced four-wave mixing

This chapter describes the resonantly enhanced FWM system which forms the basis of the work in this thesis. Rather than giving a full theoretical description of the FWM process, which is involved and has not formed part of the work undertaken for this thesis, it will be introduced in the context of previous work that has been carried out. The following sections then describe the basic experimental setup required to carry out resonantly enhanced FWM.

3.1 Introduction

The essence of the FWM experiment is simple, as illustrated in Fig. 3.1. Two pump beams, one at 780 nm and the other 776 nm, copropagate through a thermal rubidium cell. This results in the coherent generation of 5.2 µm light, which is subsequently absorbed by the glass cell, and 420 nm light, which is observed in the experiment. The frequency conversion process can be carried out very efficiently, with ~ 1 mW of 420 nm light generated for only modest pump powers (~ 40 mW) [92]. This corresponds to 80 µW of 5.2 µm power, assuming it is generated solely via FWM.

The use of a thermal vapour allows high rubidium densities to be created

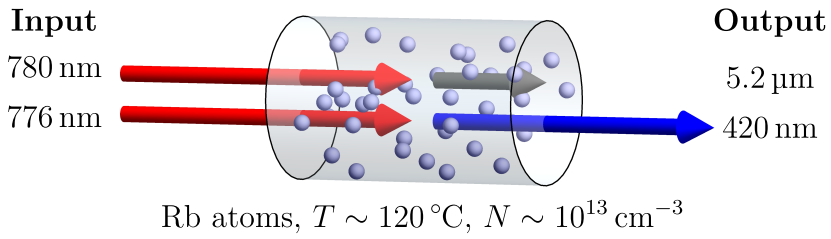

Figure 3.1: Concept of the "blue light" FWM experiment.

with a very simple experimental setup. At room temperature, the rubidium in the cell exists as both a solid and a gas, with some equilibrium vapour pressure. The partial pressure of ^{85}Rb at 20°C is $1.6{\times}10^{-5}$ Pa [108], which corresponds to a number density of $4{\times}10^{9}\,\mathrm{cm}^{-3}$. When the cell is heated, the vapour pressure increases following an empirically derived law [108] (see Appendix B), resulting in an increase in rubidium density. Heating the cell to 120°C, which can be easily achieved, results in an increase in number density by four orders of magnitude. This allows FWM to be studied over a wide range of rubidium densities.

The relevant atomic energy levels for the resonantly enhanced FWM process are shown in Fig. 3.2. Though all rubidium cells used in this thesis contain both rubidium isotopes in their natural abundances (^{85}Rb : 72% and ^{87}Rb : 28% [109]), we use ^{85}Rb as it allows for more efficient wave mixing. This is due in part to its larger abundance, but also the smaller splitting of the hyperfine ground states which, for appropriate pump detuning, allows both states to contribute to the FWM process.

As shown in Fig. 3.2, the 780 nm and 776 nm lasers couple to the ^{85}Rb $5S_{1/2} \rightarrow 5P_{3/2}$ and $5P_{3/2} \rightarrow 5D_{5/2}$ transitions, respectively, whilst the emitted 5.2 µm and 420 nm fields are quasi-resonant with the downward cascade via the $6P_{3/2}$ state. Each atomic state is further split into hyperfine structure [1], the spacings of which are included in Appendix A.

The efficiency of the FWM process is largely due to the low saturation intensity of the 5.2 µm transition, which leads to very large nonlinearities even for low powers. For sufficient pump intensity, FWM is also enhanced by initial amplified spontaneous emission (ASE) on the 5.2 µm transition [4, 96, 110]. The lifetime of

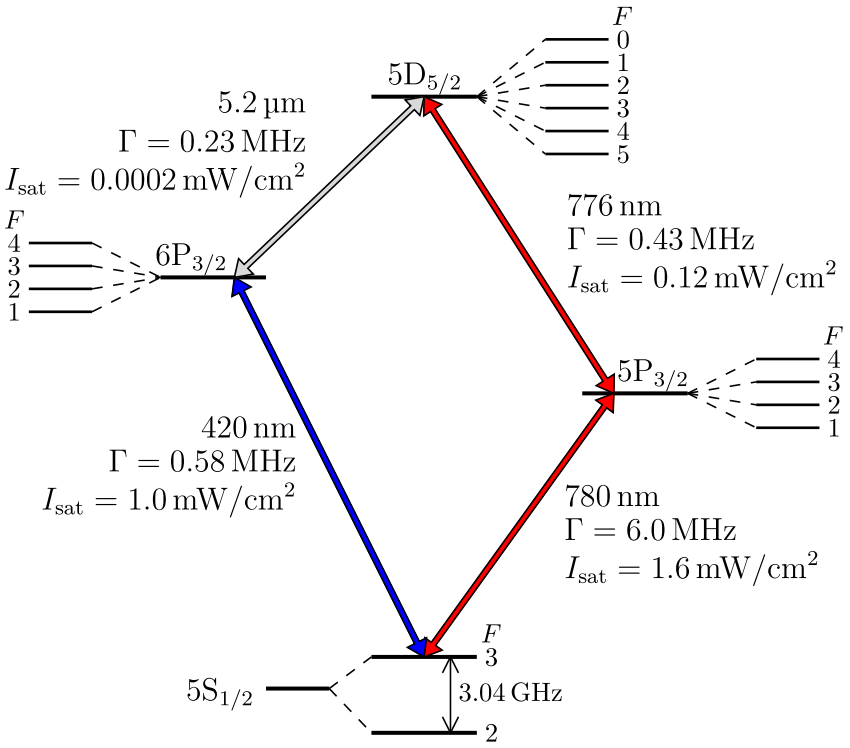

Figure 3.2: Relevant ^{85}Rb atomic structure, with the natural linewidth, Γ, and saturation intensity, I_{sat}, for each transition.

the exited state, $5D_{5/2}$, is 240 ns, whilst the intermediate states $5P_{3/2}$ and $6P_{3/2}$ are much shorter lived, with lifetimes of 32 ns and 112 ns, respectively [4]. Population transfer to the excited state therefore leads to a population inversion on the $5D_{5/2} \rightarrow 6P_{3/2}$ transition, which in turn results in ASE of the 5.2 µm field. This 5.2 µm light, combined with the pump fields, builds a strong three-photon coherence on the $5S_{1/2} \rightarrow 6P_{3/2}$ transition, leading to generation of 420 nm light. A similar FWM process has also been carried out in cesium vapour [93, 111].

As is required for a parametric wave mixing process, the four fields form a closed loop so that the initial and final state of the atoms are identical. As such, for energy conservation the angular frequency of the fields must satisfy

$$\omega_{780} + \omega_{776} = \omega_{\text{B}} + \omega_{\text{IR}}. \tag{3.1.1}$$

The generated fields also obey the wavenumber phase matching condition

$$\underline{\boldsymbol{k}}_{780} + \underline{\boldsymbol{k}}_{776} = \underline{\boldsymbol{k}}_{\text{B}} + \underline{\boldsymbol{k}}_{\text{IR}}, \tag{3.1.2}$$

which is equivalent to momentum conservation. Due to the large difference in the wavelength of the 420 nm and 5.2 µm fields, optimal phase matching is obtained for copropagating pump beams. However, if a small angle is introduced between them, then the 420 nm light is generated in a direction consistent with the above phase matching condition [91]. The phase coherence of the FWM process is inherent from the phase dependent coherent dynamics of the closed four-level system [112, 113]. A recent experiment has also shown that intensity correlations present in the pump light are transferred to the 420 nm field [114].

The blue light FWM process has been studied in two regimes. In the original experiment by Zibrov et al. in 2002 [4], and later experiments [91], the two pump lasers are single-photon resonant with their respective transitions. This process is usually carried out for relatively low rubidium densities ($\sim 10^{12}\,\mathrm{cm}^{-3}$), low pump powers ($\sim 10\,\mathrm{mW}$), and generates $\sim$µW of 420 nm emission. Theoretical analysis of this resonant FWM experiment has been carried out in Ref. [4].

However, larger conversion efficiency is observed if the 780 nm and 776 nm lasers are instead detuned by around $\Delta = +1.6\,\mathrm{GHz}$ and $-1.6\,\mathrm{GHz}$, respectively [90, 92]. Note that these are linear detunings, i.e. $\Delta/2\pi$. In other words, the 780 nm laser is detuned roughly half way between the $F = 3$ and $F = 2$ hyperfine ground states, but the pump lasers together are two-photon resonant with the $5D_{5/2}$ state. This reduces the single-photon absorption of the pump beams, allowing FWM to be carried out at higher rubidium densities ($\sim 2 \times 10^{13}\,\mathrm{cm}^{-3}$), leading to a larger resonant enhancement. Coupling to both hyperfine ground states also allows the pump light to interact with a larger fraction of the atomic population, and removes the possibility of population being optically pumped to a dark hyperfine ground state [115]. Due to the smaller ground state splitting (see Appendix A), this five-level FWM process is much more efficient in ^{85}Rb than ^{87}Rb. A similar FWM process has also been carried out with even further detuned pump beams using a single 778nm pump laser [94].

The five-level FWM system has been modeled theoretically in the PhD thesis of a previous student working on the Strathclyde FWM experiment [116], and

also in Refs. [90] and [92]. The models show that the exact pump detunings at which FWM occurs depends not only on single-photon absorption of the 780 nm beam but also on the Kerr lensing it experiences as it propagates through the cell. Peak FWM efficiency occurs where the Kerr lensing (see Sec. 2.1.1) due to the transition from each hyperfine ground state cancels.

The generated 420 nm power is also dependent on the polarisation of the pump beams. Experiments in Ref. [92] showed that the 420 nm output power is maximised for co-circularly polarised pumps, but is almost completely suppressed for pump polarisations of opposite handedness. Co-linearly polarised pump beams can be expected to produce roughly 60% of the optimal FWM efficiency. The 420 nm output power can be further optimised by adjusting the rubidium pressure in the cell. Whilst the third-order nonlinearity increases with increasing rubidium density, so does the absorption of both the pump and generated fields. Previous investigations have shown that the optimum rubidium density for FWM is around $10^{13}\,\mathrm{cm}^{-3}$ [116], though this can be expected to vary with cell length and pump power etc. For this rubidium density, and with co-circularly polarised pump light, 1 mW of 420 nm light can be generated for a total pump power of 40 mW [92]. With higher power pump beams ($\sim$ 200 mW) 420 nm output powers of 9.1 mW have been demonstrated [101].

Although the 5.2 µm light is unobserved in our experiment, it has been previously studied. Like the 420 nm light, it is generated as a coherent, directional beam [4]. However, it has been observed to be generated both copropagating with the pump beams and counterpropagating, providing further evidence of the role of amplified spontaneous emission (ASE) as an initial seed for the FWM process.

There are also other FWM processes that can occur in this system. For example, there is a second closed FWM loop which follows $5P_{3/2}$-$5D_{5/2}$-$6P_{3/2}$-$6S_{1/2}$ and generates coherent infrared beams at 2.73 µm and 1.37 µm, in addition to the 5.2 µm light [95,96,117]. Branching ratios for these transitions are included in Appendix A. Recently, FWM has been demonstrated via the $5S_{1/2}$-$5P_{1/2}$-$5D_{3/2}$-$6P_{1/2}$ loop [118], which generates blue light at 422 nm rather than 420 nm.

The remainder of this chapter describes the experimental setup required to carry out the "blue light" FWM process. The basic experiment requires the following components: two pump lasers, spectroscopy to monitor the laser frequencies (Sec. 3.2), and a heated rubidium cell in which to carry out FWM (Sec. 3.3). The FWM process itself is relatively simple to carry out, and example traces of the generated 420 nm emission are described in Sec. 3.4. For the work carried out in chapters 5 and 6 it was necessary to stabilise the laser frequencies at fixed detunings, and the laser locking techniques used to do this are described in Sec. 3.5.

At the start of my PhD an existing FWM setup was in place which was modified and used to gather the experimental results for publication [P5] (Chapter 7). I then redesigned and rebuilt the setup for the work presented in Chapters 5 and 6, primarily to allow the lasers to be locked and for the pump beams to be independently shaped. The following sections describe the components common to both the old and new setups, with the full diagram of each setup given later in Chapters 5 and 7.

3.2 Spectroscopy

The two FWM pump lasers are both extended cavity diode lasers (ECDLs). The 780 nm laser is a home built laser based on the design in Ref. [119]. It produces around 80 mW of light with a root mean square (RMS) linewidth of 0.29 MHz over 0.1 s. The 776 nm laser is a Toptica DL100 ECDL, which provides 110 mW of light (RMS linewidth 1.7 MHz (0.1 s)). The linewidths were measured relative to a passively stable cavity (Toptica Photonics FPI100 etalon).

This section introduces the saturated absorption spectroscopy and two-photon spectroscopy used to monitor the detuning of the pump lasers.

3.2.1 Saturated absorption spectroscopy

Fig. 3.3 shows the saturated absorption spectroscopy [121, 122] signal recorded when the 780 nm laser is scanned across the $5S_{1/2} \rightarrow 5P_{3/2}$ hyperfine transitions of both rubidium isotopes. This plot is composed of multiple traces, as the mode-hop free tuning range of the laser was roughly 3 GHz. The inset in Fig. 3.3 (a) shows the setup used. The 780 nm light is retroreflected through a 75 mm long, room temperature rubidium cell, and the transmission monitored on a photodiode.

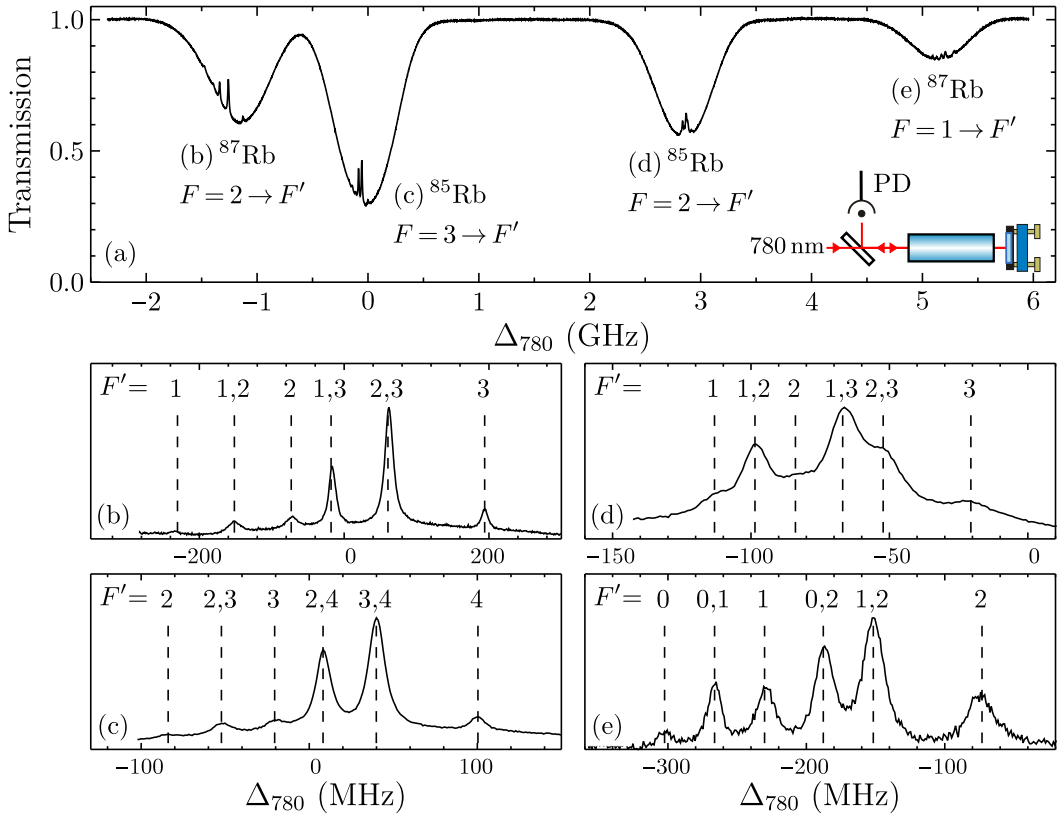

Figure 3.3: (a) Saturated absorption spectroscopy spectrum of the 780 nm transition, with zero detuning at the ^{85}Rb $5S_{1/2}\,F = 3 \rightarrow 5P_{3/2}\,F' = 4$ transition and $I_{780} \simeq 8\,\mathrm{mW/cm^2}$. Inset: Experimental setup. (b)-(e) Zoomed plots of the hyperfine features at each Doppler broadened transition, with a fitted Gaussian background subtracted and zero detuning set to the energy centre-of-mass of each transition. Dashed lines indicate expected detuning of features calculated using values from [120], see appendix A. Data is averaged over 50 traces.

The broad dips in transmission are due to Doppler broadened transitions from the two ^{85}Rb hyperfine ground states ($F = 3$ and $F = 2$), and the two ^{87}Rb hyperfine ground states ($F = 2$ and $F = 1$) to $F' = F, F \pm 1$. There are additional small peaks in transmission due to the beam being retroreflected through the cell, which are shown more clearly in Fig. 3.3 (b)-(e). For most detunings, the right-propagating beam interacts with one velocity class of atoms (with longitudinal velocity $\pm v$), and the left-propagating beam another ($\mp v$). Since the intensity of the beam is relatively high ($I_{780} \simeq 5I_{\mathrm{sat}}$) the absorption coefficient of the atoms is significantly saturated by the right-propagating beam. Close to resonance, when the two beams interact with the same atoms ($v = 0$), this saturation results in a peak in transmission of the left-propagating beam, producing the features shown in Fig. 3.3 (b)-(e). Additional "crossover" peaks occur when the light is detuned exactly halfway between two hyperfine states. In this case the light again interacts with only one velocity class, but drives transitions to one hyperfine state on the first pass, and the other on the return pass. Other effects also contribute to these spectra, for example the effect of hyperfine pumping must be considered to explain the relative height of the saturated absorption peaks [122].

3.2.2 Two-photon spectroscopy

The detuning of the 776 nm laser is monitored via two-photon spectroscopy [123–125] of the $5S_{1/2} \rightarrow 5D_{5/2}$ transitions [126]. Fig. 3.4 (a) shows an example two-photon spectrum, with the experimental setup shown in the inset. The transmission of a 10.5 mW 776 nm beam was monitored in the presence of a counter-propagating 4.8 mW 780 nm beam. Both beams had beam waists (e^{-2} intensity radius) of 0.9 mm, and the 776 nm transmission was measured using a glass plate to direct a portion of the light to a photodiode. The rubidium cell used was 25 mm long and heated to 130°C (see Sec. 3.3 for further details).

The x-axis in Fig. 3.4 is the two-photon detuning of the combined 780 nm and 776 nm light from the ^{85}Rb $5S_{1/2}\,F = 3 \rightarrow 5D_5/2\,F' = 5$ transition. The trace was taken by scanning the 776 nm detuning with the 780 nm detuning fixed at

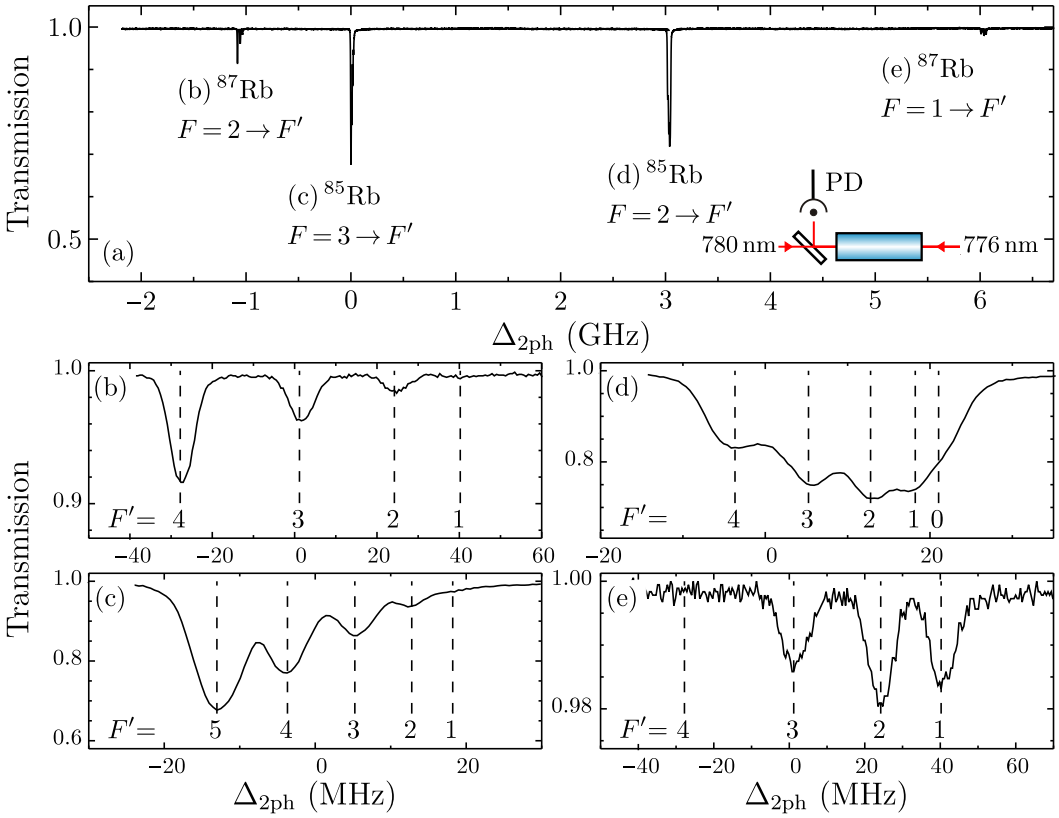

Figure 3.4: (a) Two-photon spectroscopy trace. Inset: Experimental setup. (b)-(e) Zoomed plots of the hyperfine features at each detuning labeled in (a), with zero detuning set to the energy centre-of-mass of each transition. Dashed lines indicate expected detuning of features calculated using values from [126], see appendix A. Data is averaged over 100 traces.

around 1.6 GHz.

The four groups of absorption features in Fig. 3.4 correspond to the allowed two-photon transitions from each of the rubidium hyperfine ground states. Unlike saturated absorption spectroscopy, they are not Doppler broadened. The total energy of a 776 nm photon and a counter-propagating 780 nm photon in the frame of reference of an atom moving with velocity v (towards the 776 nm beam) is [1]

$$E = \hbar(\omega_{780} - k_{780}v + \omega_{776} + k_{776}v) \approx \hbar(\omega_{780} + \omega_{776}). \tag{3.2.3}$$

Since the two pump lasers are of nearly the same wavelength $k_{780} \approx k_{776}$ and the Doppler shifts almost exactly cancel out, with a residual shift of $7\,\mathrm{kHz/ms^{-1}}$.

When the 780 nm and 776 nm light is two-photon resonant in the lab frame, all velocity classes are resonant and there is significant absorption of the 776 nm light.

3.3 Heated rubidium cell

The cell used for FWM is 25 mm long, and, as discussed in the introduction to this chapter, the rubidium density is controlled by changing the cell temperature. The cell is heated via power resistors connected to a constant current source. To improve the temperature uniformity and also reduce air currents across the beam the cell is surrounded by a metal box. This also helps to ensure that the cell windows remain hotter than the rest of the cell, which is important as it prevents condensation of rubidium in the optical path.

The temperature of the cell is determined by measuring the Doppler broadened transmission spectrum of a weak ($< 0.04\,\mathrm{mW/cm^2}$), collimated 780 nm beam through the cell. Under these conditions, the theoretical transmission spectrum of the $5S_{1/2} \rightarrow 5P_{3/2}$ transitions can be calculated following theory in Ref. [127]. Fig. 3.5 shows the predicted spectrum for a range of cell temperatures. At low temperatures, the four familiar Doppler broadened dips (see Fig. 3.3) can be seen, but as the temperature increases the medium quickly becomes completely opaque on resonance.

A quick and accurate temperature measurement can be made by measuring the peak transmission near the detunings marked A and B (inset Fig. 3.5). The transmission near detuning A is used for cell temperatures in the range $20 \rightarrow 80°C$ whilst for hotter cells ($100 \rightarrow 160°C$) the transmission near B is used. By making multiple measurements (> 5) of the peak transmission at the appropriate detuning an average temperature was calculated for a range of heater currents. The results are shown in Fig. 3.6. Error bars showing the standard error in each measurement are included but are too small to see on this scale. An empirical parabolic fit to the data (black line), with the y-intercept fixed to 20°C (room

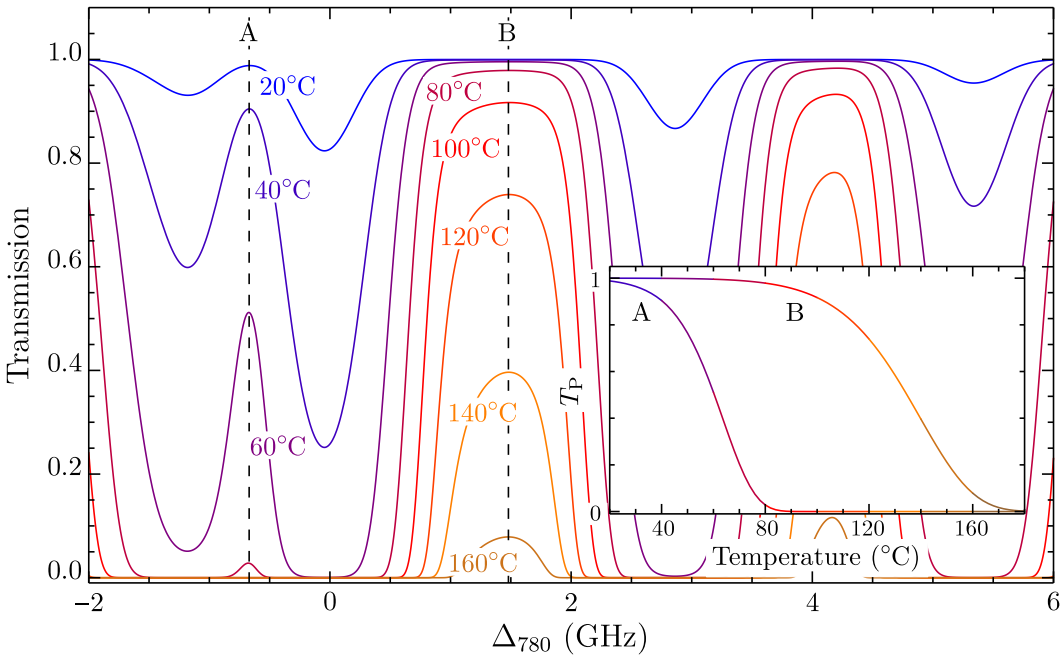

Figure 3.5: Theoretical transmission curve for a weak 780 nm beam through a 25 mm cell at different temperatures. The inset shows the temperature variation of the peak transmission, T_P, near detunings A and B.

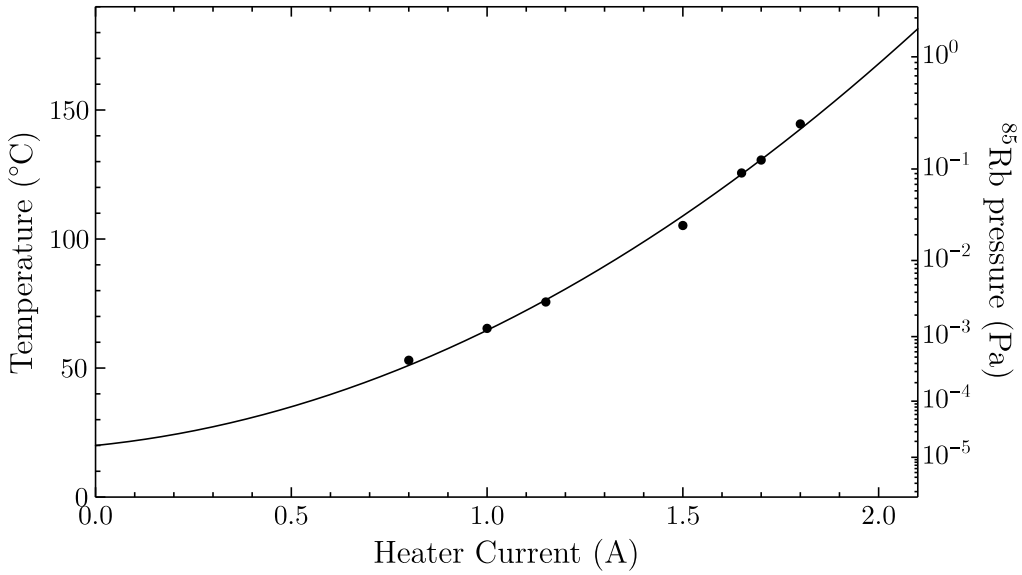

Figure 3.6: Measured temperature of the 25 mm cell as a function of heater current. The right hand y-axis shows the equivalent ^{85}Rb pressure.

temperature for 0 A), is also shown. This curve provides a calibration for the cell temperature as a function of heater current.

For the 25 mm cell, peak FWM efficiency for linearly polarised pumps was found to occur for a temperature of around 130°C, depending on pump power and focused intensity. This corresponds to a ^{85}Rb vapour pressure of 0.12 Pa or in terms of number density, $2.1 \times 10^{13}\,\mathrm{cm}^{-3}$. This is twice the optimal density in Ref. [92], where FWM was carried out with circularly polarised light and a 75 mm long cell.

Two other heated cells were used for spectroscopy at various points in this thesis, one 10 mm long and the other 75 mm. The temperature calibration curves for these cells are included in Appendix B.

3.4 FWM signal

With the two pump lasers and heated rubidium cell in place, the FWM process can be carried out relatively easily using the setup shown in Fig. 3.7 (a). The pump light is combined into a single beam and then coupled through a single mode optical fibre. The combined pump beam is then linearly polarised and focused through the FWM cell, which is heated to 130°C. Within the cell, FWM generates a coherent and directional 420 nm beam. Infrared light at 5.2 µm is also generated, but is absorbed by the glass cell. In this example a prism was used to separate the blue light from the pump beams and the generated 420 nm power measured on a photodiode. The 420 nm power as a function of 780 nm and 776 nm detuning is shown in Fig. 3.7 (b) and (c), respectively.

The pump beams are focused through the cell using a $2f$-imaging system consisting of two 200 mm achromatic lenses. The beam waist of 0.89 mm before the first lens focuses to 52 µm at the centre of the rubidium cell. This combination of lenses and waists was found to be optimal for FWM conversion efficiency in previous work [92] - there is a trade off between the peak intensity at the focus and the propagation length over which the intensity is sufficiently high for efficient

FWM.

Due to the resonant enhancement, relatively low pump powers are required. In this case, 13 mW of 780 nm light and 23 mW of 776 nm was used, which corresponds to peak focused intensities of 0.3 and 0.5 kW/cm^2, respectively. With these pump powers a maximum of 0.34 mW of 420 nm light was generated.

The 420 nm light is generated for a wide range of pump detunings, so long as the combined 780 nm and 776 nm light is close to two-photon resonance with the $5S_{1/2} \rightarrow 5D_{5/2}$ transitions. Maximum conversion efficiency occurs when the 780 nm laser is detuned roughly halfway between the two ^{85}Rb $5S_{1/2}$ hyperfine

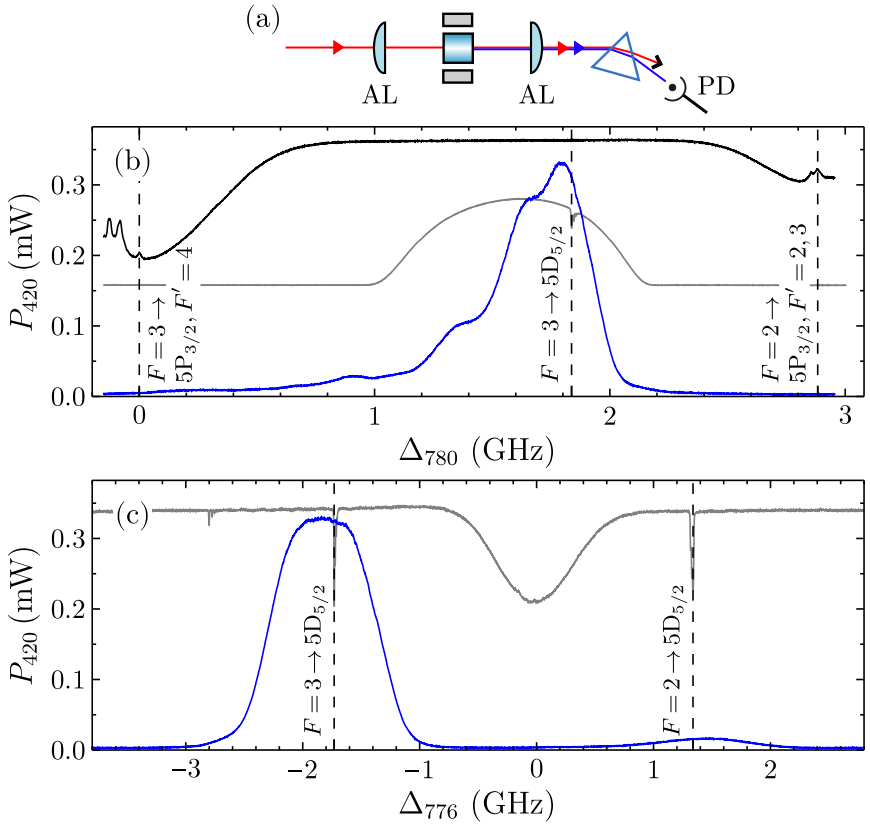

Figure 3.7: Example FWM signal. (a) Experimental setup, (b) 420 nm power directly after the cell (blue) as a function of 780 nm detuning ($\Delta_{776} = -1.8$ GHz) and (c) 776 nm detuning ($\Delta_{780} = 1.8$ GHz). Spectroscopy signals are included for reference: 780 nm saturated absorption spectroscopy (black) and two-photon spectroscopy (grey). AL: Achromatic lens, PD: Photodiode.

groundstates. These detunings minimise 780 nm absorption and Kerr lensing whilst still enabling a strong coherence to be induced on the two-photon transition [90,92]. The optimal pump detunings for peak 420 nm power in this example were $\Delta_{780} = 1.8\,\text{GHz}$ and $\Delta_{776} = -1.8\,\text{GHz}$.

Fig. 3.7 (b) shows the blue output power as a function of 780 nm detuning, with the 776 nm detuning fixed at $-1.8\,\text{GHz}$. The 420 nm emission is generated over a Doppler (and power) broadened feature, with a peak in intensity when the pump light is two-photon resonant. The blue feature has complicated substructure due to interference of different FWM pathways through the many hyperfine states of the upper levels [72, 74]. It is further complicated by Kerr lensing, predominantly of the 780 nm beam, which affects the phase-matching of the FWM process [92]. Peak FMW efficiency occurs close to zero Kerr lensing, which is halfway between the two hyperfine groundstates. The position and shape of this feature depends on various experimental parameters, including pump power, focused intensity, 776 nm detuning, cell temperature, pump polarisation and the position of the focus in the cell.

The blue power as a function of 776 nm detuning is shown in Fig. 3.7 (c), with $\Delta_{780} = 1.8\,\text{GHz}$. The 420 nm emission is generated when the pump beams are close to two-photon resonance with the transitions from the $F = 3$ (near $\Delta_{776} = -1.8\,\text{GHz}$) and $F = 2$ (near $\Delta_{776} = 1.2\,\text{GHz}$) $5S_{1/2}$ hyperfine groundstates.

As a side note, the two-photon spectroscopy shown here differs from the spectra shown in Fig. 3.4 due to a slightly different setup. Here, rather than using counter-propagating 780 nm and 776 nm beams, the transmission of a combined 780 nm and 776 nm beam after retroreflection through a rubidium cell (in this case the main FWM cell) was monitored. The resulting spectra contain the same two-photon absorption features as shown in Fig. 3.4, but also contain Doppler broadened single-photon absorption features. In Fig. 3.7 (b) the broad peak in transmission between 1 and 2.2 GHz is due to transmission of the 780 nm light which is completely absorbed close to the $5S_{1/2} \rightarrow 5P_{3/2}$ resonances. In Fig. 3.7

(c) the broad absorption feature close to zero detuning corresponds to single photon absorption of the 776 nm light, where population has first been transferred to the $5P_{3/2}$ state through single-photon 780 nm absorption.

3.5 Frequency Stabilisation

As well as taking traces of the FWM signal, it is useful to be able to stabilise the frequency of the pump lasers so that a blue beam with stable intensity and frequency can be generated. This is made non-trivial by the large detunings required for efficient FWM - the 780 nm laser must be locked at a detuning of around 1.6 GHz. To achieve this, a dichroic atomic vapour laser lock (DAVLL) is used, with the detuning further monitored via a beat note measurement with a separate 780 nm reference laser. The 776 nm laser meanwhile is locked using the standard frequency modulation technique to one of the two-photon spectroscopy features, so that the pump beams are two-photon resonant. This section describes these frequency stabilisation and monitoring techniques.

3.5.1 DAVLL lock - 780 nm

In order to lock the 780 nm laser at the required detuning an approximately linear error signal must be generated with a zero crossing roughly half-way between the $5S_{1/2} \rightarrow 5P_{3/2}$ transitions from the ^{85}Rb $F = 3$ and $F = 2$ hyperfine ground states. Furthermore, because the optimal 780 nm detuning for FWM conversion efficiency varies significantly with various experimental parameters, the frequency of the zero crossing must also be tunable. These criteria rule out the usual technique of frequency modulation locking to a saturated absorption feature [128], so instead another solution was found: the DAVLL lock [129–131].

The error signal in the DAVLL lock is generated as follows (see Fig. 3.8 (a) for the setup). Linearly polarised light propagates through a 75 mm long, room temperature rubidium cell and parallel to the direction of an applied magnetic field ($B \simeq 450$ G). The linearly polarised light can equally be described as an

equal superposition of circularly polarised components of opposite handedness (σ^+ and σ^-), and the quarter-waveplate and polarising beam splitter after the rubidium cell are set so that the transmission of each handedness is measured separately by photodiodes PD2 and PD3. The error signal is created by taking the difference between the two photodiode signals. With no applied field the difference signal would be zero, but the magnetic field causes the rubidium vapour to become dichroic: the transmission spectra of the σ^+ and σ^- components are shifted relative to each other.

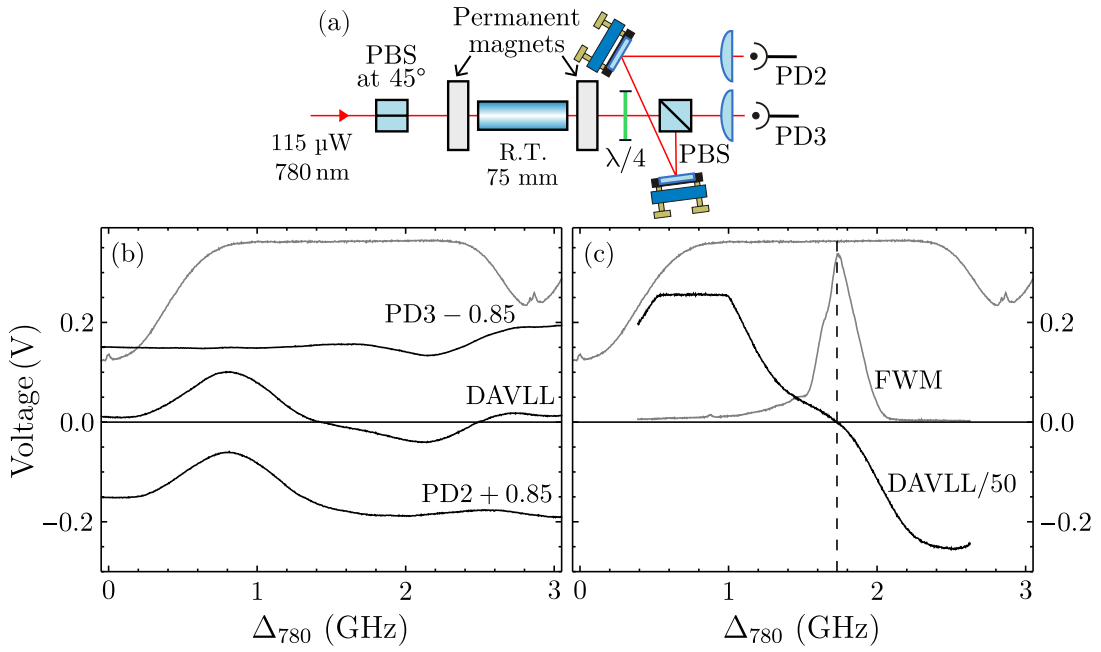

Figure 3.8: DAVLL lock for 780 nm laser (a) Experimental setup; PBS: Polarising beam splitter, R.T.: Room temperature. (b) Black: photodiode signals (offset for clarity) and initial DAVLL signal taken with an early version of the difference photodiode circuit. Note the PD2 signal is already inverted. (c) Black: the amplified DAVLL signal obtained with the final circuit, divided 50 times to show on the same scale. Grey traces show saturated absorption spectroscopy (in a separate cell) as a reference, and an example FWM spectrum is included in (c), showing the lock point aligned with peak FWM conversion efficiency. Data is averaged over 10 traces.

Each hyperfine energy level, F, is split into $2F + 1$ magnetic sublevels (labeled $m_F = -F... + F$), which correspond to different angular distributions of the electron wavefunction [1]. In an isolated atom these sublevels are degenerate, but the applied magnetic field breaks this degeneracy. This results in complicated spectra [131], but the net result is that transitions from the ground to excited state where $\Delta m_F = +1$ (which are coupled by the σ^+ light due to selection rules [1]) shift to higher energies whilst transitions where $\Delta m_F = -1$ (coupled by σ^-) shift to lower energy.

Fig. 3.8 (b) shows the PD2 and PD3 photodiode signals, which correspond to the σ^+ and σ^- components, respectively, as well as a saturated absorption trace in a separate Rb cell with no applied field for reference. Due to the limited range of the scan, the PD2 spectrum shows only the shifted transitions from the ^{85}Rb $F = 3$ groundstate, whilst the PD3 spectrum covers only the oppositely shifted transitions from the $F = 2$ groundstate. The difference between these signals creates an error signal with a zero crossing approximately halfway between the two hyperfine groundstates.

To allow the locking point to be tuned, a difference photodiode circuit was developed (see Appendix C) that allows the weighting given to each photodiode signal to be set using a variable resistor. A second stage then amplifies the signal to increase the gradient of the error signal, which results in a tighter lock. With this circuit the error signal shown in Fig. 3.8 (c) is generated. To lock the laser, this signal is passed to an integrator circuit which stabilises the laser frequency at the zero crossing. The stability of the lock is evaluated in the next subsection.

3.5.2 Beat note - 780 nm

The frequency of the 780 nm light is monitored directly by performing a beat note measurement with a second 780 nm reference laser. This laser is in an adjacent lab and is locked to a saturated absorption feature of the trapping transition in ^{87}Rb ($5S_{1/2}\,F = 2 \rightarrow\ 5P_{3/2}\,F = 2, 3$). The setup used for the beat note is shown in Fig. 3.9 (a). The radio frequency (RF) signal from the photodiode is amplified

by three 15 dB amplifiers and then monitored on an RF spectrum analyser.

The beat note measurement allows the stability of the DAVLL lock to be determined over different timescales. Monitoring the lineshape of the beat note itself (grey trace, Fig. 3.9 (b)) showed that locking the laser produces no significant broadening of the laser linewidth over timescales of 1 ms. However, on longer time scales the lock point itself wanders about the set point. The black trace in Fig. 3.9 (b) is recorded using the "max-hold" feature on the spectrum analyser to monitor the beat note for 1 minute. The frequency variation has a FWHM of 7 MHz. Over even longer time scales the lock point is subject to larger drifts. Fig. 3.9 (c) shows the drift of the peak frequency of the beat note over half an hour. This slow drift is a downside of the DAVLL lock technique, and

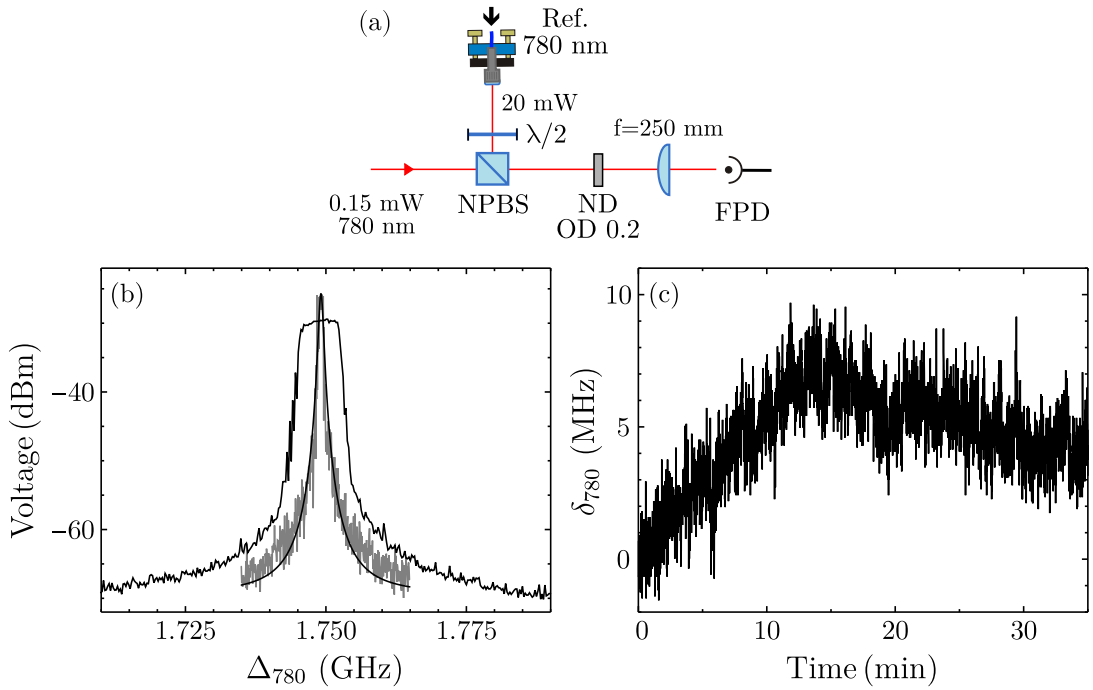

Figure 3.9: Reference beat note for 780 nm laser. (a) Experimental setup; NPBS: Non-polarising beam splitter, ND: Neutral density filter, FPD: Fast photodiode (Thorlabs DET025A). (b) Grey: Beat note between DAVLL locked 780 nm laser and reference laser, with Lorentzian fit (FWHM 0.96 MHz). Black: "Max-hold" trace beat note over 1 minute, FWHM 7 MHz. (c) Slow drift of peak beat note frequency over 35 minutes.

stems from temperature changes of the polarisation optics. To counteract this the DAVLL lock is always used in conjunction with the beat note measurement to monitor and set the lock point. The stability of the DAVLL lock could possibly be improved by using a Fresnel rhomb in place of the quarter waveplate.

3.5.3 Two-photon lock - 776 nm

Peak FWM conversion efficiency occurs when the pump lasers are two-photon resonant with the $5D_{5/2}$ excited state. Once the 780 nm laser is locked, two-photon resonance is ensured by stabilising the 776 nm frequency using the two-photon spectroscopy technique described in section 3.2.

A two-photon spectroscopy trace of the ^{85}Rb $5S_{1/2}\,F = 3 \rightarrow 5D_{5/2}$ transitions is shown in Fig. 3.10 (a). To produce an error signal for locking (with zero crossings at the resonance frequencies) the derivative of this spectroscopy signal must be found (Fig. 3.10 (b)). This is achieved using a lock-in detector [128]: a 50 kHz modulation is applied to the 780 nm laser frequency via the piezo, which in turn modulates the spectroscopy signal. The product of the applied modulation

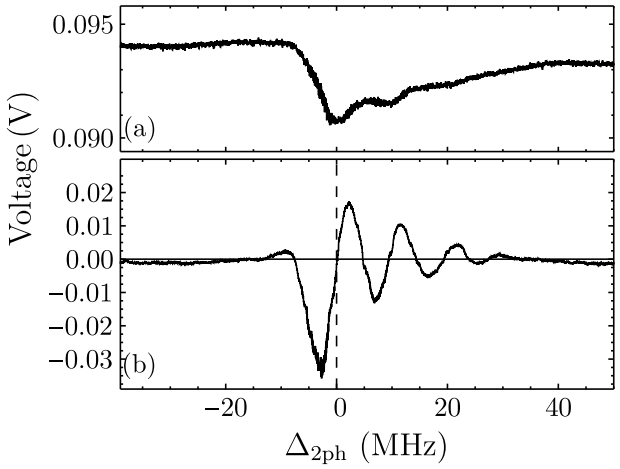

Figure 3.10: Two-photon lock to stabilise the 776 nm frequency. (a) Two-photon spectroscopy of the ^{85}Rb $5S_{1/2}\,F = 3 \rightarrow 5D_{5/2}$ transitions. (b) Derivative signal used for locking. The vertical dashed line indicates the lock point. Data is averaged over 100 traces.

and the spectroscopy signal then gives a signal proportional to the derivative.

The spectroscopy signal and derivative shown in Fig. 3.10 were taken using a 25 mm long rubidium cell at 130°C with 0.4 mW and 1.5 mW of 780 nm and 776 nm light, respectively. Both beams had waists of 0.9 mm, and the modulation applied to the 780 nm laser had an RMS amplitude of ~ 4 MHz. With this error signal the 776 nm laser was locked so that the two pump fields were resonant with the ^{85}Rb $5S_{1/2}\,F = 3 \rightarrow\ 5D_{5/2}\,F' = 5$ transition with an RMS lock stability inferred from the lock error signal of 0.27 MHz over 4 s.

3.6 Summary

This chapter has introduced and explained the basic building blocks of the FWM experiment. The two pump lasers were described, as well as the spectroscopy techniques used to monitor their frequency. The heated rubidium cell and the method used for measuring its temperature was also introduced. With these elements the FWM signal can be generated, and an example of the FWM spectrum obtained was provided. In the final section the methods used to stabilise the frequency of the pump lasers were detailed. This chapter provides the foundations of the experimental work for this thesis, and will be referenced later when describing the setup for each particular experiment.

Chapter 4

Structured light

Building on the basic FWM experiment, the bulk of this thesis studies the effect of adding transverse phase and intensity structure to the pump beams. In particular, we study the transverse mode of the generated 420 nm light when the pump light is shaped into Laguerre-Gauss (LG) modes. Following an introduction to LG modes in Sec. 4.1, the remainder of this chapter introduces the experimental setup and analysis used to carry out these experiments.

The development of the beam shaping setup contributed to the publication of two papers, Refs. [P1] and [P2]. The first, which will be discussed in Sec. 4.2, compares different methods of generating phase-only holograms. For this work my main contribution was working with T. W. Clark to take the experimental data, as well as preliminary input into the experimental software and the analysis of the results. In this chapter we present the experimental results from this paper which are most relevant to the work in this thesis. This work is discussed more fully in the thesis of T. W. Clark [132].

The second paper, Ref. [P2], compares the hologram generation methods over a wide range of simulated experimental conditions. My main contribution to this work was in the discussion and interpretation of the results. Therefore we present only the main conclusions of this paper in Sec. 4.3, with the focus on how the results informed the development of the FWM beam shaping setup.

The final element required for the FWM experiment is a method of quanti-

tatively measuring the mode decomposition of the generated 420 nm light, and, for comparison, the shaped pump beams. The experimental setup and analysis developed to do this will be described in Sec. 4.4, and is also discussed in Ref. [P3].

4.1 Laguerre-Gauss modes

Ignoring polarisation, the electric field of an optical beam propagating along z, and with transverse coordinates $\underline{\mathbf{r}}_t$, can be written as

$$E(\underline{\mathbf{r}}_t, z, t) = u(\underline{\mathbf{r}}_t, z)e^{i(kz-\omega t)}. \tag{4.1.1}$$

The complex field oscillates in time and in z, and has some finite distribution in the transverse plane, which is described by $u(\underline{\mathbf{r}}_t, z)$.

For certain transverse distributions, known as transverse modes, $u(\underline{\mathbf{r}}_t, z)$ remains the same, apart from a scale factor, as the beam propagates. The simplest of these distributions can be found by solving the paraxial wave equation, [34]

$$\nabla_t^2 u(\underline{\mathbf{r}}_t, z) + 2ik\frac{\partial u(\underline{\mathbf{r}}_t, z)}{\partial z} = 0. \tag{4.1.2}$$

This is a simplified form of the wave equation introduced in Sec. 2.1 under the assumption that the variation of $u(\underline{\mathbf{r}}_t, z)$ along z is slower than both the fast e^{ikz} oscillation along z and the transverse variations in $\underline{\mathbf{r}}_t$.

In cylindrical coordinates the most compact solutions are the Laguerre-Gauss modes, which have the form [133],

$$\begin{aligned}
&\mathrm{LG}_p^\ell(r,\theta,z) = \frac{C_p^\ell}{w}\left(\frac{r\sqrt{2}}{w}\right)^{|\ell|} L_p^{|\ell|}\left[\frac{2r^2}{w^2}\right]\ e^{-\frac{r^2}{w^2}+i(kz+\ell\theta+\Phi_S+\Phi_G)}\\
&\text{Normalisation factor}: C_p^\ell = \sqrt{2p!/\pi(p+|\ell|)!}\\
&\text{Beam width}: w = w_0\sqrt{1+(z/z_R)^2},\ \text{Beam waist}: w_0,\\
&\text{Rayleigh range}: z_R = \pi w_0^2/\lambda\\
&\text{Spherical wavefronts}: \Phi_S = kr^2 z/(2(z^2+z_R^2))\\
&\text{Gouy phase}: \Phi_G = -(2p+|\ell|+1)\arctan(z/z_R)\\
&\text{Associated Laguerre polynomial}: L_p^{|\ell|} = \sum_{j=0}^{p}(-1)^j\binom{p+|l|}{p-j}\frac{x^j}{j!}
\end{aligned} \tag{4.1.3}$$

If Eq. 4.1.2 is instead solved in Cartesian coordinates then the familiar Hermite-Gauss modes are found [34].

The transverse intensity and phase of the lower order LG modes are shown in Fig. 4.1. Each mode is described by two integers, $-\infty < \ell < +\infty$ and $p \geq 0$. Apart from the fundamental mode, the intensity profiles are ring shaped, with the p index determining the number of radial nodes. The ℓ index directly determines the transverse phase of the beam via the $e^{il\theta}$ term. The phase of each mode varies azimuthally, with the phase ramping linearly from 0 to 2π ℓ times around the circumference of the beam. For $|\ell| > 0$, the phase is therefore undefined at the centre of the beam, resulting in a zero in intensity. Although not shown, the sign of ℓ affects only the sign of the azimuthal phase variation, with the intensity profile dependent on $|\ell|$.

The propagation of the fundamental LG_0^0 (Gaussian) mode along z is shown in Fig. 4.2 (a). The overall scaling of the transverse profile is set by the beam waist, w_0, which is the $1/e^2$ intensity radius at $z = 0$. As the beam propagates it expands due to diffraction such that after one Rayleigh range, z_R, the beam width is $\sqrt{2}w_0$, but the transverse profile is otherwise unchanged.

As the beam propagates through the focus it also undergoes a phase shift of

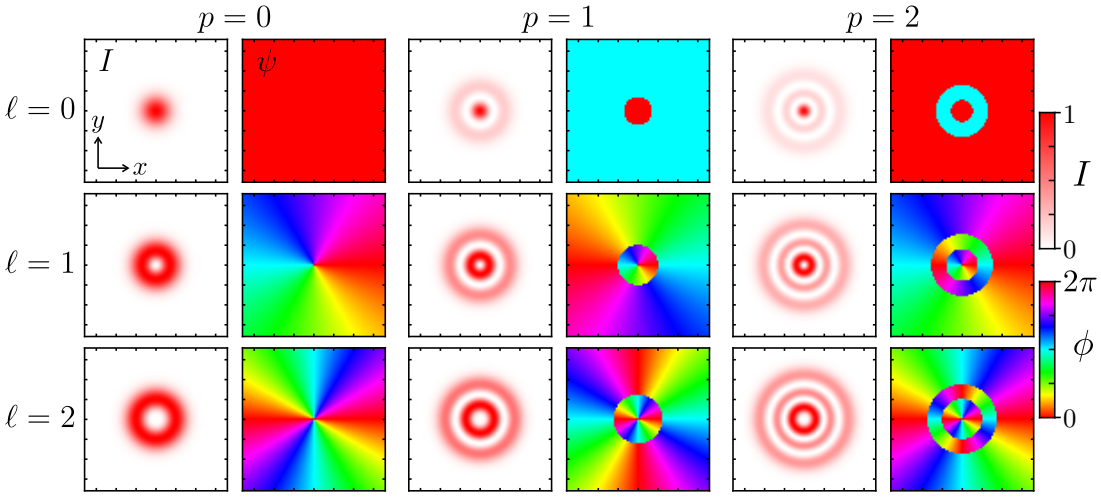

Figure 4.1: Transverse intensity, I, and phase, ϕ, of the Laguerre-Gauss modes for $0 \leq \ell \leq 2$ and $p \leq 2$.

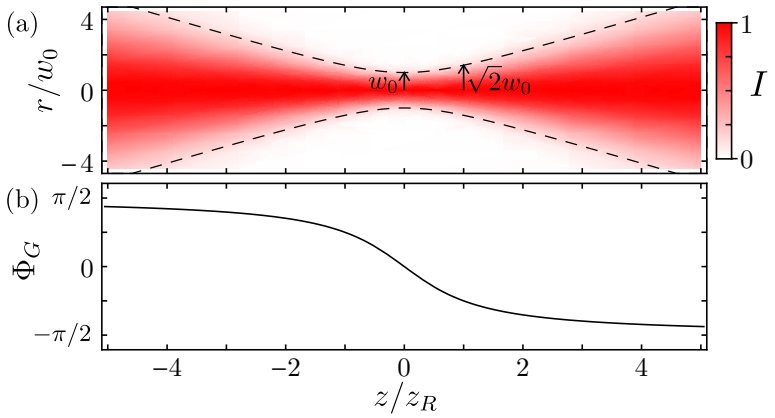

Figure 4.2: (a) Normalised intensity variation and (b) Gouy phase shift of the LG_0^0 mode propagating along z.

π relative to a plane wave. This is captured by the Gouy phase term in Eq. 4.1.3, the z-dependence of which is plotted in Fig. 4.2 (b). Due to the finite extent of the beam at the focus, it can be described as a superposition of plane waves propagating at a range of (small) angles relative to the z-axis. As a result, the beam must propagate further in order to undergo the same phase shift as a plane wave traveling directly along z, and the phase of the beam is therefore delayed. The magnitude of this phase shift increases for higher order modes, with the total phase shift given by $-(2p + |\ell| + 1)\pi$.

4.1.1 Orbital angular momentum

An important feature of the LG modes is that they carry orbital angular momentum (OAM) [41–43]. Light can carry both linear and angular momentum, and, in the paraxial approximation, the angular momentum can be futher sub-divided into two types: spin angular momentum (SAM) and orbital angular momentum (OAM) [133]. The SAM is associated with circular polarisation, and was first observed as long ago as 1936 via measurements of the torque exerted on a birefringent plate [134]. Conversely, although the existence of OAM has been known since 1932 [135], it was another sixty years before Allen *et al.* recognised that light carrying OAM could be readily generated in the lab. Specifically, they showed

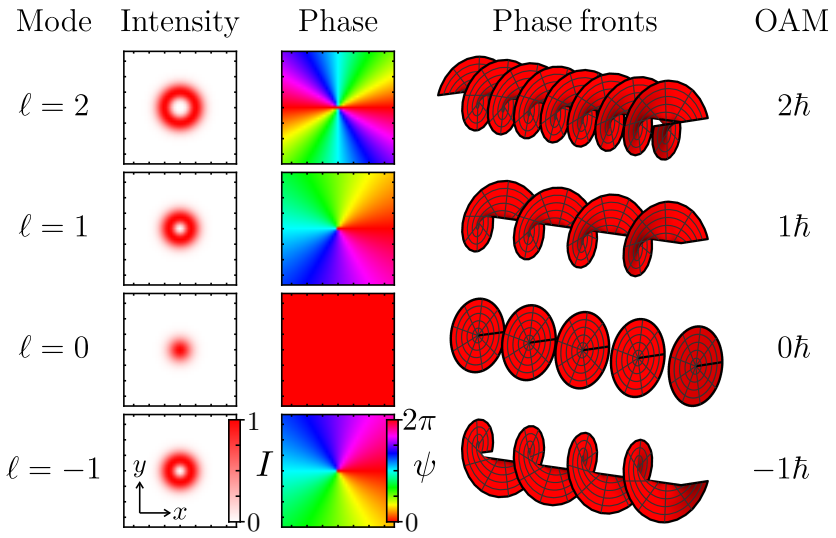

Figure 4.3: Helical wavefronts of the $p = 0$ LG modes in the limit of $w_0 >> \lambda$ and with the wavelength size exaggerated for clarity.

that any beam with an $e^{i\ell\theta}$ phase dependence carries $\ell\hbar$ of OAM per photon. Clearly the LG modes meet this criteria, with the ℓ index directly determining the OAM carried by the beam.

The link between an $e^{i\ell\theta}$ transverse phase and OAM can be explained by considering the phase fronts of the beam, shown for the first few $p = 0$ LG modes in Fig. 4.3. Whilst the phase fronts of the fundamental mode $\ell = 0$ are spherical shells, for the $l = 1$ mode they form a spiral along the z-axis. As ℓ increases more spirals are intertwined; for $l = 2$ the phase fronts form a double helix, similar to DNA, whilst a negative ℓ results in spirals of opposite handedness. At any point along the beam the electric and magnetic fields are tangential to the phase fronts, and the local momentum density, $\varepsilon_0 \underline{\mathbf{E}} \times \underline{\mathbf{B}}$, is therefore normal to the phase front. Hence, for $|\ell| > 0$, the momentum density follows a helical path, rotating around the z-axis, resulting in an associated OAM [133, 136].

Applications for OAM are wide ranging, encompassing optical manipulation, communication and quantum optics. Both SAM and OAM can be used to exert a torque on trapped particles [137–140], which can be used to drive micromachines in optical tweezer experiments [141, 142], or alternatively to impart angular momentum to Bose-Einstein condensates, leading to interesting research studying

vortices [143] and superfluidity [144].

The most relevant application for this thesis is optical communication. Light modes carrying different values of OAM are orthogonal, presenting a theoretically infinite basis which can be used to encode information. The actual number of OAM basis states is of course limited by technical considerations, but there is still the potential for high bandwidth communication. Classical communication using OAM multiplexing has been demonstrated both in free space [6,145] and in optical fibres [32,102], and OAM states have also been used for higher-dimensional quantum key distribution [146, 147].

4.1.2 LG mode generation

For a cavity to support an LG mode the entire spatial xy profile must undergo identical phase shifts and losses in a round trip to avoid breaking the cylindrical symmetry. As a result, although LG modes can be generated directly within a laser cavity [148], it is more challenging than generating the more commonly found Hermite-Gauss (HG) modes, since common cavity elements, such as Brewster plates, break the xy symmetry. However, since both LG and HG modes are complete orthonormal bases, each LG mode can be rewritten as a complex superposition of HG modes. Early methods of generating LG modes, known as astigmatic mode converters, made use of this by taking two HG modes and introducing the correct phase shift between them to generate a LG mode [149]. LG modes can also be generated from an initially Gaussian beam, perhaps most commonly using a forked diffraction grating [150], where a fixed LG mode is generated in one of the diffracted orders. Alternatively a spiral phase plate [151] - a refractive optic which introduces an $i\ell\theta$-phase dependence across the beam - or q-plate [152] - which uses geometric phase shifts to couple spin and orbital angular momentum - can be used.

Whilst these methods work well, the LG mode generated is fixed by the characteristics of the optical element. In contrast, digital holography, using devices such as a digital micro-mirrored device (DMD) [153] or spatial light modulator

(SLM), allows the generated mode to be chosen and updated in real time. In this thesis an SLM is used to generate a range of modes, as well as more general transverse patterns. The methods used to do this are described in the next section.

4.2 Holographic beam shaping

Holographic beam shaping was first introduced by Gabor in 1948 [154]. In this early demonstration, the interference pattern between a coherent reference beam and the light scattered from an object was recorded on a photographic plate. Subsequent illumination of the plate, or hologram, with the reference beam recreated an image of the original object. Digital holography follows the same principle, but rather than requiring a physical hologram formed by interference, the hologram is calculated numerically and "displayed" on a beam shaping device - in our case an SLM. The flexibility this allows has revolutionised beam shaping, but introduces a new problem: how to calculate the hologram required to produce a given optical field.

A wide variety of hologram generation methods exist. In order to select the most appropriate method for the FWM experiment, various approaches were compared both numerically and experimentally. The results from this work are presented in Ref. [P1].

4.2.1 Phase-only beam shaping

Light is inherently complex; it has both an amplitude and a phase. SLMs shape light by inducing a spatially varying phase shift across the beam. This immediately provides direct control over the phase of the beam, and, via various different methods, can also be used to shape the amplitude. An obvious approach is to use two SLMs in combination with polarisation optics to convert between phase and amplitude shaping [155, 156]. However, SLMs are expensive so we limit the problem to a single SLM. In this case, high fidelity beam shaping can be achieved

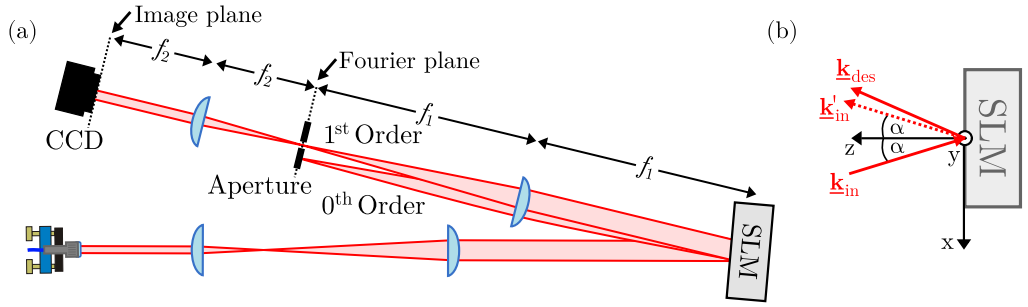

Figure 4.4: (a) Setup for beam shaping using a single SLM. (b) Wave vector diagram of input and diffracted light. For the comparison experiment, $f_1 = 300\,\text{mm}$ and $f_2 = 125\,\text{mm}$.

using iterative methods to calculate the required phase hologram [157–159]. These methods are usually most appropriate when a complex phase and intensity profile is required in a single transverse plane. For the FWM experiment the main aim is to generate propagating modes, in which case much simpler methods can be used. The usual approach is to include a phase grating in the hologram [160–165], and modulate the phase depth of the grating to achieve amplitude shaping.

In particular we focus on hologram generation methods where the desired mode is generated in the first diffracted order [166–169]. This has the advantage of spatially separating the shaped and unshaped light, allowing for higher mode purity. The setup required for this approach is shown in Fig. 4.4 (a). Light from a single-mode optical fibre is expanded using a telescope to cover the active area of the SLM. The diffracted light from the SLM is then imaged using a $4f$-telescope, with an aperture in the Fourier plane of the SLM in order to select only the first diffracted order.

4.2.2 Hologram generation methods

The aim is to use a phase only hologram $H = H(x, y)$ to generate a desired field $E_{\text{des}}(x, y) = A_{\text{des}}(x, y)e^{i\Phi_{\text{des}}}$ given an input field $E_{\text{in}}(x, y) = A_{\text{in}}(x, y)e^{i\Phi_{\text{in}}}$, such that

$$E_{\text{des}}(x, y)e^{i\underline{\mathbf{k}}_{\text{des}}\cdot\underline{r}} = e^{iH(x,y)} \times E_{\text{in}}(x, y)e^{i\underline{\mathbf{k}}'_{\text{in}}\cdot\hat{\underline{r}}}. \tag{4.2.4}$$

The orientation of the desired field wave vector $\underline{\mathbf{k}}_{\text{des}}$ and the (reflected) input wave vector $\underline{\mathbf{k}}'_{\text{in}}$ are shown in Fig. 4.4 (b).

To find the required form of the hologram, Eq. 4.2.4 can be rewritten as

$$e^{iH(x,y)} = \frac{E_{\text{des}}(x,y)}{E_{\text{in}}(x,y)} e^{i(\underline{\mathbf{k}}_{\text{des}} - \underline{\mathbf{k}}'_{\text{in}}).\hat{\underline{r}}}. \tag{4.2.5}$$

By requiring a small angle between $\underline{\mathbf{k}}_{\text{des}}$ and $\underline{\mathbf{k}}'_{\text{in}}$, the phase grating is introduced automatically due to the interference between the beams

$$(\underline{\mathbf{k}}_{\text{des}} - \underline{\mathbf{k}}'_{\text{in}}).\hat{\underline{r}} = \frac{2\pi x}{\Lambda} = \text{Mod}\left(\frac{2\pi x}{\Lambda}, 2\pi\right) = \Phi_g(x). \tag{4.2.6}$$

Eq. 4.2.5 can now be rewritten as

$$\begin{aligned} e^{iH(x,y)} &= A_{\text{rel}}(x,y) e^{i\Phi_{\text{relg}}}, \\ A_{\text{rel}}(x,y) &= A_{\text{des}}(x,y)/A_{\text{in}}(x,y) \\ \Phi_{\text{relg}}(x,y) &= \Phi_{\text{des}}(x,y) - \Phi_{\text{in}}(x,y) + \Phi_g(x). \end{aligned} \tag{4.2.7}$$

The fields are appropriately normalised so that $A_{\text{rel}}(x,y)$ is between 0 and 1, and $\Phi_{\text{relg}}(x,y)$ ranges from $-\pi$ to π.

As a first approximation, the hologram $H(x,y)$ can be simply set equal to the relative phase

$$H(x,y) = \Phi_{\text{relg}}(x,y). \tag{4.2.8}$$

For LG modes, this is equivalent to a forked diffraction grating. However, without amplitude shaping the intensity profile of the incident Gaussian is projected onto the set of LG modes with the desired ℓ. The result is a beam with the correct ℓ index, but composed of many p-modes. To improve on this, we consider holograms of the form

$$H(x,y) = f(A_{\text{rel}}(x,y))\, \Phi_{\text{relg}}(x,y), \tag{4.2.9}$$

where the function $f(A_{\text{rel}}(x,y))$ modulates the depth of the phase grating according to the relative amplitude of the fields.

In Ref. [P1] six hologram generation methods were compared. In this chapter we present the four methods most suited to the FWM experiment:

Method A

The simplest method tested was to scale the phase grating directly by the relative amplitude of the fields

$$H(x,y) = A_{\text{rel}}(x,y)\Phi_{\text{relg}}(x,y). \tag{4.2.10}$$

This method was initially solely included as a baseline for comparison, but performed remarkably well.

Method B

This method has a different form to Eq. 4.2.9, and instead takes inspiration from the original Gabor experiment. The hologram is based on the interference pattern formed between the input and desired fields, but here the resulting phase distribution is used, rather than the intensity

$$\begin{aligned} H(x,y) &= \arg(NE_{dg}(x,y) + E_{\text{in}}(x,y))\,, \\ E_{dg}(x,y) &= A_{\text{des}}(x,y)e^{i(\Phi_{\text{des}}(x,y)+\Phi_g(x))}. \end{aligned} \tag{4.2.11}$$

The normalisation factor N is included to ensure that the amplitude of the desired field never exceeds that of the input field.

Method C

Method A makes the assumption that the amplitude of light diffracted into the first order varies linearly with the grating depth, which is of course not the case. Fourier analysis shows that the diffracted amplitude is in reality given by [166]

$$A(x,y) = e^{i(1-f(A(x,y)))\pi}\text{sinc}\left[\pi(1-f(A(x,y)))\right], \quad \text{sinc}(w) \equiv \frac{\sin(w)}{w}. \tag{4.2.12}$$

Neglecting the phase term, and taking the inverse gives

$$f(A(x,y)) = 1 - \frac{1}{\pi}\text{sinc}^{-1}(A(x,y)), \tag{4.2.13}$$

thus the full hologram is given by

$$H(x,y) = \left(1 - \frac{1}{\pi}\text{sinc}^{-1}(A_{\text{rel}}(x,y))\right)\Phi_{\text{relg}}(x,y). \tag{4.2.14}$$

This method was put forward by Davis *et al.* [166] and is the method eventually chosen for the FWM experiments.

Method D

Bolduc *et al.* pointed out that neglecting the phase term in equation 4.2.12 may cause an undesired amplitude dependent phase error in the hologram [169]. As a solution they suggested the following hologram as an improvement

$$\begin{aligned} H(x,y) &= M\left(\Phi_{\text{relg}}(x,y) - \pi M\right), \\ M &= 1 + \frac{1}{\pi}\text{sinc}^{-1}(A_{\text{rel}}(x,y)). \end{aligned} \tag{4.2.15}$$

This method performed very similarly to method C in the comparison experiment, with method C eventually chosen due to its slightly simpler form.

Other methods

The other two methods considered in Ref. [P1] were proposed by Arrizòn *et al.* [167], and used amplitude scaling functions based on the zero and first order Bessel functions. These methods performed well, but the four methods detailed above performed consistently as well if not better in our comparison. However, numerical simulations in later work [P2] showed that the Arrizòn methods may outperform the others on SLM devices with reduced phase throw (see section 4.3).

4.2.3 The experiment

The experimental setup for the comparison was the same as shown earlier in Fig. 4.4 (a). Light from the 776 nm laser was coupled through a single-mode polarisation-maintaining fibre, and a $4f$-telescope used to expand the beam to a $1/e^2$ intensity radius of 4.65 mm. The angle of incidence of the beam onto the SLM (Hammamatsu LCOS X10468-02) was approximately 3°. Holograms were calculated to generate a range of modes, following each of the methods detailed

above and using a grating period of $\Lambda = 4$ SLM pixels. The waist of the modes at the SLM was set to 0.9 mm.

After the SLM, a $4f$-telescope ($f_1 = 300$ mm and $f_2 = 125$ mm see Fig. 4.4 (a)) was used to select the first diffracted order and to demagnify the beam so that it would fit on a Point Gray Chameleon CMLN-13S2M-CS camera. The aperture in the Fourier plane of the telescope was $\sim$1 mm in diameter. Images of the shaped light were taken first in the image plane of the SLM, and then after the light had propagated $0.5z_R$ and $1.0z_R$ (29.5 mm and 56.9 mm, respectively).

Input beam

So far no consideration has been given to the form of $E_{\text{in}}(x, y)$. Numerical simulations of the methods showed a substantial decrease in the beam generation accuracy if the input field is assumed to be a plane wave [P1]. Instead, single pixel imaging techniques [170, 171] were used to measure the profile of the input beam *in situ* (Fig. 4.5). The basic idea is to divide the SLM into "superpixels" and record the diffracted power when a phase grating is displayed at each pixel in turn. From this information, an image of the beam can then be reconstructed. Rather than using single superpixels, the signal to noise ratio can be improved by using an orthogonal set of patterns that cover the whole SLM. In the comparison experiment a sequence of Hadamard patterns were used to reconstruct a 32×32 pixel image of the input beam. This image was then scaled up to the 600×600 resolution of the SLM hologram to produce an image, $I_{\text{m}}(x, y)$. The input field

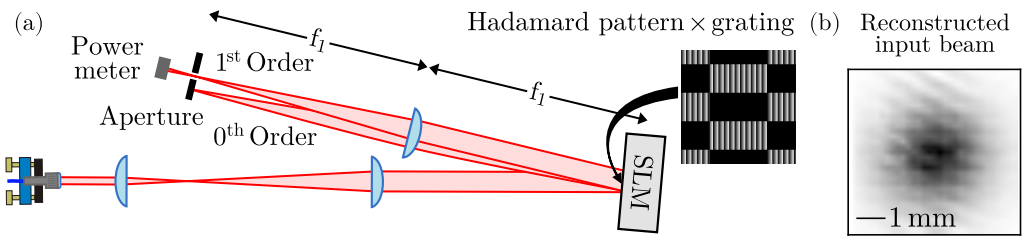

Figure 4.5: (a) Setup for single pixel imaging of input beam and (b) reconstructed intensity profile.

used in the calculations of the holograms was then

$$E_{\text{in}}(x, y) = \sqrt{I_{\text{m}}(x, y)}. \tag{4.2.16}$$

For the purposes of the comparison paper the phase fronts of the input beam were assumed to be flat. However, similar single pixel methods exist to measure the combined phase flatness of the input beam and SLM [172], which could be employed if necessary.

A drawback of the single pixel imaging technique is that it is relatively slow if a high resolution image of the input beam is required. An alternative method, which was used in the final FWM beam shaping experiment, is to instead assume the input beam is a perfect Gaussian, but use single pixel imaging to measure its waist. Only a low resolution image is required for this, and as a result the measurement is quick, and provides an accurate measurement of the beam waist directly at the SLM.

Phase flatness

Although we assumed the input beam had perfect flat phase fronts, it was apparent from astigmatism of the shaped beam that the surface of the SLM was slightly curved. To correct for this, the phase of a cylindrical lens of focal length 11m at an angle of 96° to the vertical was added to the hologram. The effect of this correction is most apparent in the far field. Fig. 4.6 shows the profile of a focused Gaussian beam before and after it had been reflected off the SLM, and then with the cylindrical lens correction. Although the correction greatly improves the astigmatism, the faint ring and remaining asymmetry indicates a more rigorous

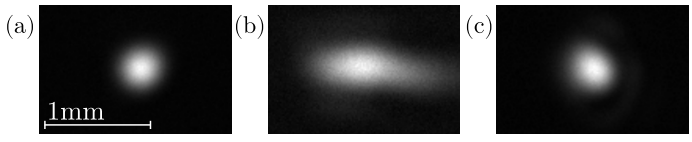

Figure 4.6: Intensity profile at the focus of a $f = 750\,\text{mm}$ lens (a) before the SLM (b) at the Fourier plane of the SLM with no correction and (c) with the cylindrical lens correction. Data from [P1].

phase correction could improve the phase flatness further. See Subsection 4.3.5 for further discussion on this topic.

4.2.4 Results

The comparison tested the ability of the hologram generation methods to produce three different shaped beams: a Gaussian, an LG_0^{10} mode, and a Ferris wheel superposition of modes ($E_{\mathrm{des}} = \mathrm{LG}_0^3 + |\frac{11}{3}|^{1/4}\mathrm{LG}_0^{11}$) [38], all with a beam waist of 0.9 mm at the SLM. The full dataset is shown in Ref. [P1], but since the relative performance of the methods was roughly the same for each beam, only the results for the Ferris wheel superposition are included here.

Fig. 4.7 (a) shows the intensity profile of the shaped beam for each hologram

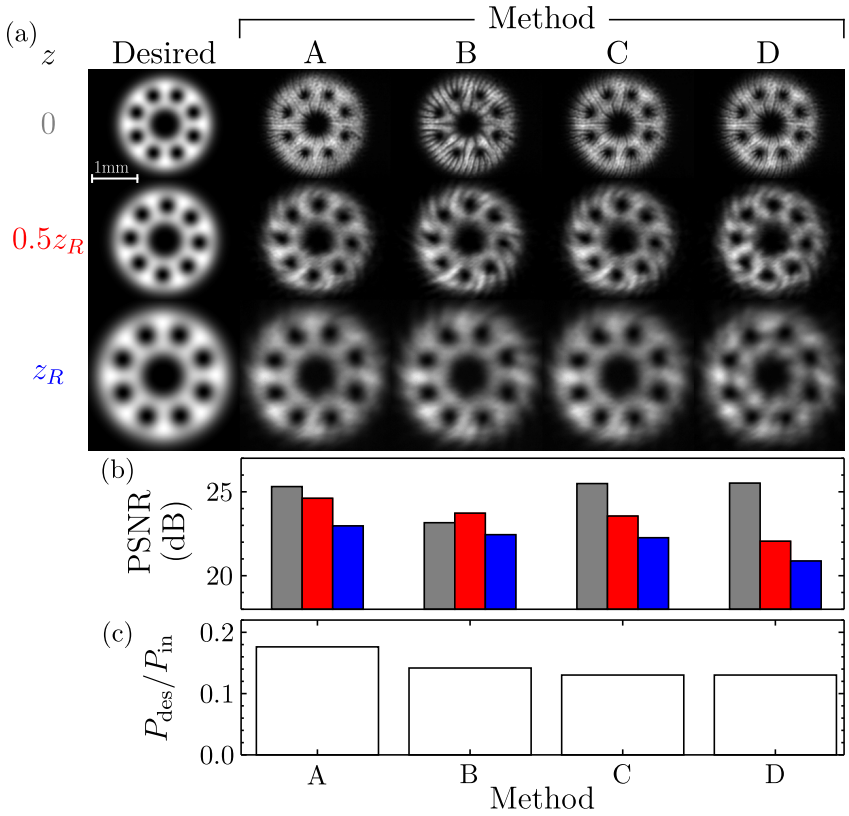

Figure 4.7: (a) Desired and measured Ferris wheel intensity profile for each hologram generation method at propagation distances $0z_R$, $0.5z_R$ and $1.0z_R$. (b) PSNR and (c) shaping efficiency for each image. Data from [P1].

generation method for three propagation lengths: $0z_R$ (the SLM image plane), $0.5z_R$ and $1.0z_R$. While the phase of the shaped beams was not measured directly, the images of the beam after propagation provide an indication of the quality of the phase shaping. In the image plane each mode shows fine substructure not present in the desired beam. The form of this structure depends on the grating pixel period chosen, and becomes less apparent for larger grating periods. These grating pixelation errors were also reproduced in the numerical simulations carried out in Ref. [P1].

To quantify the beam generation accuracy, an ideal beam profile was calculated by performing 2D fits of the expected intensity profile ($|\mathrm{LG}_0^3 + |\frac{11}{3}|^{1/4}\mathrm{LG}_0^{11}|^2$) to each image. The only free parameters were the centre position, offset, amplitude and relative phase of the modes. The Peak Signal-to-Noise Ratio (PSNR) [173] was then calculated using

$$\begin{aligned} \mathrm{PSNR} &= 10\log_{10}\left(\frac{\mathrm{MAX}_I^2}{\mathrm{MSE}}\right), \\ \mathrm{MSE} &= \frac{1}{mn}\sum_{i=0}^{m-1}\sum_{j=0}^{n-1}\left[I(i,j) - K(i,j)\right]^2, \end{aligned} \tag{4.2.17}$$

where I is the fitted ideal m by n image, the maximum value of which is MAX_I, and K is the experimental image.

Fig. 4.7 (b) shows the measured PSNR for the image plane (grey), $0.5z_R$ (red) and $1.0z_R$ (blue) images. For all methods but B the intensity distribution is created with highest accuracy in the image plane, with the quality dropping slightly as the beam propagates. This suggests there is a small discrepancy in the phase profile of the generated beams. The drop in quality is least for method B indicating the phase is replicated best with this method.

Overall, the Ferris wheel results in Fig. 4.7, and the Gaussian and LG_0^{10} results in Ref. [P1], show that methods A-D produce beams of similar quality, with methods A, C and D possibly performing slightly better than B. This is despite the different approach to amplitude shaping of each method. However, the current analysis only considers the intensity distribution of the beam in three propagation planes. This gives very little information on the phase profile of

the shaped beams, and a full characterisation of the beams may provide a larger differentiation between the methods. This could include measuring the phase of the beam directly, via interference with a reference Gaussian, or performing a full mode decomposition of the beam with a second SLM.

The shaping efficiency of each method, defined as $P_{\text{des}}/P_{\text{in}}$, where P_{des} is the power in the shaped beam and P_{in} is the power in the input beam, is shown in Fig. 4.7 (c). Methods B-D have similar efficiencies of around 13%, whilst method A is more efficient at 18%. The efficiency is intrinsically limited to 53% due to the spatial overlap of the input and desired beams, and is further reduced by the combined reflection coefficient and grating diffraction efficiency, which was 67%. Therefore the maximum efficiency that can be expected is 35%.

As a final test, the accuracy with which each method can recreate a non-propagating arbitrary image was investigated. By choosing a more complicated intensity distribution, this further compares the amplitude shaping achieved by each method. The chosen image was of a "Laser" dinghy (my preferred weekend laser), and the comparison was carried out in the same way as for the propagating modes discussed above, with the intensity profile recorded only in the image plane of the SLM. The results are shown in Fig. 4.8. As with the propagating modes, methods A, C and D perform similarly, with method B achieving slightly worse accuracy, which appears to be due to the cylindrical lens correction causing unwanted amplitude modulation.

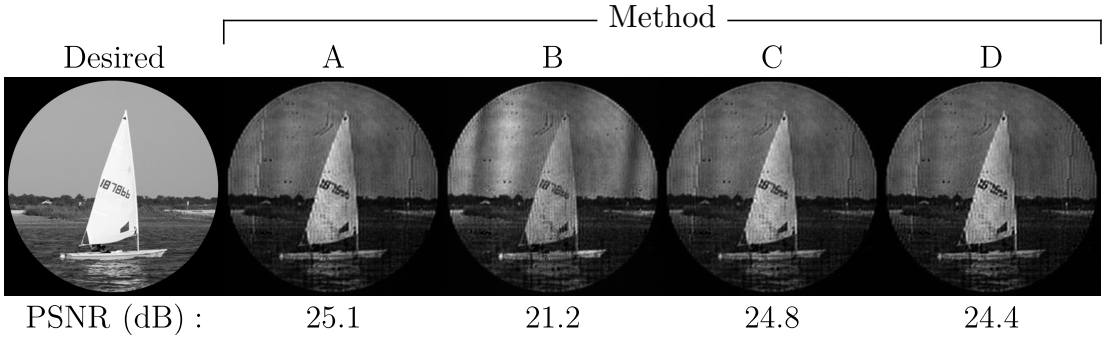

Figure 4.8: "Laser" beam generation for each method. Data from [P1].

4.2.5 Conclusion

In this section the most relevant results from Ref. [P1] have been discussed. Different methods of generating phase-only holograms were compared using two metrics: the PSNR - a measure of the beam shaping fidelity - and the shaping efficiency. All of the methods performed well, with very little to choose between methods A, C and D. Taking into account all results presented in Ref. [P1], method C possibly produces the highest quality shaped beams overall. Method A performed remarkably well given its simplicity, and also demonstrated a slight advantage in shaping efficiency. From this comparison, methods A and C were chosen as the most suitable for the FWM experiment, due to their high shaping efficiency and accuracy, respectively, and overall simplicity.

Although not discussed here, these results agreed qualitatively with the numerical simulations carried out in Ref. [P1]. The simulated intensity profiles showed remarkable similarity to the measured profiles, even down to the grating pixelation errors.

Later measurements performed after the comparison experiment, described and discussed in Sec. 4.3.4, compared the ability of methods A and C to generate a flat disk of intensity. This further test provided better differentiation between the methods, with method C eventually chosen for use in the FWM experiment due to its superior amplitude shaping.

4.3 FWM beam shaping details

In this section, we describe the beam shaping setup used for the FWM experiment. This setup was developed based on the results of the paper discussed in the previous section, and also a second, purely numerical paper [P2]. In the second paper the hologram generation methods were numerically compared over a wide range of simulated experimental conditions. The experimental choices made for the FWM setup will be explained in the context of the results from both papers.

4.3.1 The SLM

Up to this point the SLM has been treated as a "black box" that creates a programmable spatially varying phase shift. In reality the SLM works much like a liquid crystal display. A layer of birefringent liquid crystals is sandwiched between a glass plate and a dielectric mirror, as shown in Fig. 4.9. The orientation of the liquid crystal is controlled by the voltage applied at each pixel electrode, such that the horizontal component of the polarisation undergoes a voltage dependent phase shift with respect to the vertical component.

The SLM used for the FWM experiment was a Hamamatsu LCOS-X13138-02, which has 1272×1024 12.5 µm square pixels covering a 15.9×12.8 mm effective area. The near-IR dielectric mirror in this model results in a measured reflectivity of 97.4(2)%, but limits the wavelength range of the device to 800 ± 50nm.

The pixel resolution is a key parameter that determines the performance of the SLM. However, simulations in Ref. [P2] showed that for our application the accuracy and efficiency of the beam shaping is mainly limited by the number of pixels per grating period, rather than the resolution itself. All methods performed with optimum accuracy and efficiency at a reduced resolution of 200×200 pixels over a 12×12 mm area, so long as there were still sufficient pixels per grating. In this case the grating period was 600 µm, corresponding to a pixel period of 10. This is discussed further in subsection 4.3.3. For other applications the resolution is more important, for example for the generation of non-trivial light potentials for atom traps [174].

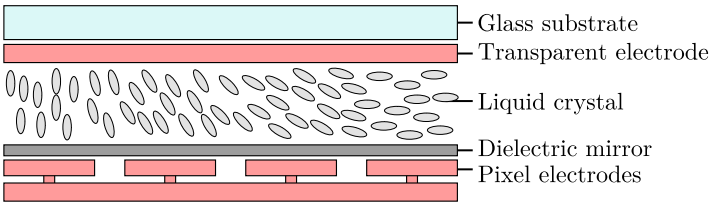

Figure 4.9: Diagram showing the LCOS (liquid crystal on silicon) SLM chip.

4.3.2 Phase throw and nonlinearity

Before each hologram is "displayed" on the SLM it must be converted to a 8-bit grey level image. The grey level at each pixel determines the applied voltage, and therefore the phase shift experienced by the horizontally polarised light. Key characteristics of the SLM are: the maximum phase shift the SLM can produce (the phase throw), the number of available phase levels (the bit depth), and the linearity of the voltage-phase shift relationship (the phase response).

Out of all of the experimental parameters considered in Ref. [P2], the phase response of the SLM had the largest effect on the accuracy of the generated beams. This confirms the importance of performing a calibration measurement to measure the phase response and correct for any nonlinearities.

There are many approaches to measuring the phase response of an SLM [175–178]. Our method is based on converting the phase shift at the SLM to a change in the ellipticity of the incident light, as shown in Fig. 4.10 (a). Initially, 45° linearly polarised light is incident on the SLM. The wave plate after the SLM is set so that a zero phase shift results in all of the light being transmitted through the polarising beam splitter (PBS). If the phase shift is instead non zero, then the polarisation becomes elliptical and the transmitted intensity drops. This can similarly be carried out using initially circularly polarised light, with the first half wave plate replaced by a quarter wave plate. The results, taken by J. W. C. Conway, are shown in Fig. 4.10, along with the extracted phase shift. The calibration shows the phase response is fairly linear, apart from at large gray levels. To account for this, the final result (shown in red) was used as a look up table when converting the phase holograms to grey levels.

The above measurement also showed that the SLM can achieve a maximum phase shift of 2.5π. The simulations in [P2] confirmed that methods A-D performed best when a full 2π phase throw is available, although a phase throw of 1.5π is sufficient. The two methods suggested in Ref. [167] showed more interesting behaviour, with one allowing high accuracy, and the other high efficiency, for phase throws of only π.

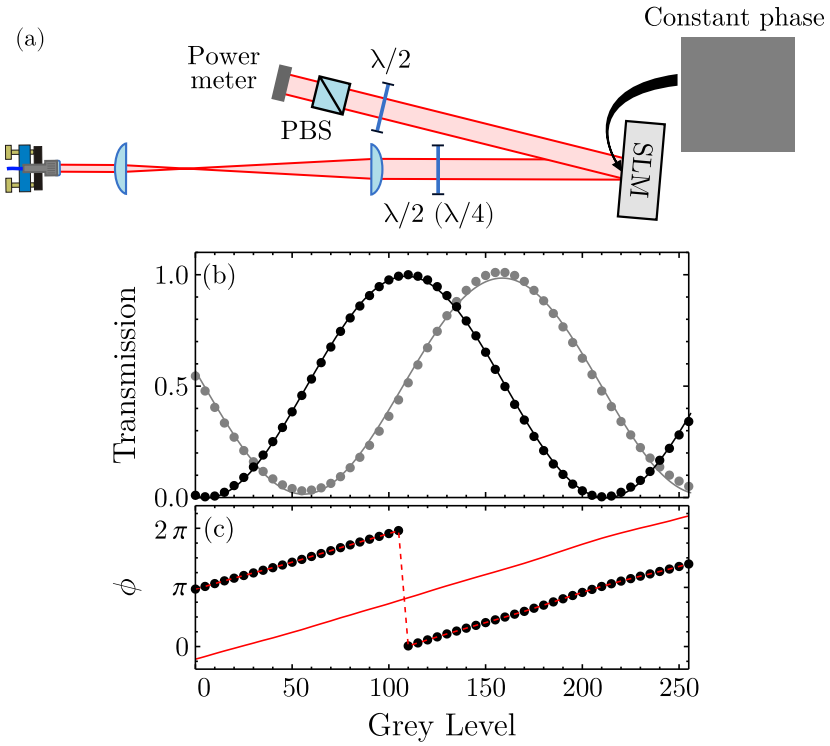

Figure 4.10: SLM phase response calibration. (a) Experimental setup. (b) PBS transmission as a function of grey level for 45° linear (black) and circular (grey) incident light, with fitted sinusoidal functions used to extract phase. (c) Extracted phase shift (black) and final look up table (red, solid), with constant phase added to shift the discontinuity.

Our SLM has 256 available grey levels, corresponding to a bit depth of 8. In the simulations the accuracy of all methods leveled of at a bit depth of 7, with the efficiency maximised for a bit depth of 4. For low bit depth devices, Method D and an additional method suggested in Ref. [161] achieved the highest accuracy, whilst methods A and B gave the highest efficiency.

4.3.3 Grating period and aperture size

All of the methods tested generate the desired beam in the first diffracted order of a phase grating. Fourier filtering is then used to separate the shaped and unshaped light. The details of the filtering process can have a large effect on both the accuracy and efficiency of the beam shaping.

Firstly, there is a trade-off when choosing the grating period. A larger grating period equates to a higher resolution phase grating, and therefore higher diffraction efficiency. However, it also means that the diffracted orders are more closely spaced, making them more difficult to separate and thus reducing the accuracy. The size of the aperture used for filtering is also important. A smaller aperture effectively removes all of the unshaped light, but at the expense of losing some of the higher spatial frequency components. There is therefore an optimal, mode dependent, aperture size which produces the highest accuracy. This expected dependence of the hologram performance on both grating period and aperture size was confirmed by simulations in Ref. [P2].

Fig. 4.11 shows the measured diffraction efficiency of the FWM SLM for different grating periods. For the experiment a grating period of 8 pixels was chosen, which produced sufficiently high diffraction efficiency, as well as orders that could be easily separated at the focus of a 250 mm lens. The aperture size was optimised by observing on a camera the point at which the high spatial frequencies began to be cut of, and then making the aperture slightly larger. This size varied with the desired mode(s).

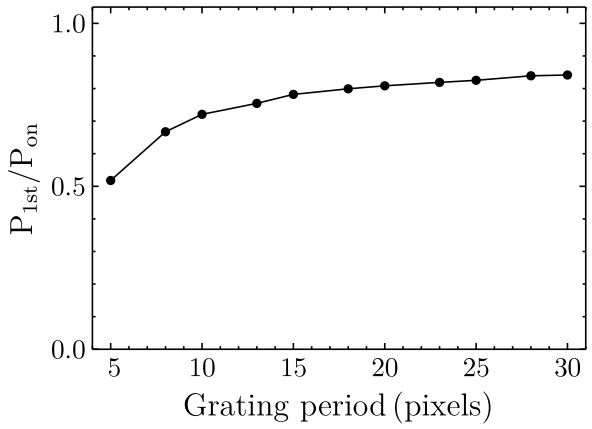

Figure 4.11: Diffraction efficiency as a function of grating period for the FWM SLM. P_{1st}: Power diffracted into the first order, P_{on}: total incident power. This measurement includes the SLM reflectivity, which was 97.4(2)%.

4.3.4 Chosen method

Given the results of the experimental [P1] and numerical [P2] comparison, methods A and C were selected as the most appropriate for the FWM experiment. There was often not much to choose between the methods, but for the parameters of our SLM these methods performed well overall and are both relatively simple. Although method A was shown to have slightly lower accuracy, the higher efficiency, both in the experiment and simulation, was attractive.

To choose between methods A and C, a final test of the amplitude shaping of the methods was carried out. In particular, their ability to generate a flat 2.8 mm disk was compared. The results are shown in Fig. 4.12, with images of the shaped beam, taken in the image plane of the SLM, in the insets in (a). Although the overall accuracy of the images is low, they show a clear differentiation between the methods. The centre of the beam is noticeably brighter for method A, which is also shown by the negative slope in the radial profile. This indicates that method A produces a hologram which does not accurately compensate for the Gaussian-profile of the input beam.

Each method assumes a given relationship between the diffraction efficiency

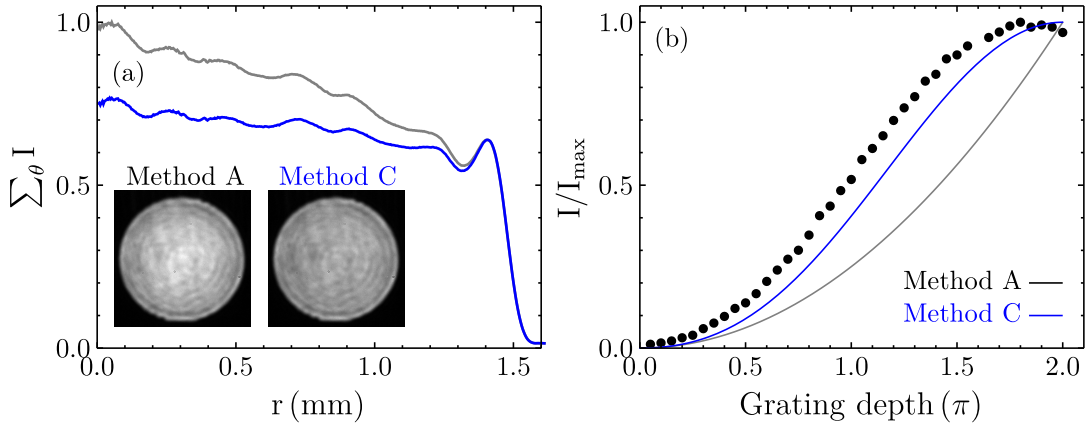

Figure 4.12: A test of the amplitude shaping of methods A and C. (a) Images of the generated disks (insets) and the mean radial profile from the centre of the disk. (b) Diffracted intensity as a function of grating phase depth (data points) and the relationship assumed by each method.

and the grating depth through the choice of $f(A_{\text{rel}})$ in Eq. 4.2.9. The blue and grey lines in Fig. 4.12 (b) show the assumed function for methods A and C, found by taking the inverse square of f, i.e.

$$\begin{aligned} &\text{Method A} : I/I_{\max} = (d/(2\pi))^2, \\ &\text{Method C} : I/I_{\max} = \text{sinc}^2\left[(2\pi - d)/2\right], \end{aligned} \tag{4.3.18}$$

where d is the grating depth. For comparison the measured diffraction efficiency as a function of grating depth is also shown (black data points). Method A substantially underestimates the diffracted intensity, and though method C does not exactly match the data, it gives a much better approximation. This is the reason for the superior amplitude shaping demonstrated by method C in Fig. 4.12 (a). As a result of this test, method C was chosen as the final method to used for the FWM experiments.

A further test of the amplitude shaping of each method would be to compare their ability to generate a beam with more radial structure, for example an LG mode with $p > 0$. For this comparison another method could be included, which, rather than assuming a relationship between the grating depth and the diffracted intensity, used a look up table based on the data points in Fig. 4.12 (b).

For accurate amplitude shaping, the intensity distribution of the input beam must also be known. For the FWM experiment we found that assuming the input beam to be a Gaussian worked well, so long as the waist of the Gaussian was measured accurately. The single pixel imaging technique described in subsection 4.2.3 proved to be the simplest and most accurate method to measure the waist directly at the SLM surface, and was also quick to do since a relatively low resolution image was required.

4.3.5 Phase flatness

Like the SLM used for the comparison experiment, the FWM SLM also introduced astigmatism into the shaped beam. To quantify this, the phase flatness of the SLM was measured against a flat reference mirror using the interferometer

shown in Fig. 4.13 (a), following the method in [179]. An example image of the interferometer output is shown in (b), where the noticeably curved fringes show the phase error introduced by the SLM. The measured phase profile of the SLM is shown in (c). This can be accounted for by including a correction in the desired field, so that

$$E_{\mathrm{des}}(x,y) = A_{\mathrm{des}}(x,y)e^{i(\Phi_{\mathrm{des}}(x,y)-\Phi_E(x,y))}, \tag{4.3.19}$$

where $\Phi_E(x,y)$ is the measured phase error of the SLM. With this correction the curvature of the of the fringes reduces, as illustrated in (d). There is however some remaining phase error, which may in part be due to noise in the measurement of the phase correction.

Rather than using the correction in (c), we found that the beam shaping accuracy was highest when a simple correction of a combined spherical and cylindrical lens was used. As a starting point, the phase of the two lenses was fit to the measured profile in (c), which resulted in the best fit shown in (e). The exact focal length of each lens could then be adjusted to account for other phase errors after the SLM. Although not ultimately used, the phase flatness measurement

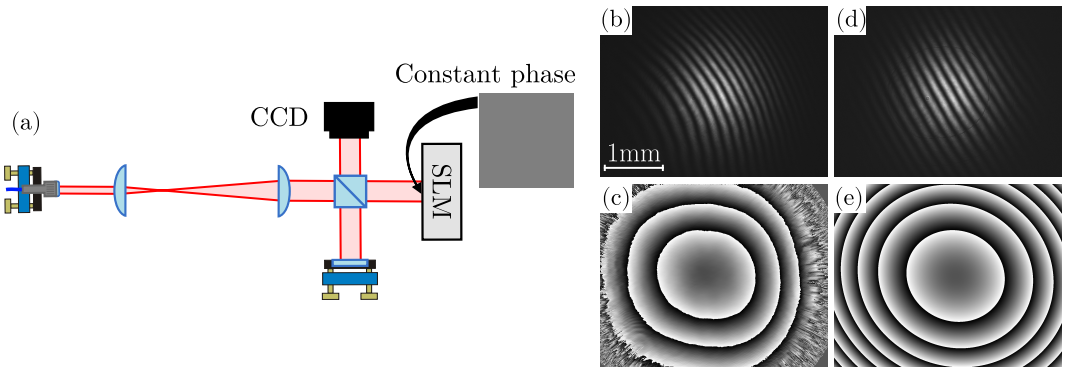

Figure 4.13: (a) Interferometer setup used to measure the phase flatness of the SLM with a 3.5 mm Gaussian beam (imaged using a 250 mm- 60 mm telescope, not shown). (b) Typical interferometer output. (c) Measured phase error of the SLM in grey levels. (d) Interferometer fringes with correction applied. (e) Phase of spherical (f_s) and cylindrical (f_c, θ_c) lenses fitted to the profile in (c), $f_s = 11.6$m, $f_c = 53.4$m, $\theta_c = 111°$ from vertical.

underlines the necessity of including at least a simple phase correction in the hologram.

In order to achieve higher beam shaping accuracy the phase correction could be improved by performing a full Zernike polynomial decomposition on the profile in Fig. 4.13 (c) and filtering out the higher order terms that contibute only noise. Alternatively, the phase flatness could be measured via a range of other methods [172, 180, 181] to achieve a more accurate measurement. However, the simple correction of a spherical and circular lens produced sufficiently high beam shaping accuracy for our application.

4.3.6 Shaping two beams independently

The final beam shaping setup used in the FWM experiment is shown in Fig. 4.14. The input beams are expanded using $4f$-telescopes so that their waist at the SLM is around 3.5 mm. This waist was chosen to allow $\mathrm{LG}^{\ell}_{p=0}$ modes with $\ell = 0 \rightarrow 8$ and a waist of 1 mm to be generated with similar powers. To allow the spatial profile of the two pump beams to be controlled independently, the SLM was split into two halves, with the 780 nm and 776 nm light incident on the right and left hand sides, respectively. The left and right holograms are additionally offset vertically to increase the space available for each. To reduce interference

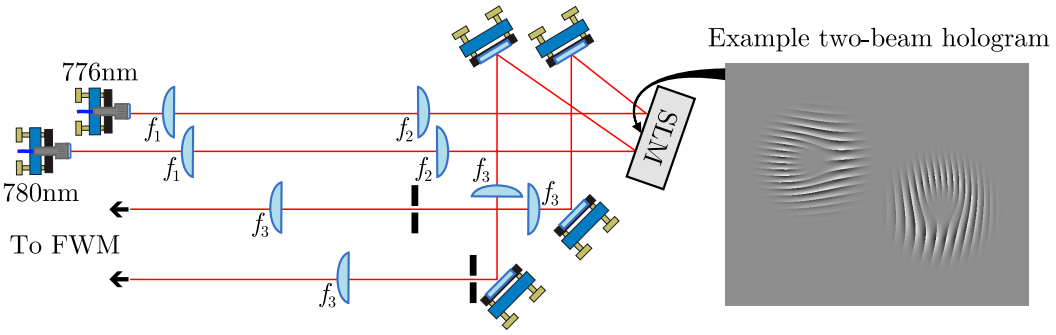

Figure 4.14: The final beam shaping setup used in the FWM experiment. Focal length of lenses: $f_1 = 100$ mm, $f_2 = 125$ mm and $f_3 = 250$ mm. The example hologram has a larger than usual grating period for clarity.

between the two holograms further, the diffraction gratings are perpendicular to one another. This means that any light that diffracts off the "wrong" grating does not appear in the shaped beam.

The holograms are generated using method C, with the phase corrections included by adding them to the phase of the desired beam before calculating the hologram. Separate phase corrections were used for each hologram, with the correction "lenses" centred on the offset position of the hologram. Using a grating period of 8 pixels, the shaped beams were easily filtered from the other diffracted orders with an aperture in the Fourier plane of a 1-1 $4f$-telescope, with $f_3 = 250\,\text{mm}$ lenses.

4.3.7 Conclusion

This section has detailed the factors taken into consideration in designing the FWM beam shaping setup. Numerical simulations in [P2] showed that the resolution and phase bit depth of the SLM was more than sufficient to produce high fidelity shaped beams, but also confirmed the need to calibrate the phase response of the device. The calibration allowed a look-up table to be generated to correct for small phase response nonlinearities, and also demonstrated that the SLM has a maximum phase throw of 2.5π. For these parameters, methods A and C were chosen as the most suitable hologram generation methods, with method C ultimately selected due to its superior amplitude shaping.

The simulations also showed the importance of choosing an appropriate grating period and aperture size. For this experiment a grating period of 8 pixels was found to provide a compromise between efficiency and accuracy, with the aperture size dependent on the generated mode. Although not investigated in the simulations, measurements of the phase flatness of the SLM indicated that a phase correction must also be included in the holograms to prevent the shaped beams being astigmatic. Finally, a method was developed to display two holograms on the SLM at once, allowing the two FWM pump beams to be shaped independently.

4.4 Mode decomposition

So far, the quality of the shaped beams has been judged simply by comparing the intensity distribution of the beam to that of the desired field. However, more information can be gained by obtaining a complete modal decomposition. This type of analysis is particularly important when the mode of the light is initially unknown, as is the case for the FWM 420 nm emission. This section details the mode decomposition method developed for use in the FWM experiment.

In the Laguerre-Gauss basis, finding the mode decomposition of a beam can be split into two problems: measuring the OAM spectrum, and therefore the ℓ indices, and finding the radial p-mode spectrum. Quantitative measurement of the OAM spectrum of a beam, or indeed single photons, can be performed in a variety of ways. In the same spirit as the beam shaping methods discussed earlier, forked diffraction gratings of varying charge can be used to convert each OAM state in turn into a Gaussian beam. Subsequent measurement of the on-axis intensity produced by each diffraction grating gives the full OAM distribution of the beam [47, 182]. Alternatively, a combination of optics can be used to convert angular momentum to transverse momentum [183], or cascaded Dove prism interferometers can be used to sort OAM states into separate output ports [184, 185].

In contrast, there are fewer established methods for determining the p-mode decomposition of a beam. The latter two methods mentioned above give either indirect [186, 187] or no information on the radial modes, and whilst the "reverse generation" method can be used in principle by cycling through holograms encoding both p and ℓ modes [165, 188], this is time consuming and requires a second SLM.

For the FWM experiment, an experimentally simple and quick method of finding the full ℓ and p-decomposition of a beam was developed, based on Fourier analysis of the interferogram produced using a Dove prism interferometer. This section will give a detailed explanation of the method, which is also discussed in

Ref. [P3].

It is important to note that the method described below is less general than, for example, performing a mode decomposition with a second SLM. In its current form, our method assumes that the beam is in a purely incoherent superposition of modes. Although this is an appropriate assumption for the 420 nm light generated in the FWM process (discussed further in Sec. 5.1), it is less clear that this is a good assumption for the pump beams. Furthermore, the method is only applicable to classical beams, rather than single photons. Despite these limitations, our method is sufficient for the present experiment.

4.4.1 Dove prism interferometer

The Dove prism interferometer used to measure the mode decompositions is shown in Fig. 4.15 (a). The beam is separated and recombined at non-polarising beam splitters, with the beam going undergoing an odd number of reflections in arm A and, due to the inclusion of a Dove prism, an even number of reflections in arm B. At the output the beam interferes with its mirror image to create an interference pattern, or interferogram. Fig. 4.15 (b) shows the experimental intensity profile, I_{beam}, and interferogram, I_T, of a beam shaped into an LG_0^4 mode using the two-beam SLM setup in Fig. 4.14 (see Sec. 5.2 for full setup). After careful alignment the interferogram, I_T, shows eight radial lobes, which are caused by interference between the $e^{\pm i\ell\theta}$ terms in the interfering beams.

The interferogram can be described theoretically by considering the electric

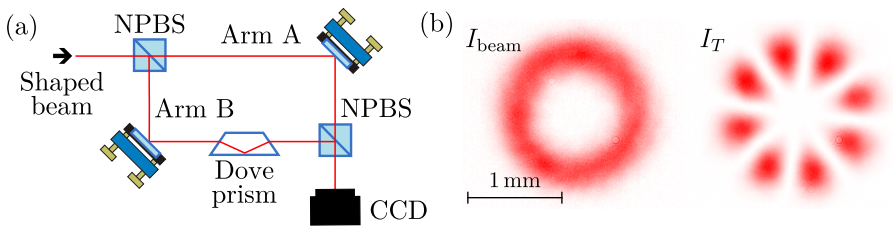

Figure 4.15: (a) Dove prism interferometer setup used for mode decomposition and (b) example output beams for a LG_0^4 mode.

field at the interferometer output, which for a single input mode is

$$E_p^\ell(r,\theta,z) = \frac{1}{\sqrt{2}}\rho_p^\ell(r,z)e^{i(\ell\theta+kz+\Phi_S+\Phi_G)} + \frac{1}{\sqrt{2}}e^{i\phi_p^\ell}\rho_p^\ell(r,z)e^{i(-\ell\theta+kz+\Phi_S+\Phi_G)}, \tag{4.4.20}$$

where $\rho_p^\ell(r,z)$ contains all of the radial dependence of the LG mode, and is given by

$$\rho_p^\ell(r,z) = \frac{C_p^\ell}{w}\left(\frac{r\sqrt{2}}{w}\right)^{|\ell|} L_p^{|\ell|}\left[\frac{2r^2}{w^2}\right]\ e^{-\frac{r^2}{w^2}}. \tag{4.4.21}$$

The ϕ_p^ℓ phase term accounts for the difference in path length, Δz, of the two arms of the interferometer, such that $\phi_p^\ell = -k\Delta z + \Phi_{G,\Delta z}$. This term is in general mode dependent due to the differing Gouy phase shift of different modes. Any difference in the phase front curvature of the two beams is neglected. The interferogram intensity profile is then

$$I_p^\ell(r,\theta) = E_p^\ell(E_p^\ell)^* = R_p^\ell(r)\left[1+\cos(2l\theta+\phi_p^\ell)\right], \tag{4.4.22}$$

where $R_p^\ell(r) = |\rho_p^\ell(r)|^2$, and the explicit z-dependence has been dropped for brevity. For a LG_0^4 mode the expected profile matches that shown in Fig. 4.15: eight lobes, whose orientation is set by the interferometer phase ϕ_p^ℓ, with the same radial intensity dependence as the input beam.

The above equation gives the interferogram produced for a single mode. If instead the input beam was *coherent* superposition of modes, then the expected interferogram would be found by taking the absolute square of the total *field* of the superposition at the interferometer output. However, the 420 nm light generated during the FWM experiment is expected to be observed as an *incoherent* superposition of modes [47] (see 5.1), in which case the *intensity* of each mode is expected to add. In this situation the total interferogram is given by

$$I_T = \sum_{\ell,p} P_p^\ell R_p^\ell(r,\theta)\left[1+\cos(2l\theta+\phi_p^\ell)\right], \tag{4.4.23}$$

where P_p^ℓ is the relative power in each mode.

For the analysis presented here, all shaped beams are assumed to be in a purely incoherent superposition of modes. This is a limitation of the method as

the beams may generally be in both a coherent and incoherent superpostition. It may be possible to extend the method to include coherent superpositions by considering a more complicated form of Eq. 4.4.23. However, the mode decompositions obtained using the existing method describe the measured mode profiles well, indicating that a incoherent superposition is sufficient for the current experiment.

4.4.2 Fourier analysis

The form of Eq. 4.4.23 means that the interferograms are readily analysed via Fourier analysis. An immediate complication however is the ϕ_p^ℓ dependence. Although for $|\ell| > 0$ this amounts only to a rotation of the lobed pattern, for $\ell = 0$ the total interferogram intensity is directly determined by ϕ_p^ℓ. Thus without knowing the interferometer phase, the relative power in $\ell = 0$ modes cannot be found directly from the interferogram.

Furthermore, Eq. 4.4.23 assumes a perfect interferometer with 50:50 reflection and transmission at each beam splitter. To account for this, and also to allow $\ell = 0$ modes to be included, a corrected interferogram is calculated from three images taken at the interferometer output: the intensity profile in interferometer arm A, $I_A(r,\theta)$, the intensity profile in arm B, $I_B(r,\theta)$, and the interferogram, $I_T(r,\theta)$, as shown for the LG_0^4 mode in Fig. 4.16 (a).

For a singe LG mode, the electric field at the interferometer output is given in term of I_A and I_B by

$$I_T(r,\theta) = I_A(r,\theta) + I_B(r,\theta) + 2\sqrt{I_A(r,\theta)I_B(r,\theta)}\cos(2l\theta + \phi_p^\ell). \tag{4.4.24}$$

With reference to this, the corrected interferogram is chosen to be

$$\begin{aligned} I_C(r,\theta) =& I_{AB}(r)\left[1 + \frac{I_T(r,\theta) - (I_A(r,\theta) + I_B(r,\theta))}{2\sqrt{I_A(r,\theta)I_B(r,\theta)}}\right], \\ I_{AB}(r) =& \frac{1}{2}\left[\overline{I_A}(r) + \overline{I_B}(r,\theta)\right]. \end{aligned} \tag{4.4.25}$$

where $\overline{I_A}(r)$ and $\overline{I_B}(r)$ are the average radial profile of I_A and I_B, respectively. The term in the square brackets in Eq. 4.4.25 contains all of the phase information

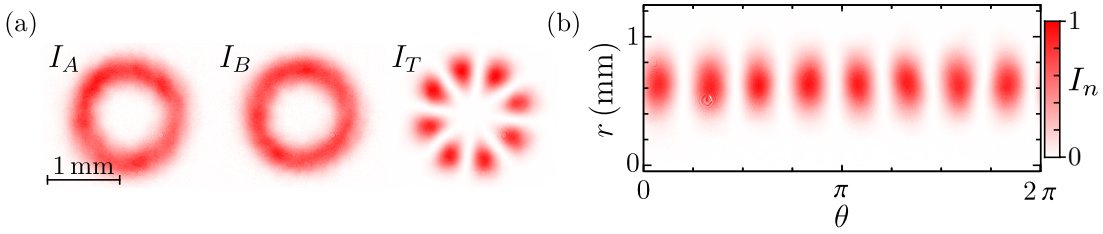

Figure 4.16: (a) Raw data and (b) corrected interferogram for the LG_0^4 beam.

present in the interferogram, whilst the radial profile of I_C is provided by the mean radial profile of the beam $I_{AB}(r)$. This removes the critical dependence of the $\ell = 0$ intensity on the interferometer phase. When I_A and I_B are both small, intensity noise can cause I_C to become very large. To avoid this the correction is only performed for pixels where both I_A and I_B are above a threshold value. The resulting corrected interferogram for the LG_0^4 mode is shown in Fig. 4.16 (b).

Analysis of the corrected interferogram then proceeds based on the assumption that I_C is well described by the incoherent mode superposition in Eq. 4.4.23, with $\phi_p^0 = 0$. The steps are as follows:

- Firstly, the $|\ell|$-decomposition of the beam is obtained. Integrating the corrected interferogram over r gives, according to Eq. 4.4.23, an azimuthal profile of the form

$$I(\theta) = \sum_\ell P^\ell \left[1 + \cos(2\ell\theta + \phi)\right], \quad P^\ell = \sum_p P_p^\ell. \tag{4.4.26}$$

  A one-dimensional Fourier transform is then performed to give

$$\tilde{I}(\omega_\theta) = \sum_\ell 2\pi P^\ell \left[\frac{\delta(\omega_\theta)}{2} + \frac{e^{i\phi}}{4}\delta(2\ell - \omega_\theta) + \frac{e^{i\phi}}{4}\delta(2\ell + \omega_\theta)\right], \tag{4.4.27}$$

  From which the $|\ell|$-decomposition for $|\ell| > 0$ is given by

$$P^{|\ell|} = \frac{2|\tilde{I}(2\ell)|}{|\tilde{I}(0)|}. \tag{4.4.28}$$

  Since the Fourier transform contains both negative and positive components, the sign of ℓ cannot be determined using this method. The azimuthal profile and $|\ell|$-decomposition of the LG_0^4 beam from Fig. 4.16 are shown below in Fig. 4.17.

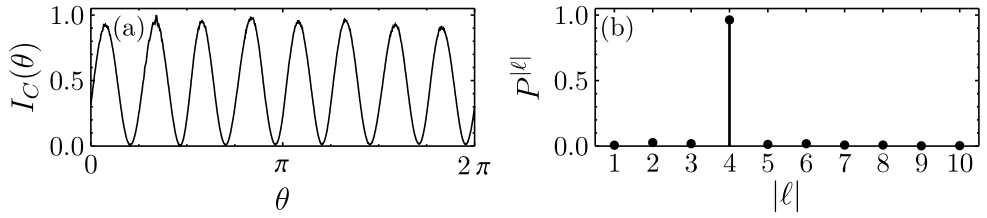

Figure 4.17: (a) Azimuthal profile and (b) $|\ell|$-decomposition of the LG_0^4 beam in Fig. 4.16.

- The second step is to choose a beam waist. Unlike the ℓ-decomposition, which is directly determined by the rotational symmetry of the beam, the p-decomposition is not uniquely defined, but depends on the chosen waist. For the analysis, the waist is set by an initial one-mode fit to the radial profile of the corrected interferogram (found by integrating I_C over θ). The ℓ index of the mode chosen for the fit is the value which contributes most to the $|\ell|$-decomposition, whilst the p index is chosen based on the expected mode.

- The p-decomposition can now be found, again for only for $|\ell| > 0$. Two-dimensional Fourier filtering is used to separate the ℓ-components of the corrected interferogram. The mean radial profile of each ℓ-component is then found, two examples of which are shown for the LG_0^4 beam in Fig. 4.18 (solid lines). Each profile is then fitted with an incoherent superposition of p-modes of the relevant ℓ-index (dashed lines). The only free parameters in the fit are the relative weightings of each mode. The full $|\ell|$-p decomposition for $|\ell| > 0$ can then be found by combining the $|\ell|$-decomposition with the fitting results.

  This step also provides some discrimination between noise and signal in the inital $|\ell|$-decomposition. If the radial fit is very poor, as for the $\ell = 2$ profile below, then this indicates that the main contribution to the profile is not light at the required ℓ value. By discarding these modes the effect of various sources of error can be reduced, including interferometer misalignment or an incorrect choice of the beam centre when unwrapping to circular coordi-

nates. The quality of the radial fit is judged based on the adjusted R^2 [189], and if this value is less than 0.8 then the corresponding $P^{|\ell|}$ value is set to zero.

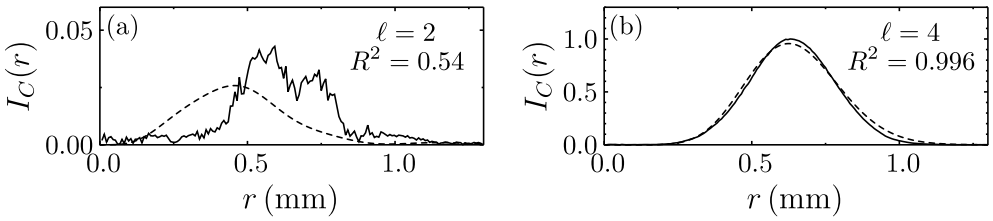

Figure 4.18: Analysis for p-decomposition of the LG_0^4 beam in Fig. 4.16. Example radial profiles of the (a) $|\ell| = 2$ and (b) $|\ell| = 4$ component of the corrected interferogram (solid lines). Dashed lines: Incoherent p-mode fit for p-decomposition. Note the different y-axis scales.

- The final step is to find the relative power in the $\ell = 0$ modes. Using the $|\ell|$-p decomposition for $|\ell| > 0$, an expression for the total radial profile due to these modes can be found. The $\ell = 0$ modes are then found by performing a final fit to the full radial profile of the corrected interferogram, using the total $|\ell| > 0$ profile, multiplied by a single scale factor, plus an incoherent sum of the $\ell = 0$ modes as the model.

The final mode decomposition obtained for the LG_0^4 beam is shown in Fig. 4.19 (a). The relative power in the target mode ($\ell = 4$, $p = 0$) is 0.97, with the majority of the rest of the power in the adjacent $p = 0$ modes. To verify the analysis, the mode decomposition is used to calculate a reconstructed radial and azimuthal interferogram profile, shown by the dashed lines in Fig. 4.19 (c) and (d). Good agreement is found between the reconstructed and experimental profiles (solid lines).

A further test of the analysis is to demonstrate the correct decomposition of a superposition of modes. Since it is difficult to generate an incoherent superposition directly, this was tested using simulated data. The electric field, beam profile and interferogram of the simulated beam are shown in Fig. 4.20 (a), along with

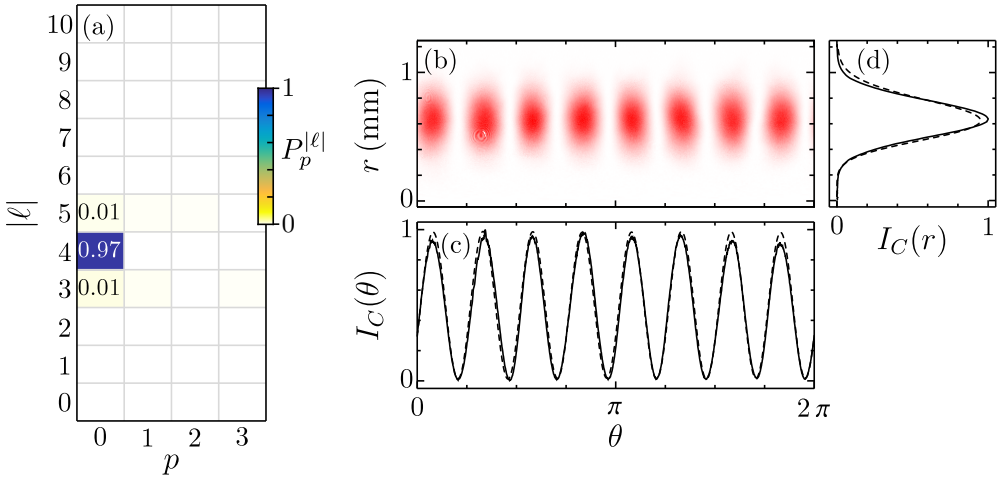

Figure 4.19: (a) Mode decomposition of the LG_0^4 beam in Fig. 4.16 for $|\ell| \leq 10$ and $p \leq 3$, (b) corrected interferogram, I_C, (c) azimuthal and (d) radial profile of I_C (solid), as well as reconstructed profiles from the mode decomposition (dashed).

the interferometer parameters used. The superposition was chosen so that the modes cover the full range of ℓ and p indices. Note the intensity on axis is near zero due to the choice of interferometer phase, which was set to 0.9π in order to fully test the measurement of $\ell = 0$ modes. The low intensity along the vertical

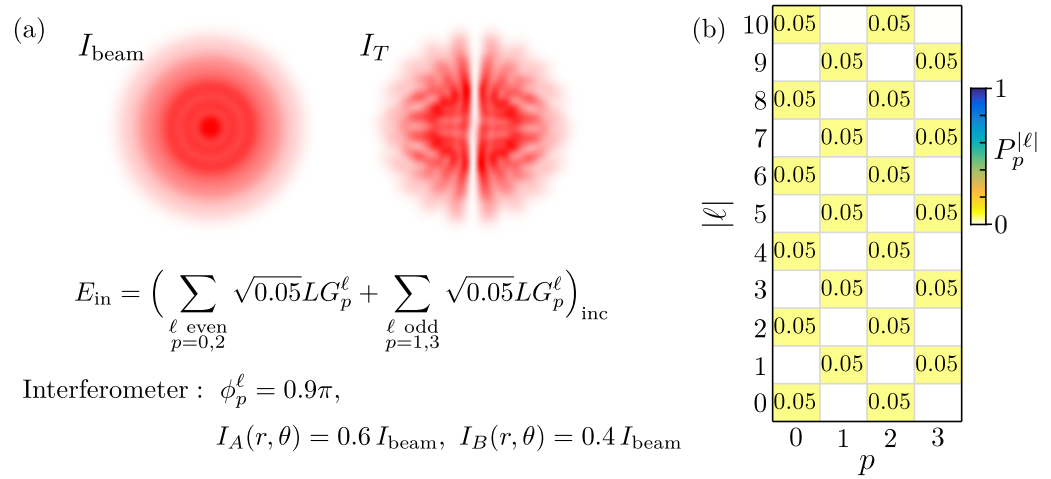

Figure 4.20: (a) Electric field, E_{in}, and beam profile, I_{beam}, of a simulated incoherent superposition, as well as the interferogram, I_T, for the interferometer parameters shown. (b) Simulated mode decomposition via Fourier analysis.

axis coincides with the axis of the extra reflection in the interferometer.

The result of the mode decomposition is shown in Fig. 4.20 (b). The only change made to the analysis was to set the beam waist to a predetermined value, rather than the usual method of an initial one mode fit. This was required since no single mode dominates and a single mode fit therefore does not choose an accurate beam waist. With this modification, the analysis correctly determines the relative power of each mode in the incoherent superposition.

4.4.3 Conclusion

Having discussed the generation of shaped beams in previous sections, this section focused on the important step of fully characterising the structured light. The measurement is based on Fourier analysis of the interferogram formed at the output of a Dove prism interferomter, and allows the full LG mode decomposition of a beam to be found. Example mode decompositions of both experimental and simulated data have been presented, showing that the analysis produces the expected results.

Experimentally, this method has the advantage of a simple setup and being quick to carry out. In practice, however the method does have limitations. For example, the interferometer must be aligned very precisely to produce evenly spaced lobes, and it is also difficult to avoid a very slight astigmatism of the beam caused by the interferometer itself. Both of these factors can distort the fringe pattern, producing errors in the mode decomoposition, particularly for larger values of ℓ as the spacing of the fringes decreases. It may be possible to correct for these effects using a more complicated analysis routine. Other improvements could also be made, for example by altering the measurement to allow the sign of ℓ to be determined, possibly by deliberately misaligning the interferometer. Perhaps the biggest limitation of the current method is that it considers only incoherent superpositions of modes. It may be possible to include coherent superpositions by considering in more detail the assumed form of the interferogram, however, in these situations a more rigorous method may be a

better choice, for example a second SLM and on-axis filtering.

This chapter as a whole has introduced all of the tools necessary to carry out FWM experiments with shaped pump light. The initial work focused on choosing an appropriate method of generating phase-only holograms for use with an SLM. Building on this, the beam shaping setup was developed, with the final setup allowing both FWM pump beams to be shaped independently. The process of developing this setup contributed to two publications, the main results from which have been presented and discussed. Finally, the method devised for analysing the shaped pump beams, as well as the generated 420 nm light has been described in this section.

Chapter 5

Spiral bandwidth of four-wave mixing

Wave mixing processes are phase coherent, that is, efficient wave mixing only takes place in the direction for which the longitudinal phase of the input fields in conserved (see Sec. 2.1.1). This is captured by the phase matching condition, which places a restriction on the k-vectors of the fields, and at the single photon level is equivalent to conservation of linear momentum [2].

In this chapter, we study four-wave mixing (FWM) with Laguerre-Gauss (LG) pump beams, as illustrated in Fig. 5.1. In this case, not only is conservation of longitudinal phase important, but conservation of *transverse* phase also plays a key role. Due to the helical phase fronts of the pump beams, the ℓ indices of the generated light must satisfy

$$\ell_{780} + \ell_{776} = \ell_{\mathrm{IR}} + \ell_{\mathrm{B}}, \tag{5.0.1}$$

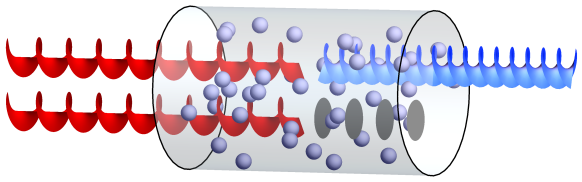

Figure 5.1: FWM with Laguerre Gauss pump beams.

or equivalently, the orbital angular momentum (OAM) of the pump beams must be conserved.

Conservation of OAM in wave mixing processes was first demonstrated for second harmonic generation [44,190]. Passing various orders of LG modes through a nonlinear crystal generated light with not only double the frequency of the input light, but also double the OAM. Subsequent demonstrations have been carried out for sum frequency generation [45] and four-wave mixing [75,86], where the OAM of the generated beam is equal to the total OAM of the two (or three) pump beams. In these processes, where a single beam is generated, OAM conservation uniquely defines the OAM state of the new field. Such processes are ideal for carrying out frequency conversion of both classical [85] and quantum [191] OAM states. Furthermore, the transverse phase coherence applies not just to OAM, but also to more general transverse phase distributions. This has allowed demonstrations of coherent frequency conversion of both transverse modes [192] and images [89].

Other wave mixing processes, such as spontaneous parametric down conversion or spontaneous FWM, generate two new optical fields. In this case, although the total OAM of the generated fields is fixed by conservation of OAM, the OAM of each field individually is not constrained. At the single photon level, this can result in OAM-entanglement [48, 193, 194], with the light generated in a coherent superposition of OAM-conserving two-photon states. One method of characterising such a state is by the width of the OAM distribution of the individual fields, otherwise known as the spiral bandwidth [49]. This gives a measure of the number of product states which contribute to the coherent superposition.

Spontaneous parametric down conversion has become the routine method for generating OAM-entangled photon pairs [47, 195], both for fundamental studies of quantum optics [27, 196, 197] and demonstrations of higher dimensional quantum technologies [146, 198, 199]. OAM-entangled photon pairs have also been generated via FWM in atomic vapours. With Guassian pump beams, the stokes and anti-stokes photons generated in a double-lambda FWM scheme in thermal rubidium vapour [66] have been shown to be entangled in a two-dimensional state

involving $\ell = 0$ and $\ell = \pm 1$ modes. Very recent work using a laser-cooled rubidium vapour [200] has investigated using high ℓ pump beams ($\ell = \pm 30$) to increase the spiral bandwidth of the generated state, allowing the measurement of an entangled state with $\ell = \pm 28$ and $\ell = \pm 32$.

The OAM state of the light generated in the "blue light" FWM system was first investigated in the context of OAM frequency conversion. Work carried out at Strathclyde [46] showed qualitatively that a pump OAM of up to $5\hbar$ is transferred completely to the 420 nm field, as is illustrated in Fig. 5.1. For OAM to be conserved the 5.2 µm light is therefore expected to be generated in the LG_0^0 mode. With both fields generated in a single OAM state, the photon pairs can be described by a product state and no entanglement is created. To date, no measurement has been made of the 5.2 µm transverse mode to confirm this. More recent work in Refs. [87, 88] have also demonstrated qualitative measurements consistent with complete transfer of the pump OAM to the 420 nm field.

The work presented in this chapter builds on these experiments and further explores, both theoretically and experimentally, the transfer of OAM in the "blue light" FWM system. Unlike previous experiments [46, 87, 88], where the 420 nm transverse mode was determined qualitatively by visual inspection of an interference pattern, we use the Fourier analysis described in Sec. 4.4 to make a quantitative measurement of the full 420 nm mode decomposition. This is further made possible due to the improved experimental control compared to the experiment in [46], where neither of the pump lasers were locked. The improved beam shaping setup also allows larger values of OAM to be studied, and we use Laguerre-Gauss, $\mathrm{LG}_{p=0}^{\ell}$, pump modes with $0 \leq \ell \leq 8$.

For low pump ℓ we find that the 420 nm light is generated predominantly in a single mode, with an ℓ-index determined by the total pump OAM, such that $\ell_\mathrm{B} = \ell_\mathrm{T} = \ell_{780} + \ell_{776}$. This is in agreement with previous results [46,87,88]. However, as the pump ℓ increases we observe a continuous broadening of the 420 nm OAM spectrum. For OAM to be conserved, this indicates that the pump OAM is shared between the 5.2 µm and 420 nm light, and that the generated photon

pairs are in fact OAM-entangled. Although further experiments are required to confirm entanglement, we use the measured ℓ-distribution of the 420 nm light to infer the available spiral bandwidth and entanglement entropy of this state for a range of pump modes. We compare FWM under two conditions: firstly, with the pump OAM shared evenly between the pump beams, and secondly with all OAM carried only by the 776 nm field (with the 780 nm field in the LG_0^0 mode). These conditions are referred to as "OAM addition" and "OAM frequency conversion", respectively.

This work is currently under consideration for publication, with the latest version of the paper available on the arXiv [P3]. Some of the preliminary theoretical calculations for the work presented in this chapter were carried out by Dalius Stulga, who completed a short summer project working on the blue light system. The experimental work, analysis, and final theoretical calculations were carried out by myself.

This chapter is structured as follows. Firstly, in Sec. 5.1 we present the theoretical model used to describe the FWM system, including the expected OAM-entangled state of the 5.2 µm and 420 nm light and the definition used for the spiral bandwidth. In Sec. 5.2 we describe the experimental setup used. The main results are then presented, with the OAM addition results in Sec. 5.3 and the OAM frequency conversion results in Sec. 5.4. Finally, Sec. 5.5 provides a summary of the main findings as well as discussion of the further experiments which would be required to verify OAM-entanglement of the 5.2 µm and 420 nm light.

5.1 Theory

In the experiment, we measure the mode decomposition of the generated 420 nm light for a range of Laguerre-Gauss (LG) pump modes. This mode decomposition can be predicted by considering the overlap of the FWM fields within the rubidium cell [46, 201]. We make the assumption that the 5.2 µm and 420 nm light is

generated as a coherent superposition of two-photon states described by

$$|\Psi\rangle = \sum_{\ell_{\mathrm{B}},p_{\mathrm{B}},\ell_{\mathrm{IR}},p_{\mathrm{IR}}} c^{\ell_{\mathrm{B}},\ell_{\mathrm{IR}}}_{p_{\mathrm{B}},p_{\mathrm{IR}}} \left|\mathrm{LG}^{\ell_{\mathrm{B}}}_{p_{\mathrm{B}}}\right\rangle_{\mathrm{B}} \left|\mathrm{LG}^{\ell_{\mathrm{IR}}}_{p_{\mathrm{IR}}}\right\rangle_{\mathrm{IR}}, \tag{5.1.2}$$

and that the probability of generating the state $\left|\mathrm{LG}^{\ell_{\mathrm{B}}}_{p_{\mathrm{B}}}\right\rangle_{\mathrm{B}} \left|\mathrm{LG}^{\ell_{\mathrm{IR}}}_{p_{\mathrm{IR}}}\right\rangle_{\mathrm{IR}}$, for a given pair of pump modes, $|\mathrm{LG}^{\ell_{780}}_{p_{780}}\rangle$ and $|\mathrm{LG}^{\ell_{776}}_{p_{776}}\rangle$, is given by [46, 201]

$$c^{\ell_{\mathrm{B}},\ell_{\mathrm{IR}}}_{p_{\mathrm{B}},p_{\mathrm{IR}}} = \int_{-L/2}^{L/2}\int_{0}^{R}\int_{0}^{2\pi} r\mathrm{LG}^{\ell_{780}*}_{p_{780}}\mathrm{LG}^{\ell_{776}*}_{p_{776}}\mathrm{LG}^{\ell_{\mathrm{B}}}_{p_{\mathrm{B}}}\mathrm{LG}^{\ell_{\mathrm{IR}}}_{p_{\mathrm{IR}}} d\theta dr dz, \tag{5.1.3}$$

where L is the cell length and R is large enough so that all modes are fully encompased by the integration region. Note that we have written $\mathrm{LG}^{\ell}_{p} = \mathrm{LG}^{\ell}_{p}(r,\theta,z)$ as short hand for the relative electric field of a Laguerre-Gauss mode, as defined in Sec. 4.1.

Although the two-photon state in Eq. 5.1.2 is coherent, the 420 nm and 5.2 µm fields individually are an incoherent mixture of modes [47]. The relative intensity of such a state is given by

$$I^{\mathrm{B}}(r,\theta,z) = \sum_{\ell_{\mathrm{B}},p_{\mathrm{B}}} P^{\ell_{\mathrm{B}}}_{p_{\mathrm{B}}} I^{\ell_{\mathrm{B}}}_{p_{\mathrm{B}}}(r,\theta,z), \quad I^{\ell_{\mathrm{B}}}_{p_{\mathrm{B}}}(r,\theta,z) = |\mathrm{LG}^{\ell_{\mathrm{B}}}_{p_{\mathrm{B}}}|^2, \tag{5.1.4}$$

with the probability of observing the 420 nm light in a particular mode found by summing over all ℓ_{IR} and p_{IR} modes

$$P^{\ell_{\mathrm{B}}}_{p_{\mathrm{B}}} = \sum_{\ell_{\mathrm{IR}},p_{\mathrm{IR}}} \left|c^{\ell_{\mathrm{B}},\ell_{\mathrm{IR}}}_{p_{\mathrm{B}},p_{\mathrm{IR}}}\right|^2. \tag{5.1.5}$$

Similarly, the intensity of the 5.2 µm light is given by

$$I^{\mathrm{IR}}(r,\theta,z) = \sum_{\ell_{\mathrm{IR}},p_{\mathrm{IR}}} P^{\ell_{\mathrm{IR}}}_{p_{\mathrm{IR}}} I^{\ell_{\mathrm{IR}}}_{p_{\mathrm{IR}}}(r,\theta,z), \quad P^{\ell_{\mathrm{IR}}}_{p_{\mathrm{IR}}} = \sum_{\ell_{\mathrm{B}},p_{\mathrm{B}}} \left|c^{\ell_{\mathrm{B}},\ell_{\mathrm{IR}}}_{p_{\mathrm{B}},p_{\mathrm{IR}}}\right|^2. \tag{5.1.6}$$

Using Eqs. 5.1.5 and 5.1.6 the predicted mode decompositions of the 420 nm and 5.2 µm light were calculated for a range of pump modes. The results are presented and compared to the experimental measurements in Sec. 5.3 and Sec. 5.4.

Beam waists

In order to calculate the integral in Eq. 5.1.3 the beam waist of each field must be known. Since the 5.2 µm field is not measured in our experiment, we make

the assumption that both generated fields follow the Boyd criterion [202]. This criterion states that, for Gaussian beams, the efficiency of a wave mixing process is maximised if the fields involved have matched Rayleigh ranges. We extend this to higher order modes and use beam waists for the simulated 420 nm and 5.2 µm fields given by

$$w_{IR} = \sqrt{\frac{5230}{780}} w_{780}, \quad w_B = \sqrt{\frac{420}{780}} w_{780}, \quad (w_{776} \simeq w_{780}). \tag{5.1.7}$$

The validity of this assumption is discussed in Sec. 5.4.

Spherical phase fronts and z-offset

For the OAM frequency conversion experiment, where only the 776 nm pump beam carries OAM, the focus of the 780 nm beam is offset to $z_{\text{off}} = 9.6$ mm before that of the 776 nm field. This is necessary in order to improve the spatial overlap of the Gaussian 780 nm light with the higher order 776 nm transverse modes, and is included in the model by performing the transformation $z \to z + z_{\text{off}}$ on the 780 nm field before calculating the integral in Eq. 5.1.3.

Separating the pump beam foci causes a mis-match in their phase front curvature. In the experiment it was observed that this caused a change in the collimation of the 420 nm field, but no significant change in the mode decomposition. We therefore assume that the overall phase front curvature of the two pump fields is phase matched with the generated two-photon field and neglect the spherical phase front term, Φ_S, when evaluating the overlap integral in this instance.

Interpretation

By considering the electric field of an LG mode, which can be written in a simplified form as

$$LG_p^\ell(r, \theta, z) = \rho_p^\ell(r, z) e^{i(\ell\theta + kz + \Phi_S(r,z) + \Phi_G(z))}, \tag{5.1.8}$$

some immediate predictions can be made about the generated modes. Here $\rho_p^\ell(r, z)$ is the radial field as defined in Eq. 4.4.21.

Firstly, the azimuthal integral in Eq. 5.1.3 will only be non zero if the ℓ indices satisfy

$$\ell_{780} + \ell_{776} = \ell_{\mathrm{IR}} + \ell_{\mathrm{B}}. \tag{5.1.9}$$

Thus only 420 nm and 5.2 µm modes that conserve OAM will be generated. The radial integral on the other hand takes into account the spatial overlap of the fields; modes with a higher physical overlap are more likely to be generated.

The z integral describes the propagation of the fields through the cell, and produces the familiar phase matching condition

$$k_{780} + k_{776} = k_{\mathrm{B}} + k_{\mathrm{IR}}, \tag{5.1.10}$$

which is satisfied for copropagating pump and generated fields. There is also another phase term dependent on z, the Gouy phase

$$\Phi_G(z) = -(2p + |\ell| + 1)\mathrm{arctan}[z/z_R]. \tag{5.1.11}$$

This term is not usually important because the propagation length in the nonlinear medium is normally much less than the Rayleigh range of the fields [190]. However, in the FWM experiment the cell length is much larger than the Rayleigh range, $L \approx 10 z_R$. In this case, in order for phase matching to be maintained between the pump and generated fields as they propagate through the cell they must have identical Gouy phases - which we refer to as Gouy phase matching. Since the Gouy phase depends on the mode order, only modes that satisfy

$$|\ell_{780}| + 2p_{780} + |\ell_{776}| + 2p_{776} = |\ell_{\mathrm{IR}}| + 2p_{\mathrm{IR}} + |\ell_{\mathrm{B}}| + 2p_{\mathrm{B}} \tag{5.1.12}$$

are well Gouy phase matched. This phase matching condition becomes particularly important for pump beams with $p \neq 0$ or where $\ell_{780} + \ell_{776} \neq |\ell_{780}| + |\ell_{776}|$. These special cases are investigated in Chapter 6.

OAM-entanglement

Based on the above analysis, three factors determine which pairs of 5.2 µm and 420 nm modes are generated: OAM conservation, Gouy phase matching and the

spatial overlap of the modes. OAM conservation is of particular importance, as it is this that leads to the two-photon state being OAM-entangled.

Using the OAM-conservation condition (Eq. 5.1.9), and defining the total pump OAM as $\ell_{\mathrm{T}}\hbar$, $\ell_{\mathrm{T}} = \ell_{780} + \ell_{776}$, we can rewrite the generated two-photon state (Eq. 5.1.2) as

$$|\Psi\rangle = \sum_{\ell_{\mathrm{B}},p_{\mathrm{B}},p_{\mathrm{IR}}} c_{p_{\mathrm{B}},p_{\mathrm{IR}}}^{\ell_{\mathrm{B}},\ell_{\mathrm{IR}}} \left|\mathrm{LG}_{p_{\mathrm{B}}}^{\ell_{\mathrm{B}}}\right\rangle_{\mathrm{B}} \left|\mathrm{LG}_{p_{\mathrm{IR}}}^{\ell_{\mathrm{IR}}}\right\rangle_{\mathrm{IR}}, \tag{5.1.13}$$

with the restriction that $\ell_{\mathrm{IR}} = \ell_{\mathrm{T}} - \ell_{\mathrm{B}}$. Carrying out the sum over p-modes, this can be rewritten in terms of OAM states, $|\ell\rangle$, as

$$|\Psi\rangle = \sum_{\ell_{\mathrm{B}}} C_{\ell_{\mathrm{B}},\ell_{\mathrm{T}}} \left|\ell_{\mathrm{B}}\right\rangle_{\mathrm{B}} \left|\ell_{\mathrm{T}} - \ell_{\mathrm{B}}\right\rangle_{\mathrm{IR}}, \quad C_{\ell_{\mathrm{B}},\ell_{\mathrm{T}}} = \sum_{p_{\mathrm{B}},p_{\mathrm{IR}}} c_{p_{\mathrm{B}},p_{\mathrm{IR}}}^{\ell_{\mathrm{B}},\ell_{\mathrm{T}}-\ell_{\mathrm{B}}}. \tag{5.1.14}$$

The two-photon state is reduced to a coherent superposition of OAM-conserving product states, which is an OAM-entangled state [18].

To characterise this state we use two measures. Firstly, we define the spiral bandwidth [49] as

$$\Delta\ell_{\mathrm{B}} = \sqrt{\sum_{\ell_{\mathrm{B}}} P_{\ell_{\mathrm{B}},\ell_{\mathrm{T}}} {\ell_{\mathrm{B}}}^2 - \left(\sum_{\ell_{\mathrm{B}}} P_{\ell_{\mathrm{B}},\ell_{\mathrm{T}}} \ell_{\mathrm{B}}\right)^2}, \quad P_{\ell_{\mathrm{B}},\ell_{\mathrm{T}}} = |C_{\ell_{\mathrm{B}},\ell_{\mathrm{T}}}|^2, \tag{5.1.15}$$

which is a measure of the number of orthogonal modes participating in the entangled state. Physically the above definition corresponds to the standard deviation of the 420 nm ℓ-distribution. Secondly, we use the Shannon entanglement entropy [203] as a measure of the degree of entanglement, which is given by

$$S = -\sum_{\ell_{\mathrm{B}}=-\infty}^{\infty} P_{\ell_{\mathrm{B}},\ell_{\mathrm{T}}} \log_2 P_{\ell_{\mathrm{B}},\ell_{\mathrm{T}}}. \tag{5.1.16}$$

5.2 Experimental setup

The experimental setup is split into two halves: before and after the optical fibres. The "pre-fibre" setup is shown in Fig. 5.2, along with the typical laser power at various points. The spectroscopy and laser locking techniques detailed in Sec. 3.2 and 3.5 are used to monitor and stabilise the frequency of the lasers. The 780 nm

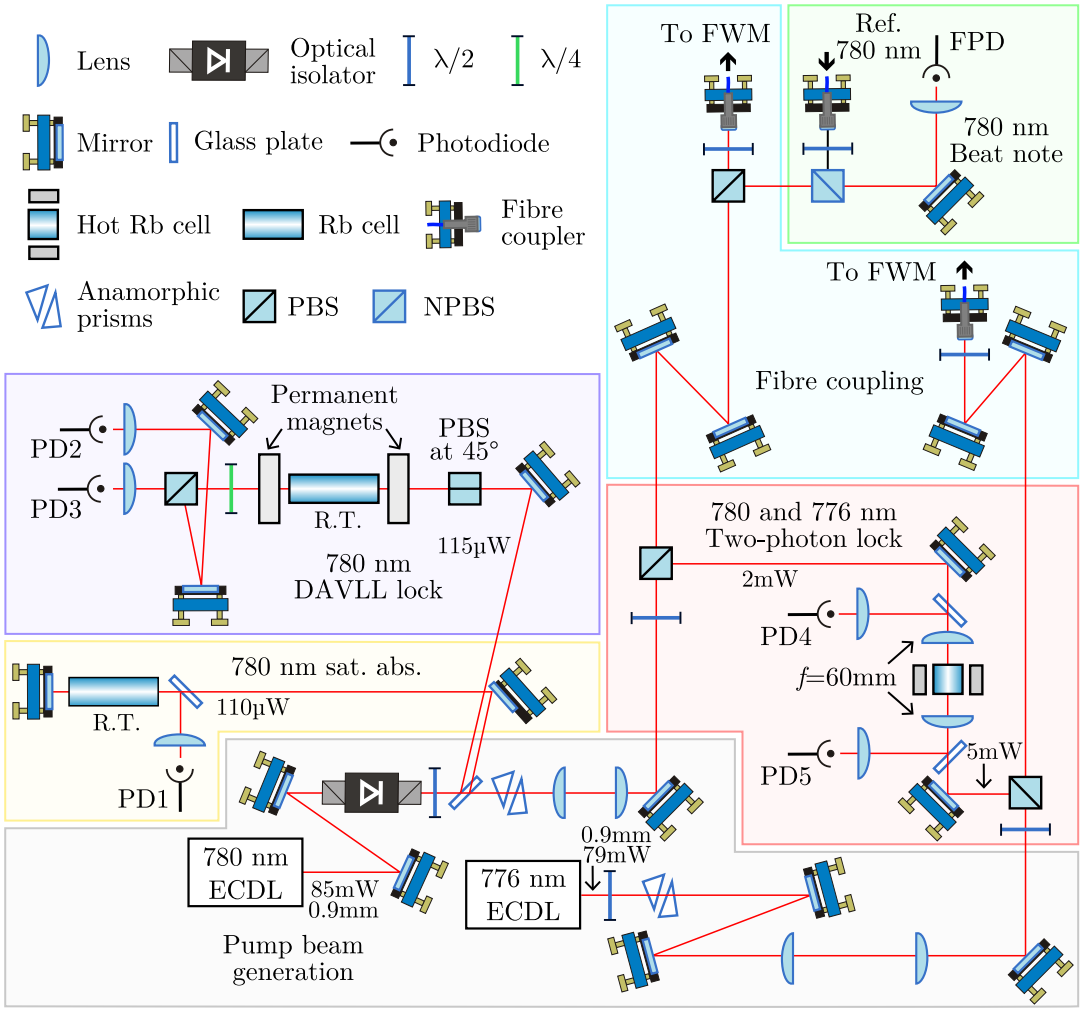

Figure 5.2: Experimental setup before the optical fibres.

laser is locked using the DAVLL lock to a detuning of +1.6 GHz from the ^{85}Rb $5S_{1/2}$ $F = 3 \rightarrow 5P_{3/2}$ $F' = 4$ transition. This detuning was chosen to minimise Kerr lensing of the 780 nm light [92, 204]. The 776 nm is then locked using the two-photon lock so that the pump lasers are two-photon resonant with the ^{85}Rb $5S_{1/2}$ $F = 3 \rightarrow 5D_{5/2}$ $F' = 5$ transition. The spectroscopy required for the two-photon lock was carried out in a 10 mm cell heated to 130°C (see Appendix B). To minimise the laser power required, the beams were focused through the cell with 60 mm lenses. With this setup, a 780 nm frequency modulation of 2 MHz rms amplitude was required to achieve a stable lock. The 780 nm and 776 nm beams are then coupled through separate single-mode polarisation-maintaining

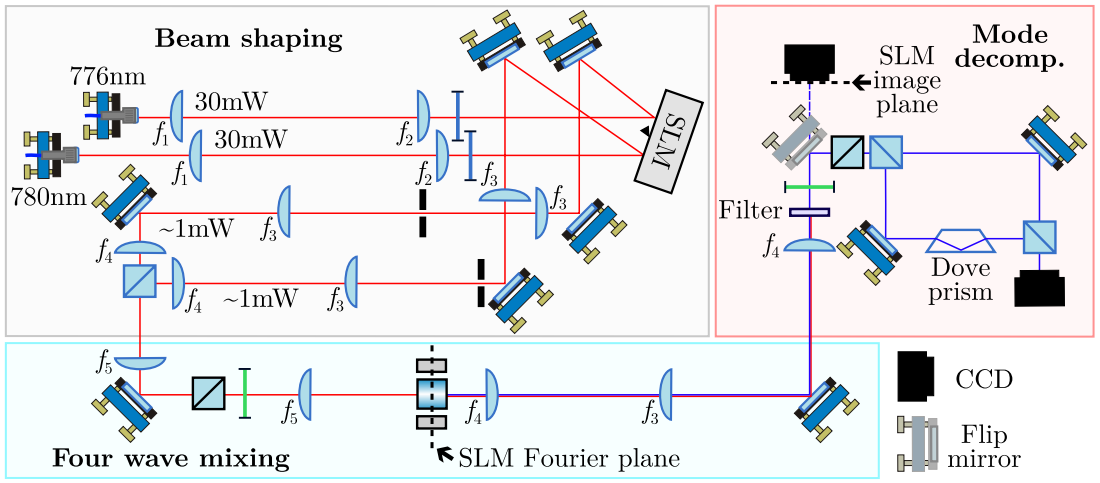

Figure 5.3: Experimental setup for FWM with shaped pump beams. The same symbols are used as detailed in the key in Fig. 5.2. $f_1 = 100\,\text{mm}$, $f_2 = 125\,\text{mm}$, $f_3 = 250\,\text{mm}$, $f_4 = 100\,\text{mm}$, $f_5 = 200\,\text{mm}$.

optical fibres to the FWM side of the setup.

The second half of the experiment is shown in Fig. 5.3. The pump beams are shaped independently into a range of LG modes with 1 mm waists at the SLM, as described in Sec. 4.3. After the 1-1 $4f$-telescopes used for Fourier filtering, an additional 100 mm-200 mm telescope is used to expand each beam. The beams are combined on a non-polarising beam splitter (NPBS) and carefully aligned so that they are exactly copropagating. The polarisation is then cleaned using a polarising beam splitter, before a quarter waveplate co-circularly polarises the beams.

The pump beams are focused through the cell using a 200 mm-100 mm telescope, with the 25 mm length cell positioned so that the beams focus to a waist of 25 µm at the centre of the cell. FWM within the cell, which was heated to 120°C, generates the 5.2 µm (which is absorbed by the cell) and 420 nm fields. A final 250 mm-100 mm telescope shrinks the beams so that they fit on the Point Gray Chameleon CMLN-13S2M-CS CCD used to record images of the beam.

The diagram in Fig. 5.3 is not to scale. In reality each telescope images the image plane of the previous one, so that the focus at the centre of the cell is in

a Fourier plane of the SLM, and the image plane of the final telescope is also an SLM image plane.

The transverse mode of the pump beams and 420 nm light are analysed separately, using a spectral filter to select the 420 nm light or by blocking the other pump beam. The intensity profile of the beams can be recorded either in the image plane of the SLM, the position of which is indicated in Fig. 5.3, or at the output of the Dove prism interferometer. Although not shown, in reality there are two interferometers, one for the pump light and one for the blue beam. They are identical apart from the wavelength range of the NPBSs. The fields are linearly polarised before the interferometers to avoid unwanted effects due to polarisation changes at the mirrors. The mode decomposition measurements are carried out as discussed in Sec. 4.4 by taking three images at the output of the interferometer: the intensity profile in arm A, I_A, the intensity profile in arm B, I_B, and the interferogram, I_T.

5.2.1 Pump beam decomposition

Using this setup, the 420 nm mode decomposition is measured for LG_0^ℓ pump beams with $0 \leq \ell \leq 8$. For comparison with the 420 nm results presented later, Figs. 5.4 and 5.5 show the beams profiles, I_A, and uncorrected interferograms, I_T, of the 776 nm and 780 nm pump modes, respectively, as well as the incoherent mode decomposition of each beam obtained following the procedure detailed in Sec. 4.4. Each decomposition considered modes with $0 \leq \ell \leq 10$ and $p \leq 3$, although only modes up to $p = 2$ are shown. The full result can be found in the dataset [205].

The relative power in the target modes, $P_t = P_0^{\ell_{776/780}}$, averaged over five measurements is also given. The measured mode purity is high for low ℓ values ($P_t > 0.96$ for $\ell < 3$) but drops slightly as ℓ increases ($P_t \simeq 0.88$ for $\ell > 6$). These results provide a benchmark with which to compare the generated 420 nm light.

The apparent decrease in mode purity for higher ℓ occurs despite the visibility of the interference fringes remaining high, which is a good indicator of high purity

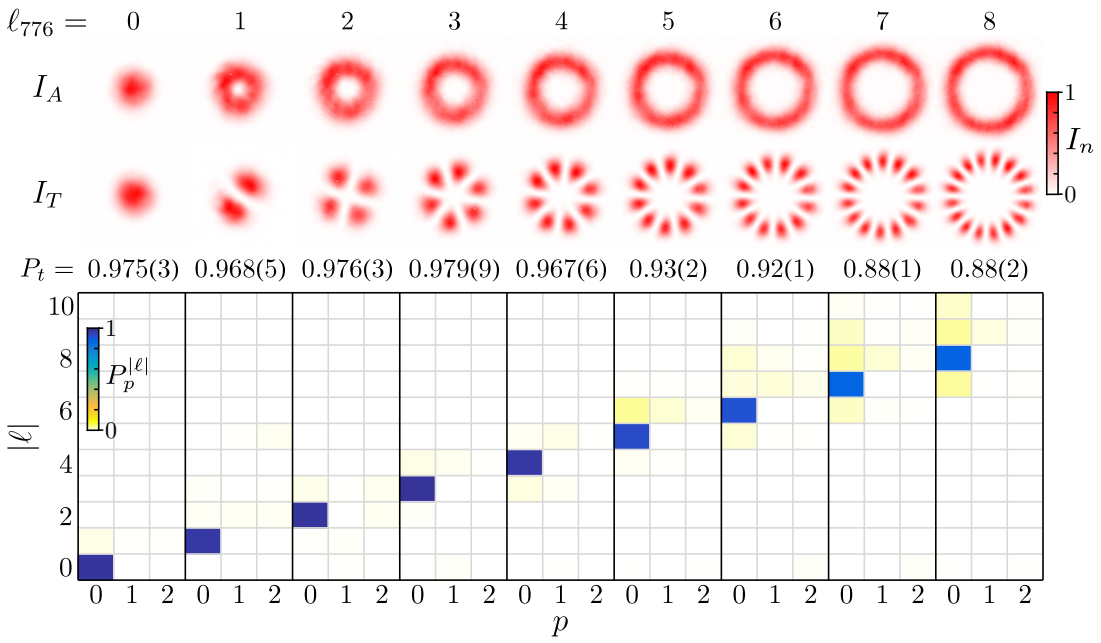

Figure 5.4: Relative intensity profile, I_A, uncorrected interferogram, I_T, and mode decomposition of the 776 nm pump modes. $P_t = P_0^{\ell_{776}}$: mean relative power in the $\mathrm{LG}_0^{\ell_{776}}$ target mode. Total power in $p > 0$ modes is $< 4\%$ in each case.

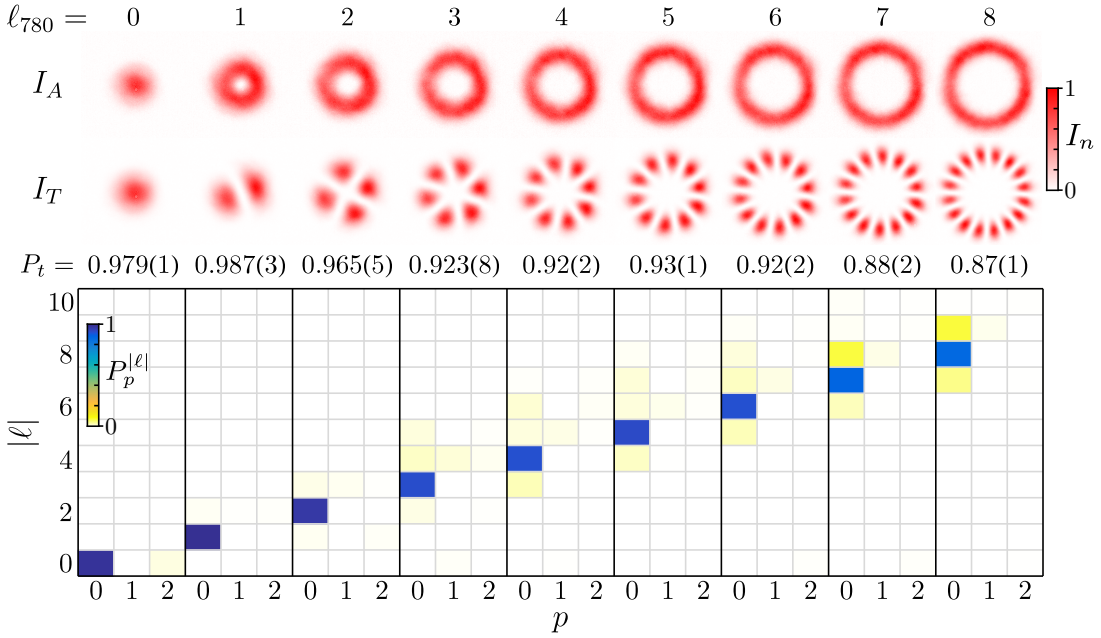

Figure 5.5: Relative intensity profile, I_A, uncorrected interferogram, I_T, and mode decomposition of the 780 nm pump modes. $P_t = P_0^{\ell_{780}}$: mean relative power in the $\mathrm{LG}_0^{\ell_{780}}$ target mode. Total power in $p > 0$ modes is $< 4\%$ in each case.

beams. The mode decomposition method used here assumes that the beams are in an incoherent superposition of modes. Whilst this is a good assumption for the generated 420 nm light [47], this is not necessarily true for the pump beams. If the pump modes are instead in a coherent superposition of modes this may lead to the measurement method under-estimating the mode purity. Other sources of error in the measurement include misalignment of the Dove prism interferometer and small amounts of astigmatism of the beam, both of which have a larger effect at higher ℓ due to the smaller fringe spacing. A more reliable measurement of the pump mode purity could be obtained by using a second SLM and on-axis filtering [188].

5.3 OAM addition

We now consider the main FWM experimental results. In the first experiment both pump beams were shaped into LG_0^ℓ modes with $0 \leq \ell = \ell_{780} = \ell_{776} \leq 8$. The relative intensity profile, I_A, and interferogram, I_T, of the 420 nm light generated by each pair of pump modes is shown in Fig. 5.6 (a).

For low ℓ pump modes ($\ell \leq 3$), the interferograms show high visibility fringes across the whole pattern, similar to the pump beam interferograms in Figs. 5.4 and 5.5. Each interferogram has 4ℓ lobes, indicating that the blue light carries OAM equal to the total OAM of the two pump beams, so that $\ell_{\mathrm{B}} = \ell_{780} + \ell_{776}$. This is in agreement with the previous observations in Refs. [46, 87].

As ℓ increases however, the visibility of the fringes at the top and bottom of the interferogram drops. The position of this modulation in visibility is determined by the geometry of the interferometer, in particular the orientation of the Dove prism that causes the extra reflection. In the interferograms shown this reflection takes place along the horizontal axis. When nearby parts of the beam interfere (along the horizontal axis) the visibility is high, but when opposite sides of the beam interfere (along the vertical axis) the visibility is low. This drop in the transverse coherence of the beam is the first indication that the 420 nm light is

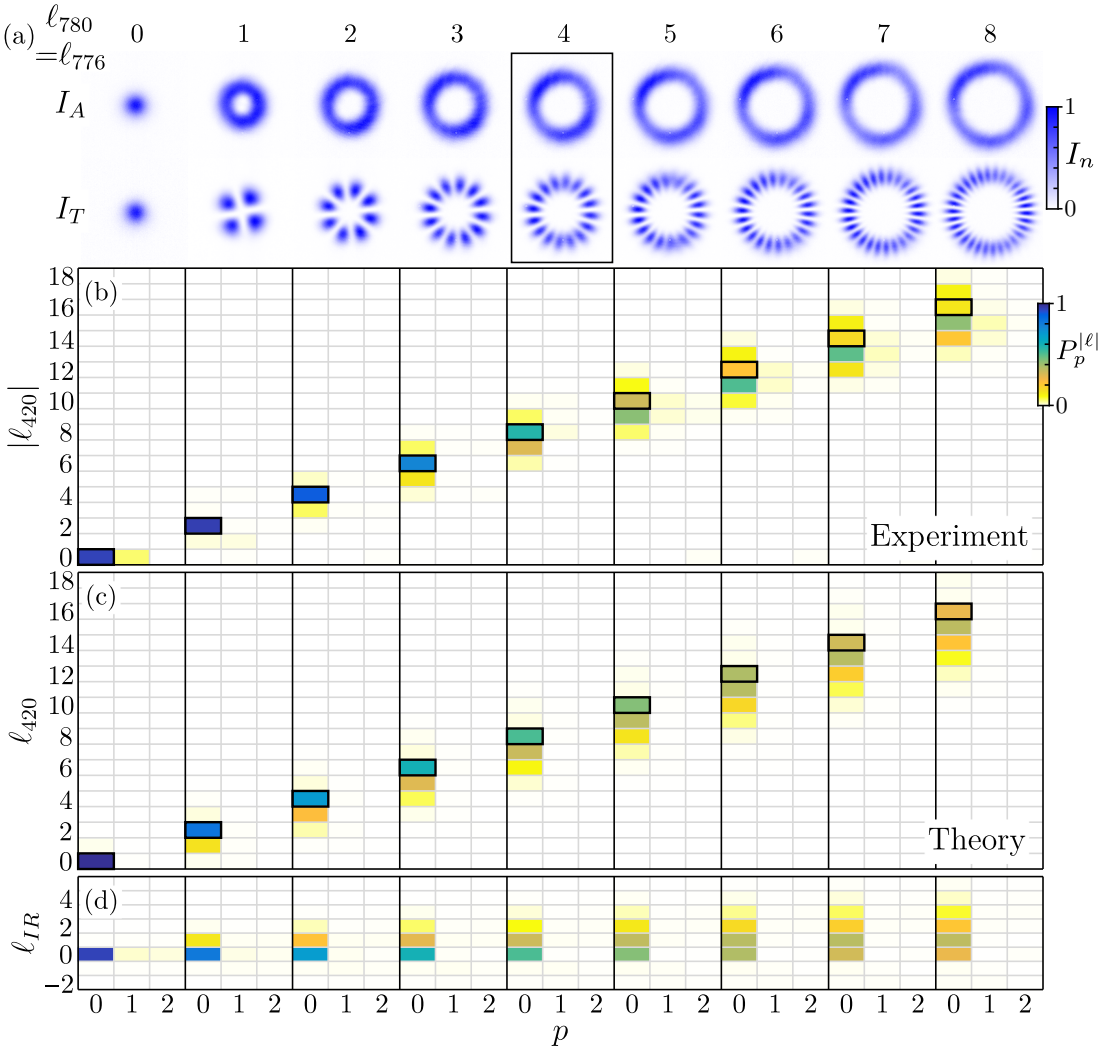

Figure 5.6: OAM addition: (a) 420 nm relative intensity profile, I_A, and uncorrected interferogram, I_T, for $\ell_{780} = \ell_{776} = 0 \rightarrow 8$. (b) Experimental and (c) theoretical mode decomposition of the 420 nm light. Boxes indicate the target 420 nm mode, $\mathrm{LG}_0^{\ell_{780}+\ell_{776}}$. Total power in $p > 0$ modes is $< 8\%$ in each case. (d) Theoretical 5.2 µm mode decomposition. The box around the $\ell = 4$ mode is used for a later comparison with OAM frequency conversion.

generated in more than one transverse mode.

The experimental mode decomposition of the 420 nm beam is shown in Fig. 5.6 (b). The Fourier analysis was carried out for $0 \leq \ell \leq 18$ and $p \leq 3$, but again only modes up to $p = 2$ are shown, with $p \leq 3$ in Ref. [205]. Although our analysis only allows $|\ell|$ to be determined, previous work has shown that the sign

of ℓ is conserved [87], so we assume that this is also the case here. The theoretical predictions for the mode decomposition of both the 420 nm and 5.2 µm light are included in Fig. 5.6 (c) and (d), respectively.

As expected from the interferograms, for low ℓ the 420 nm light is measured to be predominantly in a single mode, with $\ell_{\mathrm{B}} = \ell_{780} + \ell_{776}$. This mode is referred to as the target mode, with relative power $P_t = P_0^{\ell_{780}+\ell_{776}}$, and is highlighted by a box in each mode decomposition in Fig. 5.6 (b) and (c). When the 420 nm light is generated in this mode, OAM conservation implies that the 5.2 µm field is generated mostly in the LG_0^0 mode. This is supported by the theoretical 5.2 µm decomposition.

Fig. 5.7 shows the 420 nm target mode power, P_t, for both the experimental and theoretical results in Fig. 5.6. For $\ell \leq 2$, P_t is high, and efficient OAM addition is demonstrated. The experimental mode purity remains substantially higher than the theoretical prediction until $\ell = 4$. This may be due to the high nonlinear gain preferentially amplifying the optimal mode.

In both the experiment and theory, as ℓ increases the 420 nm ℓ-distribution continuously broadens, which is accompanied by a drop in the target mode power. Rather than being generated predominantly in the target mode, the 420 nm light is observed as an incoherent superposition of an increasing number of modes. In

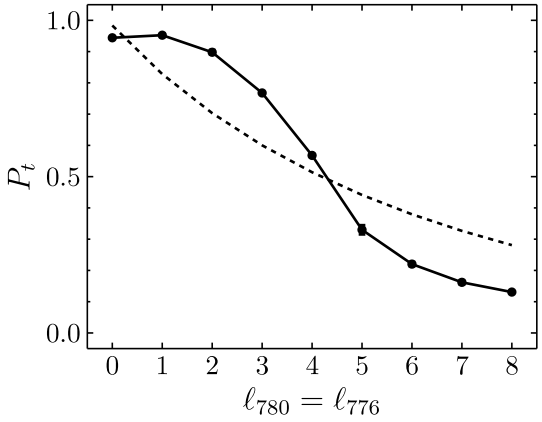

Figure 5.7: OAM addition: Relative power in the target mode, $P_t = P_0^{\ell_{780}+\ell_{776}}$. Solid line: experiment, dashed line: theory.

order to conserve OAM, when the 420 nm light is observed in a range of modes, the 5.2 µm light can no longer be generated mostly in the LG_0^0 mode. The two-photon 5.2 µm and 420 nm field is then generated as a coherent superposition of different combinations of modes that conserve OAM, of the form given in Eq. 5.1.13. Thus the observed broadening of the 420 nm ℓ-distribution strongly indicates that the 5.2 µm and 420 nm fields are generated in an OAM-entangled state.

Fig. 5.8 (a) and (b) show the inferred spiral bandwidth and entanglement entropy of the 5.2 µm and 420 nm state as a function of pump ℓ, respectively. These results are calculated from the experimental and theoretical 420 nm decomposition in Fig. 5.6 using Eqs. 5.1.15 and 5.1.16. For $\ell = 0$ pump modes the 5.2 µm and 420 nm light is generated predominantly in a single state ($|LG_0^{\ell_{780}+\ell_{776}}\rangle_{\mathrm{B}} |LG_0^0\rangle_{\mathrm{IR}}$), and experimentally we measure a mode decomposition which indicates close to zero spiral bandwidth and entanglement. However, as the pump ℓ increases the number of OAM-conserving states that contribute to the 5.2 µm and 420 nm field also increases, and both the spiral bandwidth and entanglement entropy continuously increase.

The error bars in Figs. 5.7 and 5.8 are calculated by taking the standard error of the results from five separate mode decomposition measurements. However, when performing the pump mode decomposition in Sec. 5.2.1, the results showed

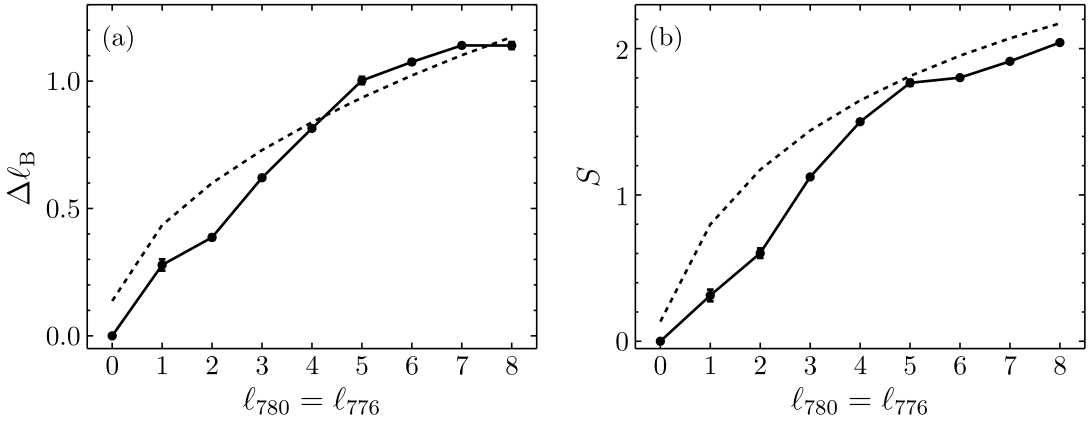

Figure 5.8: OAM addition: (a) Spiral bandwidth, $\Delta\ell_{\mathrm{B}}$ (Eq. 5.1.16), (b) entanglement entropy, S (Eq. 5.1.15). Solid line: experiment, dashed line: theory.

an apparent ℓ-dependent systematic error in the measurement method. This may also affect the 420 nm results and the error bars shown in Figs. 5.7 and 5.8 do not account for this. The experiment could be improved by using a more rigorous mode decomposition method, for example a second SLM combined with on-axis detection [188]. We note however that the main result, the broadening of the 420 nm ℓ-decomposition with increasing pump ℓ, is clear from a visual inspection of the raw interferograms. Whilst the visibility of the fringes in the pump mode interferograms (Figs. 5.4 and 5.5) remain high with increasing ℓ, the fringe visibility significantly reduces for the 420 nm light (Fig. 5.6), indicating an increase in the number of contributing OAM modes.

The dependence of the spiral bandwidth and entanglement entropy on pump ℓ is observed both experimentally and theoretically, and can be explained by considering the spatial overlap of the modes. Fig. 5.9 shows the field amplitude of the FWM beams for (a) $\ell = 1$, and (b) $\ell = 8$ pump beams. The field profiles for the 420 nm and 5.2 µm fields are plotted for two cases. The solid lines show the case where the 5.2 µm field is generated in the LG_0^0 mode and all OAM is

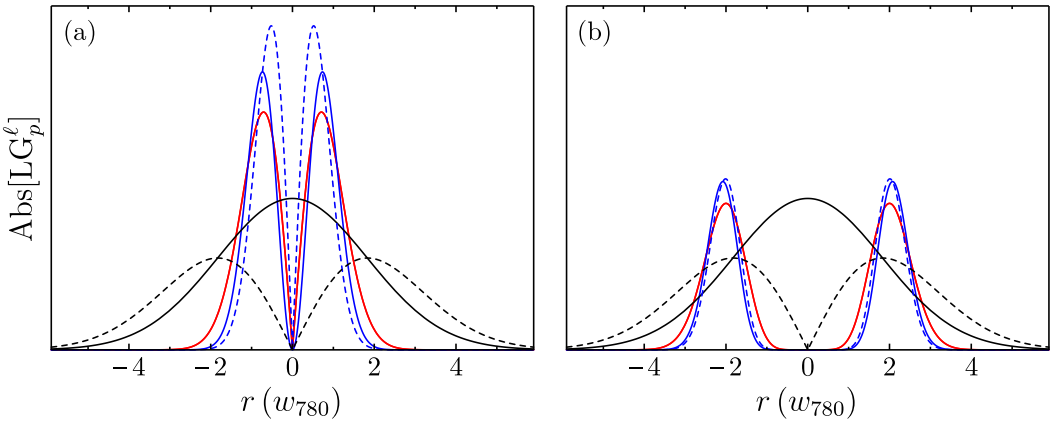

Figure 5.9: Electric field amplitude of the pump (red), 420 nm (blue) and 5.2 µm (black) light. Solid lines indicate all OAM transferred to blue, dashed lines indicate OAM is shared. (a) $\ell_{780} = \ell_{776} = 1$: $\ell_\mathrm{B} = 2$, $\ell_\mathrm{IR} = 0$ (solid), and $\ell_\mathrm{B} = 1$, $\ell_\mathrm{IR} = 1$ (dashed). (b) $\ell_{780} = \ell_{776} = 8$: $\ell_\mathrm{B} = 16$, $\ell_\mathrm{IR} = 0$ (solid), and $\ell_\mathrm{B} = 15$, $\ell_\mathrm{IR} = 1$ (dashed)

transferred to the 420 nm light, whilst the dashed lines show the profiles if the 5.2 µm field is in the LG_0^1 mode. The waist of the 420 nm and 5.2 µm fields has been set by the Boyd criterion which requires that the 5.2 µm waist is 2.6 times that of the pump.

For the $\ell = 1$ pump modes in (a) there is only significant overlap of the fields if the 5.2 µm light is generated in the LG_0^0 mode (solid line), thus for low ℓ OAM is predominantly transferred to the 420 nm light. However, the radius of an LG mode increases in proportion with $\sqrt{\ell}$, so as the pump ℓ increases so does the diameter of the pump beams. For the $\ell = 8$ pump modes in (b) the largest overlap is with the LG_0^1 5.2 µm mode, but the overlap with other higher order 5.2 µm modes also improves. The 420 nm and 5.2 µm fields are thus generated in an increasing number of OAM modes as the pump ℓ increases, resulting in the observed broadening of the 420 nm $|\ell|$-distribution, and increases spiral bandwidth of the two-photon state.

Gouy phase matching

The combination of OAM conservation and spatial overlap does not solely determine the generated modes. For example, consider the case of

$$\ell_{\mathrm{B}} = \ell_{780} + \ell_{776} + 1, \quad \ell_{\mathrm{IR}} = -1. \tag{5.3.17}$$

This pair of 5.2 µm and 420 nm modes conserve OAM, and for large ℓ will have similar overlap to the $\ell_{\mathrm{IR}} = 1$ case shown in Fig. 5.9, but the theory predicts that these modes are not produced at all. This is due to Gouy phase matching. For $p = 0$ pump modes the Gouy phase matching condition becomes

$$|\ell_{780}| + |\ell_{776}| = |\ell_{\mathrm{IR}}| + 2p_{\mathrm{IR}} + |\ell_{\mathrm{B}}| + 2p_{\mathrm{B}} \tag{5.3.18}$$

which for $\ell_{\mathrm{IR}} < 0$ requires that

$$2p_{\mathrm{IR}} + 2p_{\mathrm{B}} < 0. \tag{5.3.19}$$

Since $p \geq 0$, modes with $\ell_{\mathrm{IR}} < 0$ therefore cannot be Gouy phase matched. This causes an asymmetry between positive and negative ℓ_{IR}, and as a result the

blue light is preferentially generated with $\ell_B < \ell_{780} + \ell_{776}$. This asymmetry is replicated in the experimental results, although not to the same extent as in the theoretical prediction. A similar argument can be made for 420 nm and 5.2 µm modes with $p > 0$, which have significant spatial overlap with the pump beams, but are not generated in either the theory or experiment.

5.4 OAM frequency conversion

In the second FWM experiment, the 420 nm mode decomposition was measured for the case where only one of the pump beams carry OAM. The 776 nm field was shaped into LG_0^ℓ modes with $0 \leq \ell = \ell_{776} \leq 8$, with the 780 nm pump beam in the Gaussian LG_0^0 mode. To improve the spatial overlap of the pump beams, the 780 nm focus was axially offset to 9.2 mm ($3.8 z_R$) before that of the 776 nm beam. This was included in the theoretical model as discussed in Sec. 5.1, and was achieved experimentally by adding the phase of a spherical lens to the 780 nm hologram.

The results for this experiment are shown in Fig. 5.10, with the relative intensity profile, I_A, and uncorrected interferogram, I_T, for each ℓ_{776} pump beam in (a), and the experimental mode decomposition in (b). As before the mode decomposition was carried out for $p \leq 3$ [205], but only modes up to $p = 2$ are shown. The theoretical mode decompositions of the 420 nm and 5.2 µm light are shown in (c) and (d), respectively.

As in Sec. 5.3, for low ℓ pump beams the 420 nm light is generated mostly in a single mode, in an OAM state consistent with the OAM being predominantly transferred to the 420 nm light. This results in the 776 nm OAM state being efficiently frequency converted to 420 nm, with $\ell_B = \ell_{776}$. The relative power in the target mode, $P_t = P_0^{\ell_{776}}$, is plotted in Fig. 5.11 and is again substantially higher than predicted by the theory until $\ell_{776} = 4$. As ℓ_{776} increases, the 420 nm light is spread over an increasing number of modes, indicating an increase in the available spiral bandwidth and entanglement entropy of the 5.2 µm anf 420 nm

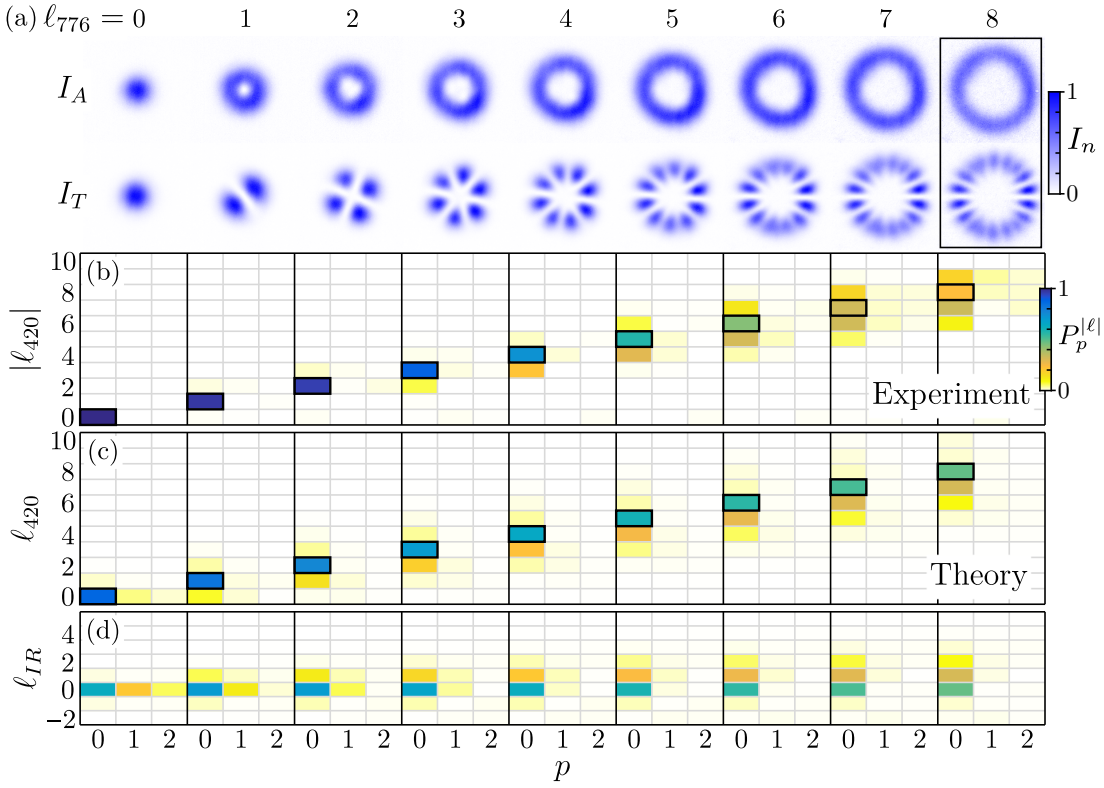

Figure 5.10: OAM frequency conversion: (a) 420 nm relative intensity profile, I_A, and uncorrected interferogram, I_T, for $\ell_{776} = 0 \rightarrow 8$. (b) Experimental and (c) theoretical mode decomposition of the 420 nm light. Boxes indicate the target 420 nm mode, $\mathrm{LG}_0^{\ell_{776}}$. Total power in $p > 0$ modes is $< 10\%$ in each case. (d) Theoretical 5.2 µm mode decomposition. The box around the $\ell_{776} = 8$ mode is used for a later comparison with OAM addition.

two-photon state, as shown in Fig. 5.12.

Naïvely, one might think it doesn't matter whether the OAM is provided by only one or both of the pump beams. However, the results imply an increase in the spiral bandwidth for a given target mode if only one pump beam carries OAM. As an example of this, the LG_0^8 target mode results in Figs. 5.6 and 5.10 are highlighted by boxes. Despite the target mode being the same, there is a large difference in the interferogram for the two cases. For OAM addition, where the pump OAM is shared (Fig. 5.6), the visibility of the fringes is relatively high, whilst for OAM frequency conversion, where the OAM is provided by only the

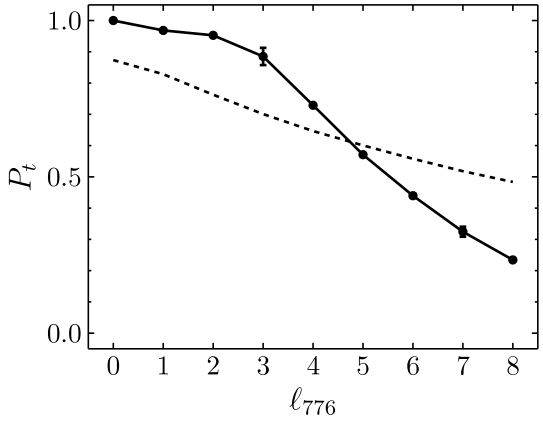

Figure 5.11: OAM frequency conversion: Relative power in the target mode, $P_t = P_0^{\ell_{776}}$. Solid line: experiment, dashed line: theory.

776 nm beam (5.10), the fringes are essentially non-existent along the vertical axis. Some of this is explained by theory, as the mode overlap with the 5.2 µm LG_0^0 mode obviously increases for $\ell_{780} = \ell_{776}$, but experimentally we observe a larger difference in spiral bandwidth than expected.

This discrepancy may be explained by our model giving a poor prediction of the 5.2 µm and 420 nm waists, especially for the OAM frequency conversion experiment. In the theoretical model we assume that the 420 nm and 5.2 µm

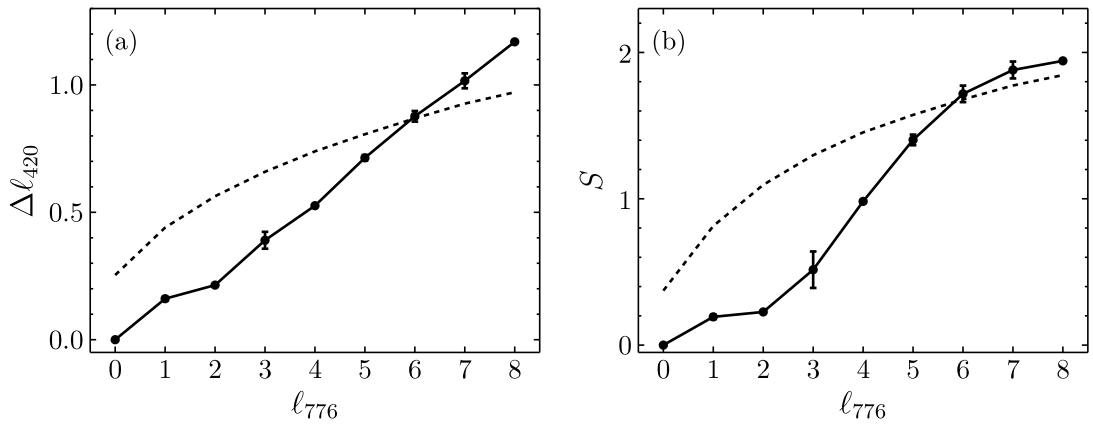

Figure 5.12: OAM frequency conversion: (a) Spiral bandwidth, $\Delta\ell_{\mathrm{B}}$ (Eq. 5.1.16), (b) entanglement entropy, S (Eq. 5.1.15). Solid line: experiment, dashed line: theory.

fields are generated with waists determined via the Boyd criterion. However, it is not obvious that this should apply to higher order modes, especially when the foci of the two pump beams are separated. Indeed measurements of the 420 nm waist show that it is in general not the same as the assumed value. Fig. 5.13 (a) and (b) show the waists of the FWM fields for OAM addition and OAM frequency conversion, respectively. The measured 420 nm waist (solid, filled blue) is consistently smaller than the predicted waist (dashed, empty blue) for both experiments, particularly for the OAM frequency conversion experiment. The beam waists of all three fields were measured in the SLM image plane after the FWM cell, so the 420 nm waist in the Fourier plane within the FWM cell is in reality larger than predicted. A more accurate prediction of the waists might be found by maximising the FWM signal in the theoretical model by varying each of the generated waists. This in turn may give better agreement between the theoretical and experimental mode decompositions.

Comparing Figs. 5.6 and 5.10 also shows the relative importance of Gouy phase matching in the two situations. In the OAM frequency conversion experiment the axially offset 780 nm focus reduces the effect of Gouy phase matching. This is apparent in both the experiment and theory via a reduction in the asym-

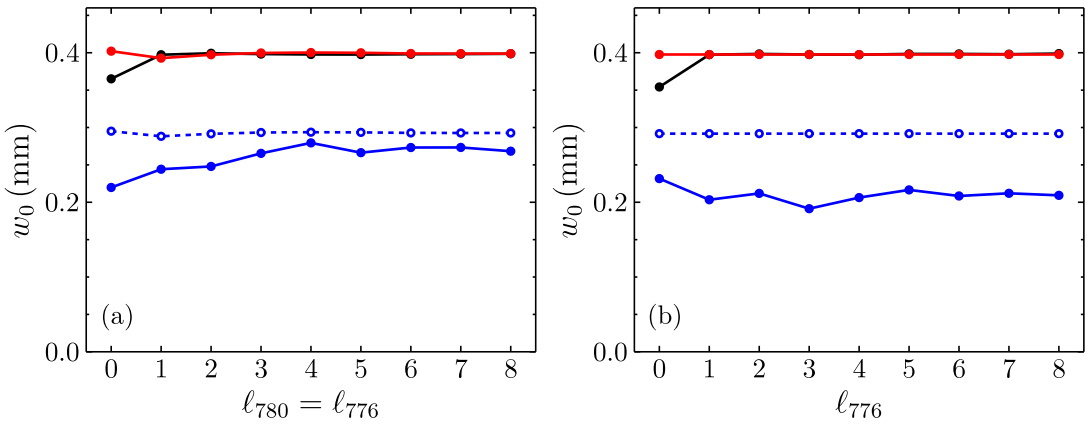

Figure 5.13: Waist of FWM beams for (a) OAM addition and (b) OAM frequency conversion. Red: w_{780}, black: w_{776}, filled blue: measured w_{B}, and empty blue: predicted w_{B}, $w_{\mathrm{B}} = \sqrt{420/780}w_{780}$.

metry between $\ell_B > \ell_{776}$ and $\ell_B < \ell_{776}$, as well as an increase in the relative power predicted to be generated in 5.2 µm modes with $p > 0$.

5.4.1 Conversion efficiency

Finally, we consider the conversion efficiency of the FWM process with shaped pump beams. Fig. 5.14 shows the 780 nm, 776 nm and 420 nm power for each pair of pump beams in the OAM addition and OAM frequency conversion experiments, as well as the conversion efficiency, $\eta = P_B/(P_{780}P_{776})$. Note the units of this conversion efficiency are %/W, rather than %. As the pump ℓ increases the conversion efficiency drops in both experiments. The overall lower efficiency in the OAM frequency conversion experiment is due to the offset focus of the 780 nm beam and reduced spatial overlap of the pump beams.

This definition of the conversion efficiency allows for comparison with [92],

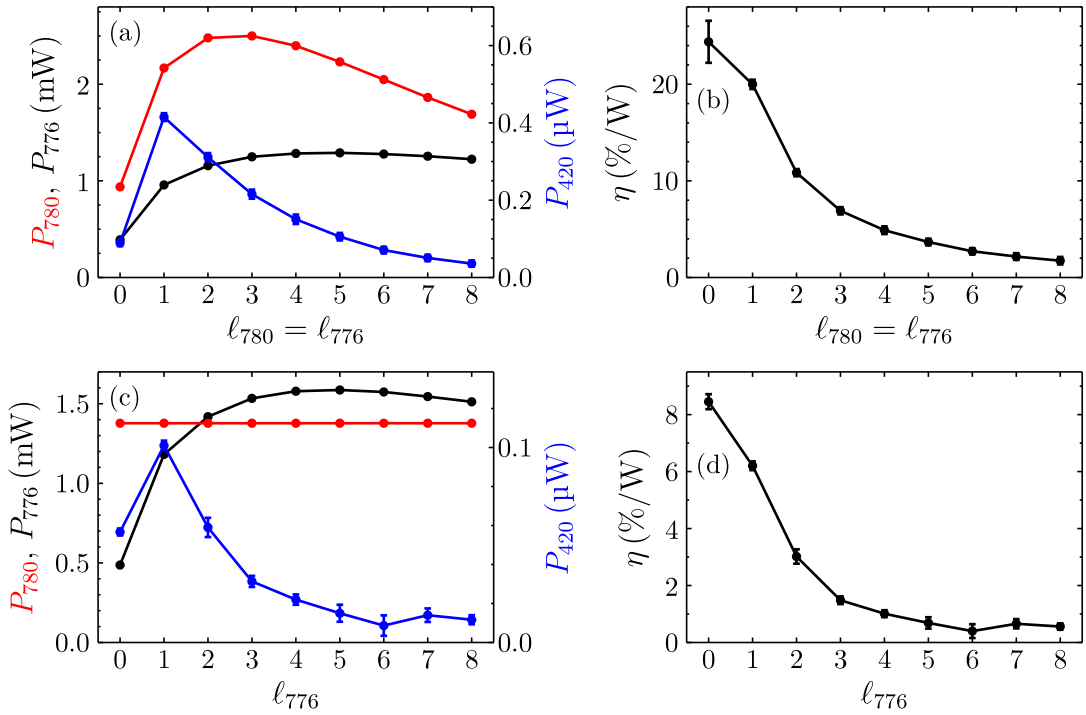

Figure 5.14: (a), (b) OAM addition beam powers and conversion efficiency. (c), (d) OAM frequency conversion beam powers and conversion efficiency. Red: 780 nm, Black: 776 nm and Blue: 420 nm. $\eta = P_B/(P_{780}P_{776})$.

where a conversion efficiency of 260 %/W was measured in an optimised experiment with Gaussian pump beams. The conversion efficiency in the current experiment is less than this. Part of this is due to the use of a shorter rubidium cell (25 mm rather than 75 mm), and also a larger input pump waist. The conversion efficiency could also be improved by increasing the cell temperature, which is slightly reduced from the optimal value of 130°C to reduce the effects of Kerr lensing.

5.5 Summary and Discussion

The work presented in this chapter is the first quantitative investigation of OAM transfer in the "blue light" FWM system. For low ℓ pump beams ($\ell < 4$) the results are consistent with previous experiments [46, 87, 88], and we observe that the 420 nm light is mostly generated in the mode with $\ell_B = \ell_{780} + \ell_{776}$, indicating that the OAM is predominantly transferred to the 420 nm field. However, as ℓ increases we observe a broadening of the 420 nm ℓ-distribution. This is the principal result of this chapter. It indicates that not only is OAM transferred to the 5.2 µm field, but that the 420 nm and 5.2 µm fields are likely to be generated in an OAM-entangled state. The available spiral bandwidth and entanglement entropy of this state was inferred from the 420 nm mode decomposition, and was found to depend on both the total pump OAM and the division of the OAM between the pump fields.

The experimental results are supported by a simple theoretical model that considers the overlap integral of the FWM fields. This model showed the importance of three factors in determining the generated modes: OAM conservation, Gouy phase matching and spatial overlap. The increasing spiral bandwidth with pump ℓ was observed both experimentally and theoretically, and can be explained by considering the pump mode-dependent spatial overlap of the modes. One limitation of the model is the need to know the waist of both generated fields, though as mentioned earlier this could possibly be calculated using the model itself. The

model could be further improved by including propagation effects, including absorption and Kerr lensing of the fields.

This work suggests that the "blue light" FWM system may be an efficient source of OAM-entangled photon pairs with widely disparate wavelengths. However, clearly further work is required to confirm this. Firstly, it must be confirmed that the "missing" OAM is indeed transferred to the 5.2 µm light. This would require the use of a sapphire cell and a measurement of the transverse mode of the 5.2 µm field, which could possibly be carried out using single-pixel imaging techniques due to the cost/availability of cameras at this wavelength. The next step would be to confirm the correlation between the 420 nm and 5.2 µm OAM state. To do this the FWM process would need to be carried out at the single photon level, and a measurement made of the coincidences, conditioned on the OAM state, of the 420 nm and 5.2 µm photons. This could be carried out using two additional SLMs and single photon detectors, though the wavelength of the generated infrared field may make this difficult. Although this would show correlation between the 420 nm and 5.2 µm OAM state, it would not alone be sufficient to confirm entanglement. To do this the photon coincidences must also be measured for superpositions of OAM states [47], which could be carried out as part of a full tomographic reconstruction of the two-photon state [206].

There are also unanswered questions that could be investigated using the current setup. For example, the mode decomposition of the 420 nm light was found to depend on the 780 nm detuning. This is expected to be due to Kerr lensing of the 780 nm beam [92, 204] changing the spatial overlap of the FWM fields. The 780 nm detuning used in this work was chosen to minimise this effect, but it would be interesting to make quantitative measurements of the mode decomposition for a range of detunings to understand the effect of the changing mode overlap. This may allow the spiral bandwidth of the two-photon state generated for a given pump ℓ to be tuned simply by changing the 780 nm detuning.

Chapter 6

Coherent beam shaping

In this chapter we extend our study of FWM with structured light to more general pump modes. We present a series of three experiments:

- OAM addition for pump beams with different ℓ indices, including addition of OAM with opposite handedness.
- Addition of radial ($p > 0$) LG modes.
- Addition of *coherent* superpositions of LG modes.

Each experiment was carried out using the same experimental setup and parameters as detailed in Chapter 5, however the data was taken before the mode decomposition procedure described in Chapter 4 was fully developed. As such we do not have the data required to obtain the full mode decomposition of the light, but present instead preliminary analysis where possible. Nevertheless, the raw experimental data in each case clearly demonstrates the coherent nature of the "blue light" FWM process, as well as the importance of Gouy phase matching in our system.

6.1 OAM addition revisited

In the first of the three experiments we revisit OAM addition. In particular we consider the case where the pump beams carry OAM of opposite handedness.

As before, the pump beams are focused to a waist of 24 µm at the centre of the rubidium cell. This corresponds to a Rayleigh range of 2.3 mm, which is short compared to the cell length of 25 mm. As a result, for the pump beams to remain phase matched with the generated fields as they propagate through the cell they must have identical Gouy phase. Assuming the Boyd criterion [202] holds, so that the fields have matched Rayleigh ranges, this places the following restriction on the mode indices of the generated light

$$|\ell_{780}| + 2p_{780} + |\ell_{776}| + 2p_{776} = |\ell_{\mathrm{IR}}| + 2p_{\mathrm{IR}} + |\ell_{\mathrm{B}}| + 2p_{\mathrm{B}}. \tag{6.1.1}$$

In order to conserve OAM, the ℓ indices must additionally satisfy

$$\ell_{780} + \ell_{776} = \ell_{\mathrm{IR}} + \ell_{\mathrm{B}}. \tag{6.1.2}$$

Where the pump modes both have $\ell \geq 0$, as in Chapter 5, the above conditions restrict the generated light to $\ell \geq 0$ and $p = 0$. However, for pump beams with opposite handedness of OAM, these conditions can instead force the generation of modes with $p > 0$. To illustrate this consider $\ell_{780} = 1$ and $\ell_{776} = -1$. Since the pump ℓ is low, and again assuming that the Boyd critereon holds, the largest spatial overlap of the FWM fields will occur if the 5.2 µm field is generated in the LG_0^0 mode (due to the large 5.2 µm waist). Conservation of OAM (Eq. 6.1.2) then dictates that $\ell_{\mathrm{B}} = 0$. In this case, in order to additionally satisfy Eq. 6.1.1, we must have $p_{\mathrm{B}} = 1$.

To test this, FWM was carried out with $\ell_{780} = 1$ and $\ell_{776} = 2 \rightarrow -2$. The results are shown in Fig. 6.1 (a), with the relative intensity profile of the 420 nm light in the *image plane* after the rubidium cell, I_b, and the interferogram at the output of the Dove prism interferometer, I_T (see Fig. 5.3).

When ℓ_{780} and ℓ_{776} are both positive we see the same behaviour as in the previous chapter; the high visibility interferogram fringes indicate that the pump OAM is transferred with high fidelity to the 420 nm light. However, for $\ell_{776} < 0$ there is a clear additional ring in the intensity profile of the beam. In all cases the interferograms indicate that $\ell_{\mathrm{B}} \approx \ell_{780} + \ell_{776}$.

Fig. 6.1 (b) shows preliminary analysis of the 420 nm radial profile. An incoherent sum of p-modes was fit to the mean radial profile of each I_b image, with the ℓ index of the fitted modes set to $\ell_B = \ell_{780} + \ell_{776}$. The results show that for $\ell_{776} \geq 0$ the blue light is generated predominantly in the $p_B = 0$ mode, whilst when $\ell_{776} < 0$ it is instead generated mostly with $p_B = 1$.

Assuming the 5.2 µm light is generated only in the LG_0^0 mode, these results are consistent with the expected 420 nm mode based on OAM conservation and Gouy phase matching. Fig. 6.1 (c) shows the predicted 420 nm mode decomposition for the case of $LG_{p_{IR}=0}^{\ell_{IR}=0}$ (i.e. not summing over all modes in Eq. 5.1.5). In each case

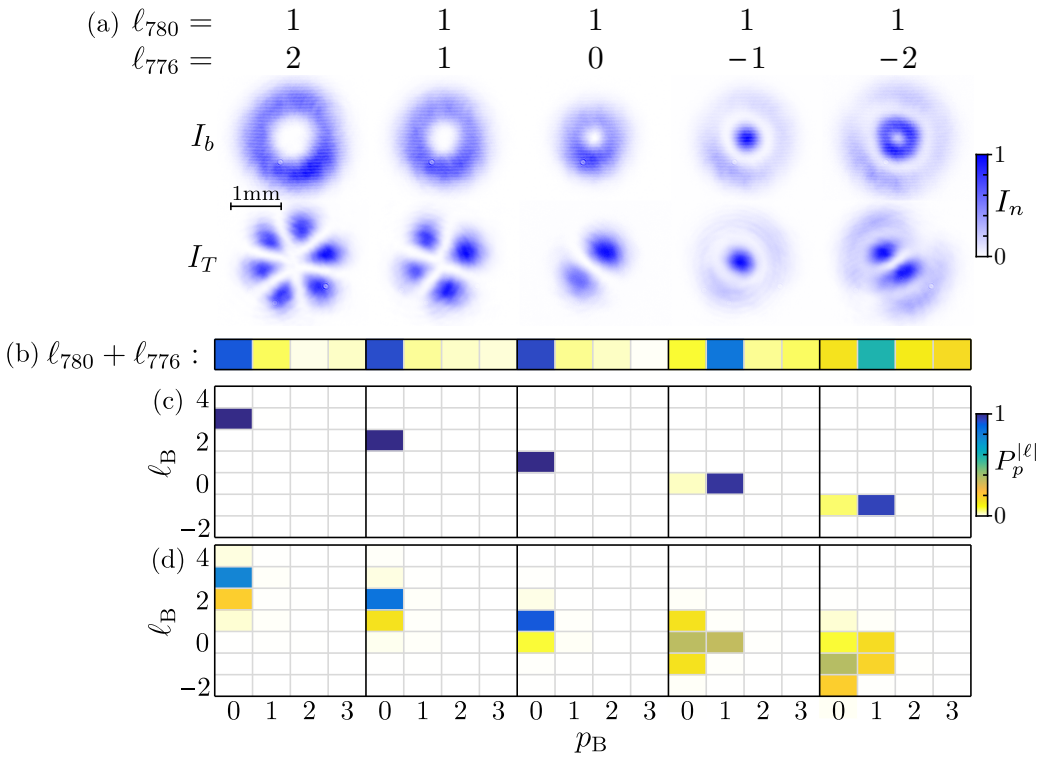

Figure 6.1: (a) Relative 420 nm intensity profile in the image plane after the rubidium cell, I_b, and interferogram at the output of the Dove prism interferometer, I_T (see Fig. 5.3), for pump modes $LG_0^{\ell_{780}}$ and $LG_0^{\ell_{776}}$. (b) Experimental radial decomposition assuming $\ell_B = \ell_{780} + \ell_{776}$. (c) Predicted 420 nm mode decomposition including only 420 nm modes generated with $LG_{p_{IR}=0}^{\ell_{IR}=0}$ and (d) summing over all $LG_{p_{IR}}^{\ell_{IR}}$ modes.

$\ell_B = \ell_{780} + \ell_{776}$, and p_B adjusts to ensure Gouy phase matching of the beams.

Fig. 6.1 (d) on the other hand shows the predicted 420 nm mode decomposition when all 5.2 µm modes are taken into account. The 420 nm and 5.2 µm light is still generated in pairs of modes which conserve both OAM and Gouy phase, but the theory predicts that this should not be restricted to two-photon states with $\mathrm{LG}_{p_{IR}=0}^{\ell_{IR}=0}$, and the 420 nm light should therefore be observed in a range of modes. For example, for $\ell_{780} = 1$ and $\ell_{776} = -1$ the allowed pairs of modes are shown in table 6.1, along with their relative weighting.

Pair	ℓ_{IR}	p_{IR}	ℓ_B	p_B	$P_{p_{IR}}^{\ell_B}$
a	1	0	-1	0	0.14
b	0	0	0	1	0.35
c	0	1	0	0	0.36
d	-1	0	1	0	0.14

Table 6.1: Possible 420 nm and 5.2 µm mode indices for $\ell_{780} = 1$ and $\ell_{776} = -1$.

The experimental result show better agreement with the theoretical prediction in Fig. 6.1 (c) than (d), which suggests the 5.2 µm light is generated mostly in the LG_0^0 mode. It is an open question why this is the case. It is possible that the nonlinear gain in the FWM process means that the modes with the highest probability of being generated are amplified preferentially. However, based on this there should still be significant power in the $p_B = 0$ modes for $\ell_{776} < 0$. It may be that the 5.2 µm $p > 0$ modes undergo preferential absorption or increased Kerr lensing, thus preventing these modes from being generated efficiently.

We note that addition of OAM with opposite handedness has previously been demonstrated in the blue light system, for $\ell_{780} = 1$ and $\ell_{776} = -1$ [87]. In this experiment the 420 nm light was observed as a ring shaped intensity profile which carried no OAM, although there is some on-axis intensity also evident. The Rayleigh range of the fields in this experiment (~ 4 cm) was roughly the same as the cell length (5 cm), and therefore Gouy phase matching is expected to be less

important.

Furthermore, an equivalent experiment has also been carried out for second harmonic generation (SHG) in a nonlinear crystal [207]. The authors observed that the second harmonic light is generated with a single ring in the near-field, but that the intensity profile changes as the beam propagates, with additional rings observed in the far-field. The number of additional rings is the same as predicted by our theory. In this experiment the Rayleigh range of the fields (10s of cm) was much longer than the crystal length (10 mm) and the Gouy phase of the modes was completely neglected from the theoretical model. However, the theory still predicted additional rings in the far-field intensity profile, in this case due to diffraction from the circular "aperture" provided by the pump beams in the wave mixing process.

So far we have only imaged the 420 nm light generated in our experiment in the far-field. An interesting further experiment would be to image in the near-field, and therefore allow further comparison with the SHG experiment described above. We note that if Gouy phase matching is neglected from our theoretical model then our theory cannot explain the observed experimental results, even under the assumption that $\mathrm{LG}_{p_{\mathrm{IR}}=0}^{\ell_{\mathrm{IR}}=0}$.

6.2 Radial LG modes

In the second of the three experiments in this chapter, we carried out FWM for pump beams with $\ell_{780} = \ell_{776} = 1$ and $p_{780}, p_{776} = 0 \rightarrow 4$.

The relative intensity profile, I_b, and interferogram, I_T, of the 780 nm pump modes are shown in Fig. 6.2 (a), with the p-decomposition of each mode in (b). Each decomposition was obtained by fitting an incoherent sum of p-modes, with $\ell = 1$, to the mean radial profile of each I_b image in (a). The intensity profile of each mode is generated with high fidelity ($P_p^1 > 0.97$), and inspection of the interferograms show that each beam is correctly generated with $\ell = 1$. However, there is a noticeable difference in the radial profile of I_b - which is taken in the

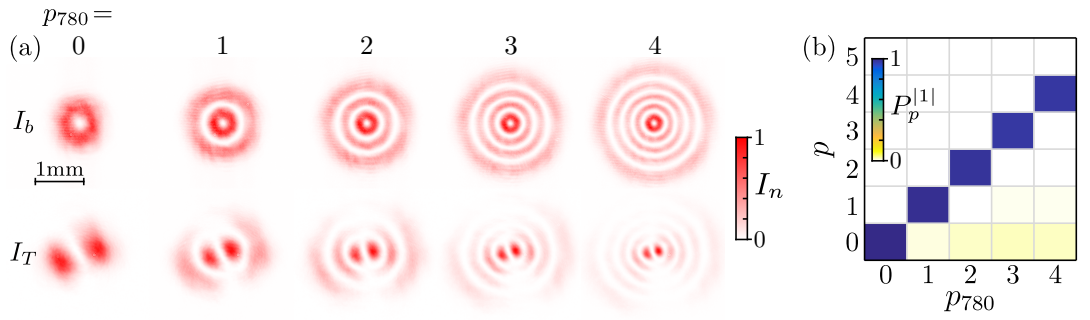

Figure 6.2: (a) Relative 780 nm intensity profile in the image plane after the rubidium cell, I_b, and interferogram at the output of the Dove prism interferometer, I_T. (b) Radial decomposition for $\ell_{780} = 1$.

image plane - and I_T - which is taken after propagation through the interferometer. This indicates that the radial phase discontinuities required for $p > 0$ may be slightly washed out, resulting in the intensity profile of the beam changing as it propagates. The 776 nm modes were generated with similar mode purity ($P_p^1 > 0.92$) and showed the same change in radial profile on propagation.

The 420 nm relative intensity profiles, I_b, and interferograms, I_T, obtained for radial pump modes are shown in Fig. 6.3. In this case, if the 5.2 µm light is generated in the LG_0^0 mode, OAM conservation and Gouy phase matching require that $\ell_\mathrm{B} = \ell_{780} + \ell_{776}$ and $p_\mathrm{B} = p_{780} + p_{776}$, i.e. both the OAM and the p-indices of the pump modes add. Inspection of the interferograms and intensity profiles indicates that this is indeed the case, with four lobes in each interferogram, and the number of radial nodes in the intensity profile consistent with $p_\mathrm{B} = p_{780} + p_{776}$.

A full theoretical analysis has not yet been carried out for this experiment, however initial calculations, for pump modes up to $p = 2$, indicate that we would expect the average p-index of the 420 nm light to be less than $p_{780} + p_{776}$, so that the total pump p-index is "shared" between the 420 nm and 5.2 µm light. The experimental results indicate that this is not the case, with the 5.2 µm light instead restricted to $p = 0$, as in Sec. 6.1.

These results highlight again the importance of Gouy phase matching in our system. This is in contrast to Ref. [190] where SHG of p-modes was investigated,

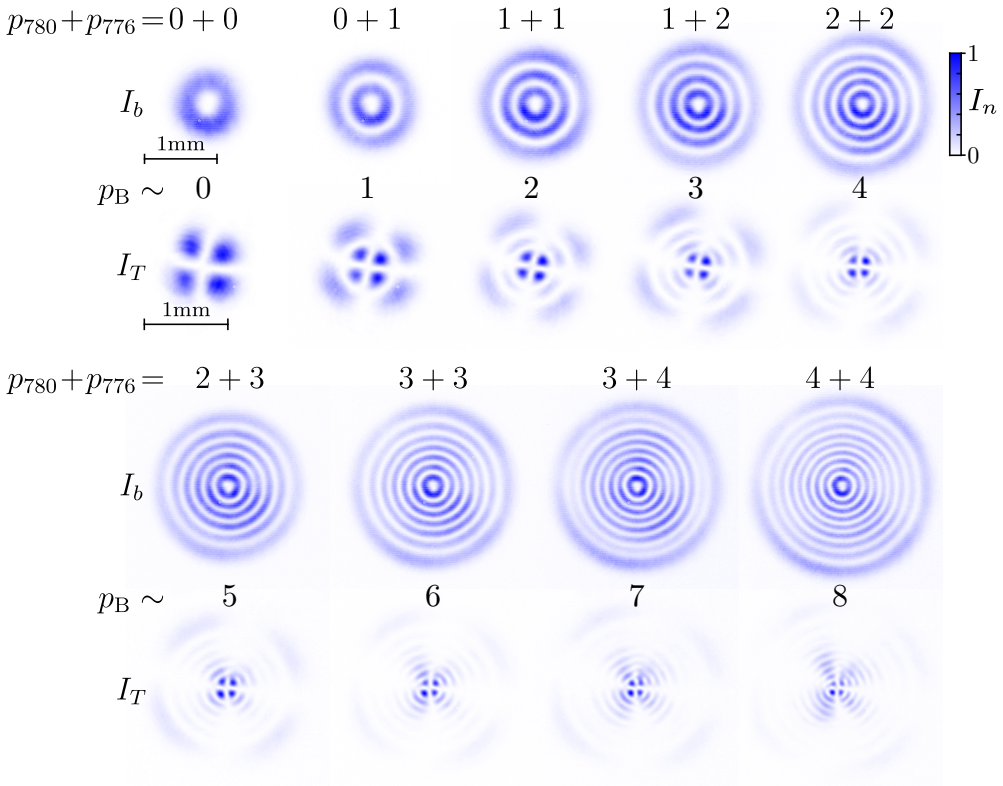

Figure 6.3: Relative 420 nm intensity profile in the image plane after the rubidium cell, I_b, and interferogram at the output of the Dove prism interferometer, I_T, for different combinations of $\mathrm{LG}^1_{p_{780}}$ and $\mathrm{LG}^1_{p_{776}}$ pump modes.

with the Rayleigh length of the beams comparable to the length of the nonlinear crystal. In this experiment the second harmonic had twice the ℓ of the pump beams but the same number of radial nodes.

6.3 Coherent superpositions

In the final experiment presented in this chapter, we investigated FWM for pump beams in a coherent superposition of LG modes. Under these conditions the 5.2 µm and 420 nm light is no longer generated in pairs of single modes which obey OAM and Gouy phase conservation, but instead in pairs of superpositions of LG modes. As a result it is possible to observe coherent interference between modes in the 420 nm beam.

To illustrated this, consider the following pump modes:

$$\begin{aligned} E_{780} &= \frac{1}{\sqrt{2}}\left(\mathrm{LG}_0^1 + \mathrm{LG}_0^{-1}\right), \\ E_{776} &= \frac{1}{\sqrt{2}}\left(\mathrm{LG}_0^1 + \mathrm{LG}_0^{-1}\right). \end{aligned} \tag{6.3.3}$$

so that the combined pump field is given by [46]

$$E_{780}E_{776} = \frac{1}{2}\left(\mathrm{LG}_0^1 + \mathrm{LG}_0^{-1}\right)_{780}\left(\mathrm{LG}_0^1 + \mathrm{LG}_0^{-1}\right)_{776}. \tag{6.3.4}$$

When this field interacts with the atoms there are four separate excitation pathways in the initial two-photon absorption. Since the pump ℓ is low, we expect the 5.2 µm light to be generated mostly in the LG_0^0 mode. In this case, OAM conservation and Gouy phase matching dictate that each excitation pathway produces the follow 420 nm modes:

$$\begin{aligned} &(\mathrm{LG}_0^1)_{780}(\mathrm{LG}_0^1)_{776} \rightarrow c_{2,0}(\mathrm{LG}_0^2)_{\mathrm{B}}, \\ &(\mathrm{LG}_0^1)_{780}(\mathrm{LG}_0^{-1})_{776} \rightarrow c_{1,-1}(\mathrm{LG}_1^0)_{\mathrm{B}}, \\ &(\mathrm{LG}_0^{-1})_{780}(\mathrm{LG}_0^1)_{776} \rightarrow c_{-1,1}(\mathrm{LG}_1^0)_{\mathrm{B}}, \\ &(\mathrm{LG}_0^{-1})_{780}(\mathrm{LG}_0^{-1})_{776} \rightarrow c_{-2,0}(\mathrm{LG}_0^{-2})_{\mathrm{B}}. \end{aligned} \tag{6.3.5}$$

The $c_{i,j}$ can be found by calculating the overlap integral of the FWM fields in each case, and give the relative weighting of each mode. Since the pump fields have the same waist, and the radial profile of the LG modes depend only on $|\ell|$, $c_{2,0} = c_{-2,0} = c_2$ and $c_{1,-1} = c_{-1,1} = c_1$. The 5.2 µm and 420 nm two-photon field is then

$$E_{\mathrm{B}}E_{\mathrm{IR}} = \left(c_2\mathrm{LG}_0^2 + c_2\mathrm{LG}_0^{-2} + 2c_1\mathrm{LG}_1^0\right)_{\mathrm{B}}\left(\mathrm{LG}_0^0\right)_{\mathrm{IR}}, \tag{6.3.6}$$

and the 420 nm light is expected to be observed as a *coherent* superposition of three modes.

This situation was studied previously at Strathclyde in Ref. [46], where the 420 nm mode superposition was studied for a range of pump beam superpositions. The measured 420 nm beams showed good agreement with theoretical predictions based on the above description. Of course, assuming that the 5.2 µm light is restricted to the LG_0^0 mode is an approximation, and further theoretical work has included other OAM states in the analysis [201].

Here we take the original Strathclyde experiment a step further by making use of the independently shaped pump beams. With inspiration from theory presented in Ref. [201], we consider the following pump modes

$$\begin{aligned} E_{780} &= \frac{1}{\sqrt{2}}\left(e^{i\phi}\mathrm{LG}_0^1 + \mathrm{LG}_0^{-1}\right), \\ E_{776} &= \frac{1}{\sqrt{2}}\left(\mathrm{LG}_0^1 + \mathrm{LG}_0^{-1}\right), \end{aligned} \tag{6.3.7}$$

which are the same as those discussed above but with an additional phase shift for one of the 780 nm modes. In this case, consideration of the four excitation pathways leads to a 420 nm field given by

$$E_{\mathrm{B}} = c_2 e^{i\phi}\mathrm{LG}_0^2 + c_2\mathrm{LG}_0^{-2} + c_1(1+e^{i\phi})\mathrm{LG}_1^0. \tag{6.3.8}$$

The phase shift in the 780 nm superposition is expected to cause the two contributions to the LG_1^0 mode (see Eqs. 6.3.5) to interfere, such that for $\phi = \pi$ there is complete destructive interference and the mode is suppressed entirely.

Fig. 6.4 (a) shows the intensity profile of the pump beams and 420 nm light as ϕ is increased from 0 to 2π. For $\phi = 0$ the 420 nm intensity profile is the same as observed in Ref. [46]. The relative power in each 420 nm mode was found by fitting a coherent superposition of LG modes to the full intensity profile, and is shown in Fig. 6.4 (b). For $\phi = 0$ the 420 nm light is composed mainly of the three modes predicted by Eq. 6.3.8.

As ϕ increases, the phase shift causes the 780 nm profile to rotate, as does the 420 nm mode due to the phase shift of the LG_0^2 component in Eq. 6.3.8. We also see the shape of the 420 nm profile change, with the relative power in the LG_1^0 mode decreasing until it is completely suppressed for $\phi = \pi$. At this point the beam is a superposition of $\ell = \pm 2$ and as such displays the characteristic four lobed intensity pattern.

Although we have used the Laguerre-Gauss basis to describe the experiment, these LG superpositions are actually Hermite-Gauss (HG) modes [149]. We see that the interference of HG modes in the wave mixing process depends on their relative orientation. We choose the LG basis here in order to use the same theoretical description as presented in Ref. [46, 201].

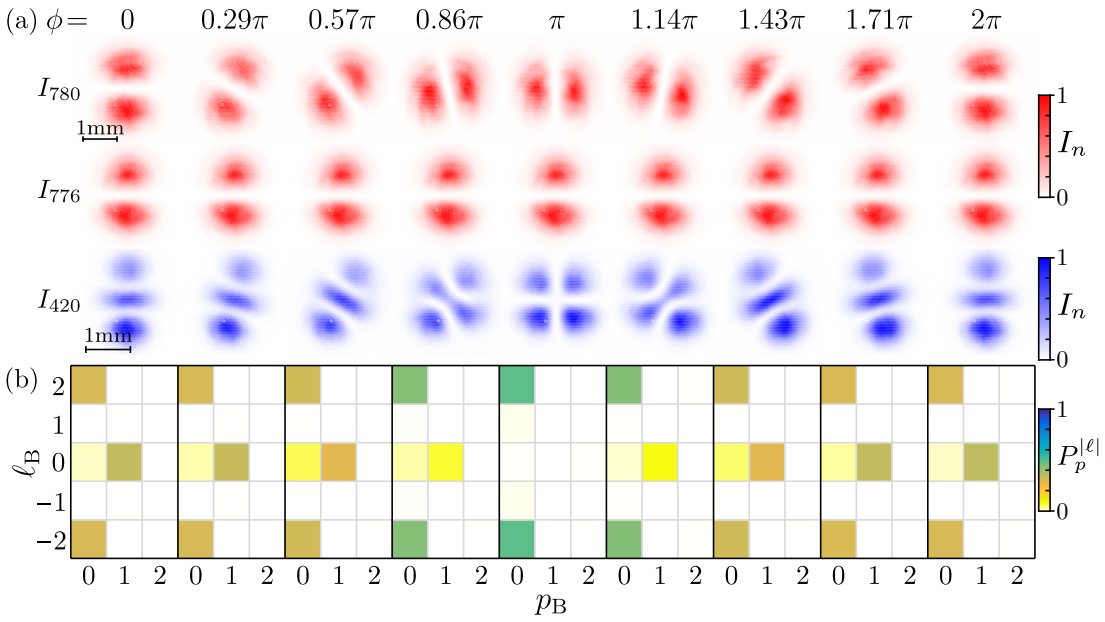

Figure 6.4: (a) Relative intensity profile of 780 nm, 776 nm and 420 nm beam as a function of ϕ. (b) Coherent mode decomposition of the 420 nm beam.

6.4 Conclusion

The OAM transfer experiment in the previous chapter showed that the transverse mode of the 420 nm light is determined by a combination of OAM conservation and Gouy phase matching. This chapter has presented experiments to test these criteria for more generalised pump modes. Although the results are so far preliminary, with only initial analysis carried out, each experiment indicates an interesting area for future study.

Working with low pump ℓ, we found results consistent with the 5.2 µm light being generated mostly in the LG_0^0 mode. In this case, for pump modes with opposite handedness of OAM, Gouy phase matching requires that the 420 nm light is generated with $p > 0$. In some sense the OAM present in the pump beams is converted to the radial index of the 420 nm light. For pump modes with $p > 0$ we have demonstrated that Gouy phase matching allows p-mode "addition". We observe that the blue light is generated in a mode with the radial profile determined by the total p-index of the pump beams.

In a final experiment, we investigated FWM with pump modes in a coherent superposition of LG modes. In this case the intensity profile of the 420 nm light is determined by the coherent interference of different FWM pathways. This interference, and the resulting mode composition of the 420 nm light, can be controlled via the relative phase of the pump mode superposition.

Chapter 7

Cavity-enhanced four-wave mixing

The final set of experiments presented in this thesis demonstrate the effect of adding feedback - in the form of a ring cavity - to the four-wave mixing (FWM) system. Resonant cavities are routinely used to enhance optical generation, whether stimulated emission, as in lasers [34], or wave mixing, as in optical parametric oscillators [14, 208]. The cavity allows the resonant light to pass through the gain medium multiple times, increasing the generated power, but also imposing strict spectral coherence on the process; only light that is in phase with itself after one round trip will constructively interfere.

Cavity-enhanced FWM has been investigated in both hot [209–211] and cold [212] atomic vapours, and previous authors have suggested that a cavity could be used to enhance the conversion efficiency of the blue light FWM process [4,90,92]. As a first demonstration of this, we focused on the low feedback regime and constructed a low-finesse ring cavity which was designed to be singly-resonant with the 420 nm light. The effect of this cavity on the 420 nm output power, linewidth and transverse mode was then investigated. This process also led to further understanding of the single-pass FWM system, for example the frequency tuning characteristics of the generated blue light.

The design of the cavity is discussed in Sec. 7.1, with the rest of the exper-

imental setup described in Sec. 7.2. The principal results of this chapter are presented in Sections 7.3 and 7.4, where we investigate the effect of the cavity for Gaussian pump beams, and show that the cavity both enhances the output power and narrows the linewidth of the generated 420 nm light. These results are published in Ref. [P5]. For this section of work I was joined in the lab by J. W. C. Conway, who helped to gather the experimental results.

The final experimental section, Sec. 7.5, considers the effect of the cavity for Laguerre-Gauss (LG) pump beams. These preliminary results show that the cavity output mode is determined by a combination of the cavity and the phase coherent FWM pumping mechanism. Finally, Sec. 7.6 summarises the results and indicates interesting areas of future research.

7.1 A low-finesse ring cavity

A variety of cavity geometries were considered to provide feedback to the FWM process. Each cavity was designed to be singly-resonant with the blue light, and not with the pump beams. This greatly simplifies both the experiment and the physics, as it means the cavity resonance condition depends only on the frequency of the blue light.

Making use of the available optics, four different cavities were tested before settling on the final design. The simplest was a plane-plane standing wave cavity, with a dichroic mirror that transmits the pump light as the input coupler, and a partially transmitting mirror as the output coupler (Fig. 7.1 (a)). Unfortunately this is not a good choice for our system as the retro-reflected pump beams interfere with the forward going FWM process, resulting in a decrease in conversion efficiency. This problem can be solved by replacing the end mirror with a diffraction grating, such that only the first diffracted order of the 420 nm light is retro-reflected (Fig. 7.1 (b)). In this case the cavity increased the conversion efficiency, but the retro-reflected blue light undergoes significant absorption on the backwards pass through the rubidium cell (since the FWM process is only

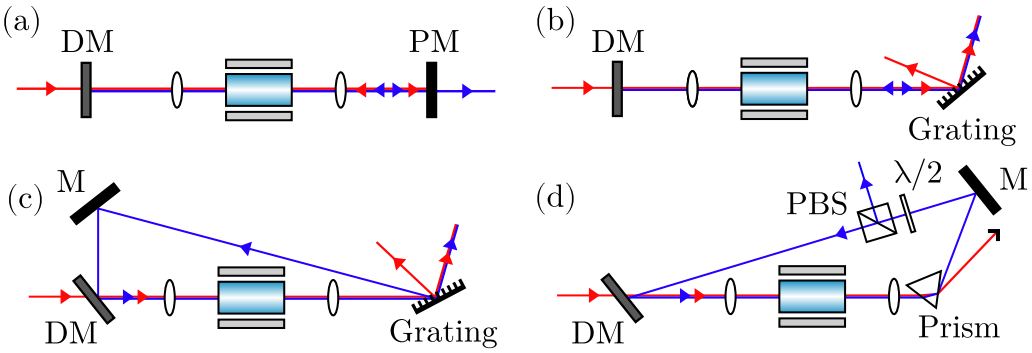

Figure 7.1: Different cavity geometries. (a) Plane-plane, (b) Littrow configuration diffraction grating, (c) ring cavity with diffraction grating, and (d) final ring cavity.

phase matched in the direction of propagation of the pump beams), thus limiting the overall gain.

Since a standing wave cavity proved to be unsuitable, the design was changed to a ring cavity (Fig. 7.1 (c)). In this case the blue light always propagates through the cell in the same direction as the pump beams, experiencing parametric gain on each pass. Although this design worked well for Gaussian beams, the odd number of reflections in a round trip makes it unsuitable for light with a varying transverse phase; on each round trip the beam would interfere with its mirror image.

The final cavity design (Fig. 7.1 (d)) used an equilateral prism, rather than a diffraction grating, to separate the 420 nm light from the pump beams. This reduces the total number of reflections per round trip to two. Both the pump and 420 nm light is horizontally polarised, and light is coupled out of the cavity using a polarising beam splitter (PBS) combined with a half wave plate. This allows the amount of feedback and output coupling to be tuned.

Using linearly polarised light is a comporomise as the FWM process is more efficient for circular polarisation [92]; however, this would be difficult to maintain around a cavity and is not compatible with our output coupling method. A more sophisticated cavity design could use polarisation optics (Fresnel rhombs due to

the wavelength range) on either side of the cell to convert from linear to circular and back again.

7.1.1 Passive cavity response

The cavity length, L, and the round trip power loss, β, are key parameters that determine the effect the cavity has on an incident - or circulating - field. For an input field, E_{in}, the steady state circulating electric field in the cavity, E, can be written as

$$E = E_{\text{in}} + \sqrt{1-\beta}e^{i\psi}E, \quad \psi = \frac{\omega L}{c}, \tag{7.1.1}$$

where ψ is the round trip phase shift of the light. Manipulating Eq. 7.1.1, it follows that the circulating intensity, I, varies with [34, 213]

$$I \propto \frac{(1-\sqrt{1-\beta})^{-2}}{1+\frac{4F^2}{\pi^2}\sin^2(\frac{\omega L}{2c})}, \quad F = \frac{\pi\sqrt[4]{1-\beta}}{(1-\sqrt{1-\beta})}. \tag{7.1.2}$$

The intensity is maximum whenever $\omega = n2\pi c/L$, where n is an integer, in which case the round trip phase shift is a multiple of 2π and the light is resonant with

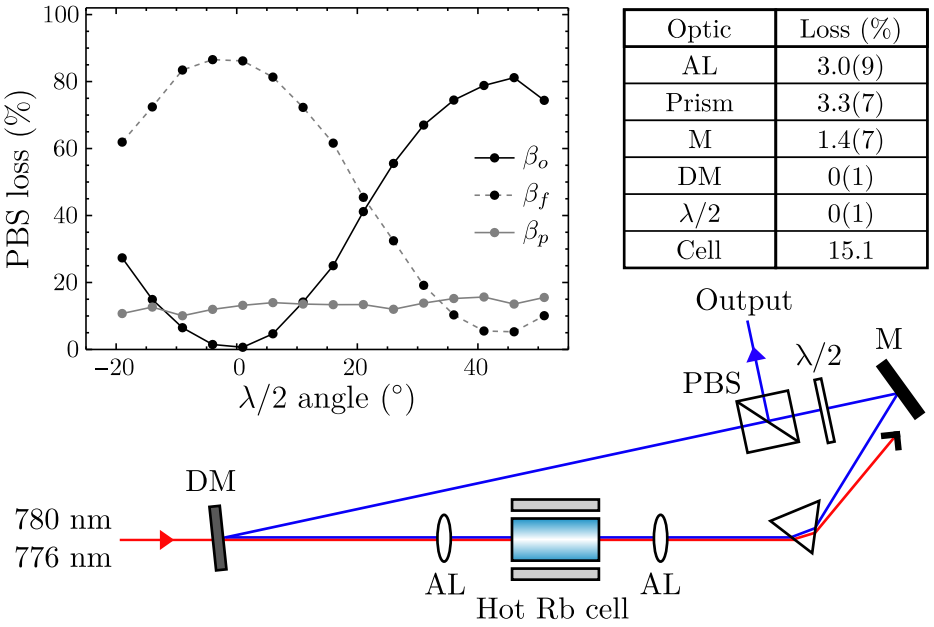

Optic	Loss (%)
AL	3.0(9)
Prism	3.3(7)
M	1.4(7)
DM	0(1)
λ/2	0(1)
Cell	15.1

Figure 7.2: Parasitic 420 nm loss at each optical element, and output coupling, β_o, feedback, β_f and parasitic loss, β_p, at the PBS as the half waveplate is rotated.

the cavity. This results in a series of intensity peaks separated in frequency by the free spectral range, $FSR = c/L$. The width of the peaks is determined by the finesse, F, which is a function of the round trip loss.

The total round trip loss, β, has two contributions: the output coupling, β_o, and the parasitic loss, β_p, such that $\beta = \beta_o + \beta_p$. The output coupling is defined as $\beta_o = P_o/P_i$, where P_i is the incident power at the PBS output coupler and P_o is the power which exits the cavity through the reflection port. The parasitic loss accounts for all other power losses within the cavity.

The loss at each of the optical elements in the cavity was measured using a power meter and is shown in the table in Fig. 7.2. There is a total parasitic loss of 8% due to the optics (not including the PBS), and the transmission loss through the rubidium cell - ignoring absorption - was estimated to be 15.1% due the the four 4% reflections at the uncoated glass surfaces. The other main contributor to the parasitic loss is the PBS. The output coupling, β_o, and transmission at the PBS were measured as a function of waveplate angle (with the cavity incomplete), and are also shown in Fig. 7.2. The PBS parasitic loss was calculated by taking the difference in power between the input beam and the sum of the power in the output ports.

From these measurements the cavity finesse was calculated for different values of the PBS output coupling, β_o, and is shown in Fig. 7.3. Due to the high parasitic losses the cavity is finesse very low, with a maximum finesse of 16 when the output coupling is minimised. As an illustration, the inset in Fig. 7.3 shows the cavity response given by Eq. 7.1.2 for Finesses of 12.8 and 3.5. These are typical of values used later in the experiment and correspond to transmission FWHMs of 14 MHz and 54 MHz, respectively. The separation of the peaks is set by the free spectral range, which was calculated to be 181.8(3) MHz, based on a measured round trip length of 164.95(25) cm.

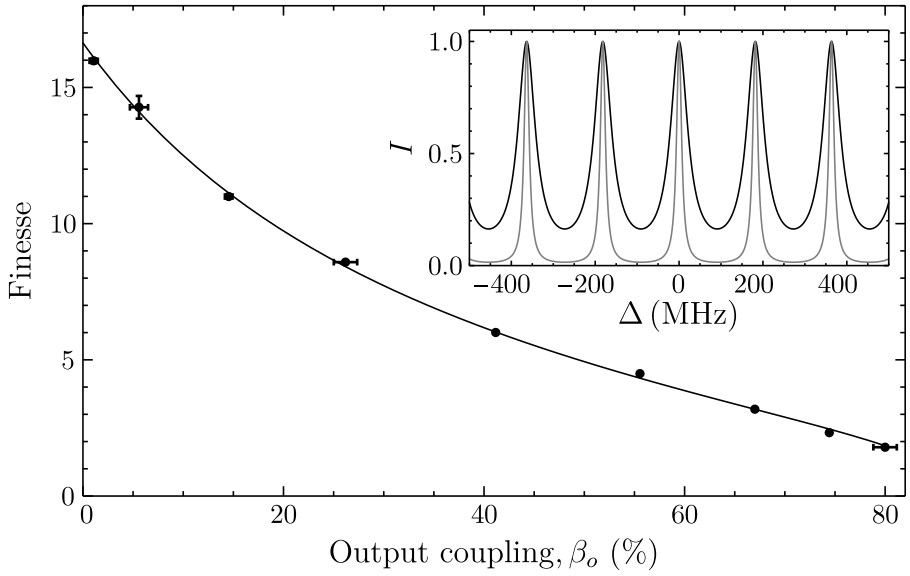

Figure 7.3: The calculated cavity finesse as a function of output coupling, with a fit using the expression for F given in Eq. 7.1.2, allowing for a small linear variation in the parasitic loss. Inset: Normalised passive cavity response for a finesse of 3.5 (black) and 12.8 (grey) and cavity length $L \approx 165\,\text{cm}$, see text.

7.2 Experimental setup

This section describes the rest of the setup required for the cavity-enhanced FWM experiments. The effect of the cavity on three parameters was demonstrated: the 420 nm output power, the linewidth and the transverse mode. The output power was measured simply by using a photodiode at the cavity output, whilst the 420 nm linewidth was measured via a beat note with a reference 420 nm ECDL. The transverse mode was measured using the same Dove prism interferometer as discussed in earlier chapters, but only qualitative rather than quantitative results were obtained.

These experiments were carried out at the start of my PhD using an earlier version of the experiment, which is shown in Fig. 7.4. In contrast to the new setup, the 780 nm and 776 nm beams were overlapped before the optical fibre. This ensures that the two beams copropagate in the same mode through the rest of the setup, but does not allow independent shaping of the two pump wavelengths.

To minimise power loss, the pump beams were overlapped using a diffraction grating close to the Littrow configuration, and the combined beam was then coupled into a single-mode polarisation-maintaining optical fibre to the FWM side of the setup.

The frequency of the 780 nm laser was monitored using saturated absorption

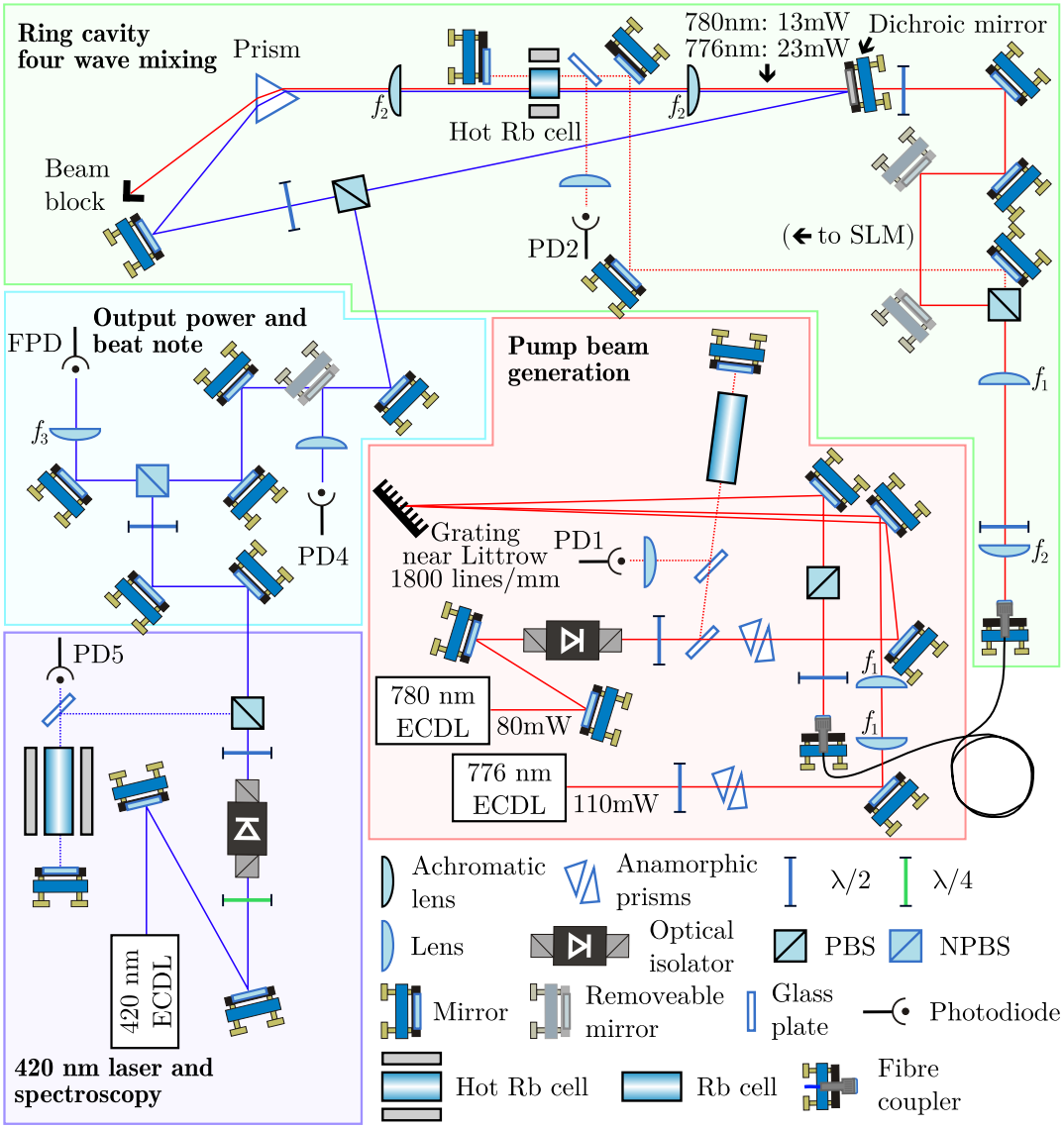

Figure 7.4: Full experimental setup for cavity-enhanced FWM. Dashed lines indicate pick-offs for spectroscopy. Abbreviations: PD: photodiode, FPD: fast photodiode, SLM: Spatial light modulator. Lenses (mm): $f_1 = 50$, $f_2 = 200$, $f_3 = 250$.

spectroscopy before the fibre, as discussed in Sec. 3.2, whilst the 776 nm frequency was monitored using two-photon spectroscopy in the FWM cell itself. Since the pick off for the two-photon spectroscopy was after the fibre, both beams were retroreflected in the cell, leading two-photon spectra with additional single photon absorption features, as shown in Sec. 3.4. Typical powers for the two-photon spectroscopy were 1 mW (780 nm) and 0.8 mW (776 nm), with a $1/e^2$ radius of 0.89 mm. As in previous chapters, the 780 nm detuning is given relative to the ^{85}Rb $5S_{1/2}$ $F = 3 \rightarrow 5P_{3/2}$ $F' = 4$ transition, and the 776 nm detuning is relative to the ^{85}Rb $5P_{3/2}$ $F = 4 \rightarrow 5D_{5/2}$ $F' = 5$ transition.

After the fibre, lenses were used to adjust the pump beam to a $1/e^2$ intensity radius of 0.89 mm. A PBS then ensured that the pump light was linearly polarised, with the transmitted light at the PBS going to the two-photon spectroscopy. At this point, for the LG mode results in Sec. 7.5 the combined pump beam was sent to the spatial light modulator (SLM) for transverse mode shaping by removing the two greyed out mirrors. In the initial experiments, however, only Gaussian pump beams were required and the SLM was bypassed. The final optic before the cavity was a half waveplate to rotate the polarisation to horizontal.

The pump beams then entered the cavity which was formed by a dichroic mirror, prism and a mirror, as discussed in Sec. 7.1. The pump light was focused at the centre of the 25 mm long rubidium cell with a $2f$-imaging system ($f = 200$ mm), to a $1/e^2$ intensity radius of 52 µm. The cell was heated to either 130°C or 90°C, which correspond to ^{85}Rb partial pressures of 0.12 Pa and 0.009 Pa, respectively, or in terms of number density, $2.1 \times 10^{13}\,\mathrm{cm}^{-3}$ and $1.8 \times 10^{12}\,\mathrm{cm}^{-3}$. After the cell, the pump light was blocked whilst the generated 420 nm light propagated around the ring cavity. Measurements of the blue light confirmed that it was horizontally polarised for horizontally polarised pump beams. For the results in Sec. 7.3, the 420 nm output power was measured directly at the cavity output using PD4.

420 nm linewidth measurement

The linewidth of the FWM 420 nm light was measured via a beat note with a reference 420 nm laser. The reference laser was a Newport Vantage tunable diode laser which provided 20 mW of 420 nm light with an RMS linewidth of 1.73 MHz over 0.1 s. This linewidth was measured by setting the laser detuning to the side of a Doppler broadened absorption feature and monitoring the noise on the transmission signal.

For the beat note measurement, the FWM 420 nm light was overlapped with light from the reference laser on a non-polarising beam splitter. A half waveplate in the reference laser's optical path was used to match the polarisation of the two fields before the combined beam was focused on a fast photodiode (Thorlabs DET025A/M). The resulting radio-frequency signal was amplified by 10 dB and then recorded using a spectrum analyser. The reference laser was deliberately detuned by about 200 MHz from the FWM light so that the resulting beat note was not lost in the DC signal from the fast photodiode.

To obtain the absolute frequency of the generated 420 nm light, the detuning of the reference laser was monitored via saturated absorption spectroscopy on the ^{85}Rb $5S_{1/2} \rightarrow 6P_{3/2}$ transition. For a combination of reasons, the absorption coefficient of this transition is significantly less than that of the 780 nm transition. Firstly, the resonant absorption coefficient varies with λ^2, this immediately reduces the absorption by a factor of roughly 1/4. Additionally, the linewidth of the 420 nm transition is ten times narrower than the 780 nm transition (0.6 MHz compared to 6 MHz). This, combined with the fact the Doppler width is broader due to its $1/\lambda$ dependence, means that the relative fraction of the atoms that the light interacts with for a given detuning is reduced by a factor of 20. This overall 80 times reduction in the absorption is compensated for by using a heated cell for the spectroscopy. By raising the temperature of the cell to 90°C the rubidium density is increased by a factor of roughly 400, more than compensating for the reduced absorption.

Fig. 7.5 (a) shows the Doppler absorption spectrum of the 420 nm transition

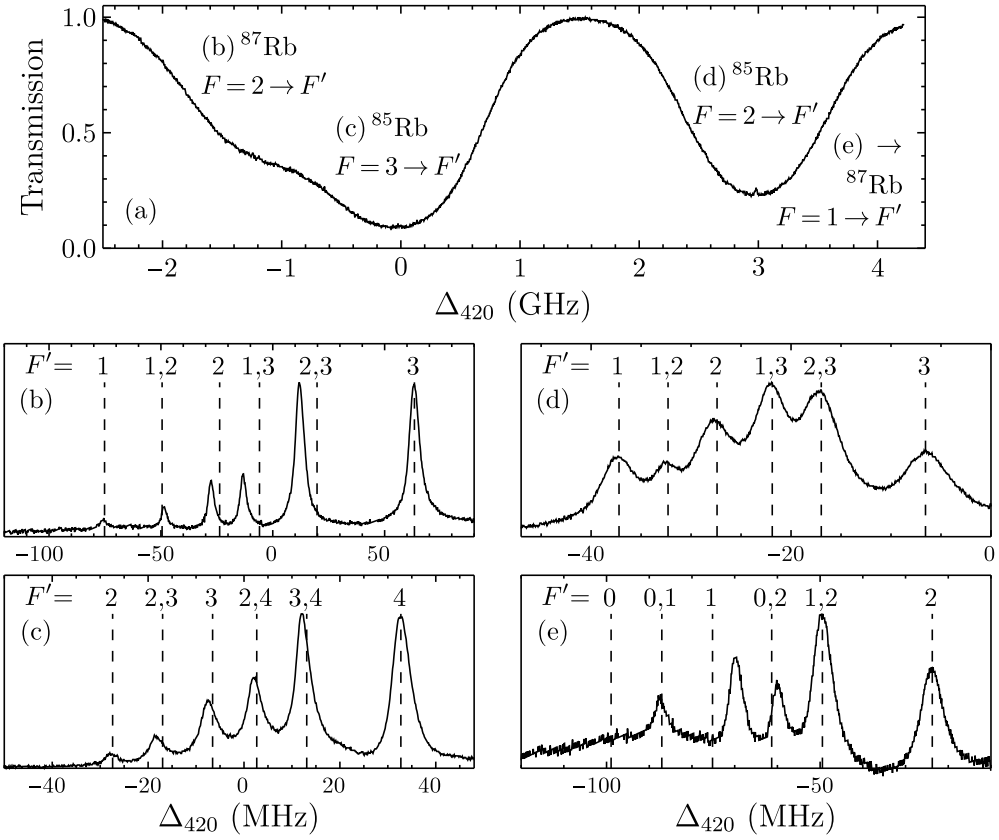

Figure 7.5: (a) 420 nm Doppler spectroscopy of the $5S_{1/2} \rightarrow 6P_{3/2}$ transitions. (b)-(e) Saturated absorption spectroscopy at each Doppler broadened transition, with a fitted Gaussian background subtracted and zero tuning set to the energy centre-of-mass of each transition. Dashed lines indicate expected detuning of features calculated using values from [120], see appendix A.

in a 90°C 75 mm long cell. Saturated absorption traces are included in (b)-(e) showing the hyperfine and crossover features at each group of Doppler broadened transitions. Although the separation of the feature matches the previously measured prediction well in (c) and (d) there is significant discrepancy in (b) and (e).

The FWM 420 nm light is generated close to the ^{85}Rb $5S_{1/2}$ $F = 3 \rightarrow 6P_{3/2}$ transition. To measure the detuning, immediately before the beat note measurement the reference laser's frequency was scanned as in Fig. 7.5 (c). From this the detuning as a function of piezo voltage was determined. The scan was then

stopped to perform the beat note measurement, and the piezo voltage recorded. This allowed the reference laser detuning, and therefore the FWM 420 nm detuning, to be calculated after the experiment.

7.3 Cavity-enhanced output power

We now move on to the first of the principal results of this chapter: the effect of the low-finesse ring cavity on the FWM 420 nm output power. For the initial measurement, the experimental conditions were set to give peak single-pass FWM conversion efficiency: a cell temperature of 130°C and maximum available pump powers of 13 mW (780 nm) and 23 mW (776 nm). These powers were measured directly before the cell, as indicated in Fig. 7.4. Whilst scanning the 776 nm laser, the detuning of the 780 nm laser was tuned until the 420 nm output power was maximised, resulting in a peak output of 340 µW directly after the cell. The 780 nm laser was then left at this detuning (+1.8 GHz) for the rest of the experiment.

To maximise the effect of the cavity, the intracavity waveplate angle was set to give only a small amount of output coupling. The feedback and output coupling at the PBS were measured to be 79% and 5%, respectively. These results combined with the other cavity losses (Fig. 7.2) give a round trip loss of 39%, which corresponds to a cavity finesse of 12.8.

Fig. 7.6 shows the variation in cavity output power as the 776 nm laser was scanned across the $5S_{1/2} \rightarrow 5D_{5/2}$ two-photon resonance. This was carried out first for single-pass FWM, with the cavity blocked after the PBS (red curve) and then with the cavity unblocked (blue curve).

For single-pass FWM there are two Doppler broadened peaks where blue light is generated, near $\Delta_{776} = -1.8$ GHz and $\Delta_{776} = 1.2$ GHz. These correspond to two photon resonance with the $5S_{1/2}$ $F = 3 \rightarrow 5D_{5/2}$ and $5S_{1/2}$ $F = 2 \rightarrow 5D_{5/2}$ transitions respectively. With the cavity unblocked, a large increase in output power is observed when the blue light, whose frequency scans with the 776 nm

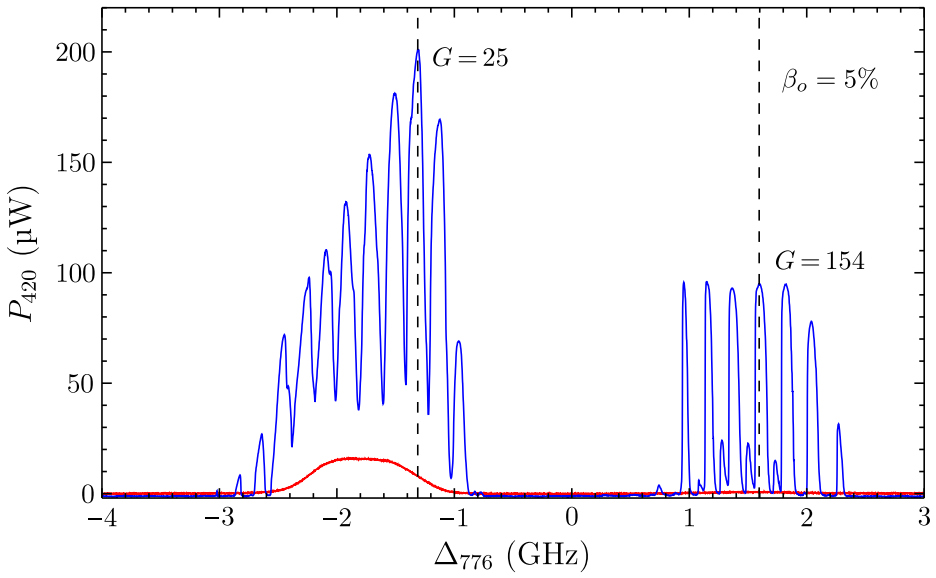

Figure 7.6: Cavity output power as a function of 776 nm detuning, for single-pass (red) and cavity-enhanced (blue) FWM. $\beta_o = 5\%$, $\Delta_{780} = 1.8$ GHz. Dashed lines indicate detunings for which the cavity gain, $G = P_C/P_{SP}$, was calculated.

detuning, is resonant with the cavity.

The cavity gain, defined as

$$G = P_{\mathrm{C}}/P_{\mathrm{SP}}, \tag{7.3.3}$$

where P_{SP} is the single-pass output power and P_{C} is the cavity-enhanced output power, is marked for the largest cavity resonance in each group. At the $F = 3$ two-photon resonance, the output power increases by 25 times compared to a single-pass, whilst at the $F = 2$ resonance there is more than 150 times the output power, despite the high round trip loss of the cavity.

The effect of the cavity can be modeled qualitatively by considering the response of the combined cavity and rubidium atom system to an input 420 nm field. For an input field, E_{in}, and a rubidium cell of length, l, the steady state circulating electric field in the cavity, E, can be written as

$$E = E_{\mathrm{in}} + \sqrt{1-\beta}e^{i\psi}e^{ik\chi l/2}E, \tag{7.3.4}$$

where χ is the electric susceptibility of the atoms at the frequency of the 420 nm field and in the presence of the pump beams. The susceptibility can be separated

into its real and imaginary parts, $\chi = \chi' + i\chi''$, so that

$$E = E_{\text{in}} + \sqrt{1-\beta} g e^{i\psi_t} E, \quad g = e^{-\chi'' kl/2}, \quad \psi_t = \omega L/c + \chi' l/2. \tag{7.3.5}$$

When the imaginary part of the susceptibility is negative the 420 nm light experiences parametric gain each time it passes through the cell. The atoms can also add a phase shift to the light, which is described by the real part of the susceptibility, χ', and can lead to frequency pulling effects [210].

In analogy to the analysis in Sec. 7.1, the cavity response is given by

$$I \propto \frac{(1 - g\sqrt{1-\beta}\,)^{-2}}{1 + \frac{4F^2}{\pi^2}\sin^2(\frac{\psi_t}{2})}, \quad F = \frac{\pi \sqrt[4]{g^2(1-\beta)}}{(1 - g\sqrt{1-\beta})}. \tag{7.3.6}$$

The FWM gain reduces the round trip loss and effectively increases the finesse of the cavity. This has two effects. Firstly, it increases the circulating power on resonance, leading to an increase in the maximum output power. Secondly, it narrows the cavity resonances. This imposes strict spectral coherence on the circulating light, resulting in a narrow linewidth.

In reality, the situation is more complicated than this simple model. The susceptibility χ depends on the detuning and coupled amplitudes of all four fields involved in the FWM process, which are in turn affected by the presence of the cavity. A full theoretical model of the system was beyond the scope of this initial demonstration. Instead, experiments were carried out in an attempt to understand three features of the cavity-enhanced trace in Fig. 7.6:

- The free spectral range of the cavity resonances.
- The on-resonance gain and the effect of varying the output coupling.
- The resonance width and broadening mechanisms that contribute to it.

7.3.1 Free spectral range

The mean free spectral range of the cavity, based on the resonance spacing in all of the data in this chapter, was measured to be 198(2) MHz. However, the optical

path length of the cavity is 164.95(25) cm, which equates to a free spectral range, $FSR = c/L$, of 181.8(3) MHz. Since we scan the 776 nm pump laser, rather than the 420 nm frequency directly, we can only expect the two values for the FSR to agree if the 420 nm frequency directly follows that of the pump lasers.

Due to energy conservation in FWM, the two generated fields must have angular frequencies that satisfy

$$\omega_{778} + \omega_{776} = \omega_{\mathrm{IR}} + \omega_{\mathrm{B}}. \tag{7.3.7}$$

As a result, if the frequency of one of the pump lasers is changed, the frequency of one (or both) of the generated fields must change to compensate. In general, one may expect the frequency of both of the generated fields to change, with the relative shift of each determined by the magnitude of the Doppler shift.

The apparent shift in frequency of an atomic transition for an atom traveling with velocity v is given by [1]

$$\delta = kv = \frac{2\pi}{\lambda}v. \tag{7.3.8}$$

The magnitude of the shift increases for shorter wavelengths as the atom crosses more phase fronts per second for a given velocity. In the FWM process, the total Doppler shift of the two-photon pump resonance is

$$\delta_{\mathrm{P}} = \delta_{780} + \delta_{776} = \frac{2\pi v}{\lambda_{780}} + \frac{2\pi v}{\lambda_{776}}. \tag{7.3.9}$$

At a particular total pump detuning, Δ_{P}, only atoms in the velocity class that is two-photon resonant with the pumps ($\Delta_{\mathrm{P}} = \delta_{\mathrm{P}}$) will interact with the light. Rearranging Eq. 7.3.9, this velocity class is given by

$$v = \frac{\Delta_{\mathrm{P}}}{2\pi(1/\lambda_{780} + 1/\lambda_{776})}. \tag{7.3.10}$$

The Doppler shift of the 420 nm transition for this velocity class can be found by substituting Eq. 7.3.10 into equation 7.3.8, and so we can expect the blue light to be generated with a detuning Δ_{B}

$$\Delta_{\mathrm{B}} = \frac{1/\lambda_{420}}{(1/\lambda_{780} + 1/\lambda_{776})}\Delta_{\mathrm{P}} \approx 0.926\Delta_{\mathrm{P}} \tag{7.3.11}$$

Similarly, for the 5.2 µm field,

$$\Delta_{\mathrm{IR}} = \frac{1/\lambda_{5230}}{(1/\lambda_{780} + 1/\lambda_{776})}\Delta_{\mathrm{P}} \approx 0.074\Delta_{\mathrm{P}}. \tag{7.3.12}$$

However, previous work with this FWM system has shown that, in practice, the frequency tuning of the 420 nm light depends on the single photon detuning of the pump lasers. For far detuned pump fields (Δ = 1THz), the frequency of the blue field tunes according to equation 7.3.11 [214], but for near resonant pump beams it directly follows that of the pump fields [115]. This indicates that in the latter case the 5.2 µm frequency does not change.

In order to determine the frequency tuning of the 420 nm light in our experiment, we coupled the three available fields (780 nm, 776 nm and 420 nm) into an etalon and measured the shift in the 420 nm frequency as each of the pump lasers' frequency was changed. The results are shown in Fig. 7.7. A global fit was performed to all of the data to account for slight frequency drifts of the unscanned laser, with a fit function of the form

$$\Delta_{\mathrm{B}} = m_{780}\Delta_{780} + m_{776}\Delta_{776} + c. \tag{7.3.13}$$

The absolute frequency was chosen arbitrarily so that $c = 0$, and the resulting

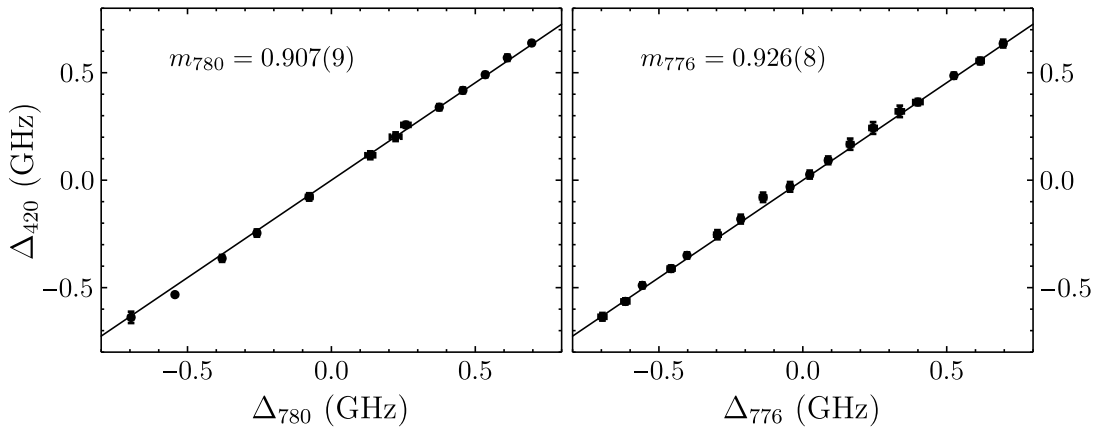

Figure 7.7: Frequency shift of the generated blue light as a function of 780 nm and 776 nm detuning, with zero detuning chosen arbitrarily. The fitted lines have gradients determined by a global fit to the data of the form $\Delta_{\mathrm{B}} = m_{780}\Delta_{780} + m_{776}\Delta_{776} + c$.

fitted values for m_{780} and m_{776} are shown in the figure. Slightly different values were found for the two gradients but, given the standard error in each, the measurement indicates that the 420 nm light tunes identically with 780 nm and 776 nm frequency. Taking the average of the two, we get

$$\Delta_B = 0.916(6)\Delta_P, \tag{7.3.14}$$

Based on this, the the separation of the cavity resonances in 776 nm frequency (198(2) MHz) equates to a 420 nm frequency change of 181(2) MHz, which is in excellent agreement with the predicted FSR from the cavity length (181.8(3) MHz). Equation 7.3.14 is also in good agreement with the tuning behavior expected based on the relative Doppler shift of the fields (Eq. 7.3.11).

7.3.2 Output coupling optimisation

The cavity-enhanced output power in Fig. 7.6 was measured with a relatively low output coupling. Although strong cavity resonances are observed, the maximum cavity output power on resonance (200 µW) is still less than the maximum single pass power that can be generated without the cavity (340 µW). There is an optimal output coupling for a laser [34], or indeed an optical parametric oscillator [215, 216], which produces the maximum output power. If there is too much output coupling then there is insufficient feedback to make full use of the available pump power. If there is too little then although the intra-cavity power can become very large, only a small fraction of the power is coupled out of the cavity.

To find this optimal output coupling for our system the cavity output power was measured for a range of waveplate angles. Fig. 7.8 shows the resulting variation in output power, as well as the peak gain (as defined in Eq. 7.3.3), as a function of output coupling. As expected, although the cavity gain decreases with increasing output coupling, the output power initially increases before reaching a peak and decreasing again. The maximum output power was achieved for large output couplings of around 60%. This is due to the high parasitic losses in the cavity.

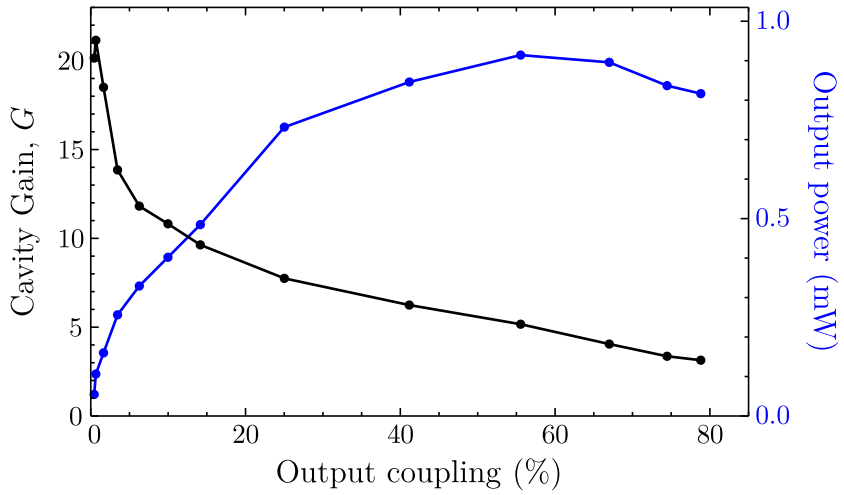

Figure 7.8: Measurement of the cavity gain ($G = P_C/P_{SP}$) and output power (P_C) as a function of output coupling.

Fig. 7.9 shows the cavity output power as a function of 776 nm detuning after the output coupling was optimised. A peak output power of 940 µW was

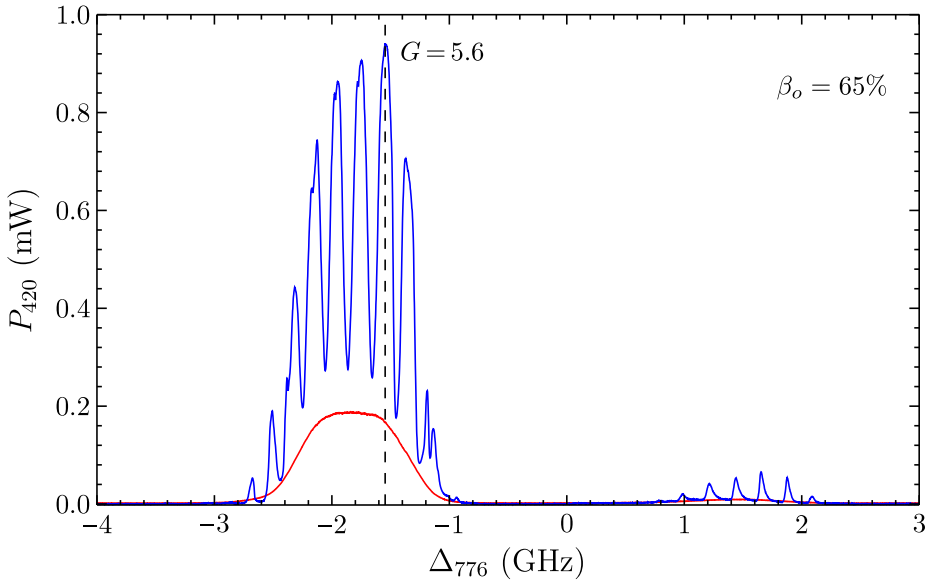

Figure 7.9: Cavity output power as a function of 776 nm detuning with optimised output coupling, $\beta_o = 65\%$. Single-pass: red, cavity-enhanced: blue. $\Delta_{780} = 1.8$ GHz. Dashed line indicates the detuning for which the cavity gain, $G = P_C/P_{SP}$, was calculated.

achieved, which is nearly three times the maximum single-pass power in the absence of a cavity. With an improved cavity design to reduce parasitic losses there is substantial scope for increasing this output power further.

7.3.3 Broadening mechanisms

Finally, we consider the width of the cavity resonances. As a first approximation, the resonance width is expected to be dependent on three factors: the passive cavity resonance width, the FWM gain, and the linewidth of the single-pass 420 nm light. To explain this, consider again the response of the cavity to an incident 420 nm field. Without the rubidium atoms the width of the cavity resonances is set by the response of the passive cavity, which depends on the output coupling. When the atoms are included, the FWM gain reduces the round trip loss and is expected to substantially narrow the cavity resonances. Finally, as we do not scan the 420 nm frequency directly, but rather the 776 nm frequency, we expect the overall resonance width to be the convolution of the narrowed cavity resonances and the linewidth of the single-pass blue light.

To understand the interplay between the various broadening mechanisms, traces were recorded of the cavity output power under different experimental conditions, varying:

- The output coupling, β_o
- The cell temperature, T
- The pump power, P_{780} and P_{776}

The results are shown in Fig. 7.10, and it is clear that all three parameters affect the resonance width. The plots in the left and right hand columns are for 65% and 5% output coupling, respectively. The middle row, (c) and (d), are the same data as figures 7.9 and 7.6, and are included here for comparison. These results were taken under optimal experimental conditions for single-pass FWM. In contrast, the top row ((a) and (b)) were taken with reduced pump power, and the bottom

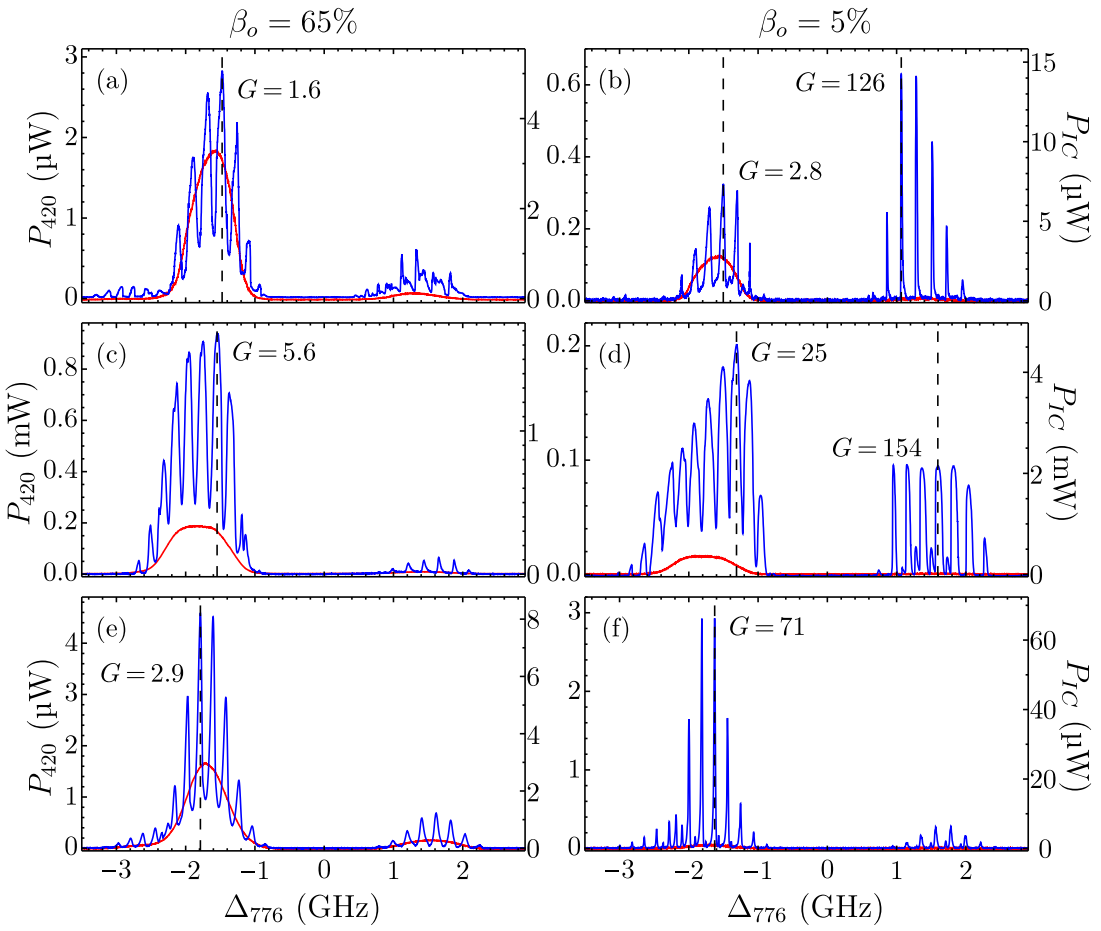

Figure 7.10: Cavity output power (left hand axis), and intracavity power (right hand axis), under different experimental conditions. Left column: $\beta_o = 65\%$, Right column: $\beta_o = 5\%$. (a), (b): Reduced pump power, $P_{780} = 1.6\,\text{mW}$, $P_{780} = 2.7\,\text{mW}$, $T = 130°\text{C}$. (c), (d): $P_{780} = 13\,\text{mW}$, $P_{780} = 23\,\text{mW}$, $T = 130°\text{C}$, note the 420 nm power is in mW for these plots. (e), (f): Reduced cell temperature, $P_{780} = 13\,\text{mW}$, $P_{780} = 23\,\text{mW}$, $T = 90°\text{C}$. The 780 nm detuning, chosen to maximise single-pass conversion efficiency, was (a,b) 1.7 GHz; (c,d) 1.8 GHz; (e,f) 1.6 GHz. Dashed lines indicate detunings for which the cavity gain, $G = P_C/P_{SP}$, was calculated.

row ((e) and (f)) with reduced cell temperature. The right hand y-axes show the 420 nm power within the rubidium cell for each set of experimental conditions - i.e. the intracavity power. These values were calculated based on the output

coupling and cavity losses between the cell and the PBS.

Passive cavity resonances

The two output couplings used in Fig. 7.10, 65% and 5%, correspond to a passive cavity finesse of 3.5 and 12.8, respectively. Accounting for the frequency tuning of the 420 nm light, these correspond to a passive cavity resonance FWHM in 776 nm frequency of 58.8 MHz and 15.5 MHz, respectively.

Single-pass 420 nm linewidth

The combined linewidth of the generated 5.2 µm and 420 nm two-photon field is determined, due to energy conservation, by the combined linewidth of the pump fields. However, the linewidth of the 420 nm light alone is less well constrained. Any pair of 5.2 µm and 420 nm photons that satisfy energy conservation and phase matching can be generated in the FWM process, but only those that experience a large third order nonlinearity will be generated efficiently. A full optical Bloch model would be required to predict the frequency width over which this occurs, with it possibly dependent on the linewidth of each transition and the power and detuning of the four fields.

As a very rough first approximation we assume that the single-pass 420 nm linewidth is related to the power broadened width of the $5S_{1/2} \rightarrow 6P_{3/2}$ transition, which is given by

$$\Gamma_P = \Gamma\sqrt{1 + \frac{I}{I_{sat}}}, \tag{7.3.15}$$

where Γ is the natural linewidth, which is 0.58 MHz, I_{sat} is the saturation intensity of the transition (see Appendix A) and I is the intensity of the light. The $1/e^2$ intensity radius of the blue light was measured to be 0.58 mm at the cell exit, corresponding to a waist of 46 µm in the cell. Using this waist and the peak intracavity power, the power broadening was estimated for each dataset in Fig. 7.10 (see Fig. 7.11 later).

We also considered the possibility of collision broadening of the linewidth. The only transition which is significantly collision broadened for our rubidium

density is the 5.2 µm transition, which is broadened to 19 MHz for the 130°C cell (calculated following Refs. [217, 218]). This may have an indirect effect on the 420 nm linewidth.

Overall resonance width

The mean FWHM of the resonances in each data set in Fig. 7.10 is shown in Fig. 7.11. In each case only the group of peaks which produces the peak output power was included (i.e. either at the $F = 2$ or $F = 3$ two-photon resonance). For comparison, the predicted widths due to the passive cavity bandwidth, Γ_{cav} (red), the single-pass linewidth, Γ_{sp} (grey), and the combined linewidth, $\Gamma_{\mathrm{cav}} + \Gamma_{\mathrm{sp}}$ (blue), for each set of experimental conditions are also shown. The single-pass linewidth was estimated based on the power broadened width of the 420 nm transition.

Where the round trip loss is high, and the FWM conversion efficiency is low, we expect the resonance width to be roughly equal to the passive cavity

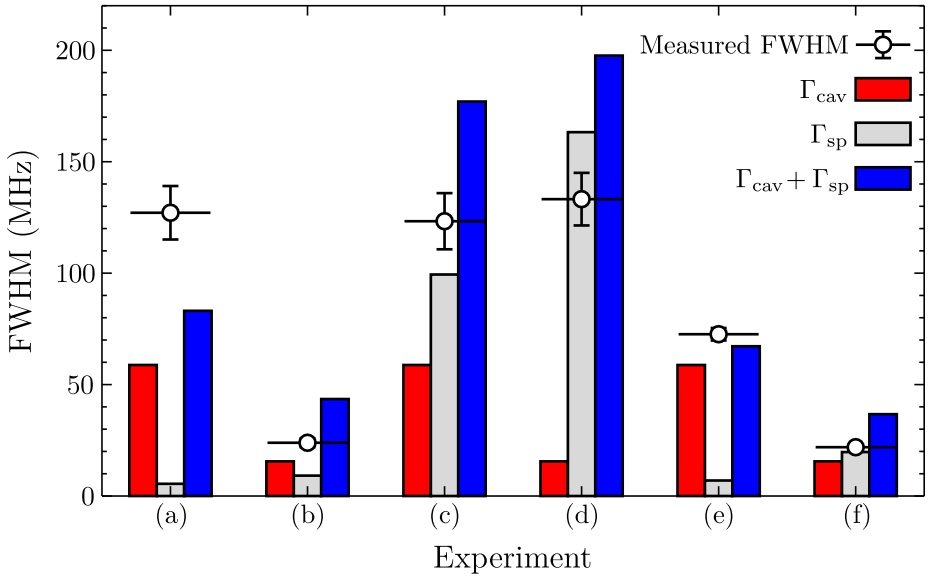

Figure 7.11: Mean resonance FWHM of each dataset in Fig. 7.10, with predicted width based on the passive cavity resonance width, Γ_{cav}, the estimated single-pass linewidth, Γ_{sp}, and the combined linewidth, $\Gamma_{\mathrm{cav}} + \Gamma_{\mathrm{sp}}$.

resonance width plus the single-pass linewidth. This is the case in datasets (a) and (e), where a high output coupling is combined with reduced FWM efficiency, due to reduced pump power and reduced cell temperature, respectively. In all other datasets the mean FWHM is closer to the estimated single-pass linewidth, Γ_{sp}. In these cases the gain of the FWM process significantly narrows the cavity resonances, and the largest contribution to the resonance width is the single-pass linewidth.

This qualitative model broadly describes the cavity-enhanced FWM spectra, but there are clearly also other factors involved. For example the positive detuning resonances in Fig. 7.10 (d) appear to saturate to a particular value, whilst other resonances, as in Fig. 7.10 (c), appear to consist of more than one peak. The peak substructure is assumed to be due to the hyperfine structure of the atomic levels. There is also significant asymmetry to some of the resonances, e.g. Fig. 7.10 (b), which indicates some kind of bistability.

For other experimental parameters we have also observed splitting of the cavity resonances. The result in Fig. 7.12 shows a spectra taken under similar condi-

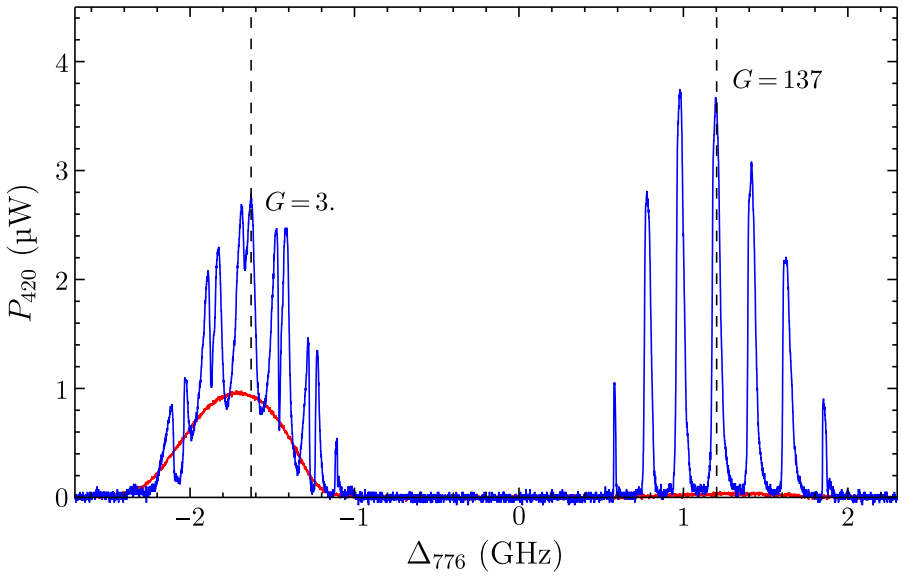

Figure 7.12: Cavity output power for an output coupling of 3%, corresponding to a finesse of 16.4. $P_{780} = 3.2\,\mathrm{mW}$, $P_{776} = 4.0\,\mathrm{mW}$, $\Delta_{780} = +1.8\,\mathrm{GHz}$, $T = 130°\mathrm{C}$.

tions as Fig. 7.10 (a) but for slightly higher pump power and slightly lower output coupling. Results presented later in the chapter (Sec. 7.5) indicate that these are not due to cavity transverse modes. They may be related to polarisation, or possibly the dispersion of the atoms.

7.4 Linewidth

The second section of experimental work in this chapter discusses the effect of the cavity on the linewidth of the 420 nm light. As discussed in Sec. 7.2, the linewidth was measured via a beat note measurement with a reference 420 nm ECDL.

We note that none of the lasers used in these measurements were locked. As a result, the frequency of both the FWM blue light (which is determined by the pump detunings) and the reference 420 nm light were subject to drifts. Care was taken to minimise the effect of this in the experiment, but absolute frequency scales carry an error of ±25 MHz unless otherwise stated.

7.4.1 Single-pass beat note

Before considering the cavity-enhanced case, initial measurements focused on the spectral characteristics of the 420 nm light generated via single-pass FWM. Previous work has reported relatively narrow linewidths, Refs. [4] and [219] give values of ≤3 MHz and <1.3 MHz, respectively. However, these results were for relatively low 420 nm power (≤15 µW), and for relatively low cell temperatures (≤100°C). As discussed in the previous section, a larger single-pass linewidth is expected in our system due to power broadening.

The beat note measured for single-pass FWM is shown in Fig. 7.13. The 780 nm and 776 nm detunings of +1.8 GHz and −1.8 GHz, respectively, were chosen to optimise the 420 nm power, and the maximum available pump powers of 13 mW (780 nm) and 23 mW (776 nm) were used. As with the output power results, the results were taken for two cell temperatures: 90°C and 130°C.

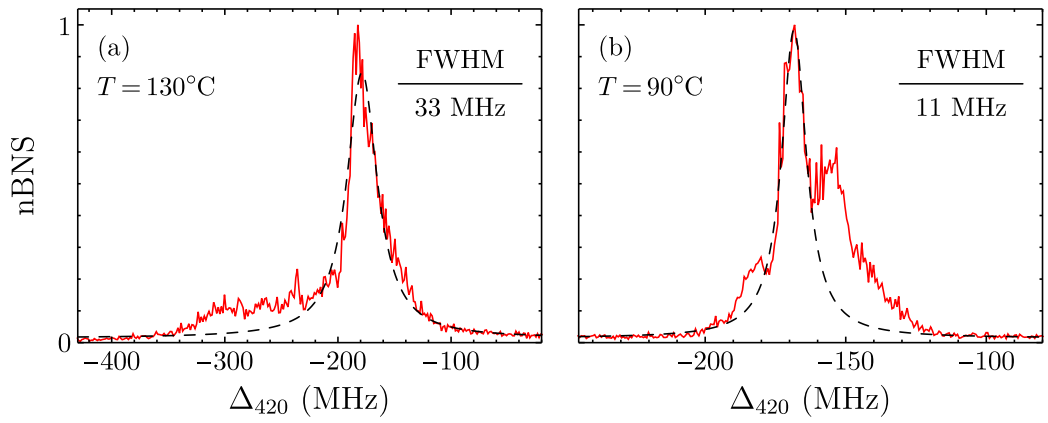

Figure 7.13: Normalised beat note signal (nBNS) for single-pass FWM with a cell temperature of (a) 130°C, and (b) 90°C. $\Delta_{780} = +1.8\,\text{GHz}$, $\Delta_{776} = -1.8\,\text{GHz}$. Detuning given relative to the ^{85}Rb $5S_{1/2}\,F = 3 \rightarrow 6P_{3/2}\,F' = 4$ transition.

If the 420 nm emission was generated from a single atomic transition we would expect a single Lorentzian peak in the beat note signal. This is clearly not the case for either of the results in Fig. 7.13, as both have many sub-features. The broadening of the individual peaks makes their separation difficult to determine, but the substructure in the 90°C result is probably due to the hyperfine structure of the $6P_{3/2}$ state (similar substructure was observed in [90]).

Despite this, we can establish the linewidth of the 420 nm light due to a single transition by fitting a Lorentzian curve to one of the subpeaks in each result, as shown by the dashed lines in Fig. 7.13. From this we obtain FWHM linewidths of 33 MHz at 130°C and 11 MHz at 90°C. These are broadly consistent with power broadening of the 420 nm transition, which we estimate to be 41 MHz (130°C) and 4 MHz (90°C) based on a 420 nm waist of 46 µm and peak single-pass powers given in Fig. 7.10.

The beat note measurement also allowed the detuning of the FWM 420 nm light relative to the $5S_{1/2}\,F = 3 \rightarrow 6P_{3/2}\,F' = 4$ transition to be measured. Previous work, again at lower 420 nm power, had shown that the 420 nm emission was generated centered on this resonance (±5 MHz) [115], but we find the maximum 420 nm power is generated slightly red-detuned from the transition in our

experiment. This is possibly due to ac Stark shifts of the atomic levels.

420 nm tuning range

In Sec. 7.3.1, it was shown that the frequency of the 420 nm light can be tuned by changing either of the pump laser frequencies. The beat note measurement gives confirmation of the range of this tuning relative to the 420 nm transition, with the recorded beat note as a function of 776 nm detuning shown in Fig. 7.14. Importantly, the 420 nm light can be tuned continuously across the 420 nm transition, which makes it suitable for applications such as second stage laser cooling of rubidium [220,221]. As the 776 nm laser is tuned, the structure of the beat note feature changes, which further supports the hypothesis that the substructure is due to hyperfine structure of the atomic states.

The frequency range over which the 420 nm light was generated with more

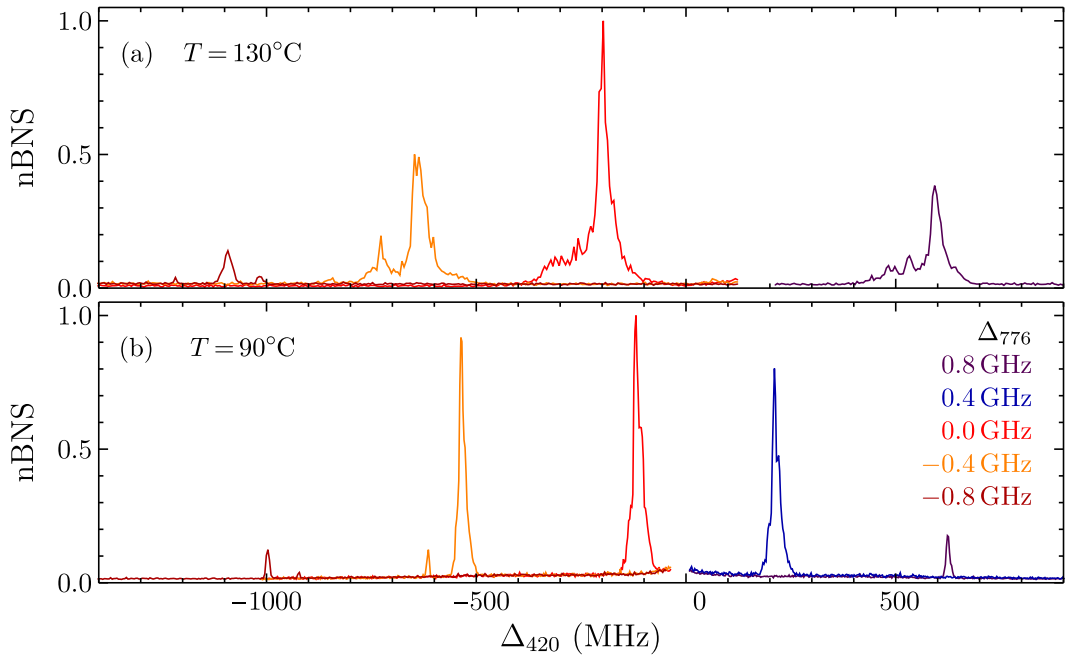

Figure 7.14: Beat note as a function of 776 nm detuning. The x-axis is again the detuning of the 420 nm light from the $5S_{1/2}$ $F = 3 \rightarrow 6P_{3/2}$ $F' = 4$ transition. The 776 nm detuning is given as the frequency shift from the optimal FWM detuning, which was 1.8 GHz.

Cell temperature (°C)	Optimum detuning (MHz)	Tuning FWHM (MHz)	
		780nm	776nm
90°C	-119(12)	544(9)	472(5)
130°C	-197(8)	243(2)	652(9)

Table 7.1: Measured 420 nm FWHM tuning range for single-pass FWM.

the half of the peak power, tuning either the 780 nm or 776 nm laser, is shown in table 7.1, along with the absolute detuning at which peak 420 nm power was generated. In each case the laser not tuned was left at the detuning for maximum FWM conversion efficiency. For a cell temperature of 90°C we observe similar tuning ranges when tuning either the 780 nm or 776 nm laser. The tuning range is comparable to the Doppler broadened FWHM of the near-infrared transitions, which is around 570 MHz at 90°C, and increases slightly to 600 MHz at 130°C [1]. When the cell is heated to 130°C, there is a substantial decrease in the 780 nm tuning range. This can be attributed to Kerr lensing of the 780 nm beam, which depends strongly on the 780 nm detuning and interferes with the FWM process.

7.4.2 Cavity linewidth narrowing

This section presents the second main result of this chapter: the first demonstration of the use of a cavity to narrow the linewidth of 420 nm light generated via FWM in rubidium vapour. For the measurement, the experimental parameters were chosen to be the same as for dataset (c) in Fig. 7.10 as these conditions produced the maximum cavity output power. The cavity output coupling was 65%, which corresponds to a passive cavity resonance width of 51 MHz. The laser powers and detunings were: $P_{780} = 13\,\mathrm{mW}$, $P_{776} = 23\,\mathrm{mW}$, $\Delta_{780} = 1.8\,\mathrm{GHz}$ and $\Delta_{776} = -1.8\,\mathrm{GHz}$, and the beat note was measured for cell temperatures of 130°C and 90°C. The results are shown in Fig. 7.15, with the single-pass results from Fig. 7.13 in red and the cavity-enhanced traces in blue.

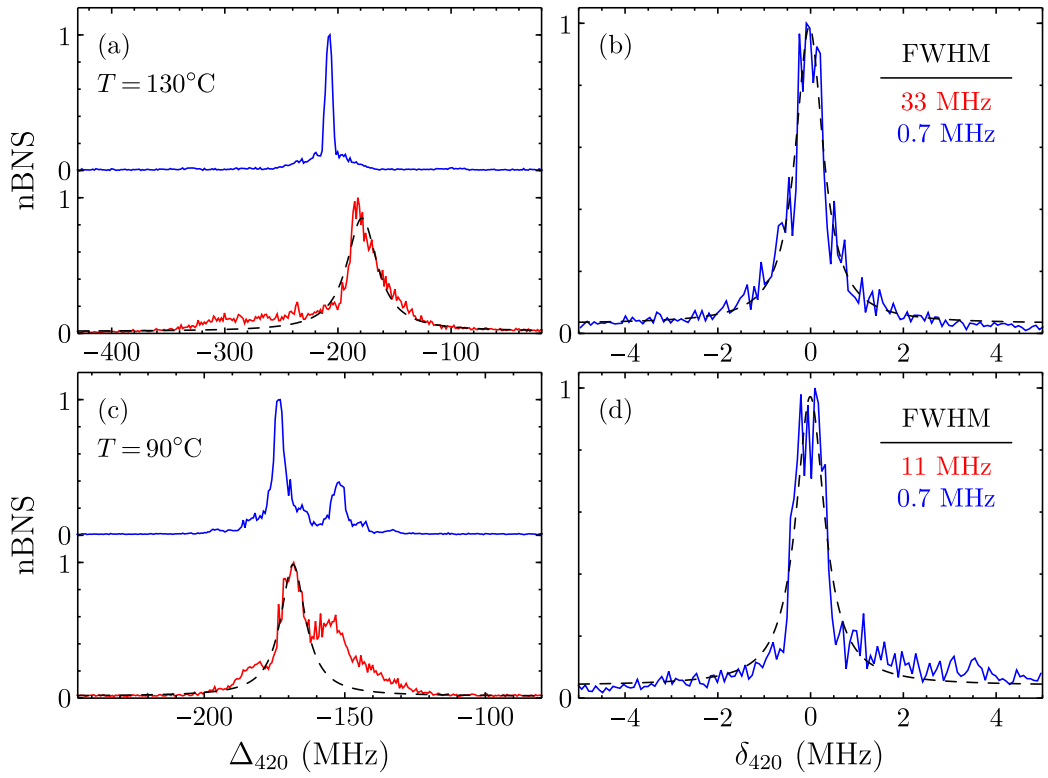

Figure 7.15: Normalised beat note signal (nBNS) for single-pass (red) and cavity-enhanced (blue) FWM with a cell temperature of (a,b) 130°C and (c,d) 90°C. (b) and (d) show a second cavity-enhanced measurement taken over a narrower frequency range (so that the measured linewidth is not limited by the resolution of the spectrum analyser).

Two cavity-enhanced traces are shown for each cell temperature. The first, shown offset vertically from the single-pass traces in Fig. 7.15 (a) and (c), were taken on the same measurement scale as the single-pass traces. These results show that the cavity significantly narrows the 420 nm linewidth, but the minimum linewidth is limited by the resolution of the spectrum analyser.

For the 130°C cell, the cavity-enhanced 420 nm light consists of a single cavity mode, as is expected since the single-pass linewidth (33 MHz) is less than the cavity free spectral range (183 MHz). With the 90°C cell, we observe two peaks in the 420 nm spectrum, which since the peak separation is less than the free spectral range, is likely due to a second transverse cavity mode being excited.

Measurements of the profile of the 420 nm light at the cavity output also showed evidence of more than one transverse mode.

The traces in Fig. 7.15 (b) and (d) show a zoomed in measurement of the cavity-enhanced beat note, with the linewidth no longer limited by the spectrun analyser resolution. Fitting Loretzian lineshapes to these plots gives a cavity-enhanced beat note linewidth of 0.7 MHz for both cell temperatures, which is significantly less than the cavity bandwidth of 51 MHz. There is sufficient gain in the FWM process that even with a very small amount of feedback the linewidth of the light is substantially narrowed.

Over the same time scale as the spectrum analyser scan (0.1 ms), the 420 nm laser was measured to have an autocorrelation linewidth of 0.5 MHz. Assuming the frequency spectrum of both the FWM and reference 420 nm light is Lorentzian, so that the FWHM of the beat note is the sum of the linewidth of each individual field [222], the cavity enhanced linewidth is estimated to be 0.2 MHz. This is less than the combined linewidth of the 780 nm and 776 nm pump lasers, which have autocorrelations of 0.2 MHz and 0.6 MHz, respectively over the same 0.1 ms timescale. Though the total linewidth of the 5.2 µm and 420 nm light is fixed by the pump linewidth due to energy conservation, the frequency of the individual fields is not fixed. The linewidth of the resonant blue light can be narrower than the pump light so long as the 5.2 µm linewidth is broader to compensate. A similar situation has been observed in singly resonant OPOs [223].

7.5 A Structured Light Laser

The previous two sections have demonstrated that for Gaussian pump beams, the low-finesse ring cavity both increases the output power and narrows the linewidth of the 420 nm light. In this final section, we consider the case of shaped pump beams. In particular, we investigate whether the phase coherence of the FWM pumping mechanism allows the cavity transverse mode to be shaped.

The transverse mode of a laser is usually determined by the intracavity optical elements [34]. Different modes can be selected by introducing a mode-dependent loss, or by enforcing a particular transverse phase [148]. Whilst this control is usually provided by specially made optics, recent work has demonstrated a "Digital laser" [224], where the round-trip transverse phase and loss is controlled using an intracavity spatial light modulator (SLM). Using this method the transverse mode of the generated laser beam can be chosen and updated in real time.

Here the aim is to shape the output mode not using intracavity elements, but by simply using the phase coherence of the FWM process. This is similar to studies of orbital angular momentum (OAM) transfer in optical parametric oscillators (OPOs) [225–227], where OAM carried by the pump light is transferred to the oscillating signal and idler fields.

7.5.1 Output power

The first test was whether the cavity resonances are still observed with shaped pump beams. These experiments were carried out by removing the greyed out mirrors in the diagram of the experimental setup (Fig. 7.4) so that the 780 nm and 776 nm pump light was sent to the SLM for shaping before being used for FWM. Since the two pump beams are already overlapped at this point, both pump fields were shaped into the same mode. For the first experiment, this was chosen to be the LG_0^1 mode. Similar shaping techniques were used as described earlier in this thesis, with the resulting intensity profile shown in the inset of Fig. 7.16. Directly before the cavity the beam waist was 1.1 mm, corresponding to a focused waist in the cell of 45 µm. The 780 nm and 776 nm input powers were 11.2 mW and 14.9 mW, respectively. The cell was heated to 120°C, and the cavity output coupling was 42%, corresponding to a finesse of 5.6. These measurements were made after the development of the 780 nm DAVLL lock described in Sec. 3.5. The 780 nm was locked with a detuning of +1.67 MHz.

Fig. 7.16 shows the resulting 420 nm output power with LG_0^1 pump beams. The power was measured on a photodiode directly at the cavity output and the

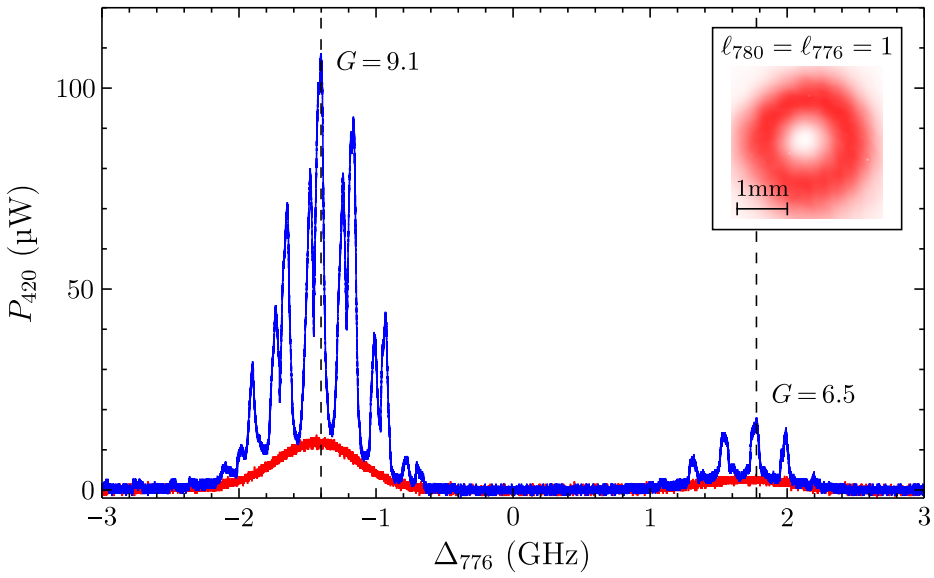

Figure 7.16: Cavity-enhanced 420 nm output power with LG_0^1 pump beams for single-pass (red) and cavity-enhanced (blue) FWM. Inset: intensity profile of the pump light. $\Delta_{780} = +1.67$ MHz.

measurement was performed first for single-pass FWM (with the cavity blocked after the PBS, red curve) and then with the cavity unblocked (blue). As with Gaussian pump beams, a large increase in the output power is observed when the 420 nm light is resonant with the cavity, with a peak cavity gain of 9.1. For negative 776 nm detuning, each cavity resonance is split, resulting in peaks similar to those seen for Gaussian beams in Fig. 7.12. The peak cavity-enhanced power was 108 µW, whilst the maximum single-pass power directly after the cell was 32 µW. The cavity therefore increases the overall conversion efficiency by a factor of 3.

7.5.2 Transverse mode

Whilst the output power measurement demonstrates a cavity-enhanced conversion efficiency, it obviously gives no information on the transverse mode. Transverse modes propagating in a cavity must reproduce themselves in one round trip in order to experience gain. This places restrictions on the modes a given cavity

can support. In particular, for a cavity to support LG modes the entire xy components of the field must undergo identical phase shifts and losses in one round trip [34]. In our cavity the prism breaks this symmetry, so it is not obvious that the 420 nm transverse mode will be the LG mode expected based on single-pass FWM.

To monitor the transverse mode, the cavity output beam was passed through a Dove prism interferometer, as described in Chapter 4, and the interferogram recorded as the 776 nm frequency was slowly scanned over the negative detuning group of cavity resonances in Fig. 7.16. For this measurement it was necessary to enclose the cavity in a box to prevent air currents from shifting the cavity resonances on quicker timescales than that of the ~ 30 s long scan. The experimental parameters were the same as for the cavity output power measurement in Fig. 7.16.

For comparison with the cavity output modes, the 420 nm intensity profile and interferogram obtained with the cavity blocked are shown in Fig. 7.17 (b). For this preliminary experiment the transverse mode of the 420 nm light was measured only qualitatively by inspection of the interferogram. However, some comparison to the theory presented in chapter 5 can be made by calculating the predicted modal superposition of the 420 nm light, and from this the expected profile of the interferogram. The results from this calculation are shown in Fig. 7.17 (b) and (c). Lower 420 nm mode purities are expected here (than in Fig. 5.6) due to the larger focused waist of the pump beams within the cell (45 µm here compared to 24 µm in the previously). This increases the Rayleigh range of the fields and reduces the effect of Gouy phase matching, with significant power now predicted in the $\ell = 3$ mode (corresponding to $\ell_{\mathrm{IR}} = -1$). The effect of the reduced purity is seen in both the experimental and theoretical interferograms as a reduced fringe visibility along the horizontal axis.

A total of 300 images of the interferogram were recorded as the 776 nm laser was scanned across the cavity resonances. The variation in the summed pixel total of these images (which is proportional to the 420 nm power) is shown in

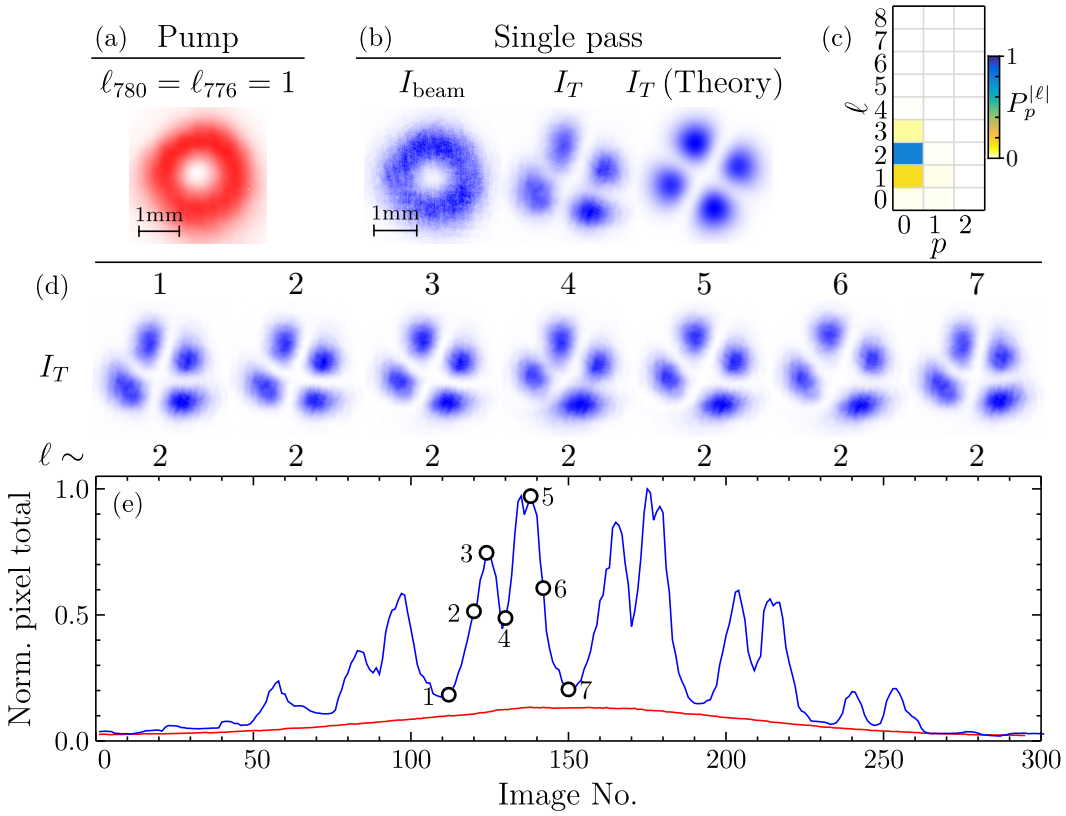

Figure 7.17: (a) Intensity profile of LG_0^1 pump beams. (b) Single-pass 420 nm relative intensity profile, interferogram, and predicted interferogram. (c) Predicted 420 nm single-pass modal superposition. (d) Cavity-enhanced interferogram images at different positions on the cavity resonance, as indicated in (e) which shows the normalised pixel total of all images both for single-pass (red) and cavity-enhanced (blue) FWM. Increasing image no. corresponds to increasing 776 nm frequency.

Fig. 7.17 (e), for both single-pass (red) and cavity enhanced (blue) FWM. The cavity resonances show a similar dependence on 776 nm detuning as in the output power measurement in Fig. 7.16.

Seven of the interferogram images were selected to illustrate the behaviour of the transverse mode over a single cavity resonance. The position of each image relative to the resonance is shown in Fig. 7.17 (e), with the images in (d). Perhaps surprisingly, the transverse mode does not change significantly across the resonance, apart from image 4 which shows a slight decrease in mode purity.

The other images, however, show the same if not higher fringe visibility than the single-pass interferogram. This indicates that the cavity output mode is almost entirely determined by the phase coherence of the FWM in this case. This may be due to the large FWM gain and relatively low cavity finesse.

To test this further the same experiment was performed with LG_0^3 pump beams. In this case the beam waist was 0.8 mm before the cell, with 780 nm and 776 nm powers of 8.1 mW and 10.9 mW, respectively. The results of this are shown

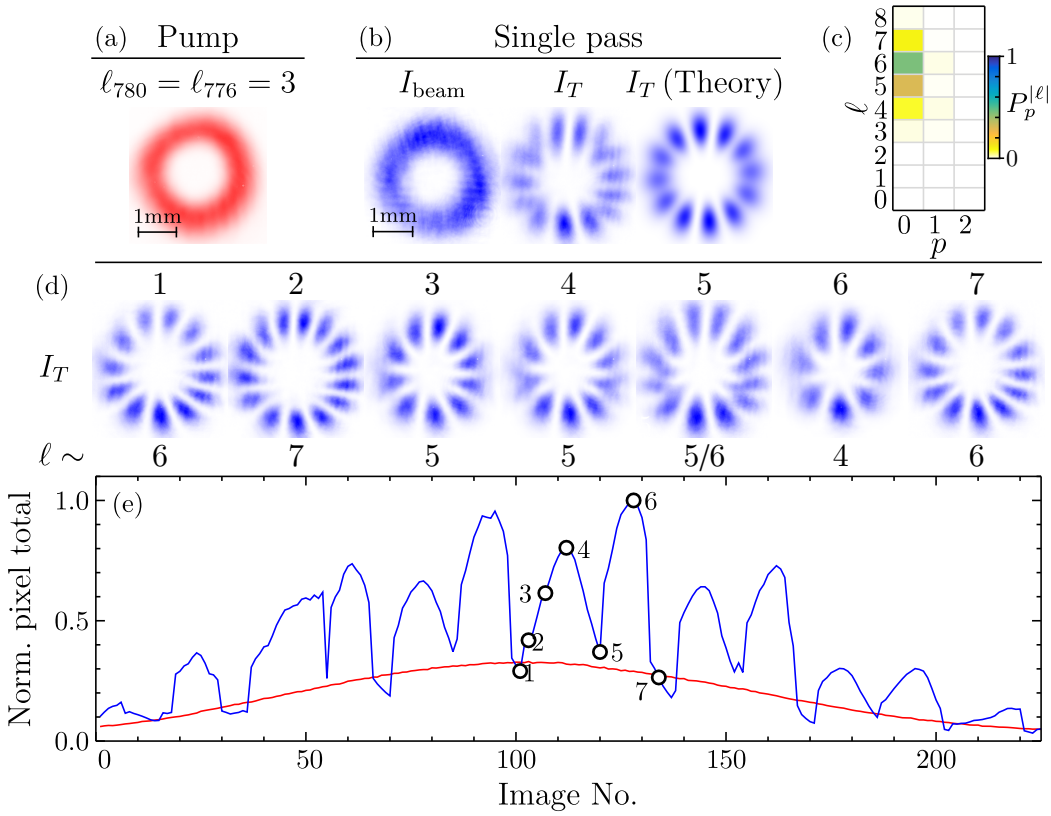

Figure 7.18: (a) Intensity profile of LG_0^3 pump beams. (b) Single-pass 420 nm relative intensity profile, interferogram, and predicted interferogram. (c) Predicted 420 nm single-pass modal superposition. (d) Cavity-enhanced interferogram images at different positions on the cavity resonance, as indicated in (e) which shows the normalised pixel total of all images both for single-pass (red) and cavity-enhanced (blue) FWM. Increasing image no. corresponds to increasing 776 nm frequency. $\Delta_{780} = +1.57$ GHz.

in Fig. 7.18. Both the predicted and experimental single-pass interferograms, and the predicted 420 nm mode decomposition, show a marked decrease in mode purity. This is due to the even larger waist of the pump beams in the rubidium cell, which is now 62 µm. This corresponds to a Rayleigh range approximately equal to half the cell length.

In these results the cavity has a much larger effect on the 420 nm transverse mode. The cavity-enhanced interferograms shown in Fig. 7.18 (d) were chosen to highlight the full range of modes generated at the cavity output, with the estimated ℓ index of the beam shown below each image. At different points across the resonance the cavity appears to select a single mode from the single-pass 420 nm mode decomposition. Each mode predicted by the theoretical 420 nm mode superposition is observed at the cavity output. Interestingly the $\ell = 6$ mode, which is predicted to be generated with the highest relative power, is only observed in images 1 and 7, which correspond to the cavity being off resonance.

The total Gouy phase shift of an LG mode as it propagates through a focus is given by $(2p + |\ell| + 1)\pi$. The even ℓ modes are therefore phase shifted by an odd multiple of π, whilst the odd ℓ modes are shifted by an even multiple of π. Based on the cavity design, the resonance frequencies of odd and even ℓ modes should therefore be separated by half a free spectral range. This would be the expected mechanism for the cavity to select a single output mode, but the order of the modes shown in Fig. 7.18 (d) does not agree with this prediction. It is possible that the true mechanism is related to the cavity affecting the FWM process itself, with the feedback and increased intracavity power on resonance changing the overlap of the fields in the cell.

7.6 Conclusion

In this chapter, the effect of a low-finesse ring cavity on the 420 nm output power, linewidth and transverse mode was investigated. The principal results, obtained with Gaussian pump beams, were that the cavity both increases the FWM 420 nm

output power, from a maximum of 340 µW single pass to 940 µW with the cavity, and narrows the linewidth of the generated 420 nm light, from 33 MHz single pass to < 1 MHz with the cavity [P5].

The cavity-enhanced output power was studied by measuring the variation in the 420 nm power as the 776 nm pump frequency was scanned. The resulting spectra showed a large increase in output power when the 420 nm light was resonant with the cavity. Measurements of the frequency tuning of the 420 nm light showed that its frequency tuned with that of the pump lasers, with a frequency shift consistent with relative Doppler shifts. Taking this into account the observed free spectral range of the cavity resonances matched the expected value based on the round trip length. The cavity-enhanced spectra were studied under a wide range of conditions; changing the pump power, cell temperature and output coupling.

There are several unexplained features of the spectra that would be interesting for further study, for example: the asymmetry of the resonances, the apparent saturation effects and, under certain conditions, the splitting of the cavity peaks. To understand these features a theoretical model would be required, taking into account the hyperfine structure of the atoms, and the coupled amplitudes of the FWM fields. Further experiments could also help aid understanding, for example it would be interesting to monitor the pump power at the exit of the rubidium cell as a function of pump frequency, to observe to what extent the pump is depleted on resonance.

The cavity was also shown to narrow the linewidth of the 420 nm light. The single-pass linewidth was found to be broadly consistent with power broadening of the 420 nm transition. With the cavity output coupling optimised for peak output power, the cavity generated nearly 1 mW of light with a linewidth narrowed to < 1 MHz. The absolute frequency of the 420 nm light was also measured, with maximum 420 nm power generated around 200 MHz red detuned from the $5S_{1/2}\,F = 3 \rightarrow 6P_{3/2}\,F' = 4$ transition. The light could be tuned to either side of the transition, with a FWHM range of up to 650 MHz.

The main limiting factor in the linewidth measurements was that there was no locking mechanism for the lasers at the time of the experiment. If the measurements were repeated with locked lasers, it would be interesting to determine how much feedback is necessary to observe linewidth narrowing, for example by measuring the cavity-enhanced linewidth as a function of output coupling.

There is scope for increasing the 420 nm power by increasing the pump power and reducing the (large) round trip loss of the cavity. The largest losses are due to the 4% reflections each glass surface of the rubidium cell. This could be reduced by using an anti-reflection coated or Brewster cut cell. With these improvements, the narrow linewidth, tunable light could be of use for rubidium cold atom experiments, for example for second stage laser cooling of ^{85}Rb [220, 221]. A recent experiment has shown that the blue light FWM process can also be enhanced by using a build-up cavity for the pump beams, although in this case the FWM process was two-photon excited by 778 nm light [228]. It may be possible to further increase the output power in our experiment by using a cavity that is resonant with both the 420 nm light and the 776 nm pump.

In a final, preliminary experiment, cavity-enhanced FWM with shaped pump beams was investigated. For $\ell = 1$ pump beams the cavity improved the conversion efficiency with which the pump OAM was transferred to the 420 nm light threefold. For higher ℓ pump beams ($\ell = 3$), where the single-pass 420 nm light was generated in a range of ℓ modes, the cavity output mode varied across the cavity resonance, with the cavity selecting different modes from the single-pass superposition for different detunings. Whilst further experiments are required to fully characterise the modes generated, it was clear that the OAM carried by the beam varied substantially. For OAM to be conserved this implies that the cavity also affects the 5.2 µm transverse mode, even though it is not resonant in the cavity. With a sapphire cell it would be interesting to measure this effect directly. Alternatively, if a cavity could be used to constrain the transverse mode of the 5.2 µm light to a Gaussian, then this effect could be used to ensure the blue light is generated in a single, well defined OAM state. This would allow large

values of OAM to be frequency converted with high fidelity.

Chapter 8

Conclusion

8.1 Summary

The work in this thesis has investigated a resonantly enhanced four-wave mixing (FWM) process in rubidium vapour, which allows for efficient frequency conversion of 780 nm and 776 nm light to new fields at 5.2 µm and 420 nm [4, 90–92]. Using this system, research was carried out in two main areas: the coherent frequency conversion of structured light, and the effect of adding feedback, in the form of a low-finesse ring cavity, to the FWM process.

Chapters 1 and 2 set the scene for the work carried out in this thesis, providing context for the experiments undertaken and giving a brief outline of the physics behind wave mixing processes and resonant light-atom interactions. The "blue light" FWM system was then introduced in Chapter 3, with a detailed description of the experimental components necessary to carry out the basic FWM experiment. This included the techniques used to monitor and lock the laser frequencies, as well as the heated rubidium cell.

Chapters 4, 5 and 6 detail our investigation of FWM with structured light. We chose to work with Laguerre-Gauss (LG) modes, which have helical phase fronts and carry an associated orbital angular momentum (OAM). The motivation for this section of work was to better understand the coherent interaction of these modes, which have potential applications in increasing the bandwidth

and security of quantum communication systems, with atomic vapours. This is of particular relevance for atomic-vapour-based transverse-mode quantum memories.

The first step was to develop the experimental setup required to shape an initially Gaussian beam into the required LG modes. This work is presented in Chapter 4. Initially, we compared different methods of generating phase-only holograms for use with a spatial light modulator (SLM), in order to select the most appropriate method for the FWM experiment. This resulted in a paper published in Optics Express [P1], which compares the beam shaping accuracy of six different hologram generation methods. In particular, we chose methods designed to shape an incident beam into propagating modes, and the ability of each method to generate a Gaussian, LG and and LG superposition was tested. This work is a useful reference for any application which requires a straightforward method of generating these simple modes.

The second section in Chapter 4 describes the development of the FWM beam shaping setup. This section of work was further informed by a simulated evaluation of the influence of various experimental parameters on the SLM beam shaping quality, as reported in Ref. [P2]. This paper is another useful resource for beam shaping applications, and shows the effect of the grating period, aperture size, hologram resolution, number of grey levels, phase throw and phase linearity on beam shaping accuracy and efficiency. Based on the conclusions of Refs. [P1] and [P2], a setup was designed and built which allows the two FWM pump beams to be shaped independently using a single SLM.

Chapter 5 details the first of the main experiments presented in this thesis: a quantitative study of OAM transfer in the "blue light" FWM system. Previous work had demonstrated that OAM carried by the pump beams could be transferred to the generated fields, with measurements of the 420 nm transverse mode consistent with all OAM being transferred to the 420 nm light [46, 87, 88]. These experiments indicate that the FWM process could be an efficient method of frequency converting OAM states from the near-infrared to the blue.

In the current work, which is at present under consideration for publication and can be found on the arXiv [P3], we used Fourier analysis of the interferogram formed at the output of a Dove prism interferometer to perform the first quantitative measurements of the 420 nm transverse mode. We found that for low ℓ pump beams ($\ell < 4$) our results are consistent with the previous work, and the 420 nm light is predominantly generated in a single OAM mode, with $\ell_{\mathrm{B}} = \ell_{780} + \ell_{776}$. However as the pump ℓ increased we observed a continuous broadening of the 420 nm ℓ distribution. This indicates that the pump OAM is shared between the 5.2 µm and 420 nm light, and that the generated two-photon state is OAM-entangled. To characterise this state we inferred the spiral bandwidth and entanglement entropy from the measured 420 nm mode decomposition, finding that both parameters increase with increasing pump OAM. This interpretation of the experimental results was supported by a simple theoretical model that was used to predict the OAM distribution between the two generated FWM fields.

Our result indicates that, at least under the conditions in our experiment, our system is not a robust method of frequency converting OAM states, particularly for higher pump ℓ (for $\ell < 3$ the total pump OAM is transferred to the blue light with a fidelity > 0.9). Instead, it may be an efficient source of OAM-entangled photon pairs with widely differing wavelengths. Very recently a purely near-infrared FWM process carried out in a cold rubidium vapour has been shown to generate OAM-entangled photon pairs [200]. As is inferred in our system, the spiral bandwidth of the entangled state is found to increase for increasing pump OAM.

The experiments in Chapter 5 showed the importance of three factors in determining the transverse mode of the generated 420 nm light: OAM conservation, the spatial overlap of the fields, and Gouy phase matching. In Chapter 6, a series of three preliminary experiments were presented that investigated these effects further. The work in this chapter is currently being prepared for publication [P4]. The first experiment considered FWM for pump beams carrying opposite hand-

edness of OAM. For pump OAM of the same handedness, we observe 420 nm light in an LG mode with the radial index, p, equal to zero, however, for opposite handedness the 420 nm light is instead generated with $p > 0$. This appears to be a direct result of Gouy phase matching, which requires that the mode order of the pump and generated light is conserved. The effects of Gouy phase matching were further seen when FWM was performed for pump modes with $p > 0$, in which case we observed the 420 nm light in a mode consistent with addition of both the OAM and p-indices of the pump beams. The final experiment in this chapter demonstrated FWM for pump beams in a coherent superposition of LG modes. By varying the relative phase of the pump mode superposition, the mode content of the generated 420 nm light could be controlled via interference of the different FWM pathways. Although the work in Chapter 6 is so far preliminary, each experiment demonstrates an interesting area for future study, both to further understanding of the coherent interaction between structured light and atoms, and for developing novel methods of controlling this interaction to produce the desired mode.

In the final experimental chapter, Chapter 7, we studied the effect of adding an external cavity to the FWM system. These results were the first demonstration that a cavity could be used to both enhance the output power and narrow the linewidth of the generated 420 nm light. Using a low-finesse ring cavity, singly-resonant with the 420 nm field, the peak cavity output power was 940 µW, compared to a maximum of 340 µW for a single pass, and the 420 nm linewidth narrowed from 33 MHz for a single pass to < 1 MHz with the cavity. This work led to a publication in Optics Letters [P5]. This chapter also developed further understanding of the single-pass FWM process, including the absolute frequency and frequency tuning characteristics of the 420 nm light, which was found to be consistent with relative Doppler shifts.

The final experimental results in this thesis combined the two main research themes and investigated FWM in an external cavity with LG pump modes. The aim of this experiment was to demonstrate that the cavity output mode could be

controlled via our FWM pumping mechanism. This would allow the transverse mode, which would usually be fixed by the intracavity losses, to be updated in real time, simply by updating the SLM hologram used to shape the pump beams. Preliminary measurements for $\ell = 1$ and $\ell = 3$ pump modes indicated that the cavity output mode could indeed be controlled in this way, with the transverse mode determined by a combination of the phase coherence of the FWM process and the feedback provided by the cavity. For $\ell = 3$ pump modes, the single pass 420 nm light was generated in a range of ℓ modes and the cavity was observed to select a single mode from the superposition, resulting in a high purity output mode. This effect could be used to constrain the 420 nm light to a single transverse mode, enabling the frequency conversion of large OAM states.

8.2 Future Work

The research in this thesis could be developed in a number of directions. To continue with the work in Chapters 5 and 6, the most important next step is to measure the transverse mode of the 5.2 µm light. This would require the use of a rubidium cell with sapphire windows and a photodiode or camera capable of detecting 5.2 µm light. A measurement of the 5.2 µm transverse mode as a function of pump ℓ should confirm that the OAM "missing" from the 420 nm beam for larger pump ℓ is transferred to the 5.2 µm field. Measurement of the 5.2 µm transverse mode would also aid further understanding of the preliminary results presented in Chapter 6. An open question from this chapter is to understand why the 5.2 µm light appears to not be generated with $p > 0$. Understanding this may provide further insight into the FWM process.

In Chapter 5 our results indicated that the 420 nm and 5.2 µm light is likely to be generated in an OAM-entangled state. Having confirmed that the OAM is shared between the two generated fields for classical light, further work would still be required to demonstrate entanglement. To do this the FWM process would need to be carried out at low light levels, such that single photon detectors

could be used to perform coincidence measurements on the 420 nm and 5.2 µm fields. An initial experiment could be to measure the OAM-conditioned coincidences. We expect that coincidences would only be observed for photon pairs that conserve the total pump OAM. To verify that the 5.2 µm and 420 nm light is OAM-entangled a further measurement would be required, as it is necessary to demonstrate that the two-photon state is a coherent superposition of product states, rather than just a mixture. The signature of this is that the correlations between the 5.2 µm and 420 nm light are still observed when the coincidences are measured in another basis, for example, one consisting of superpositions of OAM states [47]. To fully characterise the experiment, a tomographic reconstruction of the quantum state of the 5.2 µm and 420 nm photon pairs could be performed [206].

In our experiment, the pump beams are coherently converted to new optical fields via the interaction between the incident light and the rubidium atoms. These results are relevant for transverse mode quantum memories, where the same interaction is instead used to stop and store the input light, and then read it out at a later time. Although we work with an atomic vapour, the techniques presented in Chapter 5 and 6 are well-suited for use with cold atoms, and should inform future experiments developing long-timescale high-dimensional quantum memories [99].

Finally, we consider the future prospects of the cavity-enhanced FWM experiment. Improvements in the cavity-enhanced output power could be made through developing a cavity with reduced round trip loss. In particular, the main losses in the cavity came from the rubidium cell itself and the polarising beam splitter used as the output coupler. These losses could be reduced by using an anti-reflection coated cell and a different design of output coupler, for example, a partially reflecting mirror.

The results presented at the end of Chapter 7, for cavity-enhanced FWM with shaped pump beams, also merit further investigation. When the cavity selects a single 420 nm transverse mode, OAM conservation suggests that this also deter-

mines the OAM carried by the non-resonant 5.2 µm light. A direct measurement of this would be of interest. Furthermore, this effect may have applications in efficient frequency conversion and addition of large OAM states, which cannot be achieved in our single-pass FWM system. A cavity, singly resonant with the 5.2 µm light, could be used to constrain the infrared field to a Gaussian mode, thus forcing all of the pump OAM onto the 420 nm field.

Bibliography

[P1] T. W. Clark, R. F. Offer, S. Franke-Arnold, A. S. Arnold, and N. Radwell, "Comparison of beam generation techniques using a phase only spatial light modulator," Opt. Express **24**, 6249 (2016).

[P2] N. Radwell, R. F. Offer, A. Selyem, and S. Franke-Arnold, "Optimisation of arbitrary light beam generation with spatial light modulators," J. Opt. **19**, 095605 (2017).

[P3] R. F. Offer, D. Stulga, E. Riis, S. Franke-Arnold, and A. S. Arnold, "Spiral bandwidth of four-wave mixing in Rb vapour," arXiv[physics.atom-ph]1805.08190 (2018).

[P4] R. F. Offer, E. Riis, S. Franke-Arnold, and A. S. Arnold, "Coherent beam shaping via four wave mixing in rubidium vapour," (2018).

[P5] R. F. Offer, J. W. C. Conway, E. Riis, S. Franke-Arnold, and A. S. Arnold, "Cavity-enhanced frequency up-conversion in rubidium vapor," Opt. Lett. **41**, 2177–2180 (2016).

[1] C. J. Foot, *Atomic Physics* (Oxford University Press, 2014).

[2] R. W. Boyd, *Nonlinear Optics* (Academic Press, 2008), 3rd ed.

[3] J. A. Armstrong, N. Bloembergen, J. Ducuing, and P. S. Pershan, "Interactions between light waves in a nonlinear dielectric," Phys. Rev. **127**, 1918 (1962).

[4] A. S. Zibrov, M. D. Lukin, L. Hollberg, and M. O. Scully, "Efficient frequency up-conversion in resonant coherent media," Phys. Rev. A **65**, 051801 (2002).

[5] L. Allen, M. W. Beijersbergen, R. J. C. Spreeuw, and J. P. Woerdman, "Orbital angular momentum of light and the transformation of Laguerre-Gaussian laser modes," Phys. Rev. A **45**, 8185 (1992).

[6] J. Wang, J.-Y. Yang, I. M. Fazal, N. Ahmed, Y. Yan, H. Huang, Y. Ren, Y. Yue, S. Dolinar, M. Tur, and A. E. Willner, "Terabit free-space data transmission employing orbital angular momentum multiplexing," Nature Phot. **6**, 488 (2012).

[7] S. P. Walborn, D. S. Lemelle, M. P. Almeida, and P. H. Souto Ribeiro, "Quantum key distribution with higher-order alphabets using spatially encoded qudits," Phys. Rev. Lett. **96**, 090501 (2006).

[8] T. H. Maiman, "Stimulated optical radiation in ruby," Nature **187**, 494 (1960).

[9] R. W. Minck, R. W. Terhune, and C. C. Wang, "Nonlinear Optics," Appl. Opt. **5**, 1595 (1966).

[10] P. A. Franken, A. E. Hill, C. W. Peters, and G. Weinreich, "Generation of optical harmonics," Phys. Rev. Lett. **7**, 118 (1961).

[11] M. Bass, P. A. Franken, A. E. Hill, C. W. Peters, and G. Weinreich, "Optical mixing," Phys. Rev. Lett. **8**, 18 (1962).

[12] D. W. Faries, K. A. Gehring, P. L. Richards, and Y. R. Shen, "Tunable far-infrared radiation generated from the difference frequency between two ruby lasers," Phys. Rev. A **180**, 363 (1969).

[13] J. A. Giordmaine and R. C. Miller, "Tunable coherent parametric oscillation in $LiNbO_3$ at optical frequencies," Phys. Rev. Lett. **14**, 973 (1965).

[14] S. Harris, "Tunable optical parametric oscillators," Proc. IEEE **57**, 2096 (1969).

[15] P. D. Maker and R. W. Tehrune, "Study of optical effects due to an induced polarization third order in the electric field strength," Phys. Rev. **137**, A801 (1965).

[16] J. F. Ward and G. H. C. New, "Optical third harmonic generation in gases by a focused laser beam," Phys. Rev. **185**, 57 (1969).

[17] P. D. Maker, R. W. Terhune, M. Nisenoff, and C. M. Savage, "Effects of dispersion and focusing on the production of optical harmonics," Phys. Rev. Lett. **8**, 21 (1962).

[18] G. Grynberg, A. Aspect, and C. Fabre, *Introduction to Quantum Optics* (Cambridge University Press, 2010).

[19] D. C. Burnham and D. L. Weinberg, "Observation of simultaneity in parametric production of optical photon pairs," Phys. Rev. Lett. **25**, 84 (1970).

[20] S. Friberg, C. K. Hong, and L. Mandel, "Measurement of time delays in the parametric production of photon pairs," Phys. Rev. Lett. **54**, 2011 (1985).

[21] C. K. Hong and L. Mandel, "Theory of parametric frequency down conversion of light," Phys. Rev. A **31**, 2409 (1985).

[22] T. B. Pittman, Y. H. Shih, D. V. Strekalov, and A. V. Sergienko, "Optical imaging by means of two photon quantum entanglement," Phys. Rev. A **52**, R3429 (1995).

[23] Y. H. Shih, A. V. Sergienko, M. H. Rubin, T. E. Kiess, and C. O. Alley, "Two-photon entanglement in type-II parametric down-conversion," Phys. Rev. A **50**, 23 (1994).

[24] P. G. Kwiat, K. Mattle, H. Weinfurter, A. Zeilinger, A. V. Sergienko, and Y. Shih, "New high-intensity source of polarization-entangled photon pairs," Phys. Rev. Let.. **75**, 4337 (1995).

[25] D. Bouwmeester, J.-W. Pan, K. Mattle, M. Eibl, H. Weinfurter, and A. Zeilinger, "Experimental quantum teleportation," Nature **390**, 575 (1997).

[26] M. Halder, A. Beveratos, N. Gisin, V. Scarani, C. Simon, and H. Zbinden, "Entangling independent photons by time measurement," Nat. Phys. **3**, 692 (2007).

[27] Y. Zhang, M. Agnew, T. Roger, F. S. Roux, T. Konrad, D. Faccio, J. Leach, and A. Forbes, "Simultaneous entanglement swapping of multiple orbital angular momentum states of light," Nat. Commun. **8**, 632 (2017).

[28] A. K. Ekert, "Quantum cryptography based on Bell's theorem," Phys. Rev. Lett. **67**, 661 (1991).

[29] N. Gisin, G. Ribordy, W. Tittel, and H. Zbinden, "Quantum cryptography," Rev. Mod. Phys. **74**, 145 (2002).

[30] I. Khan, B. Heim, A. Neuzner, and C. Marquardt, "Satellite-Based QKD," Opt. Photonics News **Feb**, 26 (2018).

[31] N. Gisin and R. Thew, "Quantum communication," Nat. Photon. **1**, 165 (2007).

[32] N. Bozinovic, Y. Yue, Y. Ren, M. Tur, P. Kristensen, H. Huang, A. E. Willner, and S. Ramachandran, "Terabit-Scale orbital angular momentum mode division multiplexing in fibres," Science **340**, 1545 (2013).

[33] H. Rubinsztein-dunlop *et al.*, "Roadmap on structured light," J. Opt. **19**, 013001 (2017).

[34] A. E. Siegman, *Lasers* (Oxford University Press, 1986).

[35] Q. Zhan, "Cylindrical vector beams: from mathematical concepts to applications," Adv. Opt. Photonics **1**, 1 (2009).

[36] D. Gao, W. Ding, M. Nieto-Vesperinas, X. Ding, M. Rahman, T. Zhang, C. T. Lim, and C.-W. Qiu, "Optical manipulation from the microscale to the nanoscale: Fundamentals, advances and prospects," Light Sci. Appl. **6**, 1 (2017).

[37] E. Wegel, A. Göhler, B. C. Lagerholm, A. Wainman, S. Uphoff, R. Kaufmann, and I. M. Dobbie, "Imaging cellular structures in super-resolution with SIM, STED and Localisation Microscopy: A practical comparison," Sci. Rep. **6**, 27290 (2016).

[38] S. Franke-Arnold, J. Leach, M. J. Padgett, V. E. Lembessis, D. Ellinas, A. J. Wright, J. M. Girkin, P. Ohberg, and A. S. Arnold, "Optical ferris wheel for ultracold atoms," Opt. Express **15**, 8619 (2007).

[39] N. Radwell, G. Walker, and S. Franke-Arnold, "Cold-atom densities of more than 10^{12} cm^{-3} in a holographically shaped dark spontaneous-force optical trap," Phys. Rev. A **88**, 043409 (2013).

[40] H. Kim, W. Lee, H. G. Lee, H. Jo, Y. Song, and J. Ahn, "In situ single-atom array synthesis using dynamic holographic optical tweezers," Nat. Commn. **7**, 13317 (2016).

[41] A. M. Yao and M. J. Padgett, "Orbital angular momentum: origins, behavior and applications," Adv. Opt. Photonics **3**, 161 (2011).

[42] S. Franke-Arnold and N. Radwell, "Light served with a twist," Opt. Photonics News **June**, 28 (2017).

[43] M. J. Padgett, "Orbital angular momentum 25 years on," Opt. Express **25**, 11265 (2017).

[44] K. Dholakia, N. B. Simpson, M. J. Padgett, and L. Allen, "Second-harmonic generation and the orbital angular momentum of light," Phys. Rev. A **54**, R3742 (1996).

[45] Y. Li, Z.-Y. Zhou, D.-S. Ding, and B.-S. Shi, "Sum frequency generation with two orbital angular momentum carrying laser beams," J. Opt. Soc. Am. B **32**, 407–411 (2015).

[46] G. Walker, A. S. Arnold, and S. Franke-Arnold, "Trans-spectral orbital angular momentum transfer via four-wave mixing in Rb vapor," Phys. Rev. Lett. **108**, 243601 (2012).

[47] A. Mair, A. Vaziri, G. Weihs, and A. Zeilinger, "Entanglement of the orbital angular momentum states of photons," Nature **412**, 313–316 (2001).

[48] S. Franke-Arnold, S. M. Barnett, M. J. Padgett, and L. Allen, "Two-photon entanglement of orbital angular momentum states," Phys. Rev. A **65**, 033823 (2002).

[49] J. P. Torres, A. Alexandrescu, and L. Torner, "Quantum spiral bandwidth of entangled two-photon states," Phys. Rev. A **68**, 050301(R) (2003).

[50] M. Erhard, R. Fickler, M. Krenn, and A. Zeilinger, "Twisted photons: New quantum perspectives in high dimensions," Light Sci. Appl. **7**, 17146 (2018).

[51] W. D. Phillips, "Nobel Lecture: Laser cooling and trapping of neutral atoms," Rev. Mod. Phys. **70**, 721 (1998).

[52] M. H. Anderson, J. R. Ensher, M. R. Matthews, C. E. Wieman, and E. A. Cornell, "Observation of Bose-Einstein condensation in a dilute atomic vapor," Science **269**, 198 (1995).

[53] A. D. Cronin, J. Schmiedmayer, and D. E. Pritchard, "Optics and interferometry with atoms and molecules," Rev. Mod. Phys. **81**, 1051 (2009).

[54] D. Budker and M. Romalis, "Optical magnetometry," Nat. Phys. **3**, 227 (2007).

[55] A. D. Ludlow, M. M. Boyd, J. Ye, E. Peik, and P. O. Schmidt, "Optical atomic clocks," Rev. Mod. Phys. **87**, 637 (2015).

[56] H. J. Kimble, "The quantum internet," Nature **453**, 1023 (2008).

[57] T. Chanelière, D. N. Matsukevich, S. D. Jenkins, T. A. B. Kennedy, M. S. Chapman, and A. Kuzmich, "Quantum telecommunication based on atomic cascade transitions," Phys. Rev. Lett. **96**, 093604 (2006).

[58] R. T. Willis, F. E. Becerra, L. A. Orozco, and S. L. Rolston, "Correlated photon pairs generated from a warm atomic ensemble," Phys. Rev. A **82**, 053842 (2010).

[59] M. Namazi, C. Kupchak, B. Jordaan, R. Shahrokhshahi, and E. Figueroa, "Ultralow-noise room-temperature quantum memory for polarization qubits," Phys. Rev. Appl. **8**, 034023 (2017).

[60] P. Vernaz-Gris, K. Huang, M. Cao, A. S. Sheremet, and J. Laurat, "Highly-efficient quantum memory for polarization qubits in a spatially-multiplexed cold atomic ensemble," Nat. Commun. **9**, 363 (2018).

[61] P. R. Hemmer, D. P. Katz, J. Donoghue, M. Cronin-Golomb, M. S. Shahriar, and P. Kumar, "Efficient low-intensity optical phase conjugation based on coherent population trapping in sodium." Opt. Lett. **20**, 982 (1995).

[62] M. Jain, H. Xia, G. Y. Yin, A. J. Merriam, and S. E. Harris, "Efficient nonlinear frequency conversion with maximal atomic coherence," Phys. Rev. Lett. **77**, 4326 (1996).

[63] M. D. Lukin, P. R. Hemmer, and M. O. Scully, "Resonant nonlinear optics in phase-coherent media," Adv. At. Mol. Opt. **42**, 347 (2000).

[64] Y.-Q. Li and M. Xiao, "Enhancement of nondegenerate four-wave mixing based on electromagnetically induced transparency in rubidium atoms." Opt. Lett. **21**, 1064 (1996).

[65] F. E. Becerra, R. T. Willis, S. L. Rolston, and L. A. Orozco, "Nondegenerate four-wave mixing in rubidium vapor: The diamond configuration," Phys. Rev. A **78**, 013834 (2008).

[66] Q. F. Chen, B. S. Shi, Y. S. Zhang, and G. C. Guo, "Entanglement of the orbital angular momentum states of the photon pairs generated in a hot atomic ensemble," Phys. Rev. A **78**, 053810 (2008).

[67] V. Boyer, A. M. Marino, R. C. Pooser, and P. D. Lett, "Entangled Images from Four-Wave Mixing," Science **321**, 544–547 (2008).

[68] R. T. Willis, F. E. Becerra, L. a. Orozco, and S. L. Rolston, "Four-wave mixing in the diamond configuration in an atomic vapor," Phys. Rev. A **79**, 033814 (2009).

[69] F. E. Becerra, R. T. Willis, S. L. Rolston, H. J. Carmichael, and L. A. Orozco, "Nondegenerate four-wave mixing in rubidium vapor: Transient regime," Phys. Rev. A **82**, 043833 (2010).

[70] R. T. Willis, F. E. Becerra, L. A. Orozco, and S. L. Rolston, "Photon statistics and polarization correlations at telecommunications wavelengths from a warm atomic ensemble," Opt. Express **19**, 14632 (2011).

[71] A. Macrae, T. Brannan, R. Achal, and A. I. Lvovsky, "Tomography of a high-purity narrowband photon from a transient atomic collective excitation," Phys. Rev. Lett. **109**, 033601 (2012).

[72] M. Parniak and W. Wasilewski, "Interference and nonlinear properties of four-wave-mixing resonances in thermal vapor: Analytical results and experimental verification," Phys. Rev. A **91**, 023418 (2015).

[73] A. Leszczyński, M. Parniak, and W. Wasilewski, "Phase matching alters spatial multiphoton processes in dense atomic ensembles," Opt. Express **25**, 284 (2017).

[74] D. J. Whiting, R. S. Mathew, J. Keaveney, C. S. Adams, and I. G. Hughes, "Four-wave mixing in a non-degenerate four-level diamond configuration in the hyperfine PaschenBack regime," J. Mod. Opt. **65**, 119 (2018).

[75] S. Barreiro and J. W. Tabosa, "Generation of light carrying orbital angular momentum via induced coherence grating in cold atoms," Phys. Rev. Lett. **90**, 133001 (2003).

[76] D. a. Braje, V. Balić, S. Goda, G. Y. Yin, and S. E. Harris, "Frequency mixing using electromagnetically induced transparency in cold atoms," Phys. Rev. Lett. **93**, 183601 (2004).

[77] S. Du, E. Oh, J. Wen, and M. H. Rubin, "Four-wave mixing in three-level systems: Interference and entanglement," Phys. Rev. A **76**, 013803 (2007).

[78] E. Brekke, J. O. Day, and T. G. Walker, "Four-wave mixing in ultracold atoms using intermediate Rydberg states," Phys. Rev. A **78**, 063830 (2008).

[79] A. G. Radnaev, Y. O. Dudin, R. Zhao, H. H. Jen, S. D. Jenkins, A. Kuzmich, and T. a. B. Kennedy, "A quantum memory with telecom-wavelength conversion," Nat. Phys. **6**, 894 (2010).

[80] K. Liao, H. Yan, J. He, S. Du, Z.-M. Zhang, and S.-L. Zhu, "Subnatural-linewidth polarization-entangled photon pairs with controllable temporal length," Phys. Rev. Lett. **112**, 243602 (2014).

[81] B. Srivathsan, G. K. Gulati, B. Chng, G. Maslennikov, D. Matsukevich, and C. Kurtsiefer, "Narrow band source of transform-limited photon pairs via four-wave mixing in a cold atomic ensemble," Phys. Rev. Lett. **111**, 123602 (2013).

[82] L. Zhao, X. Guo, C. Liu, Y. Sun, M. M. T. Loy, and S. Du, "Photon pairs with coherence time exceeding 1 µs," Optica **1**, 84 (2014).

[83] Y.-W. Cho, K.-K. Park, J.-C. Lee, and Y.-H. Kim, "Engineering frequency-time quantum correlation of narrow-band biphotons from cold atoms," Phys. Rev. Lett. **113**, 063602 (2014).

[84] D. J. Whiting, N. Šibalić, J. Keaveney, C. S. Adams, and I. G. Hughes, "Single-photon interference due to motion in an atomic collective excitation," Phys. Rev. Lett. **118**, 253601 (2017).

[85] D.-S. Ding, Z.-Y. Zhou, B.-S. Shi, X.-B. Zou, and G.-C. Guo, "Linear up-conversion of orbital angular momentum," Opt. Lett. **37**, 3270 (2012).

[86] M. Cao, Y. Yu, L. Zhang, F. Ye, Y. Wang, D. Wei, P. Zhang, W. Guo, S. Zhang, H. Gao, and F. Li, "Demonstration of CNOT gate with Laguerre Gaussian beams via four-wave mixing in atom vapor," Opt. Express **22**, 20177 (2014).

[87] A. M. Akulshin, I. Novikova, E. E. Mikhailov, S. A. Suslov, and R. J. McLean, "Arithmetic with optical topological charges in stepwise-excited Rb vapor," Opt. Lett. **41**, 1146–1149 (2016).

[88] A. Chopinaud, M. Jacquey, B. Viaris de Lesegno, and L. Pruvost, "High helicity vortex conversion in a rubidium vapor," Phys. Rev. A **97**, 063806 (2018).

[89] D. S. Ding, Z. Y. Zhou, W. Huang, B. S. Shi, X. B. Zou, and G. C. Guo, "Experimental up-conversion of images," Phys. Rev. A **86**, 033803 (2012).

[90] T. Meijer, J. D. White, B. Smeets, M. Jeppesen, and R. E. Scholten, "Blue five-level frequency-upconversion system in rubidium." Opt. Lett. **31**, 1002 (2006).

[91] A. M. Akulshin, R. J. McLean, A. I. Sidorov, and P. Hannaford, "Coherent and collimated blue light generated by four-wave mixing in Rb vapour." Opt. Express **17**, 22861–22870 (2009).

[92] A. Vernier, S. Franke-Arnold, E. Riis, and A. S. Arnold, "Enhanced frequency up-conversion in Rb vapor." Opt. Express **18**, 17020–17026 (2010).

[93] C. V. Sulham, G. A. Pitz, and G. P. Perram, "Blue and infrared stimulated emission from alkali vapors pumped through two-photon absorption," Appl. Phy. B **101**, 57 (2010).

[94] E. Brekke and L. Alderson, "Parametric four-wave mixing using a single cw laser." Opt. Lett. **38**, 2147 (2013).

[95] J. F. Sell, M. A. Gearba, B. D. DePaola, and R. J. Knize, "Collimated blue and infrared beams generated by two-photon excitation in Rb vapor." Optics letters **39**, 528–31 (2014).

[96] A. Akulshin, D. Budker, and R. McLean, "Directional infrared emission resulting from cascade population inversion and four-wave mixing in Rb vapor." Opt. Lett. **39**, 845 (2014).

[97] R. M. Camacho, P. K. Vudyasetu, and J. C. Howell, "Four-wave-mixing stopped light in hot atomic rubidium vapour," Nat. Photon. **3**, 103–106 (2009).

[98] D.-S. Ding, Z.-Y. Zhou, B.-S. Shi, and G.-C. Guo, "Single-photon-level quantum image memory based on cold atomic ensembles," Nat. Commun. **4**, 2527 (2013).

[99] A. Nicolas, L. Veissier, L. Giner, E. Giacobino, D. Maxein, and J. Laurat, "A quantum memory for orbital angular momentum photonic qubits," Nat. Photon. **8**, 234 (2014).

[100] V. Parigi, V. D'Ambrosio, C. Arnold, L. Marrucci, F. Sciarrino, and J. Laurat, "Storage and retrieval of vector beams of light in a multiple-degree-of-freedom quantum memory," Nat. Commun. **6**, 7706 (2015).

[101] J. F. Sell, M. a. Gearba, B. D. DePaola, and R. J. Knize, "Collimated blue and infrared beams generated by two-photon excitation in Rb vapor." Opt. Lett. **39**, 528 (2014).

[102] A. Wang, L. Zhu, S. Chen, C. Du, Q. Mo, and J. Wang, "Characterization of LDPC-coded orbital angular momentum modes transmission and multiplexing over a 50-km fiber," Opt. Express **24**, 11716 (2016).

[103] P. Meystre and M. Sargent, *Elements of Quantum Optics (Google eBook)* (Springer, 2007).

[104] P. Lallemand and N. Bloembergen, "Self-focusing of laser beams and stimulated raman gain in liquids," Phys. Rev. Lett. **15**, 1010 (1965).

[105] L. T. Vuong, T. D. Grow, A. Ishaaya, A. L. Gaeta, G. W. 't Hooft, E. R. Eliel, and G. Fibich, "Collapse of optical vortices," Phys. Rev. Lett. **96**, 133901 (2006).

[106] D. A. Steck, "Rubidium 85 D line data," .

[107] W. Demtröder, *Laser Spectroscopy Volume 1* (Springer, 2008), 4th ed.

[108] A. N. Neseyanov, *Vapor pressure of the chemical elements*, English Edition, edited by Robert Gray (Elsevier, Amsterdam, 1963).

[109] D. R. Lide, ed., *CRC Handbook of Chemistry and Physics* (CRC Press, Boca Raton, 2001), 82nd ed.

[110] A. M. Akulshin, D. Budker, and R. J. McLean, "Parametric wave mixing enhanced by velocity-insensitive two-photon excitation in Rb vapor," J. Opt. Soc. Am. B **34**, 1016 (2017).

[111] J. T. Schultz, S. Abend, D. Döring, J. E. Debs, P. A. Altin, J. D. White, N. P. Robins, and J. D. Close, "Coherent 455 nm beam production in a cesium vapor." Opt. Lett. **34**, 2321–2323 (2009).

[112] G. Morigi, S. Franke-Arnold, and G.-L. Oppo, "Phase-dependent interaction in a four-level atomic configuration," Phys. Rev. A **66**, 053409 (2002).

[113] S. Kajari-Schröder, G. Morigi, S. Franke-Arnold, and G.-L. Oppo, "Phase-dependent light propagation in atomic vapors," Phys. Rev. A **75**, 013816 (2007).

[114] Y. S. Ihn, K.-K. Park, Y. Kim, Y.-T. Chough, and Y.-H. Kim, "Intensity correlation in frequency upconversion via four-wave mixing in rubidium vapor," J. Opt. Soc. Am. B **34**, 2352 (2017).

[115] A. Akulshin, C. Perrella, G.-W. Truong, R. McLean, and A. Luiten, "Frequency evaluation of collimated blue light generated by wave mixing in Rb vapour," J. Phys. B **45**, 245503 (2012).

[116] A. Vernier, "Phase Dependent Atom Optics Faculty of Physical Sciences University of Glasgow," Ph.D. thesis, Glasgow University (2011).

[117] A. M. Akulshin, R. J. Mclean, E. E. Mikhailov, and I. Novikova, "Distinguishing nonlinear processes in atomic media via orbital angular momentum transfer," Opt. Lett. **40**, 1109 (2015).

[118] N. I. P. Rajapati, A. L. M. A. Kulshin, and N. Ovikova, "Comparison of collimated blue light generation in 85 Rb atoms via the D_1 and D_2 lines," J. Opt. Soc. Am. B **35**, 1133 (2018).

[119] A. S. Arnold, J. S. Wilson, and M. G. Boshier, "A simple extended-cavity diode laser," Rev. Sci. Instrum. **69**, 1236 (1998).

[120] E. Arimondo, M. Inguscio, and P. Violino, "Experimental determinations of the hyperfine structure in the alkali atoms," Rev. Mod. Phys. **49**, 31 (1977).

[121] K. B. MacAdam, A. Steinbach, and C. Wieman, "A narrowband tunable diode laser system with grating feedback, and a saturated absorption spectrometer for Cs and Rb," Am. J. Phys. **60**, 1098 (1992).

[122] D. A. Smith and I. G. Hughes, "The role of hyperfine pumping in multilevel systems exhibiting saturated absorption," Am. J. Phys. **72**, 631 (2004).

[123] F. Biraben, B. Cagnac, and G. Grynberg, "Experimental evidence of two-photon transition without doppler broadening," Phys. Rev. Lett. **32**, 643 (1974).

[124] T. W. Hänsch, K. C. Harvey, G. Meisel, and A. L. Schawlow, "Two-photon spectroscopy without doppler broadening using a CW dye laser," IEEE J. Qauntum Elec. **11**, 50 (1974).

[125] M. D. Levenson and N. Bloembergen, "Observation of two-photon absorption without doppler broadening on the 3S-5S transition in sodium vapor," Phys. Rev. Lett. **32**, 645 (1974).

[126] F. Nez, F. Biraben, R. Felder, and Y. Millerioux, "Optical frequency determination of the hyperfine components of the $5s_{1/2}$-$5D_{3/2}$ two-photon transitions in rubidium," Opt. Commun. **102**, 432 (1993).

[127] P. Siddons, C. S. Adams, C. Ge, and I. G. Hughes, "Absolute absorption on rubidium D lines: Comparison between theory and experiment," J. Phys. B **41**, 155004 (2008).

[128] G. D. Rovera, G. Santarelli, and A. Clairon, "A laser diode system stabilized on the Caesium D_2 line," Rev. Sci. Instrum. **65**, 1502 (1994).

[129] K. L. Corwin, Z. T. Lu, C. F. Hand, R. J. Epstein, and C. E. Wieman, "Frequency-stabilized diode laser with the Zeeman shift in an atomic vapor." Appl. Opt. **37**, 3295 (1998).

[130] V. V. Yashchuk, D. Budker, and J. R. Davis, "Laser frequency stabilization using linear magneto-optics," Rev. Sci. Instrum. **71**, 341 (2000).

[131] A. Millett-Sikking, I. G. Hughes, P. Tierney, and S. L. Cornish, "DAVLL lineshapes in atomic rubidium," J. Phys. B **40**, 187 (2007).

[132] T. W. Clark, "Sculpting shadows," Ph.D. thesis (2016).

[133] S. M. Barnett and R. Zambrini, *Quantum Imaging,* ed. Mikhail I. Kolobov (Springer, 2007).

[134] R. A. Beth, "Mechanical detection and measurement of the angular momentum of light," Phys. Rev. **50**, 115 (1936).

[135] C. G. Darwin, "Notes on the theory of radiation," Proc. R. Soc. Lond., A Contain. Pap. Math. Phys. Character **136**, 36 (1932).

[136] L. Allen and M. J. Padgett, "Poynting vector in Laguerre-Gaussian beams and the interpretation of their angular momentum density," Opt. Commun. **184**, 67 (2000).

[137] M. E. J. Friese, T. A. Nieminen, N. R. Heckenberg, and H. Rubinsztein-Dunlop, "Optical alignment and spinning of laser-trapped microscopic particles," Nature **394**, 348 (1998).

[138] Y. Arita, M. Mazilu, and K. Dholakia, "Laser-induced rotation and cooling of a trapped microgyroscope in vacuum," Nat. Commun. **4**, 2374 (2013).

[139] A. T. O'Neil, I. MacVicar, L. Allen, and M. J. Padgett, "Intrinsic and extrinsic nature of the orbital angular momentum of a light beam," Phys. Rev. Lett. **88**, 053601 (2002).

[140] V. Garcés-Chávez, D. McGloin, M. J. Padgett, W. Dultz, H. Schmitzer, and K. Dholakia, "Observation of the transfer of the local angular momentum density of a multiringed light beam to an optically trapped particle," Phys. Rev. Lett. **91**, 093602 (2003).

[141] P. Galajda and P. Ormos, "Complex micromachines produced and driven by light," Appl. Phys. Lett. **78**, 249 (2001).

[142] G. Knöner, S. Parkin, T. A. Nieminen, V. L. Y. Loke, N. R. Heckenberg, and H. Rubinsztein-Dunlop, "Integrated optomechanical microelements," Opt. Express **15**, 5521 (2007).

[143] M. F. Andersen, C. Ryu, P. Cladé, V. Natarajan, A. Vaziri, K. Helmerson, and W. D. Phillips, "Quantized rotation of atoms from photons with orbital angular momentum," Phys. Rev. Lett. **97**, 170406 (2006).

[144] C. Ryu, M. F. Andersen, P. Cladé, V. Natarajan, K. Helmerson, and W. D. Phillips, "Observation of persistent flow of a Bose-Einstein condensate in a toroidal trap," Phys. Rev. Lett. **99**, 260401 (2007).

[145] G. U. Xie, Y. O. Ren, Y. Yan, H. Huang, N. Ahmed, L. Long, Z. Zhao, C. Bao, M. Tur, S. Ashrafi, and A. E. Willner, "Experimental demonstration of a 200-Gbit/s free-space optical link by multiplexing Laguerre-Gaussian beams with different radial indices," Opt. Lett. **41**, 3447 (2016).

[146] M. Mafu, A. Dudley, S. Goyal, D. Giovannini, M. McLaren, M. J. Padgett, T. Konrad, F. Petruccione, N. Lütkenhaus, and A. Forbes, "Higher-dimensional orbital-angular-momentum-based quantum key distribution with mutually unbiased bases," Phys. Rev. A **88**, 032305 (2013).

[147] M. Mirhosseini, O. S. Magaña-Loaiza, M. N. O'Sullivan, B. Rodenburg, M. Malik, M. P. Lavery, M. J. Padgett, D. J. Gauthier, and R. W. Boyd, "High-dimensional quantum cryptography with twisted light," N. J. Phys. **17**, 033033 (2015).

[148] R. Oron, N. Davidson, A. a. Friesen, and E. Hasman, *Chapter 6, Transverse mode shaping and selection in laser resonators in Progress in Optics,* Ed. E. Wolf, vol. 42 (Elsevier, 2001).

[149] M. W. Beijersbergen, L. Allen, H. E. L. O. van der Veen, and J. P. Woerdman, "Astigmatic laser mode converters and transfer of orbital angular momentum," Opt. Commun. **96**, 123 (1993).

[150] V. Y. Bazhenov, M. V. Vasnetsov, and M. S. Soskin, "Laser beams with screw dislocations in their wavefronts," JETP Lett. **52**, 429 (1990).

[151] M. W. Beijersbergen, R. P. C. Coerwinkel, M. Kristensen, and J. P. Woerdman, "Helical-wave-front laser-beams produced with a spiral phaseplate," Opt. Commun. **112**, 321 (1994).

[152] L. Marrucci, C. Manzo, and D. Paparo, "Optical spin-to-orbital angular momentum conversion in inhomogeneous anisotropic media," Phys. Rev. Lett. **96**, 163905 (2006).

[153] M. Mirhosseini, O. S. Magana-Loaiza, C. Chen, B. Rodenburg, M. Malik, and R. W. Boyd, "Rapid generation of light beams carrying orbital angular momentum," Opt. Express **21**, 30204 (2013).

[154] D. Gabor, "A new microscopic principle," Nature **161**, 777 (1948).

[155] L. G. Neto, D. Roberge, and Y. Sheng, "Full-range, continuous, complex modulation by the use of two coupled-mode liquid-crystal televisions." Appl. Opt. **35**, 4567 (1996).

[156] L. Zhu and J. Wang, "Arbitrary manipulation of spatial amplitude and phase using phase-only spatial light modulators," Sci. Rep. **4**, 7441 (2014).

[157] S. Tao and W. Yu, "Beam shaping of complex amplitude with separate constraints on the output beam," Opt. Express **23**, 1052 (2015).

[158] L. Wu, S. Cheng, and S. Tao, "Simultaneous shaping of amplitude and phase of light in the entire output plane with a phase-only hologram," Sci. Rep. **5**, 15426 (2015).

[159] D. Bowman, T. L. Harte, V. Chardonnet, C. D. Groot, S. J. Denny, G. L. Goc, M. Anderson, P. Ireland, D. Cassettari, and G. D. Bruce, "High-fidelity phase and amplitude control of phase-only computer generated holograms using conjugate gradient minimisation," Opt. Express **25**, 11692 (2017).

[160] J. P. Kirk and A. L. Jones, "Phase-only complex-valued spatial filter," J. Opt. Soc. Am. **61**, 1023 (1971).

[161] R. W. Cohn and M. Liang, "Approximating fully complex spatial modulation with pseudorandom phase-only modulation," Appl. Opt. **33**, 4406 (1994).

[162] V. Arrizón, U. Ruiz, G. Mendez, and A. Apolinar-Iribe, "Zero order synthetic hologram with a sinusoidal phase carrier for generation of multiple beams," Opt. Express **17**, 2663 (2009).

[163] J. Albero, P. García-Martínez, J. L. Martínez, and I. Moreno, "Second order diffractive optical elements in a spatial light modulator with large phase dynamic range," Opt. Lasers Eng. **51**, 111 (2013).

[164] A. S. Ostrovsky, C. Rickenstorff-Parrao, and V. Arrizón, "Generation of the "perfect" optical vortex using a liquid-crystal spatial light modulator," Opt. Lett. **38**, 534 (2013).

[165] A. Forbes, A. Dudley, and M. McLaren, "Creation and detection of optical modes with spatial light modulators," Adv. Opt. Photonics **8**, 200 (2016).

[166] J. A. Davis, D. M. Cottrell, J. Campos, M. J. Yzuel, and I. Moreno, "Encoding amplitude information onto phase-only filters." Appl. Opt. **38**, 5004 (1999).

[167] V. Arrizón, U. Ruiz, R. Carrada, and L. A. González, "Pixelated phase computer holograms for the accurate encoding of scalar complex fields," J. Opt. Soc. Am. A **24**, 3500 (2007).

[168] T. Ando, Y. Ohtake, N. Matsumoto, T. Inoue, and N. Fukuchi, "Mode purities of Laguerre-Gaussian beams generated via complex-amplitude modulation using phase-only spatial light modulators." Opt. Lett. **34**, 34 (2009).

[169] E. Bolduc, N. Bent, E. Santamato, E. Karimi, and R. W. Boyd, "Exact solution to simultaneous intensity and phase encryption with a single phase-only hologram," Opt. Lett. **38**, 3546 (2013).

[170] S. S. Welsh, M. P. Edgar, R. Bowman, P. Jonathan, B. Sun, and M. J. Padgett, "Fast full-color computational imaging with single-pixel detectors," Opt. Express **21**, 23068 (2013).

[171] N. Radwell, K. J. Mitchell, G. M. Gibson, M. P. Edgar, R. Bowman, and M. J. Padgett, "Single-pixel infrared and visible microscope," Optica **1**, 285 (2014).

[172] T. Čižmár, M. Mazilu, and K. Dholakia, "In situ wavefront correction and its application to micromanipulation," Nat. Photon. **4**, 388 (2010).

[173] Q. Huynh-Thu and M. Ghanbari, "Scope and validity of PSNR in image/video quality assessment," Electron. Lett. **44**, 800 (2008).

[174] V. A. Henderson, P. F. Griffin, E. Riis, and A. S. Arnold, "Comparative simulations of Fresnel holography methods for atomic waveguides," New J. Phys. **18**, 025007 (2016).

[175] A. Bergeron, J. Gauvin, F. Gagnon, D. Gingras, H. H. Arsenault, and M. Doucet, "Phase calibration and applications of a liquid-crystal spatial light modulator," Appl. Opt. **34**, 5133 (1995).

[176] P. Clemente, V. Durán, L. Martínez-León, V. Climent, E. Tajahuerce, and J. Lancis, "Use of polar decomposition of Mueller matrices for optimizing the phase response of a liquid-crystal-on-silicon display," Opt. Express **16**, 1965 (2008).

[177] F. P. Ferreira and M. S. Belsley, "Direct calibration of a spatial light modulator by lateral shearing interferometry," Opt. Express **18**, 7899 (2010).

[178] J. Xia, C. Chang, Z. Chen, Z. Zhu, T. Zeng, P. Y. Liang, and J. Ding, "Pixel-addressable phase calibration of spatial light modulators: A common-path phase-shifting interferometric microscopy approach," J. Opt. **19**, 125701 (2017).

[179] M. Takeda, H. Ina, and S. Kobayashi, "Fourier-transform method of fringe-pattern analysis for computer-based topography and interferometry," J. Opt. Soc. Am. **72**, 156 (1982).

[180] R. W. Bowman, A. J. Wright, and M. J. Padgett, "An SLM-based Shack-Hartmann wavefront sensor for aberration correction in optical tweezers," J. Opt. **12**, 124004 (2010).

[181] D. Engström, M. Persson, J. Bengtsson, and M. Goksör, "Calibration of spatial light modulators suffering from spatially varying phase response," Opt. Express **21**, 16086 (2013).

[182] G. Rui, B. Gu, Y. Cui, and Q. Zhan, "Detection of orbital angular momentum using a photonic integrated circuit," Sci. Rep. **6**, 28262 (2016).

[183] G. C. Berkhout, M. P. Lavery, J. Courtial, M. W. Beijersbergen, and M. J. Padgett, "Efficient sorting of orbital angular momentum states of light," Phys. Rev. Lett. **105**, 153601 (2010).

[184] J. Leach, M. Padgett, S. Barnett, S. Franke-Arnold, and J. Courtial, "Measuring the Orbital Angular Momentum of a Single Photon," Phys. Rev. Lett. **88**, 257901 (2002).

[185] N. González, G. Molina-Terriza, and J. P. Torres, "How a Dove prism transforms the orbital angular momentum of a light beam." Opt. Express **14**, 9093 (2006).

[186] A. Dudley, T. Mhlanga, M. Lavery, A. McDonald, F. S. Roux, M. Padgett, and A. Forbes, "Efficient sorting of Bessel beams," Opt. Express **21**, 165 (2013).

[187] M. P. Lavery, D. J. Robertson, A. Sponselli, J. Courtial, N. K. Steinhoff, G. A. Tyler, A. E. Wilner, and M. J. Padgett, "Efficient measurement of an optical orbital-angular-momentum spectrum comprising more than 50 states," New J. Phys. **15**, 013024 (2013).

[188] D. Flamm, D. Naidoo, C. Schulze, A. Forbes, and M. Duparre, "Mode analysis with a spatial light modulator as a correlation filter," Opt. Lett. **37**, 2478 (2012).

[189] L. Fahrmeir, T. Kneib, S. Lang, and B. Marx, *Regression Models, Methods and Applications* (Springer, 2013).

[190] J. Courtial, K. Dholakia, L. Allen, and M. J. Padgett, "Second-harmonic generation and the conservation of orbital angular momentum with high-order Laguerre-Gaussian modes," Phys. Rev. A **56**, 4193 (1997).

[191] Z. Y. Zhou, S. L. Liu, Y. Li, D. S. Ding, W. Zhang, S. Shi, M. X. Dong, B. S. Shi, and G. C. Guo, "Orbital angular momentum-entanglement frequency transducer," Phys. Rev. Lett. **117**, 103601 (2016).

[192] F. Steinlechner, N. Hermosa, V. Pruneri, and J. P. Torres, "Frequency conversion of structured light," Sci. Rep. **6**, 21390 (2015).

[193] F. M. Miatto, A. M. Yao, and S. M. Barnett, "Full characterization of the quantum spiral bandwidth of entangled biphotons," Phys. Rev. A **83**, 033816 (2011).

[194] A. M. Yao, "Angular momentum decomposition of entangled photons with an arbitrary pump," New J. Phys. **13**, 053048 (2011).

[195] M. Agnew, J. Leach, M. Mclaren, F. S. Roux, and R. W. Boyd, "Tomography of the quantum state of photons entangled in high dimensions," Phys. Rev. A **84**, 062101 (2011).

[196] J. Leach, B. Jack, J. Romero, M. Ritsch-Marte, R. W. Boyd, A. K. Jha, S. M. Barnett, S. Franke-Arnold, and M. J. Padgett, "Violation of a Bell inequality in two-dimensional orbital angular momentum state-spaces," Opt. Express **17**, 8287 (2009).

[197] A. C. Dada, J. Leach, G. S. Buller, M. J. Padgett, and E. Andersson, "Experimental high-dimensional two-photon entanglement and violations of generalized Bell inequalities," Nat. Phys. **7**, 677 (2011).

[198] S. Gröblacher, T. Jennewein, A. Vaziri, G. Weihs, and A. Zeilinger, "Experimental quantum cryptography with qutrits," New J. Phys. **8** (2006).

[199] G. Vallone, V. D'Ambrosio, A. Sponselli, S. Slussarenko, L. Marrucci, F. Sciarrino, and P. Villoresi, "Free-space quantum key distribution by rotation-invariant twisted photons," Phys. Rev. Lett. **113**, 060503 (2014).

[200] D.-s. Ding, M.-x. Dong, W. Zhang, S. Shi, Y.-c. Yu, Y.-h. Ye, G.-c. Guo, and B.-s. Shi, "Experimental demonstration of quantum wrenching orbital angular momentum memory," arXiv[quant-ph]1806.10407 (2018).

[201] R. N. Lanning, Z. Xiao, M. Zhang, I. Novikova, E. E. Mikhailov, and J. P. Dowling, "Gaussian-beam-propagation theory for nonlinear optics involving an analytical treatment of orbital-angular-momentum transfer," Phys. Rev. A **96**, 013830 (2017).

[202] G. D. Boyd and D. A. Kleinman, "Parametric interaction of focused gaussian light beams," J. Appl. Phys. **39**, 3597 (1968).

[203] J. Leach, E. Bolduc, D. J. Gauthier, and R. W. Boyd, "Secure information capacity of photons entangled in many dimensions," Phys. Rev. A **85**, 060304(R) (2012).

[204] G. Walker, "Trans-spectral transfer of orbital angular momentum and creation of an ultra high density cold atom trap," Ph.D. thesis, University of Glasgow (2013).

[205] R. F. Offer, D. Stulga, E. Riis, S. Franke-Arnold, and A. S. Arnold, "Spiral banwidth of four wave mixing in Rb vapour dataset," http://dx.doi.org/10.15129/96db0ebb-aace-494f-8e61-d4a064fcadbb (2018).

[206] B. Jack, J. Leach, H. Ritsch, S. M. Barnett, M. J. Padgett, and S. Franke-Arnold, "Precise quantum tomography of photon pairs with entangled orbital angular momentum," N. J. Phys. **11**, 103024 (2009).

[207] L. J. Pereira, W. T. Buono, D. S. Tasca, K. Dechoum, and A. Z. Khoury, "Orbital-angular-momentum mixing in type-II second-harmonic generation," Phys. Rev. A **96**, 053856 (2017).

[208] C. Fabre, P. F. Cohadon, and C. Schwob, "CW optical parametric oscillators: single mode operation and frequency tuning properties," Quantum Semiclass. Opt. **9**, 165 (1997).

[209] E. E. Mikhailov, J. Evans, D. Budker, S. M. Rochester, and I. Novikova, "Four-wave mixing in a ring cavity," Opt. Eng. **53**, 102709 (2015).

[210] D. Kutzke, O. Wolfe, S. Rochester, D. Budker, I. Novikova, and E. Mikhailov, "Tailorable dispersion in a four-wave mixing laser," Opt. Lett. **42**, 2846 (2017).

[211] H. Zhou, Y. Han, S. Che, D. Wang, and J. Zhang, "Resonant intracavity four-wave mixing in a composite atom-cavity system," Opt. Commun. **425**, 38–43 (2018).

[212] A. Schilke, C. Zimmermann, P. W. Courteille, and W. Guerin, "Optical parametric oscillation with distributed feedback in cold atoms," Nat. Photon. **6**, 101 (2012).

[213] G. R. Fowles, *Introduction to Modern Optics* (Dover, 1989), 2nd ed.

[214] E. Brekke and E. Herman, "Frequency characteristics of far-detuned parametric four-wave mixing in Rb," Opt. Lett. **40**, 5674 (2015).

[215] F. Zernike and J. E. Midwinter, *Applied Nonlinear Optics* (John Wiley & Sons, 1973).

[216] F. J. Duarte, *Tunable Lasers Handbook* (Academic Press, 1995).

[217] E. L. Lewis, "Collisional relaxation of atomic excited states, line broadening and interatomic interactions," Phys. Rep. **58**, 1 (1980).

[218] L. Weller, R. J. Bettles, P. Siddons, C. S. Adams, and I. G. Hughes, "Absolute absorption on the rubidium D1 line including resonant dipole-dipole interactions." J. Phys. B **44**, 195006 (2011).

[219] A. Akulshin, C. Perrella, G.-W. Truong, A. Luiten, D. Budker, and R. McLean, "Linewidth of collimated wavelength-converted emission in Rb vapour," Appl. Phys. B **117**, 203 (2014).

[220] P. M. Duarte, R. A. Hart, J. M. Hitchcock, T. A. Corcovilos, T.-L. Yang, A. Reed, and R. G. Hulet, "All-optical production of a lithium quantum gas using narrow-line laser cooling," Phys. Rev. A **84**, 061406(R) (2011).

[221] D. C. Mckay, D. Jervis, D. J. Fine, J. W. Simpson-Porco, G. J. A. Edge, and J. H. Thywissen, "Low-temperature high-density magneto-optical trapping of potassium using the open 4S$\rightarrow$ 5P transition at 405 nm," Phys. Rev. A **84**, 063420 (2011).

[222] T. Okoshi, K. Kikuchi, and A. Nakayama, "Novel method for high resolution measurement of laser output spectrum," Electron. Lett. **16**, 630 (1980).

[223] J. F. Young, R. B. Miles, and S. E. Harris, "Pump Linewidth Requirement for Optical Parametric Oscillators," J Appl. Phys. **42**, 497 (1971).

[224] S. Ngcobo, I. Litvin, L. Burger, and A. Forbes, "A digital laser for on-demand laser modes." Nat. Commun. **4**, 2289 (2013).

[225] M. Martinelli, J. A. O. Huguenin, P. Nussenzveig, and A. Z. Khoury, "Orbital angular momentum exchange in an optical parametric oscillator," Phys. Rev. A **70**, 013812 (2004).

[226] B. C. Santos, A. Z. Khoury, and J. A. O. Huguenin, "Transfer of orbital angular momentum in a multimode parametric oscillator," Opt. Lett. **33**, 2803 (2008).

[227] A. Abulikemu, T. Yusufu, R. Mamuti, S. Araki, K. Miyamoto, and T. Omatsu, "Octave-band tunable optical vortex parametric oscillator," Opt. Express **24**, 15204 (2016).

[228] E. Brekke and S. Potier, "Optical cavity for enhanced parametric four-wave mixing in rubidium," Appl. Opt. **56**, 46 (2017).

[229] U. Rapol, A. Krishna, and V. Natarajan, "Precise measurement of hyperfine structure in the $5P_{3/2}$ state of ^{85}Rb," Eur. Phys. J. D **23**, 185 (2003).

[230] S. Bize, Y. Sortais, M. S. Santos, C. Mandache, A. Clairon, and C. Salomon, "High-accuracy measurement of the ^{87}Rb ground-state hyperne splitting in an atomic fountain," Europhys. Lett. **45**, 558 (1999).

[231] J. Ye, S. Swartz, P. Jungner, and J. L. Hall, "Hyperfine structure and absolute frequency of the ^{87}Rb $5P_{3/2}$ state," Opt. Lett. **21**, 1280 (1996).

[232] M. S. Safronova and U. I. Safronova, "Critically evaluated theoretical energies, lifetimes, hyperfine constants, and multipole polarizabilities in ^{87}Rb," Phys. Rev. A **83**, 052508 (2011).

[233] L. Aldridge, P. L. Gould, and E. E. Eyler, "Experimental isotope shifts of the $5^2S_{1/2}$ state and low-lying excited states of Rb," Phys. Rev. A **84**, 034501 (2011).

[234] R. L. Kurucz and B. Bell, "Atomic line data," https://www.cfa.harvard.edu (1995).

[235] O. S. Heavens, "Radiative Transition Probabilities of the Lower Excited States of the Alkali Metals," J. Opt. Soc. Am. **51**, 1058 (1961).

Appendix A

Rubidium atomic structure

The relevant atomic states of ^{85}Rb and ^{87}Rb are shown in Figs. A.1 and A.2, respectively. The hyperfine structure of each state was calculated following Ref. [120] using magnetic dipole constants, A, and electric quadrupole constants, B, shown below in table A.1. The relative energy of the ^{85}Rb and ^{87}Rb atomic states is given by the isotope shift, values for which are shown in table A.2. Transition parameters, including the linewidth, Γ, and saturation intensity, I_{sat}, are shown in table A.3, with the branching ratio of the allowed transitions from each state given in table A.4.

Atomic state	A (MHz)	B (MHz)	Source
^{85}Rb $5S_{1/2}$	1011.910813(2)	-	[120]
^{85}Rb $5P_{3/2}$	25.038(5)	26.011(22)	[229]
^{85}Rb $5D_{5/2}$	-2.1911(12)	2.6804(200)	[126]
^{85}Rb $6P_{3/2}$	8.179(12)	8.190(49)	[120]
^{87}Rb $5S_{1/2}$	3417.341305452145(45)	-	[230]
^{87}Rb $5P_{3/2}$	84.7185(20)	12.4965(37)	[231]
^{87}Rb $5D_{5/2}$	-7.4923(3)	1.2713(20)	[126]
^{87}Rb $6P_{3/2}$	27.700(17)	3.953(24)	[120, 232]

Table A.1: Rb hyperfine structure constants.

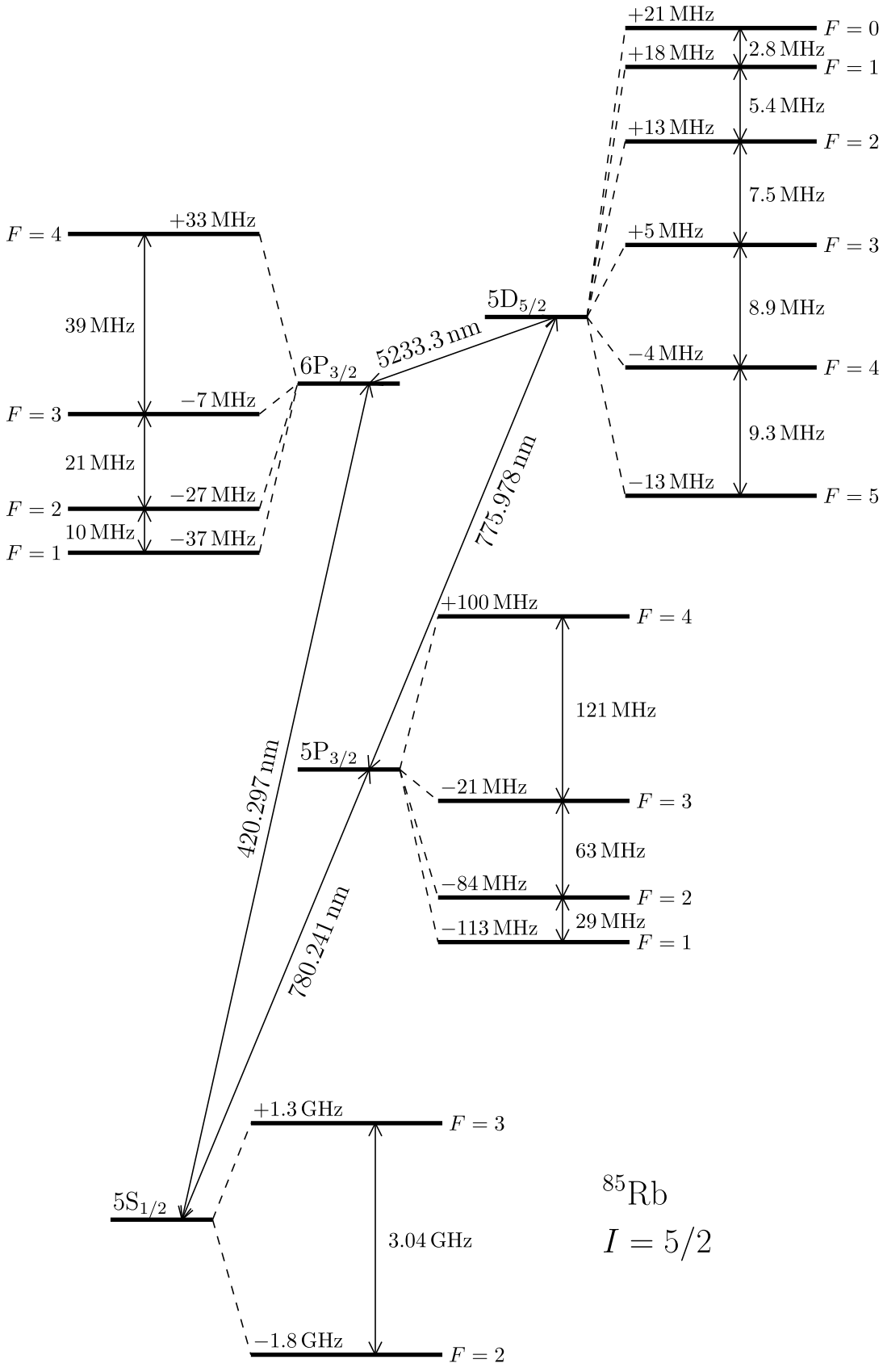

Figure A.1: Relevant ^{85}Rb atomic states.

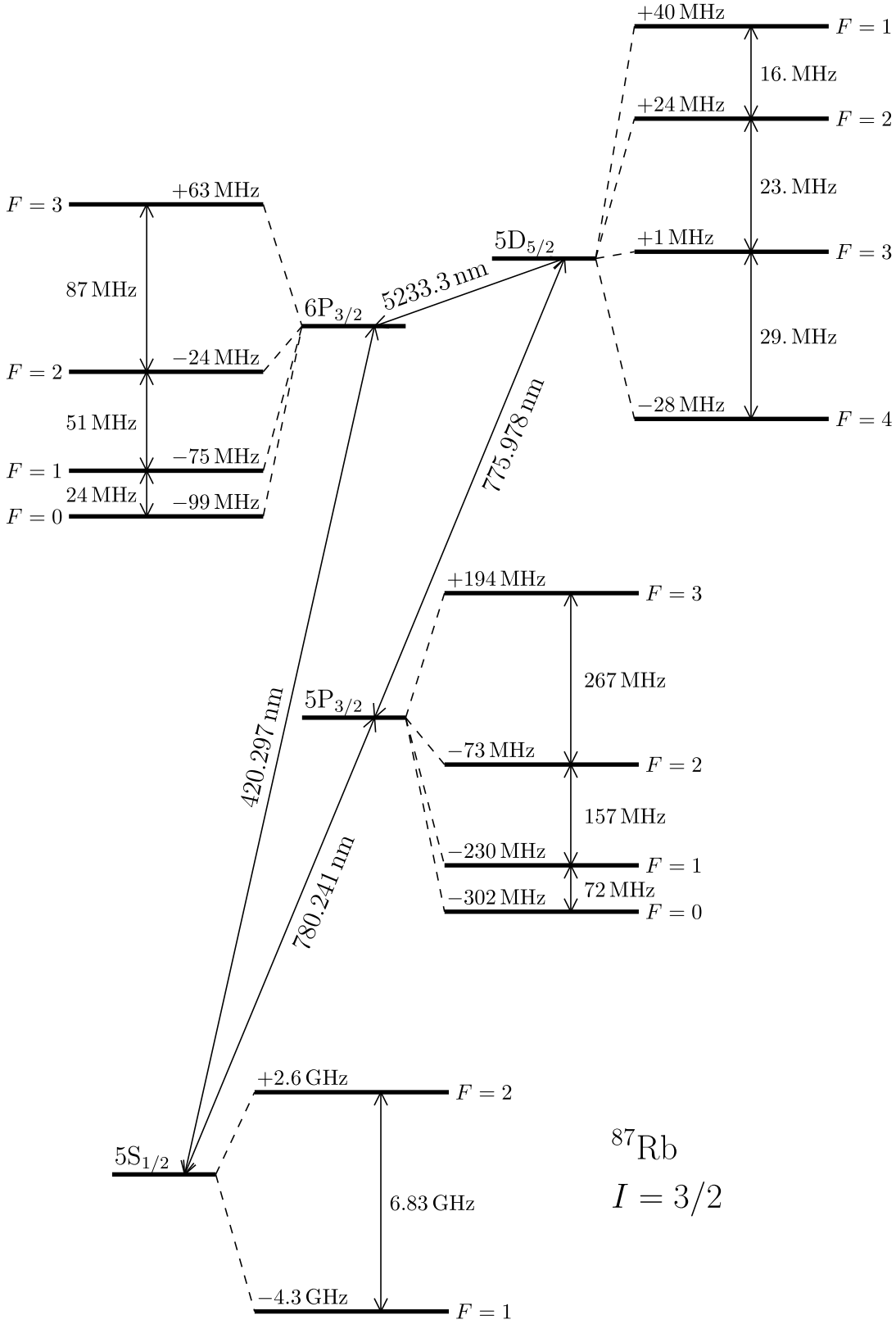

Figure A.2: Relevant ^{87}Rb atomic states.

Atomic state	$\delta^{85-87} = (E_{85} - E_{87})/h$ (MHz)
$5S_{1/2}$	164.35(95)
$5P_{3/2}$	86.31(95)
$5D_{5/2}$	1.32(95)
$6P_{3/2}$	40.2(12)

Table A.2: Isotope shift, δ^{85-87}, of each atomic state. Values taken from Ref. [233].

Transition	λ (nm)	Γ (MHz)	I_{sat} (mW/cm^2)	f
$5S_{1/2} \rightarrow 5P_{3/2}$	780.241	6.0	1.64	0.69
$5P_{3/2} \rightarrow 5D_{5/2}$	775.978	0.43	0.12	0.073
$6P_{3/2} \rightarrow 5D_{5/2}$	5233.3	0.23	0.00021	1.78
$5S_{1/2} \rightarrow 6P_{3/2}$	420.297	0.58	1.03	0.019

Table A.3: Rb transition parameters. Wavelength, λ, and linewidth, Γ, extracted from Ref. [234]. Saturation intensity, I_{sat}, calculated using $I_{\text{sat}} = \frac{\hbar\omega^3\Gamma}{12\pi c^2}$. Absorption oscillator strength, f, calculated using $f = (2J'+1)/(2J+1)(4\pi^2\varepsilon_0 m_e c^3\Gamma)/(e^2\omega_0^2)$.

Transition		Wavelength (nm)	Branching ratio
$5P_{3/2}$	$\rightarrow 5S_{1/2}$	780	1
$5D_{5/2}$	$\rightarrow 5P_{3/2}$	776	0.65
	$\rightarrow 6P_{3/2}$	5233	0.35
$6P_{3/2}$	$\rightarrow 5S_{1/2}$	420	0.31
	$\rightarrow 6S_{1/2}$	2732	0.49
	$\rightarrow 4D_{5/2}$	2253	0.18
	$\rightarrow 4D_{3/2}$	2253	0.020

Table A.4: Branching ratios of rubidium transitions extracted from Ref. [235], wavelengths from [234].

Appendix B

Heated rubidium cells

This appendix includes details on the dependence of the rubidium vapour pressure on temperature, as well as current-temperature calibration curves for the 75 mm and 10 mm heated cells.

B.1 Rubidium vapour pressure

The equilibrium vapour pressure of solid rubidium, P_{S} (in Torr), at temperature, T, is given by [108]

$$\log_{10} P_{\mathrm{S}} = -94.04826 - \frac{1961.258}{T} - 0.03771687 \times T + 42.57526 \times \log_{10} T. \quad \text{(B.1.1)}$$

The melting point of rubidium is 39.31°C [109]. Above this temperature the vapour pressure for liquid rubidium, P_{L}, must be used

$$\log_{10} P_{\mathrm{L}} = 15.88253 - \frac{4529.635}{T} - 0.00058663 \times T - 2.99138 \times \log_{10} T. \quad \text{(B.1.2)}$$

From these equations, the vapour pressure in Pascals is found by multiplying by a factor of 133.323, and the partial pressure of ^{85}Rb and ^{87}Rb can be found by multiplying by their relative abundances, 72.17% and 27.83%, respectively [109].

The number density, N, can be calculated from the vapour pressure, P (in Pa), using

$$N = \frac{P}{k_{\mathrm{B}} T}. \quad \text{(B.1.3)}$$

Fig. B.1 shows the partial vapour pressure and number density of ^{85}Rb and ^{87}Rb as a function of temperature. The most often used temperatures in this thesis are marked by light grey lines as a guide. A temperature change of 40°C covers a range of more than one order of magnitude in both pressure and number density.

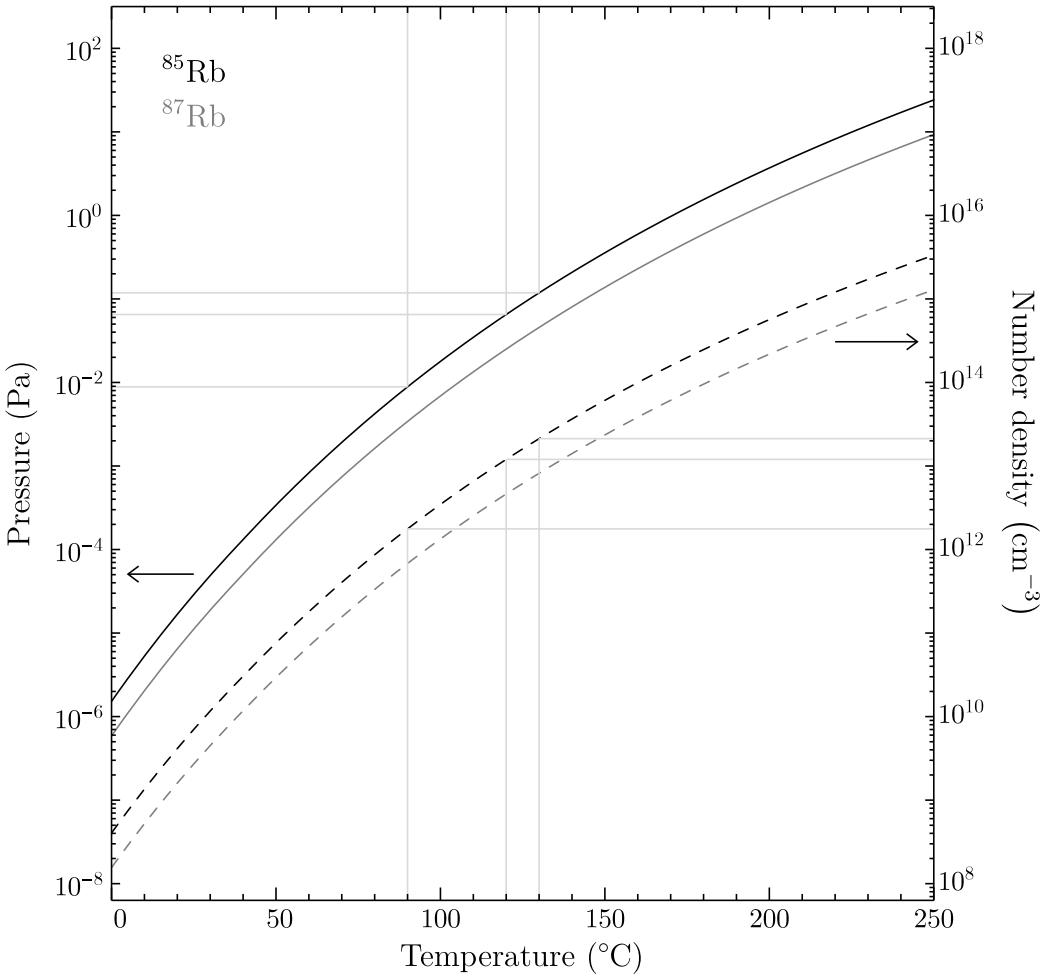

Figure B.1: Partial vapour pressure (solid lines) and number density (dashed lines) of ^{85}Rb (black) and ^{87}Rb (grey) as a function of temperature. The light grey lines provide guides for the most commonly used temperatures in this thesis: 90, 120 and 130°C.

B.2 75 mm cell

Early FWM experiments at the start of this thesis were carried out in a 75 mm long heated rubidium cell. This cell was also used for the 420 nm saturated absorption spectroscopy setup used in Chapter 7. The temperature vs heater current calibration curve is included here for reference (Fig. B.2). The temperature measurements were carried out using the same procedure as described in Sec. 3.3.

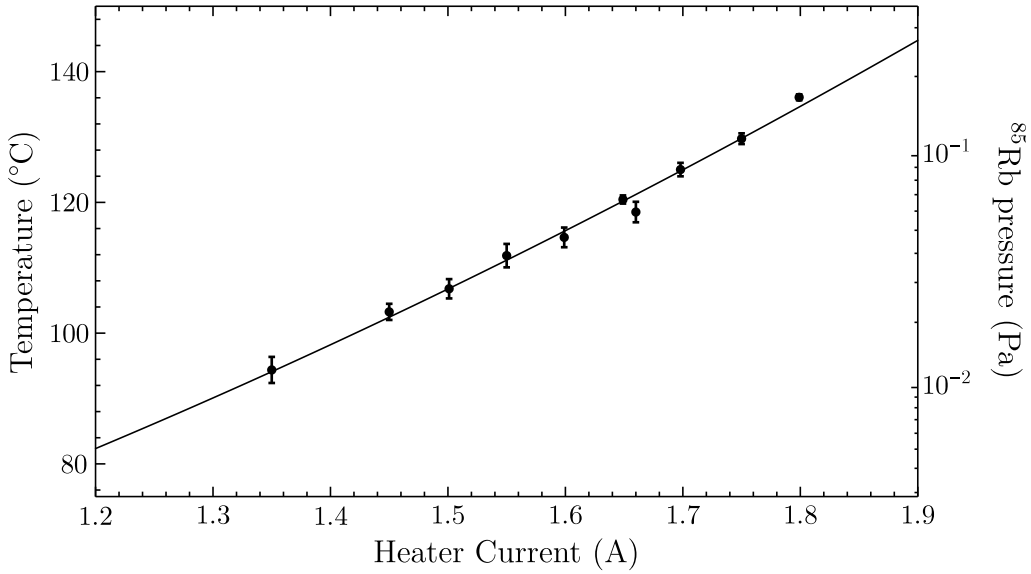

Figure B.2: Temperature versus heater current calibration of the 75 mm long cell. The error bars show the standard error in each measurement.

B.3 10 mm cell

A 10 mm long heated rubidium cell was used for the two-photon spectroscopy 776 nm lock in chapters 5 and 6. The temperature vs heater current calibration curve for this cell is included here for future reference. These temperature measurements were carried out using a combination of the method described in Sec. 3.3 and also by directly fitting the Doppler broadened transmission spectrum with the theoretical, temperature dependent Voigt profile.

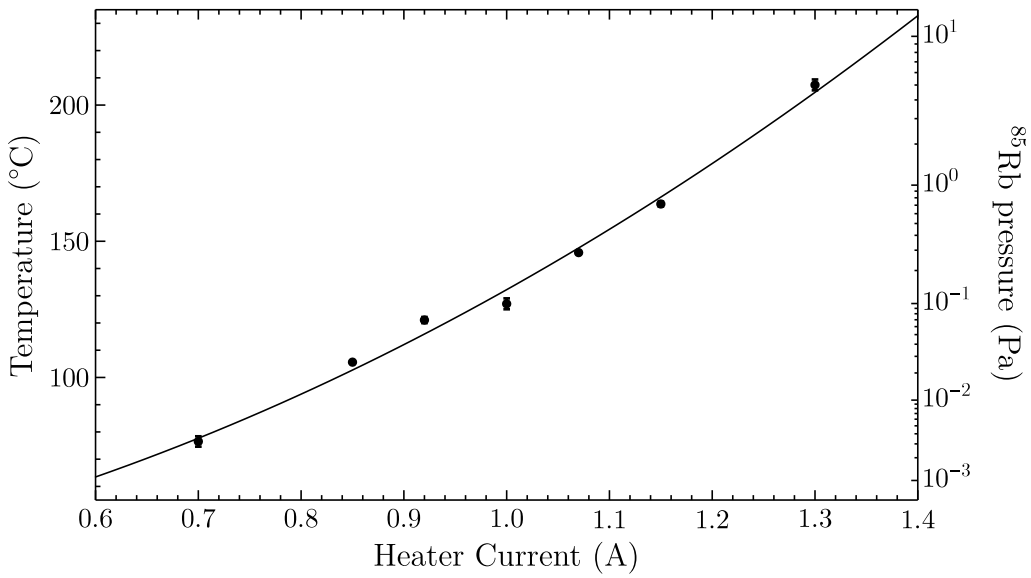

Figure B.3: Temperature versus heater current calibration of the 10 mm long cell. The error bars show the standard error in each measurement.

This cell is also anti-reflection coated and was originally purchased after carrying out the cavity-enhanced FWM experiment with a view to decreasing the round trip losses. Initial measurements of the transmission of an off resonance 420 nm beam showed that 92(1)% of the light was transmitted through the cell.

Appendix C

DAVLL lock electronics

The difference photodiode circuit developed for the DAVLL lock is shown in Fig. C.1, along with the subsequent amplification and inverting stages. The inverting stage allows the sign of the error signal gradient to be flipped, which may be necessary if the raw DAVLL signal is anti-locking rather than locking.

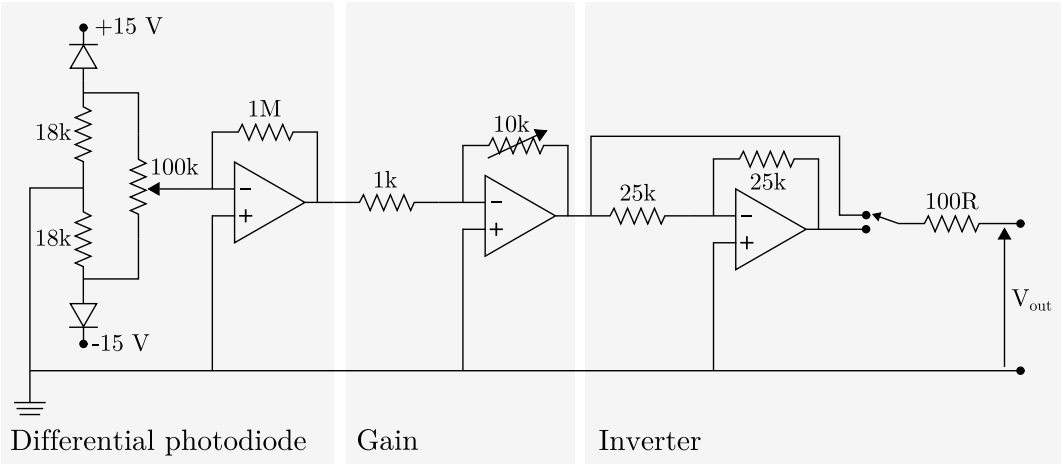

Figure C.1: Electronic circuit used to generate the error signal for the DAVLL lock.